**EECMS**

# Looking Through Rainbow Coloured Glasses: Radio Spectral Variability and its Physical Origins

**Kathryn Ross**
0000-0002-8666-6588

This thesis is presented for the Degree of
Doctor of Philosophy
of
Curtin University

August 2022

To the best of my knowledge and belief this thesis contains no material previously published by any other person except where due acknowledgement has been made. This thesis contains no material which has been accepted for the award of any other degree or diploma in any university.

Kathryn Ross

*"You've had an advantage because you obviously just got in to make a quota when you wouldn't have otherwise."*

— An ex-friend

# Acknowledgements

First and foremost, I acknowledge the Noongar people as the owners and custodians of Wadjak Noongar Boodjar, the land on which the majority of this work was completed.

This thesis may have taken 3.5 years, but it is the culmination of decades of work and the goal of a young, keen, inquisitive kid. It has been made possible by so many people throughout my life, sparking interest, encouraging me, and planting the idea of being a scientist. To all the people who have been a part of my life in this time, thank you.

To my supervisors. To Joe, who always encouraged new ideas and never doubted my capacity to fill them. To Nick, for the countless hours of observing and for spotting the connections when I become too focused to notice. And to Natasha, who took a chance on a keen student from the other side of the country with no experience in radio astronomy or galaxies, thank you for seeing my potential and taking the time to help me in more ways than I can count. When I started this PhD, I had crippling self doubt and Imposter Syndrome. Thanks to each of you, for not only helping me grow as a scientist but for helping me grow as a person with confidence in myself. I would not be the scientist I am today without you.

Thank you to my family. All of you made sure to keep me grounded when my head grew too big but were never short on support. I could always count on the encouragement and excitement about my project even when no one had any idea what I was doing. Thank you for the obscure grammar questions, virtual

# Abstract

Variability offers a unique opportunity to study both dynamic processes of sources as well as the intervening media between source and observer. Unfortunately, radio variability surveys have, until recently, largely been limited to small populations or single frequencies. In this Thesis, we aim to characterise the variability in the low-frequency radio sky with broadband spectral coverage and determine its physical origins. We focus on radio active galactic nuclei (AGN), and specifically a subset of AGN that show a far more compact morphology and a peak in their spectral energy distribution, giving rise to their name peaked-spectrum sources (PS sources). Identifying the cause of the spectral peak seems to be key in the understanding of PS sources and their evolutionary pathways to large scale typical AGN, yet they remain shrouded in mystery. The variability of PS sources offers a novel strategy to inform on the properties of these sources and their role in AGN evolution.

In this work, we first conduct a blind search for low-frequency spectral variability of $21,000$ sources covering $\sim5,000$ square degrees. This search is performed using 16 flux density measurements between $100$–$231\,$MHz with two epochs separated by roughly 1 year, making it the largest spectral variability survey at publication. We identify $\sim1.5\%$ of the population as variable, consistent with past variability surveys. Using the broad spectral coverage we demonstrate that sources that show variability but maintain a constant spectral shape are consistent with variability due to propagation effects, namely, scintillation. Alternatively, sources with a changing spectral shapes are inconsistent with refractive interstel-

lar scintillation (RISS) and must be due to internal processes, most likely flares from AGN where the jets are pointed towards the observer. We also identify PS sources as an intrinsically variable population compared to typical AGN. We identified a population (33%) of sources that were previously mis-classified as PS sources, which we posit are in fact blazars.

Building on this blind survey, we conduct a targeted spectral variability survey of 15 variable PS sources with increased temporal (every few months) and spectral coverage (up to 10 GHz), and demonstrate the importance of broadband spectral coverage for identifying the physical origins of the variability. We find over 85% of the sources continue to show variability in the targeted survey at megahertz frequencies, yet no sources show any significant variability at gigahertz frequencies on the timescales of months. By characterising the spectral variability, we distinguish between variability due to scintillation and intrinsic mechanisms, in particular, the majority of the sources show scintillation. We also identify three PS sources as frustrated, and one showing an evolving synchrotron component consistent with recent jet activity.

Lastly, we use high resolution imaging via very long baseline interferometry (VLBI) to compare predictions of morphologies based on our analysis of spectral variability. We show the inference of compact features and extended structures based entirely on the variability are consistent with direct imaging of the sources.

In summary, in this Thesis we demonstrate that spectral variability is a novel technique that can be used to isolate reliable populations of PS sources, the likely evolutionary scenarios of PS sources, and determine the high resolution (milliarcsecond) morphological structures of sources without the need for expensive VLBI observations. This Thesis demonstrates the importance of spectral coverage in differentiating between origins of variability, and illustrates the plethora of information one can gain on both source and intervening media once the origins of the variability are determined. Variability in the radio sky is still a largely unexplored parameter space, rich with possibilities, that upcoming instruments

particularly the Square Kilometre Array, are uniquely placed to delve into.

# Contents

# List of Figures

# List of Tables

# Chapter 1

# Introduction

*This section serves as an introduction to the astrophysical objects relevant to this thesis, in particular, radio galaxies, active galactic nuclei, peaked-spectrum sources and blazars. It aims to provide an overview of their structure and emission processes. As this Thesis explores variability with a particular focus on peaked spectrum sources, this Chapter also reviews relevant physical processes that produce variability and the current and upcoming studies of such variability. Further, it seeks to review our current understanding of peaked spectrum sources. The questions that arise regarding the evolutionary scenario of peaked spectrum sources and the limitations of current variability studies highlight the importance of this Thesis and the results herein. We adopt the standard $\Lambda$-cold dark matter cosmological model, with $\Omega_{\mathrm{M}} = 0.286$, $\Omega_{\Lambda} = 0.714$, and the Hubble constant $H_0 = 69.6 \, km \, s^{-1} \, Mpc^{-1}$ (Wright, 2006; Hinshaw et al., 2013)*

## 1.1   Radio Galaxies

The vast majority of radio galaxy hosts are old elliptical galaxies (at low redshift) with a central supermassive black hole (SMBH), the activity of which produces vast extended radio structures. The overall radio structures of these galaxies are fuelled by the central SMBH as it pulls in surrounding matter into an orbiting ac-

cretion disk of hot plasma. The magnetic field of the SMBH then accelerates the particles to almost the speed of light and ejects the relativistic charged particles in thin streams called "jets". In the innermost regions close to the SMBH, the jets are bipolar along the spin axis of the black hole. In some cases, the jets then appear to blossom out and expand into mushroom shaped clouds, or "lobes", due to back-flow of the relativistic plasma from the ends of the jets. This is particularly relevant for FRII galaxies according to the Fanaroff-Riley (FR) classification, discussed further in Section 1.1.1. These distinct regions are clearly visible in the radio galaxy Centaurus A shown in Figure 1.1. These particular galactic cores, given their active influence on their environment, are called active galactic nuclei (AGN). The entire structure fuelled by the AGN can extend well beyond the host galaxy, up to millions of light-years ($\sim 5\,\mathrm{Mpc}$) across.

Radio emission from AGN are dominated by *synchrotron radiation*, the emission from a charged, relativistic particle as it follows a magnetic field along a helical path. Synchrotron radiation is a non-thermal process unlike the thermal emission from stars and gas within galaxies that dominates the emission at shorter wavelengths but fades at low frequencies due to Rayleigh-Jeans law. As a result, the emission at low frequencies is dominated by synchrotron radiation, rather than the thermal emission. However, radio galaxies may also be star-forming and thus produce radio emission due to the thermal emission coming from the star forming regions as well as synchrotron from supernova shocks. Furthermore, star formation and accretion can both be present, particularly in high mass, high redshift galaxies (Barthel et al., 2012). In purely star forming galaxies, the radio emission is dominated by synchrotron emission at $\nu < 10\,\mathrm{GHz}$. At flux densities below $\sim 0.1\,\mathrm{mJy}$ at $1.4\,\mathrm{GHz}$, the population of radio sources begins to be dominated by star-forming galaxies rather than the non-thermal synchrotron emitting AGN (Padovani et al., 2015).
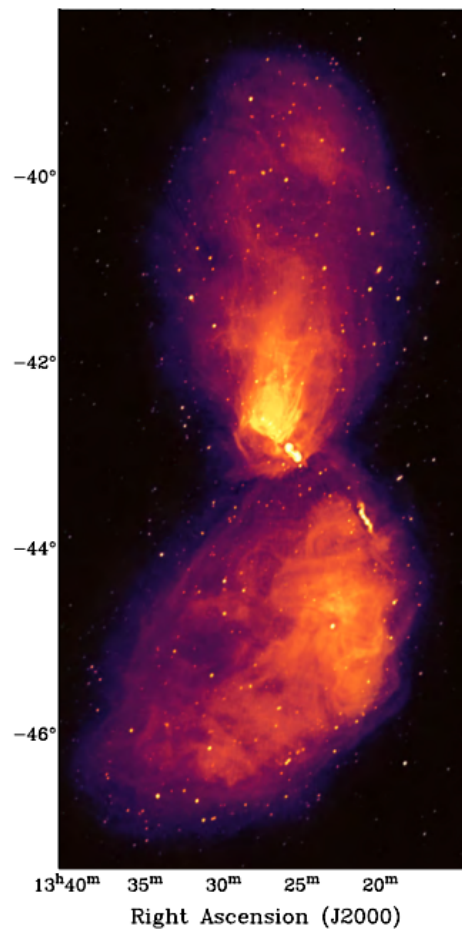
Figure 1.1: Centaurus A, as imaged by the MWA. Centaurus A displays the large diffuse lobes typically associated with AGN. Figure from McKinley et al. (2022).

## 1.1.1 Active Galactic Nuclei

The AGN core can be highly luminous across the entire electromagnetic spectrum, with each frequency regime probing and informing on different physical areas and processes of the AGN itself. AGN typically consist of an accretion disk surrounded by a dusty torus, and the synchrotron jets emitted perpendicular to the plane of the disk, see Figure 1.2. Observations of AGN at mid infra-red (MIR) wavelengths are sensitive to the emission from the hot dust and gas surrounding and obscuring the AGN (Jarrett et al., 2011; Lonsdale et al., 2015). At radio frequencies, the emission is dominated by the synchrotron emitting regions of the jets and/or lobes. The complex processes behind what triggers the AGN and the feedback mechanisms between the AGN and host galaxy are still largely uncertain (Tadhunter et al., 2021; Hardcastle & Croston, 2020). Further, the sub-classes depending on accretion flow, excitation and luminosity states, and viewing angle present a complex puzzle that also has high dependence on selection effects present in observing programs. A schematic of the different sub-classes of AGN based on several observable properties are presented in Figure 1.2. For the purpose of this Thesis, we focus on radio-loud AGN, a population consisting of jetted AGN with flux densities dominated by the non-thermal synchrotron emission associated with black hole activity. A complete review of AGN (and the sub-classes of optically selected, or $\gamma$-ray selected etc.) is presented in the review Padovani et al. (2017).

The jets of an AGN are the collimated streams of relativistic charged particles extending from the core of the AGN up to scales of $< 10^6$ pc (Padovani et al., 2017), while the lobes are diffuse large clouds extending up to several mega-parsec (Mpc) scales (Oei et al., 2022). Radio-bright AGN have previously been classified based on the distribution of luminosity across the jets and/or lobes, referred to as the Fanaroff-Riley (FR) (Fanaroff & Riley, 1974). FR I galaxies are most luminous near the centre of the galaxy and become fainter with increasing radius, whereas FR II galaxies have brightened "hot spots" at the edges of the lobes at the largest
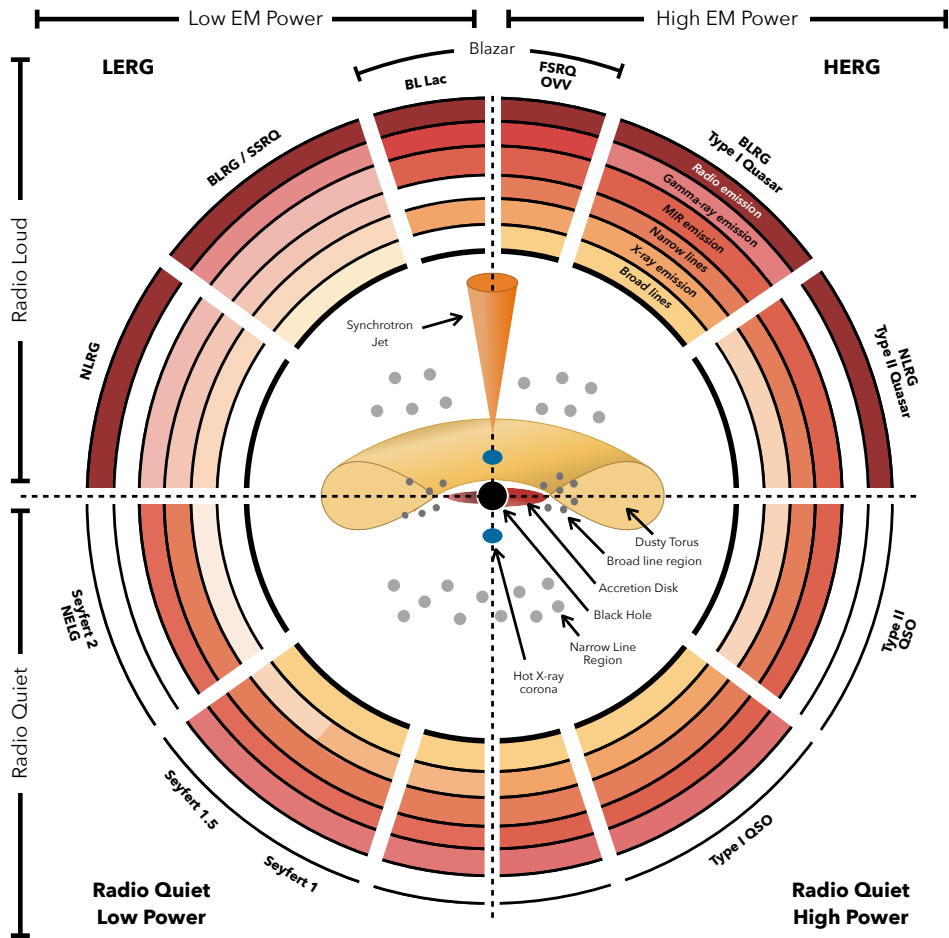
Figure 1.2: Unification scheme of AGN based on viewing angle and other observable properties. Figure from Thorne et al. (2022).

distance from the core. Thus for FR II galaxies, the jets can extend as far as the lobes. While FR I galaxies are more commonly observed, this Thesis will focus on FR II galaxies, which are more relevant to our analysis. One can differentiate between the core and lobes based on their spectral energy distribution (SED), a plot of their emission as a function of wavelength. For a region of plasma emitting synchrotron emission, a spectrum of emission arises from the combination of emission from individual particles, where the emission from each electron depends on its energy and the local magnetic field strength. Thus, the spectrum for optically thin emission, depends on the distribution of energies of the charged particles within the emitting region. The energy distribution of the charged particles generally follows a non-thermal power-law distribution with spectral index, $\alpha$[1]. Thus we can model the SED due to synchrotron emission according to a typical power-law relation:

$$S_\nu = S_0 \nu^{\alpha}, \tag{1.1}$$

where $S_\nu$ is the flux density measured in Jansky (Jy), where $1\,\mathrm{Jy} = 10^{-26}\,\mathrm{Wm}^{-2}\mathrm{Hz}^{-1}$ at a given frequency $\nu$.

In the core and jets, the electrons are highly energetic creating a pseudo flat power-law spectrum with a spectral index $> -0.5$, compared to the lobes which follow a steeper spectral index $\leq -0.5$ (Wall, 1975). Consequently, the overall flux density of the entire source is dominated by the lobes at lower frequencies, and by the flat-spectrum core at higher frequencies as the emission from the lobes fades.

The core of a radio galaxy can only continue to produce jets for as long as it has a supply of fuel for the accretion disk in the form of gas, dust, or stars from the galaxy or surrounding environment. Periods of little to no activity from the AGN are considered the "quiescent" phase. Constraining the active to

---

[1]We note, an alternative of this equation is often used with $S_\nu = S_0 \nu^{-\alpha}$. We endeavour to use the form mentioned in Equation 1.1 so the sign of $\alpha$ denotes the spectral slope to reduce confusion when referring to PS sources in the optically thin vs optically thick regimes.

quiescent phases can inform on the AGN feedback properties and environmental factors resulting in the triggering of the AGN. In the quiescent phase, without the continued injection of energy from the AGN, the lobes begin to expand and fade with the high energy particles fading first (Quici et al., 2021). The fading higher energy particles produce a spectral break at higher frequencies in the radio SEDs with a steeper spectrum above the break. As the lobes continue to age, the spectral break moves to lower frequencies and the spectra steepens further, this is discussed further in Section 1.2.2.1. The rapidly cooling and expanding lobes are considered remnants of the previous AGN activity and represent the final stage of the life-cycle of AGN. However, recent observations have found AGN with multiple phases of activity, suggesting the AGN itself has episodic activity (Shabala et al., 2020). Understanding the environmental factors and feedback mechanisms required for the AGN to be triggered and produce jets is vital if we are to link each stage of the life-cycle.

### 1.1.2 Blazars

Blazars are a sub-class of AGN with one clear geometric differentiating feature: the relativistic jet is pointed roughly towards the observer (generally on angles $\leq 15 - 20°$ from the line of sight). Given the only difference between a blazar and typical AGN is a geometric orientation, one would expect similar observational properties. However, as the relativistic jets of a blazar are ejected towards the observer, the emission is blue-shifted and Doppler boosted creating a class of object that appears to behave entirely differently to typical AGN. Likewise, blazars emit radiation across the entire electromagnetic spectrum, resulting in several classes of blazars based on specific, and often arbitrary, observational properties. For example, BL Lac objects were traditionally identified by a weak or feature-less optical spectrum, but increasing populations demonstrate the difficulty in distinguishing between BL Lac objects and flat spectrum radio quasar (FSRQ) (Giommi et al., 2012; Cheng et al., 2022). For the purpose of clarity, in this

Thesis, we refer to any AGN with jets emitted towards the observer as blazars.

As the jets are beamed towards the observer, blazars can appear considerably brighter than in their rest-frame due to Doppler boosting, resulting in a brightness temperature, $T_b$, above the limit from inverse-Compton losses $T_b > 10^{12}$ K (Kellermann & Pauliny-Toth, 1969). A Doppler factor, $\delta = \left[\Gamma - (\Gamma^2 - 1)^{1/2}\cos(\theta)\right]^{-1}$, determines the degree of relativistic beaming, and relates to both the viewing angle, $\theta$, and a Lorentz factor, $\Gamma$, (Madau et al., 1987).

Blazars are often characterised by bright radio emission, rapid large-amplitude flux density variability across a range of frequencies and sometimes large polarisation (Middei et al., 2022). This variability can be caused by either intrinsic source evolution (typically on rapid timescales due to time dilation) or extrinsic factors like interstellar scintillation (ISS) (see Section 1.2.1 for more details). Variability monitoring of blazars has found both long-term ($\sim$years) (Tinti et al., 2005; Richards et al., 2011; Malik et al., 2022) and rapid ($\sim$hours – days) (Lovell et al., 2003, 2008; Liu et al., 2017; Koay et al., 2019; Sukharev et al., 2020) variability attributed to both intrinsic and extrinsic origins or a combination of the two. Furthermore, blazars have been found to have periods of "flaring" activity, where a compact region is launched from the central core emitting synchrotron radiation where low-frequencies are absorbed due to synchrotron self-absorption (SSA), the model for SSA is explained further in Section 1.1.3.1. In these periods of flaring, the radio SED of blazars is dominated by the jet component recently launched producing an overall peaked spectrum. However, as the component ages and fades, the synchrotron peak fades and the SED flattens, generally on timescales of years or decades (Torniainen et al., 2005). As a result, flaring blazars are often misclassified as a subset of compact AGN known as peaked spectrum sources (discussed in Section 1.1.3). Recent observations of blazars at megahertz frequencies have also suggested the alignment of the jet axis may precess producing rapid variability and rare morphologies (Pajdosz-Śmierciak et al., 2022).

The dynamic nature of blazars makes them a particularly interesting subset

of AGN. Until recently, catalogues of blazars have been heavily influenced by selection effects depending on their initial detection strategy. Recent developments of a unification has sought to simplify blazar classifications by using a select few intrinsic properties over several observed properties (Giommi et al., 2012). However, the dynamic and broad range of characteristics associated with blazars can often make identifying blazars difficult or misclassifying them as a different subset of AGN.

### 1.1.3   Peaked Spectrum Sources

A subset of AGN are found to have a far more compact morphology than typical AGN, $\leq 20\,\mathrm{kpc}$ (Phillips & Mutel, 1982; Tzioumis et al., 2010), with a peak in their SEDs. Initially, these sources were classified according to their peak frequency, $\nu_p$ and morphology, e.g. Gigahertz-peaked spectrum (GPS) sources named as such given their $\nu_p \gtrsim 1\,\mathrm{GHz}$. Details of all sub-classes of compact AGN with a peaked spectrum are presented in Table 1.1; there is often a fair amount of overlap between the sub-classes. Furthermore, many of the sub-classes rely on observational properties that may differ with further improvements in observations. Several observational properties also seem to follow a continuous trend across all sub-classes of PS sources, e.g. the linear size-turnover relation, discussion further below (O'Dea & Baum, 1997; O'Dea & Saikia, 2021). It is thus likely all sub-classes are all the same astrophysical object at different evolutionary stages and/or at different redshifts. Consequently, in this Thesis we collectively refer to all sources with a peak in their spectra as peaked-spectrum sources (PS sources) and discuss their evolution as a whole rather than via their sub-classifications.

The linear size turnover relation of PS sources is an inverse relation between the rest-frame turnover frequency and their linear size (Owsianik & Conway, 1998). This relation is presented in Figure 1.3 for a population of PS sources presented by Keim et al. (2019). Fanti et al. (1990) found the linear size turnover relation was still evident even after accounting for random orientations in the

| Classification, Acronym | $\nu_p$ | Size | Morphology |
|---|---|---|---|
| High-frequency peakers, HFP | $\gtrsim 5\,\mathrm{GHz}$ | $<500\,\mathrm{pc}$ | Typically core-jet or doubles |
| Gigahertz-peaked spectrum, GPS | $0.5 \geq \nu_p \leq 5\,\mathrm{GHz}$ | $<1\,\mathrm{kpc}$ | Typically core-jet or doubles |
| Megahertz-peaked spectrum, MPS | $<1\,\mathrm{GHz}$ | $\leq 20\,\mathrm{kpc}$ | Generally similar to GPS but on a larger scale |
| Compact steep spectrum, CSS | $\leq 0.4\,\mathrm{GHz}$ | $\leq 20\,\mathrm{kpc}$ | Core-jet or triple, $\alpha \leq -0.5$ and high frequencies |
| Compact symmetric object, CSO | no constraint | $<1\,\mathrm{kpc}$ | Triple or compact double |

Table 1.1: Sub classes of PS sources in order of their peak frequency, with descriptions of their spectral and morphological properties. The class of GPS sources were the initial population of PS sources found and thus a handful were identified with $\nu_p \gtrsim 500\,\mathrm{MHz}$. However, the class MPS was then coined upon the discovery of a large population of PS sources with $\nu_p$ at low megahertz frequencies, despite several GPS sources having $\nu_p$ at megahertz frequencies.

sky and thus biases due to Doppler boosting. This suggests the relation is an intrinsic property relating to PS sources as a whole. The continuous nature of the linear size turnover relation for all sub-classes of PS sources is further supporting evidence that the sub-classifications of PS sources are likely different evolutionary stages of the same astrophysical object.

PS sources are widely accepted to be the progenitors of typical, large-scale AGN, although the evolutionary pathway from this compact phase is unclear. Two contending theories hypothesise the nature and evolutionary pathway of PS sources:

- *youth scenario*: where the age of the PS source is $\leq 10^5$ years and has not yet had ample time to grow to the large-scale AGN (O'Dea & Baum, 1997; Owsianik & Conway, 1998; Tinti & de Zotti, 2006);

- *frustration scenario*: when the PS source is confined by a dense cloud of the interstellar medium (ISM) of the host galaxy environment (van Breugel et al., 1984; Wilkinson et al., 1984; O'Dea et al., 1991).
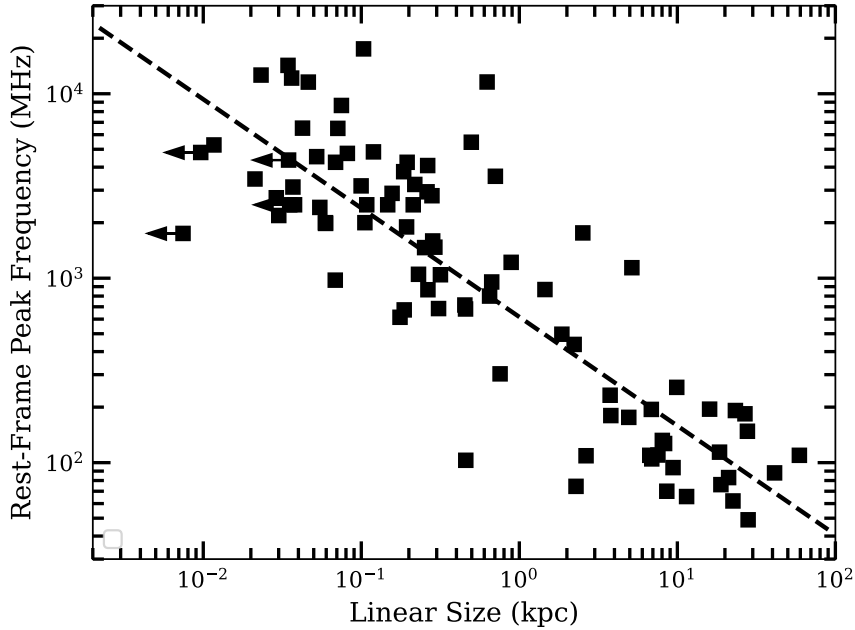
Figure 1.3: Intrinsic peak frequency versus linear size of PS sources. The dashed line is the fit to the relation found by Orienti & Dallacasa (2014). Arrows indicate maximum linear sizes for unresolved sources. Figure adapted from Keim et al. (2019).

In both the youth and frustration scenarios, the spectral peak is described by absorption at low frequencies. In the youth scenario, the absorption is typically explained due to synchrotron self-absorption. Conversely, the frustration scenario often relates to free-free absorption. While these absorption mechanisms are not necessarily the main criteria for each scenario, they are often consistent and used as a piece of evidence in a larger analysis. The absorption mechanisms for the youth and frustration scenarios are discussed further in Section 1.1.3.1 and Section 1.1.3.2 respectively. Differentiating between youth and frustration is crucial to characterise internal properties of the source itself (i.e. magnetic field and electron energy distribution) or details of the external surrounding media (i.e. thermal electron distribution, homogeneity of the ISM) respectively (O'Dea & Saikia, 2021). However, insufficient spectral coverage (particularly below the peak frequency) has led to both absorption mechanisms being consistent with observations. Thus, distinguishing between youth and frustration scenarios is

often still challenging with ambiguous results.

Producing a population of reliable PS sources to distinguish between the youth and frustration scenarios has been limited by observational constraints. Identifying PS sources has previously largely relied on combining flux density measurements from several surveys (Sadler, 2016). Consequently, populations were biased to identifying PS sources that were bright and peak at $\gtrsim 1\,\mathrm{GHz}$. Furthermore, there is growing evidence that a fraction of PS sources are transient, only temporarily displaying a spectral peak (Torniainen et al., 2005), thereby contaminating PS populations making population-wide conclusions unreliable. Likewise, recent simulations of evolving PS sources suggest they may only be temporarily frustrated by the local ISM and once they break free, quickly grow and evolve to typical AGN, on timescales of $\leq 10^6\,\mathrm{years}$ (Bicknell et al., 2018). Research into individual PS sources has provided strong evidence for both evolutionary scenarios, but statements about the PS population as a whole have been hampered by the limitations in the observations required to produce a large, reliable sample of PS sources.

Using the GaLactic and Extragalactic All-Sky Murchison Widefield Array (MWA) (GLEAM) survey (Wayth et al., 2015; Hurley-Walker et al., 2017), over 1,400 PS sources with peak frequencies from $0.072 \leq \nu_p \leq 1.4\,\mathrm{GHz}$ were identified (Callingham et al., 2017). Due to the lower frequency of the GLEAM survey, from 72 to 231 MHz, the PS sources identified by Callingham et al. (2017) have a lower peak frequency than previous PS sources identified; this is shown in Figure 1.4. The population presented by Callingham et al. (2017) is ideal to investigate the properties of PS sources in the optically-thick regime and PS sources, where the peak frequencies is above GLEAM frequencies. Given Callingham et al. (2017) were sensitive to $\nu_p \leq 1.4\,\mathrm{GHz}$, this population is likely to probe PS sources in the "older" stage of evolution compared to PS sources with $\nu_p$ at frequencies of several gigahertz. We discuss the evidence and implications for both the youth and frustrations scenarios in the following sections.
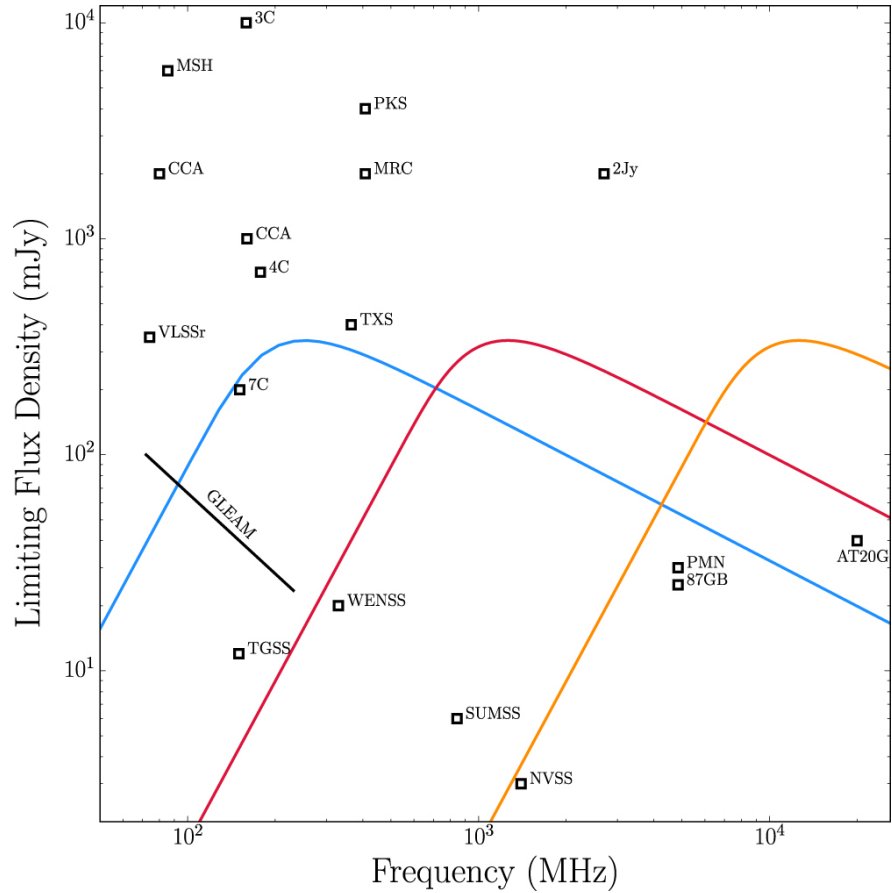
Figure 1.4: Sensitivities of radio surveys and their frequencies compared to example PS source SEDs. Example SEDs with a SSA spectral model with peaks at 200, 1000, 10,000 MHz are plotted in blue, red, and orange respectively. The GLEAM survey is plotted with a black line due to the large spectral coverage and varying limiting sensitivities. Figure from Callingham et al. (2017).

### 1.1.3.1 The Youth Scenario

The main hypothesis of the youth scenario assumes most PS sources are the progenitors to radio-loud AGN. It relies entirely on PS sources having a clearly defined pathway of growth from initial AGN triggering and jet formation, to giant radio galaxies (GRGs), extending up to 5 Mpc. However, the excess of compact PS sources relative to GRG suggests not all PS sources will evolve to the scale of GRG, likely influenced by the power and environment of the AGN (Kunert-Bajraszewska et al., 2010; Wołowska et al., 2017). One of the strongest pieces of evidence in support of the youth scenario is the clear continuity between the properties of PS sources and typical AGN, e.g. their similar yet small-scale morphology, comparable host galaxies, and modelled growth of the lobes. Such a continuous evolutionary path is supported by the linear size turnover relation. In the youth scenario, this relation suggests PS sources evolve from a highly compact ($\leq$500 pc) AGN with a spectral peak $\geq$ 5 GHz and as the source ages, the peak frequency decreases and the size increases (An & Baan, 2012). From this evolution, it follows that compact sources continue to expand and age into typical AGN morphologies (Readhead et al., 1996; Alexander, 2000).

The youth scenario often assumes the absorption at low frequencies is mostly due to SSA, while not necessarily required for the youth scenario, it is typically consistent. In this process, the energy emitted by the synchrotron radiation is then further scattered by other relativistic charged particles. In the case of the jets and lobes of PS sources, the synchrotron radiation produced by the gyrating electrons is then scattered (appearing to be "absorbed") by the same relativistic electrons producing the initial synchrotron radiation in the plasma. The likelihood of low-energy photons being scattered within the plasma is much higher. This produces a greater level of apparent absorption at low frequencies where only low-frequency emission from the outermost shell of the plasma is visible (Callingham et al., 2015). Higher frequencies probe further into the plasma as the higher energy photons become more likely to "escape" the plasma. Thus,

the size of the plasma shell directly relates to the optical depth, and the peak frequency is the frequency at which the optical depth is unity. The peak frequency of the spectrum corresponds to the transition frequency from optically thick (i.e. opaque) to optically thin (i.e. transparent).

The SSA spectral model can be parameterised according to (Kellermann, 1966):

$$S_\nu = S_0 \left( \frac{\nu}{\nu_p} \right)^{\frac{\beta-1}{2}} \left[ \frac{1 - e^{-\tau_\nu}}{\tau_\nu} \right],$$

where                                                                                        (1.2)

$$\tau_\nu = \left( \frac{\nu}{\nu_p} \right)^{\frac{-(\beta+4)}{2}},$$

where $\beta$ is the non-thermal spectral index for a single, homogeneous, synchrotron-emitting region and $\tau_\nu$ is the optical depth at a given frequency $\nu$. Modifications of this spectral model include adding multiple SSA regions with their own electron energy distributions (i.e. spectral index). In this case, the observed spectrum is the sum of each individual SSA spectrum. This can produce an overall flatter and broader spectral peak[2]. In an SSA model, the peak frequency directly relates to the source size. Thus, the linear size and turnover relation is a natural product of this scenario (Snellen et al., 2000).

Recent observations of PS sources have provided further evidence for the youth scenario. High resolution imaging using very long baseline interferometry (VLBI) clearly finds PS sources with a similar morphology to typical AGN on far smaller spatial scales (Phillips & Mutel, 1982; Tzioumis et al., 2010). Likewise, observations of the proper motion hot-spots in the lobes of PS sources using VLBI has estimated their kinematic age to be $\leq 3 \times 10^3$ years (Polatidis & Conway, 2003). This is further supported by measurements of their spectral ages from $10^2$ – $10^5$ yrs (Murgia, 2003).

Despite the sizeable and increasing evidence in support of the youth scenario, its largest downfall is the large ratio of PS sources relative to older counterparts

---

[2]We present the equations for double and triple SSA models in Appendix A

(O'Dea & Baum, 1997; An & Baan, 2012). The excess of "young" sources suggests a sizeable fraction of PS sources must be prevented from ageing. This is supported by recent dynamical modelling of populations that find a log-distribution of AGN active time, i.e. many young AGN do not maintain a constant fuelling of the jets and lobes, resulting in a population of fading young sources (Shabala et al., 2020). There is increasing evidence that many sources show intermittent periods of activity resulting in a population of short-lived young sources that are already switched off and fading (Kunert-Bajraszewska et al., 2006; Orienti et al., 2010; Callingham et al., 2015).

#### 1.1.3.2  The Frustration Scenario

The frustration scenario postulates that PS sources are confined by the dense gas and dust in their local host galaxy environment. Consequently, the frustrated PS sources have a stagnated growth and are not necessarily "young" (van Breugel et al., 1984; Wilkinson et al., 1984; O'Dea et al., 1991). As the frustration scenario relies heavily on the environment surrounding the compact AGN and the nature of the host galaxy ISM, observational evidence relies on demonstrated interactions between the jets and ISM hindering the jet propagation.

The spectral peak of PS sources in the frustration scenario typically arises from absorption of the radio photos emitted by the relativistic electrons by the surrounding medium through inverse Bremsstrahlung or free-free absorption (FFA). As with the youth scenario, FFA is not necessarily required for the frustration scenario, but is typically the most consistent model. In FFA, the energy emitted by the relativistic charged particles from the source are absorbed by an ionized screen. The nature of the FFA spectral model is dependent on several properties of the absorbing plasma: the uniformity of the plasma screen itself (i.e. homogeneous or inhomogeneous morphology), and whether it is external or intermixed with the charged particles producing the non-thermal emission (external or internal screen). In the external homogeneous FFA case (herein referred to simply

16

as FFA), a uniform screen covers the entire emitting region, i.e. the size of the screen is assumed larger than the lobes as viewed by the observer (Kellermann, 1966). In the case of PS sources, we assume the electrons emit photons due to synchrotron radiation and thus follow a non-thermal power-law distribution, according to Equation 1.2, where the spectral index of the synchrotron emission is $\alpha = (\beta - 1)/2$. We can thus write the FFA spectral model as (Bicknell et al., 1997):

$$S_\nu = S_0 \nu^\alpha e^{-\tau_\nu},$$

where

$$\tau_\nu = \left(\frac{\nu}{\nu_p}\right)^{-2.1},$$

(1.3)

where $\tau_\nu$ is the optical depth. As with the SSA spectral model, the peak frequency, $\nu_p$, is the frequency at which the free-free optical depth is unity and the transition point between the optically thick and thin regimes.

The FFA model assumes the absorbing ionised plasma is external and separate to the emitting plasma of the source itself. If we now consider the possibility the ionised plasma is interspersed with the emitting plasma of the source itself, we can parameterise according to (Tingay & de Kool, 2003):

$$S_\nu = S_0 \nu^\alpha \left(\frac{1 - e^{-\tau_\nu}}{\tau_\nu}\right)$$

where, as with the FFA model in Equation 1.3, the optical depth $\tau_\nu \propto \nu_p^{-2.1}$. Therefore, in the optically thick regime ($\nu < \nu_p$), the spectral index is $\alpha_{\text{thick}} = \alpha - 2.5$.

A more complex FFA model is presented by Bicknell et al. (1997), in which the jet produces a bow-shock into the local ISM as it propagates through and interacts with the dense medium. Such a scenario is consistent with sources being *temporarily* frustrated while still confined within the ISM (Bicknell et al., 2018). This produces a range of optical depths and an overall "clumpy" or inhomogeneous plasma that has been photo-ionised by the bow shock. A schematic of the

jet and ISM interaction is presented in Figure 1.5. Due to the non-uniformity of the ionised plasma, we refer to this model as the inhomogeneous free-free absorption (inFFA) model. We assume the range of optical depths, $\tau_{\mathrm{ff}}$, in the inFFA model can also be described by power-law distribution, with a index $p$, according to:

$$\tau_{\mathrm{ff}} \propto \int (n_e^2 T_e^{-1.35})^p dl, \tag{1.4}$$

where $n_e$ is the free electron density and $T_e$ the electron temperature and assuming $p > -1$[3]. Bicknell et al. (1997) present the spectral model for inFFA assuming the scale of inhomogeneities in the ISM is far smaller than the scale of the lobes, we define the inFFA spectral model as:

$$S_\nu = S_0(p+1)\gamma \left[ p + 1, \left( \frac{\nu}{\nu_p} \right)^{-2.1} \right] \left( \frac{\nu}{\nu_p} \right)^{2.1(p+1)+\alpha} \tag{1.5}$$

where $\gamma$ is the lower incomplete gamma function of order $p+1$. Again, this model assumes a single emitting region with a non-thermal power-law distribution.

The geometric nature of the inFFA spectral model leads to the natural conclusion the peak frequency can vary significantly within the population (Bicknell et al., 1997). Likewise, the velocity of the clouds moving into/out of the line of sight, can induce apparent variability from the changing optical depth.

As with the SSA spectral model, each FFA spectral model can be modified by increasing the number of emitting regions. We present the equations for spectral models with multiple emitting regions for both SSA and FFA spectral models in Appendix A.

Evidence in support of the frustration scenario has been built from growing evidence of interactions between the AGN jets and host galaxy ISM environment. The asymmetric morphology of many PS sources is consistent with the jets interacting with a dense environment (Kameno et al., 2000; Saikia & Gupta, 2003; Rossetti et al., 2006). Frustrated sources have also been identified by their

---

[3]It is worth noting, when $p = -1$, this model reduces to the homogeneous FFA model.
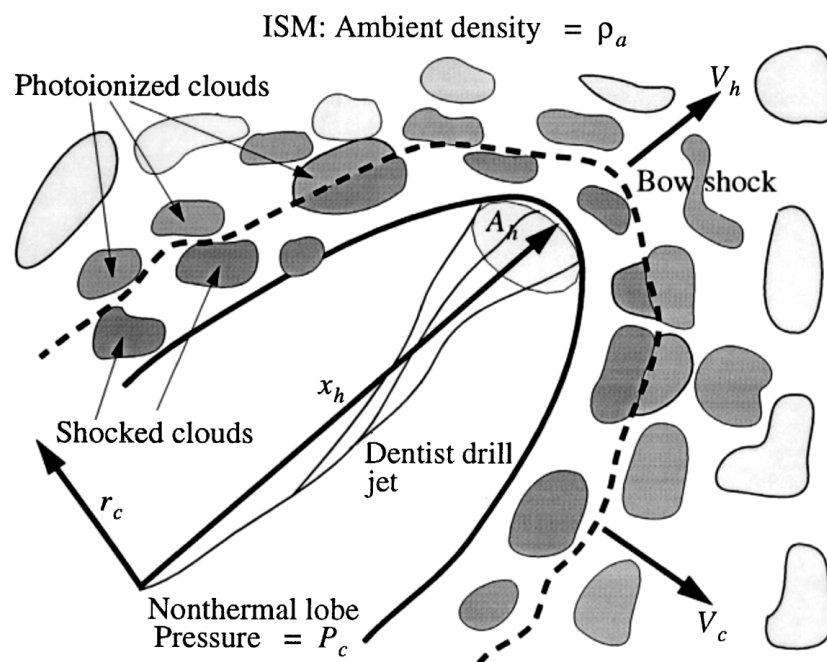
Figure 1.5: Diagram of PS source interacting with the surrounding ISM producing photoionised regions and a range of optical depths, as theorised in an inhomogeneous free-free absorption scenario for PS sources. Figure from Bicknell et al. (1997).

steep optically-thick spectral index, where $\alpha_{\mathrm{thick}} > 2.5$ (Callingham et al., 2017), which cannot be reproduced via a purely SSA spectral model, but requires further absorption that can be explained by FFA.

As discussed in Section 1.1.3.1, the downfall of the youth scenario is the excess of compact sources. The frustration scenario would resolve this excess of compact sources, however, conclusive population statistics are still lacking as the frustration scenario has only been confirmed for a handful of PS sources (Peck et al., 1999; Kameno et al., 2000, 2003; Marr et al., 2014; Callingham et al., 2015; Tingay et al., 2015). Furthermore, at first glance the linear size of frustrated sources is not a natural product of the frustration scenario, but can be recovered in simulations of evolving frustrated sources (Bicknell et al., 1997). These numerical simulations have reproduced this relation by assuming PS sources are only *temporarily* frustrated for $1 - -2\,\mathrm{Myr}$ (Bicknell et al., 2018). Such simulations predict young AGN with high jet power will eventually break free from the dense environment and continue to evolve to typical AGN but a fraction ($\sim$30%) of weaker jet power AGN will be unable to break through (An & Baan, 2012). Thus, even though the linear size turnover relation is a natural by-product of the youth scenario, it cannot be used as evidence in support of the youth scenario over the frustration scenario for the entire population. However, a handful of PS sources have been determined to be frustrated based on the position below the linear size turnover relation (Keim et al., 2019). In this case, the PS source appears compact beyond what would be expected for a purely young, SSA source, suggesting another factor must also be contributing further to the confinement of the source. Regardless of the mechanism producing the spectral peak of PS sources, the compact morphology and dynamic processes often leads place this population as a prime focus for variabiltiy surveys.

## 1.2 Variability

Variability can largely be characterised into two main processes: intrinsic variability, relating to the source itself, or extrinsic, relating to propagation effects along the line-of-sight. Distinguishing between these two scenarios is often limited by both the spectral and temporal coverage of observations. At gigahertz frequencies, as the flux density is often dominated by components with small (∼pc) spatial scales, in the regions close to the AGN core itself, variability on timescales of months to years was not unexpected. Whereas, at megahertz frequencies, as the flux density is largely dominated by the extended (∼kpc to Mpc) structures, i.e. the lobes, variability on human-observable timescales was not initially expected.

The first observations of variability at radio wavelengths was of the Sun and it was generally thought extra-galactic sources would not show variability on observable timescales (Payne-Scott, 1949). However, monitoring of Hydra-A found flux density variations around 10–30% at megahertz frequencies (Slee, 1955). Interestingly, as Hydra-A was not yet known to be a radio galaxy and associated to the optical host, the rapid (∼yearly) variability raised significant issues if the variations arose due to intrinsic mechanisms, suggesting Hydra-A must be only a few parsec away. Even after radio sources were attributed to extra-galactic sources, rapid variability continued to raise contradictions between expected source sizes and variability timescales.

Radio variability was originally explored in the context of scattering due to the Solar wind, known as interplanetary scintillation (IPS) (Hewish et al., 1964; Clarke, 1964). However, Hunstead (1972) identified four extra-galactic radio sources exhibiting variability at 408 MHz on timescales of months, inconsistent with IPS expectations. This initial discovery presented several large questions relating to the physical processes of radio sources, previously considered too large to exhibit short-term variability at such frequencies. If found to be intrinsic to the source, the variability detected by Hunstead (1972) would suggest a brightness

temperature, $T_b$, well above the inverse Compton scattering limit of $T_b > 10^{12}\,\text{K}$. Furthermore, scattering due to a further screen, namely interstellar scintillation (ISS), was not considered as the angular scales of the turbulence to produce the flux density variations were considered too small compared to the astrophysical structures. It was thus interpreted that the estimates of source sizes obtained from previous VLBI observations may have largely overestimated the source size, potentially from an incorrect redshift, or that the low-frequency variability arose from different physical regions or by new physical mechanisms compared to the higher frequency variability. All these conclusions seemed to conflict with models for radio galaxies at the time. Further monitoring of these sources found they were instead varying due to extrinsic effects, namely, due to scattering from the ISM (Fanti et al., 1979).

Since this initial discovery, several physical mechanisms have been identified and/or theorised to produce variability at radio frequencies. In Section 1.2.1 and Section 1.2.2, we describe the physical properties of several extrinsic and intrinsic variability processes respectively. In Section 1.3 we outline the observational limitations for detecting and classifying variability and summarise the results of previous variability surveys.

### 1.2.1 Extrinsic Variability

As the name suggests, extrinsic variability relates to processes extrinsic to the source itself, i.e. variations caused by propagation effects along the line-of-sight. Scintillation is the process where the light is scattered due to a turbulent and inhomogeneous intervening medium. To avoid confusion between the terms scattering and scintillation, in this Thesis, we will refer to scattering as the physical process producing the observed effect of scintillation. A well known example of scintillation is the twinkling of stars. In this scenario, the light from the stars is scattered as it propagates through the turbulent atmosphere of the Earth, producing an apparent variability, or twinkling. Stars are observed to twinkle since

the angular scale of stars is smaller than the turbulent scales of the atmosphere. Conversely, planets have a much larger angular scale, larger than the angular scale of turbulence in the atmosphere and thus we do not see planets twinkling. Therefore, by characterising the scintillation, one can infer details of the source morphology as well as the properties of the intervening medium. For example, several Indigenous cultures observed the twinkling of stars and used it to predict the temperature changes, humidity, and winds (Hamacher et al., 2019). By characterising the scintillation of astrophysical sources due to different turbulent media, we can infer details of various intervening media.

We characterise the properties of scattering through classical wave propagation theory, and thus we can understand the expected observational effects of scintillation of astrophysical objects. In this section, we outline the theory of scattering based on the optics involved in wave propagation through a turbulent medium.

Scattering can be divided into two distinct regimes relating to the strength of the scattering: weak and strong. As a wavefront propagates through the turbulent medium, referred to as the phase screen or scattering screen, random phase fluctuations are introduced, which relate to the properties of the scattering screen. We assume a Kolmogorov turbulence (Armstrong et al., 1995) in a thin scattering screen at a finite distance from the observer and a source sufficiently far away that we can approximate it as an infinite distance from the screen. To understand the properties of the scattered wavefront, we will define two relevant spatial scales: the Fresnel scale, $r_F$, and the diffraction length scale, $r_{diff}$. The Fresnel scale can be considered as the spatial scale of the scattered wavefront, and $r_{diff}$ is the length scale where the root mean squared (RMS) phase difference is 1 radian. Using the Fresnel-Kirchoff diffraction theory (Born & Wolf, 1980), and again assuming Kolmogorov turbulence (Narayan, 1992), we define the $r_F$ as:

$$r_F = \sqrt{\frac{\lambda D}{2\pi}}, \tag{1.6}$$

where $\lambda$ is the wavelength of the scattered wave and $D$ is the distance to the screen (Narayan, 1992).

For a turbulent scattering screen moving with a velocity relative to the line-of-sight, we define the modulation index as the amplitude of the RMS flux density variations. The modulation will depend on the properties of the scattering screen itself, so first we assume the overall scattering strength of the screen, $\xi$, can be found according to:

$$\xi = 7.9 \times 10^3 \, \mathrm{SM}^{0.6} \, D^{0.5} \, \nu^{-17/10}, \tag{1.7}$$

where SM is the scattering measure of the screen, which is a cumulative effect from the inhomogeneities along the line of sight, $D$ is the distance to the scattering screen and $\nu$ is the observing frequency[4]. We can also define $\xi = 1$ as the transition point between weak and strong scattering, where the weak regime refers to the regime where $\xi < 1$ and strong where $\xi > 1$. Observing scintillation at various wavelengths, timescales, and lines of sight probes these different regimes, an example of the scattering regimes and the associated timescales and modulation is represented in Figure 1.6.

From Equation 1.7, we can see for a given scattering measure, relative to the line of sight, we can calculate the frequency at which $\xi = 1$, referred to as the transition frequency, $\nu_0$ (Walker, 1998). As a transition frequency is often easier to conceptualise than the more abstract scattering strength, we consider the strong and weak regimes as the regimes where the observing frequency, $\nu$, is far less and far more than $\nu_0$, respectively. Furthermore, we can see the $\nu_0$ depends on the properties of the scattering screen. However, calculating $\nu_0$ relies on the scattering measure for a given line of sight. Thus, in practice, accurate estimates of $\nu_0$ relies on the characterising observations of scintillation for every line of sight. Current estimates of the scattering measure are derived from observations of scintillation of pulsars and maps of the ISM of the Milky Way. From Equation 1.7, we can

---

[4]We note, Equation 1.7 is from the erratum Walker (2001) but the derivation is presented in Walker (1998).

## Scintillation Regimes
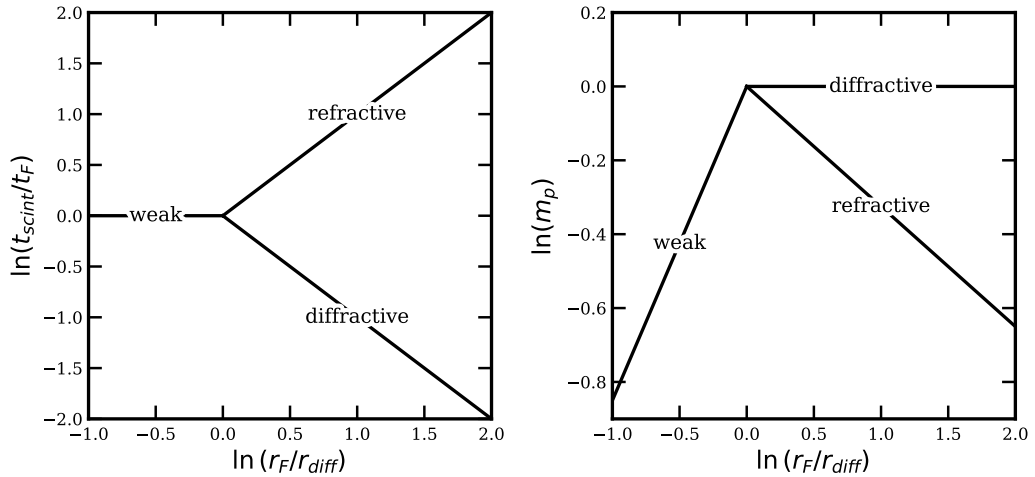


Figure 1.6: Schematic of the different scintillation regimes: weak, strong diffractive and strong refractive. (left) The timescales of scintillation relative to the Fresnel timescale, $t_F$, and (right) modulation index, $m_p$. Regimes are defined according to the relation between the Fresnel scale, $r_F$, and the diffraction length scale, $r$diff, where strong occurs when $r_F >> r_{\text{diff}}$, weak occurs when $r_F << r_{\text{diff}}$, and the transition between weak at strong occurs at $r_F \approx r_{\text{diff}}$. Figure adapted from Narayan (1992).

see $\xi \propto \left(\frac{\nu_0}{\nu}\right)^{17/10}$, thus the strength of the modulation is influenced by observing frequency relative to the transition frequency. Likewise, we can also determine which scattering regime is relevant based on the observing frequency relative to the transition frequency. That is, if $\nu > \nu_0$, the weak scattering regime is relevant since $\xi < 1$, and vice versa for the strong regime.

In the rest of this section, we will continue by reviewing the optics of the different scattering regimes and the observational effects produced. Section 1.2.1.1 discusses the weak scattering regime and the examples of observed weak scintillation of astrophysical objects. While Sections 1.2.1.3 and 1.2.1.2 outline the two categories of strong scattering, refractive and diffractive respectively. For clarity, we use the subscript *weak*, *diss* and *riss* when referring to the parameters of weak, diffractive and refractive scattering respectively. Alternatively, to differentiate from the scintillation parameters defined in terms of observable properties, we use subscript $p$ and $e$ when referring to scintillation for a point source and

extended source respectively.

### 1.2.1.1 Weak Scattering

In the weak scattering regime, there are only small variations and the only relevant spatial scale is the Fresnel scale. For scales larger than the Fresnel scale, the scattering patterns overlap and smear each other out, cancelling out any variations (Narayan, 1992). Thus, both the timescale, and spatial scales relevant to weak scattering are directly related to the Fresnel scale, $r_F$.

We define $\theta_{\mathrm{weak}}$ as the angular size limit for a source to be considered a point source relative to the scattering disk. In the weak regime, $\theta_{\mathrm{weak}}$ is directly related to the Fresnel angle, $\theta_F$, according to:

$$\theta_{\mathrm{weak}} = \theta_F = \frac{r_F}{D}, \tag{1.8}$$

where $D$ the distance to the scattering screen, as defined before. The timescale of modulation, $t_{\mathrm{weak}}$, is then simply the time to traverse the coherent scale of scattering, in this case the Fresnel scale. Thus, the timescale of modulation is given by the Fresnel timescale, $t_F$:

$$t_{\mathrm{weak}} = t_F = \frac{r_F}{v}, \tag{1.9}$$

where $v$ is the transverse velocity of the screen.

In order to easily conceptualise the expected properties of weak scintillation, we now parameterise the timescale and angular size in terms of $\nu_0$ following Walker (1998). Firstly, we consider the angular size limit, $\theta_{\mathrm{weak,screen}}$:

$$\theta_{\mathrm{weak,screen}} = \theta_F \sqrt{\frac{\nu_0}{\nu}}, \tag{1.10}$$

where $\theta_F$ is the Fresnel angle and corresponds to the angular size when $\nu = \nu_0$ (Walker, 1998). Sources with an angular size $\theta_{\mathrm{src}} < \theta_{\mathrm{screen}}$ are considered a point

source relative to the scattering screen.

Likewise, the timescale of modulation can be parameterised according to:

$$t_{\text{weak},p} \approx t_F \sqrt{\frac{\nu_0}{\nu}}, \tag{1.11}$$

where $t_p$ is in units of hours and $t_F$ is approximated to be 2 hours (Walker, 1998).

The modulation index, or the rms amplitude of the flux variations, for scintillation is directly related to the strength of the scattering, i.e. to $\xi$. It can be determined from the amplitude of the "phase structure function" (Narayan, 1992)[5]. In the weak regime, for a point source (where $\theta_{\text{src}} \leq \theta_{\text{weak,screen}}$) the modulation index, $m_p$ is found to be:

$$m_{\text{weak},p} = \xi^{5/6} = \left(\frac{\nu_0}{\nu}\right)^{17/12}, \tag{1.12}$$

where the exponent 5/6 is a direct result of the assumption of Kolmogorov turbulence.

While there is a strict limit on the source size for sources to be exhibit weak scintillation, extended sources can still show weak scintillation. The overall scintillation is a superposition of the scattering from every scattered wave, thus the modulation index is dampened and the timescale increases, as the extended structure cancels more of the variations. To estimate the timescale and modulation for a resolved source of angular size $\theta_{\text{src}}$, we assume the source can be approximated to a Gaussian intensity profile. In this case, the relevant scale is no longer $r_F$, but instead $D\theta_{\text{src}}$ (Narayan, 1992). Thus the timescale of scattering for an extended source, $t_{weak,e}$, can be modified from Equation 1.9 to:

$$t_{\text{weak},e} = \frac{D\theta_{\text{src}}}{v}, \tag{1.13}$$

---

[5]The derivation of the structure function and thus the amplitude of the flux variations is presented in Narayan (1992), however, for the purpose of this Thesis we are only concerned with the modulation index as a function of observable quantities.

for a scattering screen at distance $D$, with a velocity $v$. From Equation 1.13, it follows the timescale of scintillation thus increases relative to $\theta_{\text{src}}$ according to:

$$t_{\text{weak},e} = t_{\text{weak},p} \frac{\theta_{\text{src}}}{\theta_F}, \tag{1.14}$$

where $t_{\text{weak},e}$ and $t_{\text{weak},p}$ are in units hours and $t_{\text{weak},p}$ is often approximated to 2 hours (Walker, 1998).

The modulation index for an extended source is again derived by the rms amplitude of the fluctuations. The modulation index is dampened such that:

$$m_{\text{weak},e} = m_{\text{weak},p} \left( \frac{\theta_F}{\theta_{\text{src}}} \right)^{7/6}, \tag{1.15}$$

Thus in practice, while weak scintillation has a strict angular scale limit, source with structure greater than this limit can still show significant weak scintillation, but detecting this scintillation becomes increasingly harder as the source size increases.

When considering weak scintillation due to the ISM, weak interstellar scintillation (WISS) becomes relevant at higher frequencies (when $\nu > \nu_0$). As the observing frequency increases relative to $\nu_0$, from Equation 1.12, we can see $m_p$ decreases until the scintillation is insignificant. Similarly, from Equation 1.11, the timescale also decreases with increasing frequency, making it harder to detect. Furthermore, the strict limit of angular scales means only sources with a significant fraction of their emission on scales $\leq \theta_{\text{screen}}$ will show significant WISS.

Perhaps most notably, weak scintillation has been observed as IPS. As the scattering screen is far closer to Earth in IPS compared to WISS, the apparent velocity of the screen relative to the observer is also much greater. Consequently, the timescales of modulation due to IPS are much shorter than for WISS, typically found to be on $\sim 1\,\text{s}$ timescales at $\sim 150\,\text{MHz}$. While $\theta_{\text{screen}}$ increases for IPS compared to WISS, there is still a strict limit on the source size for IPS to be significant. It was discovered by Margaret Clarke in 1964, that only compact

extra-galactic sources $< 2$ arcseconds were found to show variability due to IPS (Clarke, 1964). The possibility of using IPS to identify sub-arcsecond structures at megahertz frequencies led to the construction of the Cambridge IPS array that was later used by Jocelyn Bell-Burnell when she discovered pulsars. More recently, IPS studies have been used to determine properties of the solar wind, space weather, and coronal mass ejections (Morgan et al., 2018; Iwai et al., 2021; Liu et al., 2021).

### 1.2.1.2 Strong Diffractive Scattering

Unlike weak and strong refractive scattering, which is associated with random phase fluctuations that produce focusing and de-focusing effects, diffractive scintillation is more easily conceptualised in terms of a wavefront spreading out after passing through a narrow aperture. Diffractive scattering is perhaps most widely recognised in the context of Young's slits experiment. In this experiment, light from a distant point source passes through a narrow slit (the scattering screen), and spreads outwards producing an effective cone of scattered light. The diffracted wave interferes with that from the other slit and produces an interference pattern, commonly referred to as the fringe pattern or interference fringes, with bright and dim regions corresponding to the regions of constructive and deconstructive interference respectively. As a result, the observer detects a blurred or broadened image, referred to as scatter broadening, with a fringe pattern. The spacing between the fringes is directly related to the wavelength, thus diffractive scattering is strongly related to the observing wavelength, making it a narrowband effect.

As with weak scattering in Section 1.2.1.1, we begin by defining the angular scales and timescales relevant to diffractive scattering. Since the light is diffracted producing a cone of scattered light, the angular scale relevant to diffractive scattering is the scale of this cone. However, as mentioned above, the fringe pattern is directly proportional to the wavelength as well as the aperture sizes and spacing

between apertures. We can therefore consider coherent regions in our scattering screen. Given $r_{\mathrm{diff}}$ relates to the length scale where the RMS phase difference is 1 radian, we can consider these coherent regions to be of the order $r_{\mathrm{diff}}$ with separation $r_{\mathrm{diff}}$ (Narayan, 1992). Thus our relevant angular size limit, $\theta_{\mathrm{diss}}$, is related to $r_{\mathrm{diff}}$ instead of the Fresnel scale, according to:

$$\theta_{\mathrm{diss}} \approx \frac{r_{\mathrm{diff}}}{D} \approx \frac{\lambda}{r_{\mathrm{diff}}}, \tag{1.16}$$

where $\lambda$ is the wavelength. Again the timescale for the scattering is the time taken to traverse the coherent regions, but unlike with weak scattering, our relevant scale is $r_{\mathrm{diff}}$:

$$t_{\mathrm{diss}} = \frac{r_{\mathrm{diff}}}{v}, \tag{1.17}$$

for a screen with transverse velocity, $v$.

As with weak scattering, we parameterise the timescale and angular size in terms of $\nu_0$. Following Walker (1998), the timescale of scintillation for a point source is

$$t_{\mathrm{diss},p} = t_{\mathrm{diss}} \left( \frac{\nu}{\nu_0} \right)^{6/5}, \tag{1.18}$$

where $t_p$ is in units hours and again, we approximate $t_{\mathrm{diss}}$ to be 2 hours (Walker, 1998). Likewise, the angular size limit of the screen:

$$\theta_{\mathrm{diss,screen}} = \theta_{\mathrm{diss}} \left( \frac{\nu}{\nu_0} \right)^{6/5}, \tag{1.19}$$

where $\theta_{\mathrm{diss}}$ is related to $r_{\mathrm{diff}}$ according to Equation 1.16. To determine the modulation index, instead of considering the RMS amplitude of the flux variations, we can use the fact that the relative length scale for diffractive scintillation is $r_{\mathrm{diff}}$, which by definition means the modulation index will be unity, i.e.:

$$m_{\mathrm{diss},p} = 1, \tag{1.20}$$

30

for a point source with size $\theta_{\mathrm{src}} \leq \theta_{\mathrm{diss,screen}}$.

It is worth noting, as the fringe pattern has a strong dependence on the frequency, a high frequency resolution is needed to observe diffractive scintillation. We define a frequency resolution of $\Delta\nu$ according to:

$$\frac{\Delta\nu}{\nu} = \left(\frac{\nu}{\nu_0}\right)^{17/5}, \tag{1.21}$$

where a frequency resolution of at least $\Delta\nu$ is needed to detect the interference fringes characteristic of diffractive scintillation.

Unlike both weak and strong refractive scattering, since the angular size limit in the diffractive scattering regime relies on $r_{\mathrm{diff}}$, the limit on source size is extremely strict, e.g. at $150\,\mathrm{MHz}$, for high Galactic latitudes, the angular size limit is $\sim 0.03\,\mu\mathrm{as}$. Consequently, the only known observations of diffractive scintillation is the diffractive interstellar scintillation (DISS) of incredibly compact sources like pulsars (and perhaps some masers), the only known sources compact enough for diffractive scintillation to be relevant (Rickett, 1990; Narayan, 1992). Furthermore, the timescales of DISS are also related to $r_{\mathrm{diff}}$ and are thus incredibly short, generally on sub-second timescales. Thus, all other known radio sources, particularly AGN, are far too extended for any diffractive scintillation to be detected. Just as with weak scintillation, the modulation index is dampened and the timescale increased for diffractive scintillation of an extended source. However, as the angular source limit is so strict, deriving these scaling relations is irrelevant in the context of scintillation of AGN[6].

### 1.2.1.3 Strong Refractive Scattering

Strong refractive scattering arises from the refraction of light through a lens. As with concave and convex lenses, refraction creates a focusing and de-focusing effect that can make a light source appear brighter or fainter respectively. Fur-

---

[6]Scaling relations for diffractive scintillation of an extended source are presented in Walker (1998).

thermore, refraction can make an image appear to shift positions, an effect often associated when looking through water. Thus we can consider diffractive scattering as creating a broadening effect and refractive scattering as producing a wandering effect.

In the context of refractive scattering, the associated length scale is attributed to the lens creating the refraction. The characteristic length scale of refractive scattering is simply the radius of the scattering screen (or lens), $r_F{}^2/r_{\text{diff}}$. Thus we can determine the angular size limit with respect to this length scale:

$$\theta_{\text{riss}} = \frac{r_F{}^2}{r_{\text{diff}}} \frac{1}{D} = \frac{r_{\text{ref}}}{D}, \tag{1.22}$$

where $r_{\text{diff}} >> r_F$ and $r_{\text{ref}}$ is the size of the scattered broadened image from diffraction (Narayan, 1992).

We can then set the timescale of modulations as the time to traverse the size of the correlation length, $r_{\text{ref}}$:

$$t_{\text{riss}} = \frac{r_{\text{ref}}}{v}, \tag{1.23}$$

where $v$ is the velocity of the scattering screen. Since the length scale associated with refractive scattering (i.e. $r_F{}^2/r_{\text{diff}}$) is far larger than both the Fresnel scale and $r_{\text{diff}}$, the timescale is much longer than for either weak scattering or diffractive scattering. Likewise, refractive scattering is a broadband effect.

To determine the modulation index, again we determine the RMS amplitude of the flux variations. In the refractive scattering regime, the amplitude depends on the RMS focal length of the variations (Narayan, 1992), which depends on $r_{\text{ref}}$. We can thus solve for the RMS amplitude and and find the modulation index, $m_{\text{riss},p}$ and parameterise it with respect to observable quantities:

$$m_{\text{riss},p} = \xi^{-1/3} = \left(\frac{\nu}{\nu_0}\right)^{17/30}, \tag{1.24}$$

where the exponent $-1/3$ arises from the assumption of Kolmogorov turbulence

(Walker, 1998). From Equation 1.24, we can see that observing at frequencies where $\nu << \nu_0$, the modulation index due to refractive scintillation produces a very low amplitude of modulation. Deriving the timescale of scintillation via the same scaling relation, we find the characteristic timescale for refractive scintillation:

$$t_{\mathrm{riss},p} = t_{\mathrm{riss}} \left( \frac{\nu_0}{\nu} \right)^{11/5}, \tag{1.25}$$

where $t_{\mathrm{riss},p}$ is in units of hours and $t_{\mathrm{riss}}$ is often assumed to be 2 hours (Walker, 1998). Finally, deriving the angular size limit of the screen:

$$\theta_{\mathrm{riss},\mathrm{screen}} = \theta_F \left( \frac{\nu_0}{\nu} \right)^{11/5}, \tag{1.26}$$

Since $\theta_{\mathrm{riss},\mathrm{screen}}$ is also proportional to $\nu/\nu_0$, it is also evident that for frequencies where $\nu << \nu_0$, the angular size limit of the screen becomes less strict. Thus, in the context of refractive scintillation, we see a broadband, slowly varying, low amplitude modulation. For interstellar scintillation, even though the scattering screen is at large distances (often assumed $\sim 500\,\mathrm{pc}$), the large length scale associated with refractive scintillation means observing refractive interstellar scintillation (RISS) is still achievable for many AGN. However many AGN will be resolved relative to $\theta_{\mathrm{riss},\mathrm{screen}}$, so we can scale the modulation index and timescale according to the same factors outlined in Section 1.2.1.1. Therefore, for sources where $\theta_{\mathrm{src}} > \theta_{\mathrm{riss},\mathrm{screen}}$, we find the timescale will be lengthened according to:

$$t_{\mathrm{riss},e} = t_{\mathrm{riss},p} \left( \frac{\theta_{\mathrm{src}}}{\theta_{\mathrm{riss},\mathrm{screen}}} \right), \tag{1.27}$$

Likewise, the modulation index will be dampened according to:

$$m = m_p \left( \frac{\theta_{\mathrm{screen}}}{\theta_{\mathrm{src}}} \right)^{7/6} \tag{1.28}$$

As noted in Section 1.2, RISS was first observed at $408\,\mathrm{MHz}$ for a population of compact AGN that showed modulation on timescales of months (Hunstead,

1972). Initially believed to be intrinsic to the source, the short timescale of modulation implied a non-physical brightness temperature of the source. By considering the ISM as a turbulent medium that produces scintillation, the rapid variations at low-frequencies could be explained. Interestingly, scintillation was already previously observed and characterised for DISS of pulsars and IPS of compact AGN, but RISS of AGN was largely overlooked until the monthly variability at megahertz frequencies. Thus, by the 1970's, scintillation had been observed in all regimes: i.e. weak scintillation observed as IPS, strong diffractive scintillation observed as DISS of pulsars, and RISS now explaining the rapid monthly variability of AGN. The different scintillation regimes, i.e. weak and strong refractive, associated with IPS and RISS respectively, is a large contributing factor to the different timescales associated with each. Furthermore, it is worth noting, that length scale of weak scattering (i.e. $r_F$) is far smaller than the length scale for refractive scattering (i.e. $r_{\mathrm{ref}}$). However, the distance to the scattering screen in IPS is far shorter than the distance to the scattering screen in ISM ($\sim 300\,\mathrm{km}$ compared to $\sim 320\,\mathrm{pc}$). Consequently, the angular source size limit is far less restrictive in IPS than RISS. For example, at $150\,\mathrm{MHz}$, the angular source size limit for IPS is $\sim 2\,\mathrm{arcseconds}$, compared to $25\,\mathrm{mas}$ for RISS. As a result, any source known to vary due to RISS should be compact enough to show IPS, but the inverse is not necessarily true. Furthermore, this may explain why RISS was initially overlooked at low-frequencies. The stricter source size limit for RISS can be advantageous, providing information on smaller structures of AGN than IPS. Furthermore, a detailed analysis of sources that show IPS but not RISS can provide a narrow range of source sizes and morphology of sources that may have a compact feature embedded in an extended structure that does not dominate the overall flux for IPS to be significant. Understanding the spatial scales associated with each scintillation regime and characterising scintillation can therefore provide information on source structure at resolutions comparable (and sometimes superior) to VLBI.

## 1.2.2 Intrinsic Variability

Intrinsic variability refers to a broad range of processes where variations are caused by processes associated with the source itself or its immediate environment. As outlined in Section 1.1.1, observing at different frequencies probes different regions of the AGN. Similarly, observing variability at specific frequencies probes the sizes and dynamical processes of the regions associated with emission at those frequencies. In this Section, we focus in particular at the processes that produce variability at radio wavelengths, typically associated with the jets and/or lobes of the AGN, and the observational properties of those processes. An overview of variability in different frequency regimes (such as optical or X-Ray) is included in the recent review Padovani et al. (2017).

At radio frequencies, the AGN emission is dominated by the synchrotron radiation, where the overall SED is directly related to the energy of the particles in the synchrotron emitting region and any sources of opacity. Consequently, intrinsic variability at radio frequencies can relate to changes in the energy of the particles in the synchrotron emitting region, e.g. shocks in the jets or adiabatic cooling and ageing, both discussion in Section 1.2.2.2 and Section 1.2.2.1 respectively. Alternatively, intrinsic variability can arise from changes in the viewing properties, e.g. a variable opacity from the ISM of the AGN host galaxy or jet precession, both are discussed in Section 1.2.2.3 and Section 1.2.2.4 respectively.

### 1.2.2.1 Cooling and Ageing

After the initial ejection from the AGN core, synchrotron emitting regions in the jets and lobes will age (i.e. lose energy) and appear to "cool" via three main mechanisms: adiabatic losses, synchrotron cooling and inverse Compton cooling (Manolakou & Kirk, 2002). Inverse Compton cooling is due to scattering of the electrons by the photons of the cosmic microwave background (CMB), as such, it is a constant loss rate with time as the source evolves (Manolakou & Kirk, 2002) and is more prominent at higher frequencies. Similarly, synchrotron losses are

also more prominent at higher frequencies as the higher energy particles radiate their energy faster. Consequently, the combination of synchrotron losses and inverse Compton cooling produce a break in the synchrotron spectrum, referred to as the break frequency, $\nu_b$, where the synchrotron losses dominate the energy injection. Thus as the plasma ages, even with continuous injection of energy, the synchrotron losses will produce a steepening above $\nu_b$, known as the continuous injection model with losses (CI model; Jaffe & Perola, 1973).

Without continued energy injection, the combination of synchrotron losses and inverse Compton scattering produces a spectral steepening with a decreasing $\nu_b$, the CI$_{off}$ model (Komissarov & Gubanov, 1994). Thus, remnant radio-loud AGN (also referred to as dying radio galaxies), where the core is no longer fuelling the jets and lobes by injecting energy, can be identified by particularly steep spectra at higher frequencies (e.g. Quici et al., 2021).

As well as the synchrotron losses and inverse Compton scattering, the plasma will expand resulting in adiabatic losses. As the plasma region expands, the energy of the electrons will decrease (Shklovskii, 1960). Thus, the electron energy is inversely proportional to the linear size of the plasma region, assuming the plasma is expanding isotropically (Tingay et al., 2015). Unlike synchrotron losses and inverse Compton cooling, adiabatic losses do not produce a change in the shape of the electron energy distribution, only a decrease in the overall flux density. However, for a plasma that is synchrotron-self absorbed, the adiabatic expansion and cooling influences spectral shape in the optically thick region (O'Dea & Saikia, 2021). As the plasma in the self-absorbed component expands, the opacity decreases, resulting in an overall *increase* in flux density (in the optically thick region) while $\nu_p$ decreases (van der Laan, 1966). From a SSA model, the flux density at $\nu_p$ can be calculated (in the observed frame of reference) according to:

$$S_{\nu_p} = \left( \frac{\pi^3 m_e^3 \nu_p^5 \theta_S^4}{0.94 eB \sin(\theta)} \right)^{\frac{1}{2}}, \tag{1.29}$$

where $\theta_S$ is the angular source size in milliarcseconds, $S_{\nu_p}$ is the flux density in

GHz, and the magnetic field, $B$, in Gauss is at an angle $\theta$ to the line of sight and $m_e$ and $e$ the electron mass and electron charge respectively (Tingay et al., 2015). Thus for a given SSA component, as it expands ($\theta_S$ increases), $\nu_p$ shifts to lower frequencies according to Equation 1.29. Sufficient spectral sampling (particularly at and around $\nu_p$) and temporal coverage to see the evolution of $\nu_p$ can therefore be used to constrain the source size and expansion rate (Alexander et al., 2020).

Hence, for components where the peak is due solely to SSA, adiabatic expansion will produce different effects in the optically thick and thin regimes (O'Dea & Saikia, 2021). Namely, in the optically thin region, the flux density will decrease (on top of losses due to synchrotron losses and inverse Compton cooling), while $\nu_p$ shifts to lower frequencies, and in the optically thick regime, the flux density will increase. Therefore, attributing variability due to adiabatic expansion can be used to estimate the age of the SSA component and characterise PS sources (e.g. Tingay & de Kool, 2003; Dallacasa & Orienti, 2016). However, this can complicated by potential anisotropic expansion.

Tidal disruption events (TDEs) are a specific outflow event from a SMBH that has disrupted a star as it is accreted (see Alexander et al. (2020) for a recent review). The resulting material ejected produces synchrotron emission and is often also self absorbed and is visible for typically 1–2 years (Goodwin et al., 2022). Consequently, TDEs offer a unique opportunity to monitor and characterise the entire evolution of a synchrotron component as it ages. Radio monitoring of TDEs have demonstrated the decreasing $\nu_p$ and decreasing flux density in the optically thin region of the SED after the radio peak (Goodwin et al., 2022), exactly as predicted above.

### 1.2.2.2 Shocks

Particles, typically in the surrounding ambient environment or within the jets, can be injected with more energy, or "re-energised", by shocks from the expansion of the radio source (Worrall et al., 2012; Beaklini & Abraham, 2014). Regions that

have been re-energised by shocks can compensate for the losses due to adiabatic expansion. Recent models have been proposed incorporating episodic activity creating "shells" representing discrete plasma regions (Jamil et al., 2010). In this model, the shocks can arise from two shells colliding, referred to as internal shocks. With a sufficient number of ejection events, there is enough re-energisation of the plasma that a flat spectrum or PS can be reproduced (Jamil et al., 2010). Therefore, PS sources can be a consequence of several internal shock events producing a sufficient re-energisation.

Monitoring of the variable AGN 3C 273 during the flare in 2010 found a 170 day delay between the initial $\gamma$-ray flare and radio flare (Marscher & Gear, 1985; Beaklini & Abraham, 2014). Such a delay is consistent with a shock re-energising the plasma within the jet producing the initial $\gamma$-ray flare, then propagating along the jet with increasing opacity until it is optically thin at radio frequencies.

Thus, shocks can produce variability in both the optically thick and optically thin regions. Internal shocks can produce flares with a delay from the initial flare at high frequencies to low frequencies as the the shocked region becomes optically thin. Furthermore, in the optically thick region, the opacity can change on short timescales due to inhomogeneities in the ISM caused by shocks from the jet expansion. With increasing evidence for episodic activity of AGN (Konar & Hardcastle, 2013; Shabala et al., 2020; Hardcastle & Croston, 2020), identifying the shock interactions between the episodes can be incredibly useful to determine the timescales of AGN activity and velocities of ejecta.

### 1.2.2.3 Variable Opacity

For components embedded or surrounded by clouds, inhomogeneities in the clouds can result in variability as the different clumps move into the line-of-sight (Tingay et al., 2015; Bicknell et al., 2018). Such a scenario is most relevant in the context of frustrated PS sources, which create a bow shock disturbing the ISM an creating

photo-ionised and shocked clouds (Bicknell et al., 2018). Shown in Figure 1.5, as the jets expand into the dense surrounding ISM, they heat the ambient clouds and impart energy to the clumpy surrounding ISM. This turbulent disturbed ISM can create a variable opacity as regions of different electron temperatures or densities move into the line of sight (Tingay et al., 2015).

Clouds of different electron temperatures and/or densities have different opacities due to free-free absorption (or inverse Bremsstrahlung). For a given electron density and temperature, the free-free opacity, $\tau$, is given by:

$$\tau = 1.1 \times 10^{-25} \nu^{-2.1} \int n_e{}^2 T_e{}^{-1.35} dl, \qquad (1.30)$$

where $n_e$ is the electron density in units of $\mathrm{cm}^{-3}$, $T_e$ is the electron temperature in units $10^4\,\mathrm{K}$ (Lang, 1980; Bicknell et al., 1997). As the opacity scales with $\nu^{-2.1}$, at lower frequencies, the overall flux density will decrease due to a greater level of absorption. Furthermore, as $\tau$ is related to the electron temperature and electron density, an inhomogeneous ISM with regions of differing electron temperatures and densities results in a variable optical depth as the regions move into and out of the line-of-sight. The timescale of such variability is related to the velocity of the clouds relative to the line-of-sight. The change in opacity (i.e. from $\tau_{\mathrm{ff}}$ to $\tau_{\mathrm{ff}} + \Delta\tau_{\mathrm{ff}}$) can thus be calculated from the changes in flux density according to:

$$\Delta\tau = -\ln\left[1 - \frac{\Delta S}{S_0 e^{-\tau_{\mathrm{ff}}}}\right], \qquad (1.31)$$

where $\Delta S$ is the change in flux density and $S_0$ is the flux density of the component being covered by the absorbing cloud (from the perspective of the observer) (Tingay et al., 2015).

One can therefore see rapid changes in the flux density due to a variable optical depth as regions in the ISM cover the emitting region. Likewise, large differences in the electron temperatures and/or densities of the ISM clouds can produce variations on timescales faster than could be explained by cooling and

ageing alone. Where ageing and cooling of a compact component means $\nu_p$ shifts to lower frequencies only, a variable opacity can shift $\nu_p$ to either higher or lower frequencies. A variable $\nu_p$ can therefore be used to distinguish between a variable opacity from free-free absorption or variations due to adiabatic expansions (e.g. Tingay et al., 2015).

#### 1.2.2.4   Jet Precession

For blazars, where the orientation of the jets is towards the observer, small changes in the orientation (as the jet processes) can produce significant variability across a range of wavelengths (Raiteri et al., 2017). Furthermore, the precession of the jet can result in changes in the Doppler factor, producing a large change in observed flux density (Rieger, 2004).

As discussed in Section 1.1.1, emission from the lobes will typically dominate at lower frequencies, while the core will typically dominate at higher frequencies. Therefore, jet precession can explain a delay in variability at longer wavelengths (Raiteri et al., 2017). A schematic for jet precession is presented in Figure 1.7, which shows that synchrotron emission from certain regions dominates the emission at certain wavelength. For example, the optical emission does not propagate far along the jet. As the jet precesses, viewing angle varies relative to the observing frequency due to the different emitting regions. Thus, in this schematic, the top observer will be sensitive to emission at optical and infrared wavelengths while the lower observer will be sensitive to millimetre wavelength emission from the same jet but not the optical emission.

The timescales of variability due to jet precession is observed to be far shorter than the timescales associated with cooling and ageing of a synchrotron component, due to the beaming of the jets (Ostorero et al., 2004; Pajdosz-Śmierciak et al., 2022). Jet precession can also account for the quasi-periodic nature of variability of blazars (Ostorero et al., 2004; Kudryavtseva et al., 2011). While it is probable jets that are not oriented roughly towards the observer also precess, de-
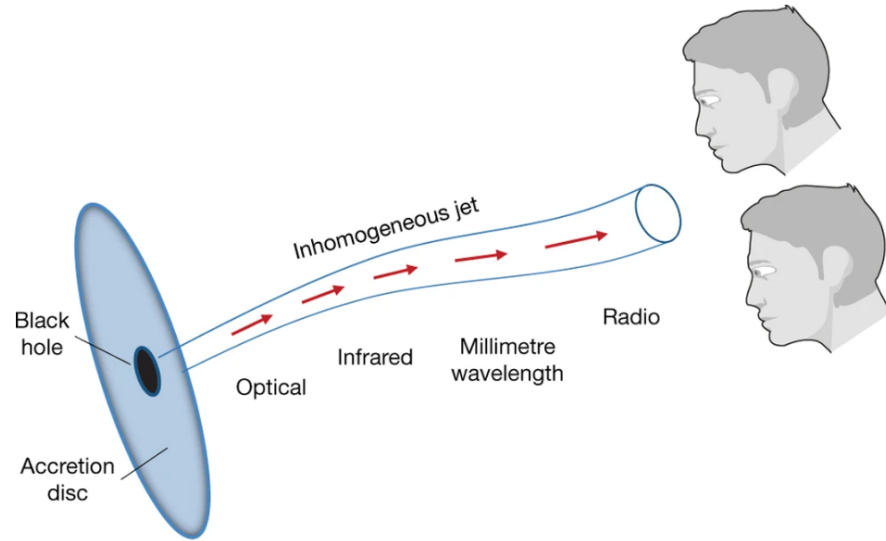
Figure 1.7: A schematic for the model of a precessing blazar. Two example observers are presented on the right, each observer has a different alignment relative to the jet and thus see enhanced emission in specific wavelengths. In this case, the top observer will see optical emission while the lower observer will be sensitive to millimetre wavelengths. Figure from Raiteri et al. (2017).

tecting variability from this precession is not viable as the evidence for precession comes from large scale morphologies. Jet precession of AGN not oriented towards the observer can be inferred from extended emission from previous episodes of activity with a different orientation to current or more recent episodes of activity (Hernández-García et al., 2017; Pajdosz-Śmierciak et al., 2022). Thus, jet precession often also suggests episodic activity of AGN and blazars (Pajdosz-Śmierciak et al., 2018).

## 1.3  Observing Radio Variability

From Section 1.2 it is clear the timescales and frequencies of variability are both highly dependent on the process producing the variability. Furthermore, with sufficient temporal and spectral coverage, it is possible to distinguish between various origins of variability; e.g. ISS produces a broadband rapid ($\sim$hourly at GHz frequencies) variability, while ageing and cooling of a synchrotron component

can produce a shifting peak frequency, at least over several years. It is critical, therefore, to design variability surveys and monitoring campaigns such that the expected time cadences are sufficiently sampled at relevant frequencies. However, observing with large spectral and temporal coverage is observationally expensive and until recent advances in telescope capabilities, many variability surveys were limited to small populations, small spectral coverage and/or small temporal coverage. We provide an overview of variability surveys to date in Section 1.3.1 and focus on the variability of PS sources in particular.

### 1.3.1 Variability Surveys

Several blind variability surveys have been conducted covering large sky areas and using a range of different instruments. Consistently, these surveys report only a small fraction of radio sources as being variable, typically around 1–2% (Carilli et al., 2003; de Vries et al., 2004; Ofek et al., 2011). However, the majority of these surveys have targeted variability at gigahertz frequencies (Quirrenbach et al., 1989, 1992; Fan et al., 2007; Bower et al., 2011).

Surveys searching for scintillation have probed a range of time cadences (minutes – months). After the discovery of monthly variability at 408 MHz (Hunstead, 1972), rapid variability in the radio sky was detected in the 1980's at higher frequencies on shorter timescales (Heeschen, 1984). In particular, intraday variability (IDV) was detected at centimetre wavelengths and attributed to ISS rather than intrinsic processes (Heeschen, 1984; Bignall et al., 2003). This led to targeted surveys into IDV due to ISS, most notably, the MicroArcsecond Scintillation-Induced Variability (MASIV) survey (Lovell et al., 2003, 2008). Of the 443 compact sources with a flat spectrum, over half showed significant (2–10%) variability on timescales as short as 2 days (Lovell et al., 2008). The galactic latitude dependence and comparison of modulation at 5 GHz from MASIV with the 15 GHz modulation detected by the Owens Valley Radio Observatory (OVRO) confirmed the origins of IDV to be due to ISS (Jauncey et al., 2020).

While typically IDV and ISS have been found to be caused by the general clumpy ISM, extreme and rapid scintillators have also been found to scintillate due to a scattering screen from nearby hot stars (Walker et al., 2017), and even a long (∼0.1 pc) thin plasma filament in the ISM (Wang et al., 2021). IDV due to a scattering screen from nearby hot stars has used to detect the $\mu$as scale at which a compact component becomes optically thick (Bignall et al., 2003). Likewise, IDV at 15 GHz in the OVRO monitored blazars identified the Orion-Eridanus star forming region as a significant source of scintillation (Koay et al., 2019). It is worth noting however, in these ISS surveys, the use of multi-frequency observations was critical to eliminate the possibility of intrinsic origins to the variability. Furthermore, many of the variability surveys probing rapid (≤monthly) variability only detected small populations of variable sources as the sky coverage was often compromised for time coverage. Recent IPS surveys using the MWA have detected a large population of variable sources (Morgan et al., 2019). For a flux complete sample, Chhetri et al. (2018) estimate ∼10% of the population show significant variability due to IPS at 150 MHz for sources brighter than ∼100–375 mJy. As the population was a flux complete sample, the proximity to the Sun has a minimal effect on the prevalence of IPS, rather it is the structure of the scintillating sources. Thus, this IPS survey suggests variability due to weak scintillation may be as common as 10%, compared to the 2% estimated for ISS. The large field of view of the MWA paired with the larger angular size limit for IPS compared to ISS, presents a hopeful opportunity to produce large populations of variable radio sources.

Recent searches for longer term variability (∼months – decades), has also revealed only a small fraction of the overall radio population as being variable (≤ 2%). The longer duration variability (particularly at higher frequencies), is often more sensitive to intrinsic origins of variability. However, the longer time cadences probed often results in several observational limitations. Until recently, survey speeds of telescopes has meant variability surveys have been limited by

small sample sizes (Tingay et al., 2015; Mooley et al., 2016; Sarbadhicary et al., 2021), small spectral coverage or single frequencies (de Vries et al., 2004; Bell et al., 2019) or by combining a range of surveys or archival observations with sparse temporal coverage (de Vries et al., 2004; Torniainen et al., 2005; Murphy et al., 2017; Nyland et al., 2020). The confidence of such variability surveys in identifying the origins of any observed variability is thus severely hindered. Variability surveys with sufficient spectral coverage have identified distinct forms of variability in spectral shape, hinting to different physical origins. Torniainen et al. (2005) identify a population of PS sources that display only a temporary PS classification, confirmed by (Nyland et al., 2020; Wołowska et al., 2021) who identified PS sources that flatten over ∼decades. A recent survey with MeerKAT identified a population of 21 long-term (∼yearly) variable radio sources with unique spectral variability (Driessen et al., 2022). Figure 1.8 presents the light curves for four of these variable sources along with their spectral index, calculated across the MeerKAT L-band (856–1712 MHz), with time. From Figure 1.8, it is clear two of the variables show a consistent spectral shape while the other two show a stark difference with clear variability in the spectral shape. The importance of spectral coverage in determining the physical origins of variability is further demonstrated in a comprehensive spectral variability analysis of the nearby PS source, PKS 1718–649 (Tingay et al., 2015). The broadband coverage in both the optically thick and thin regimes of PKS 1718–649 was used to identify independent origins of variability in these regimes: adiabatic expansion and cooling in the optically thin and variable opacity from free-free absorption in the optically thin.

Clearly, spectral information is critical in distinguishing between intrinsic and extrinsic origins. In the case of intrinsic variability origins, the spectral coverage is also critical to be used for constraining the evolutionary scenarios, e.g. measuring the decreasing $\nu_p$ in TDEs (Goodwin et al., 2022). However, the survey capability and technological limitations of instruments have limited the scope of spectral
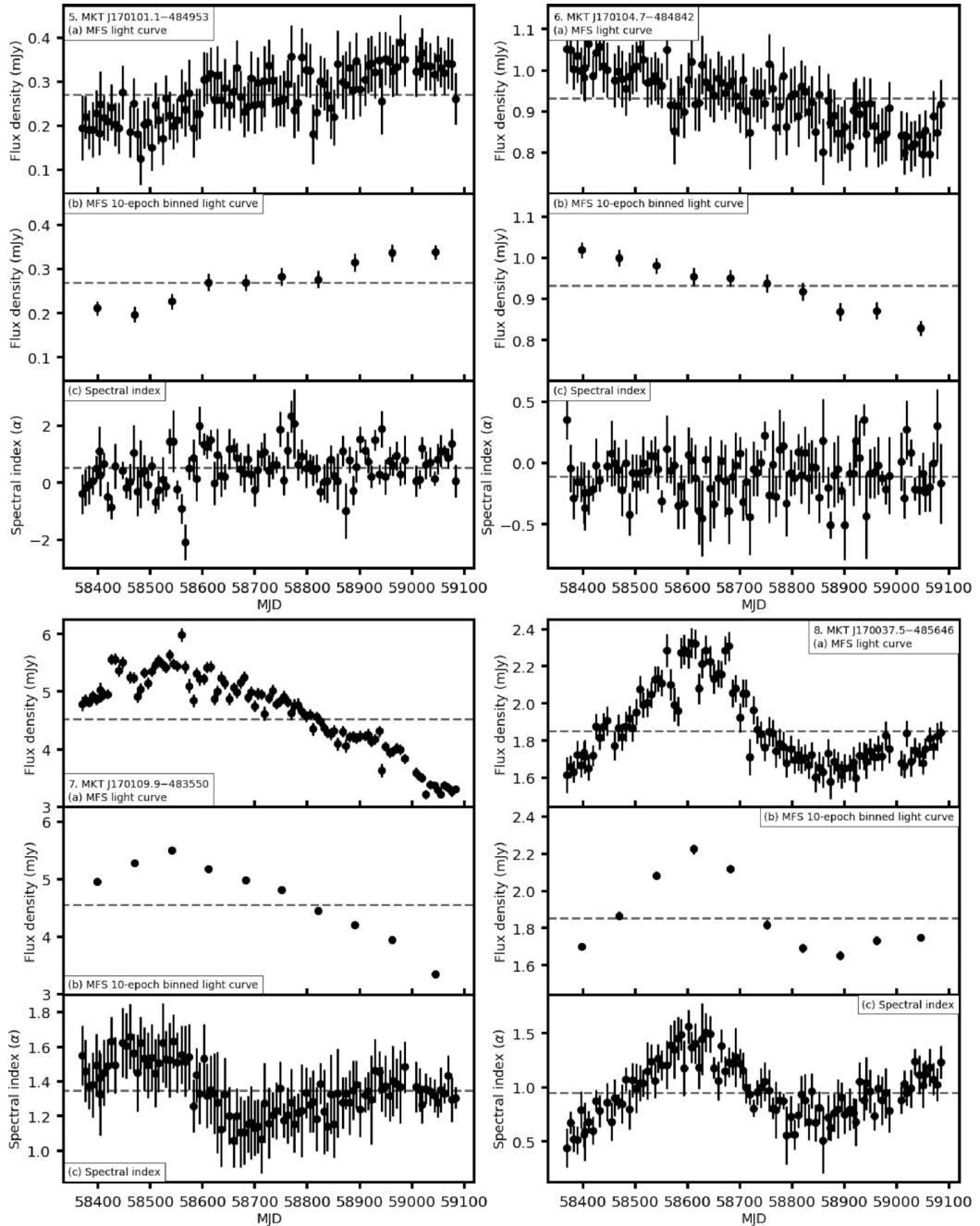
Figure 1.8: Lightcurves (top panel), binned lightcurves (middle panel) and spectral index with time (bottom panel) for four of the variables identified by MeerKAT (Driessen et al., 2022). Spectral indecies are calculated across the MeerKAT L-band covering 856–1712 MHz. For top two sources, the lightcurves show significant variability while the spectral index shows no significant variability. Alternatively, the bottom two sources show both significant flux density variability and spectral index variability. Figure from Driessen et al. (2022)

variability to date. Thus, the variable radio sky is still largely an unexplored parameter space with sufficient evidence that there is a plethora of information to be extracted.

Despite the limitations of spectral variability surveys to date, almost universally, PS sources are found to dominate the variable radio sky (Morgan et al., 2019; Nyland et al., 2020; Koay et al., 2018). However, the propensity of variable PS sources to lose their peaked shape with time (Torniainen et al., 2005; Wołowska et al., 2021) suggests a large fraction of PS populations is contaminated with sources only showing a temporary PS. However, until the MWA catalogue of PS sources was produced (Callingham et al., 2017), most catalogues of PS sources to date have been limited to identifying only the brightest sources peaking at $\sim 1\,\mathrm{GHz}$, due to a lack of available low-frequency observations, and by combining observations from a range of epochs and instruments (Sadler, 2016). Many catalogues of PS sources are thus biased to sources with a peak in the gigahertz regime, and are sensitive to contamination from sources showing only a temporary PS.

## 1.4 Radio Telescopes

### 1.4.1 The Murchison Widefield Array

The MWA is a low-frequency (MHz) array based in remote Western Australia on Wajarri country on the Murchison Radio-astronomy Observatory (MRO) site. It is a precursor to the Square Kilometre Array (SKA), which will be partly built on the same site. The remote location of the MRO was selected to avoid the radio frequency interference (RFI) produced from human activity.

The MWA design strategy is a large number of small antennas to optimise the field of view (610 sq. deg at 150 MHz) and sensitivity (Tingay et al., 2013). Furthermore, the distribution of antennas is such that there is a dense core and smooth distribution out to the largest baseline, resulting in an excellent instan-

taneous $u, v$-coverage, and thus high quality images can be reconstructed from short time integrations. Paired with the broad spectral coverage (70–300 MHz), and small instantaneous bandwidth (30.72 MHz), the MWA is an ideal instrument for conducting all sky surveys with a large fractional bandwidth. Such a survey is the GaLactic and Extragalactic All-sky MWA (GLEAM) survey (Wayth et al., 2015; Hurley-Walker et al., 2017), discussed further in Section 1.4.1.1.

From its initial construction, the MWA has had several notable phases and upgrades. Phase I consisted of 2,048 small dual-polarisation bow-tie antennas grouped together in a $4 \times 4$ grid called a 'tile'. In Phase I, the largest baseline was $\sim 2.8$ km, corresponding to an angular resolution of $\sim 2$ arcminutes at 150 MHz. Phase I was in operation from 2013 – 2017, during which all observations for the GLEAM survey were taken. In 2017, the MWA was upgraded to Phase II with 4,096 antennas arranged in 256 tiles and two distinct configurations, 'compact' and 'extended' (Wayth et al., 2018). Due to limitations of the correlator and receivers, only 128 of the available 256 could be operational at any time and a switch between each configuration required manually switching the tiles included in the overall array. The compact configuration of the MWA Phase II array configuration largely consists of two densely packed hexagonal tile configurations, with the majority of baselines within 200 m. The lack of longer baselines and large redundancy between baseline lengths make the compact configuration better suited to Epoch of Re-ionisation science, where imaging is not required. Conversely, the extended configuration is aimed at prioritising imaging capabilities, consisting of a subset of the Phase I array and an additional 56 long baseline tiles. The extended configuration boasts baselines up to 5.3 km, effectively increasing the resolution from Phase I by a factor of two. However, since the Phase II extended configuration was still limited to 128 tiles, the increase in tiles at longer baselines compromises the shorter baselines and hence the sensitivity to extended structure. As this Thesis is predominantly concerned with compact sources, far smaller than the angular resolution of the MWA, a loss

of sensitivity to extended structure is not of major concern. The tile arrangement and instantaneous $u, v$-coverage of the Phase II extended configuration is presented in Figure 1.9.
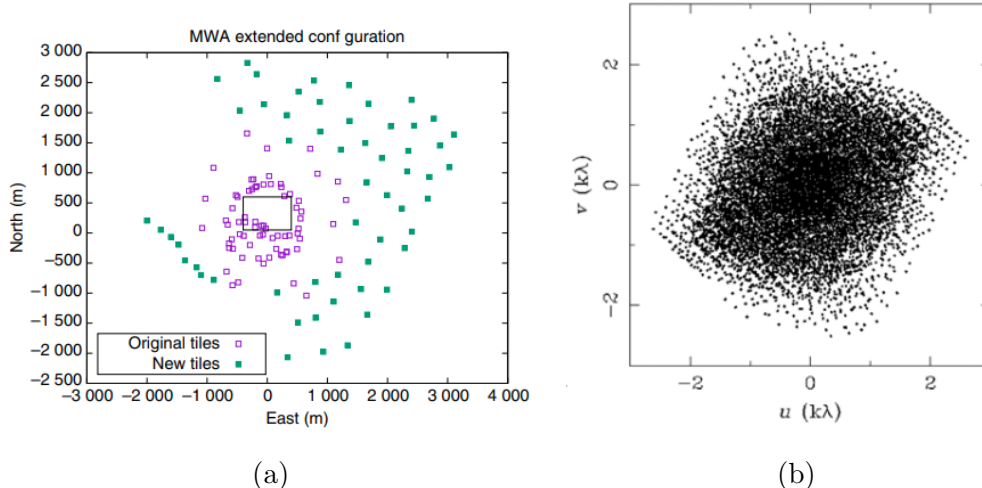


Figure 1.9: MWA Phase II extended tile configuration (a) and instantaneous $u, v$ coverage (b). In Figure (a), the purple squares denote the placement of tiles from the MWA Phase I that are included in the extended configuration, and the filled green squares correspond to the additional 56 long baseline tiles introduced in Phase II. The instantaneous $u, v$ coverage is determined for a zenith pointing at 154 MHz. Figure from Wayth et al. (2018)

#### 1.4.1.1 The GLEAM Survey

The GLEAM survey covers the entire radio sky below a declination of $+25°$, across 72–231 MHz (Wayth et al., 2015; Hurley-Walker et al., 2017). Due to the unique capabilities of the MWA, the GLEAM survey implemented an observing strategy that ensured quasi-simultaneous spectral coverage by cycling through a sequence of two minute snapshot observations in five frequency bands of width 30.72 MHz; the frequency bands covered 72–103, 103–134, 139–170, 170–200, 200–231 MHz. Each frequency band was then divided into 4 sub-bands each of roughly 8 MHz bandwidth, resulting in 20 individual flux density measurements across roughly 150 MHz bandwidth and covering a sky area of ∼30,000 sq. degrees, making the GLEAM survey the widest fractional bandwidth radio survey at publication

48

(Hernández-García et al., 2017). The GLEAM survey is set to be surpassed in sensitivity and angular resolution by the upcoming GLEAM-eXtended survey (Hurley-Walker et al., 2022), which takes advantage of the MWA Phase II extended upgrade.
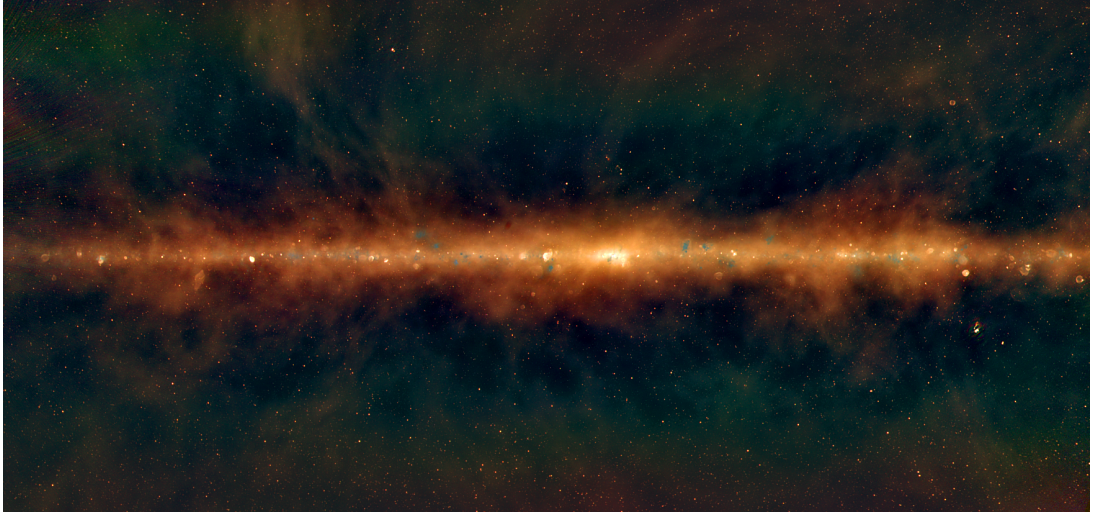


Figure 1.10: The GLEAM 'gold' image. Image credit: Dr. Natasha Hurley-Walker and the GLEAM-team.

One of the key advantages of the GLEAM survey is its large "fractional" bandwidth and large population (>300,000 sources in the extra-galactic catalogue alone). The spectral coverage allows for the detection of curvature and/or a spectral peak within the MWA bandwidth from quasi-simultaneous observations. Consequently, PS sources could be identified by either the detection of a spectral peak or from a positive spectral index (suggesting a spectral peak at higher frequencies), more than doubling the population of known PS sources (Callingham et al., 2017). Furthermore, the low frequencies probed by the MWA place it as an ideal instrument to study PS sources with low frequency peaks (i.e. MPS sources) and to obtain spectral coverage in the optically thick regime of PS sources, crucial for distinguishing between absorption mechanisms.

### 1.4.2 The Australia Telescope Compact Array

The ATCA consists of six dishes of diameters 22 m separated by a maximum distance of 6 km outside of Narrabri on Kamilaroi country and is part of the Australia Telescope National Facility (ATNF). Unlike the MWA, the ATCA utilises a small number of larger antennas in an East-West array. Consequently, the instantaneous $u, v$-coverage is far less than the MWA boasts. However, all but the furthest dish (CA06) can be moved along a 3-km track to multiple positions to produce a range of array configurations with different $u, v$-coverage and resolutions to suit specific science cases.

While the ATCA can observe across 1.1 to 105 GHz (limited by $2 \times 2048$ MHz bandwidth of the Compact Array Broadband Backend (CABB) correlator, (Wilson et al., 2011)), in this Thesis, ATCA observations are only taken in the L band (centered at 2.1 GHz), C band (centered at 5.5 GHz), and X band (centered at 9 GHz). The majority of the observations used in this Thesis were taken with ATCA in a 6 km configuration (i.e. prioritising resolution over $u, v$-coverage and extended structure sensitivity). In these configurations, the angular resolution of typical ATCA observations ranges from $\sim 1$ arcsecond at X band to $\sim 9$ arcseconds at L band.

### 1.4.3 The Long Baseline Array

The LBA is the only VLBI facility in the Southern hemisphere capable of milliarcsecond resolutions. It is a combination of 10 stations across South Africa, Australia and New Zealand, including the ATCA (in phased array mode). The network map of the LBA is presented in Figure 1.11. As the LBA is an ad-hoc array combining antennas of varying sizes controlled by several institutes, coordinating observations is limited to only a handful of times a year and the correlation of data is performed at the Pawsey Supercomputing Centre using the DiFX software (Deller et al., 2007). The LBA can observe across 1.4 GHz to 22 GHz. The sparse $u, v$-coverage (compounded if individual stations are offline during the few

observing periods) poses a significant hurdle when imaging with the LBA.
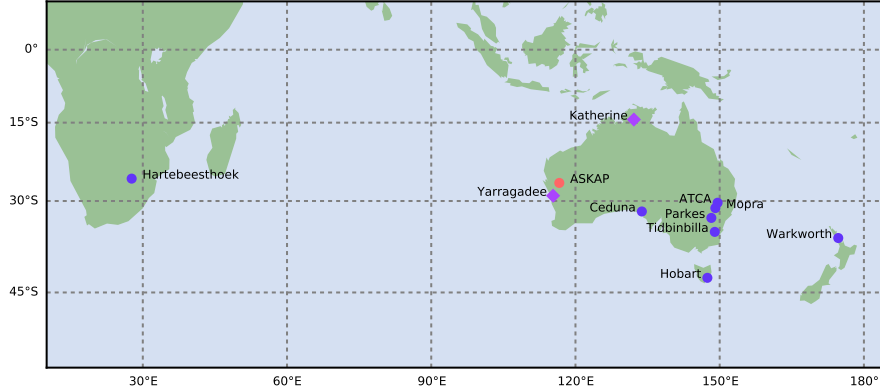


Figure 1.11: Figure showing the locations of stations used in the LBA. All but ASKAP were used in this Thesis.

## 1.5   Open Questions

Variability in the radio sky is a largely unexplored field, limited by the instrumental capabilities to date. However, with the advancement of several instruments, such as the MWA and the ATCA, we are now entering a new era of variability surveys that can survey large populations, across multiple frequencies, within a reasonable time-frame. In this work, we will investigate radio variability with a particular focus on broadband spectral coverage. Furthermore, we focus on PS sources in particular as a population known to be more variable than typical AGN. We demonstrate the use of spectral variability in characterising the absorption mechanisms of PS sources and their likely evolutionary pathways. This Thesis seeks to establish the statistical approaches and propose robust and reproducible methods, which will be vital with more spectral variability surveys.

Firstly, in Chapter 2, we conduct a blind survey of spectral variability using two epochs of the GLEAM survey. From this we develop a statistical approach to identify and characterise variability. In Chapter 3, we build on the blind survey by conducting a targeted spectral variability survey for a population of PS sources identified as variable in our blind survey. Here we are able to determine the physical origins of the spectral variability, and distinguish between intrinsic and extrinsic origins. Furthermore, we use the spectral variability to infer properties of the PS sources, including source sizes and absorption mechanisms. Chapter 4 uses VLBI to directly image the high resolution (milliarcsecond) structures of variable PS sources to compare to the predicted structures from spectral variability. Finally in Chapter 5, we summarise the results of this Thesis and the implications for future spectral variability surveys, presenting an extension of the statistical approach used in this work to cope with increased temporal coverage.

# Chapter 2

# A Blind Search for Spectral Variability

## 2.1 Context

One of the greatest limitations in conducting large population variability surveys with a broad spectral coverage has been the technological capabilities of available instruments. To reduce the computational and observational cost of spectral variability surveys, previous studies have ultimately compromised on the population size, frequency coverage, time sampling and/or relied on only gigahertz frequencies where variability is more common and expected. The MWA overcomes these hurdles due to its large field of view, broad spectral coverage at megahertz frequencies and impressive instantaneous $(u, v)$-coverage. With the development of the MWA and similar instruments, it has now become possible to survey a large population of radio sources, with large fractional bandwidth in a short period of time. The GLEAM Survey is one of the first such surveys in this new era of instrumentation. Covering almost $25,000$ square degrees with 20 flux densities measurements across $72$–$231\,\mathrm{MHz}$, the GLEAM survey was the largest fractional bandwidth and sky coverage survey at release. While not the primary goal of the GLEAM Survey, Franzen et al. (2021) processed GLEAM observations of a region

53

of over $5,000$ square degrees centred on the South Galactic Pole (SGP) that was observed in two separate epochs roughly one year apart. The multi-epoch, and large spatial and spectral coverage of the GLEAM SGP data release made this a fitting initial study of spectral variability.

As outlined in Section 1.2.1, estimated theoretical timescales of variability at megahertz frequencies due to RISS to be roughly $1.4$ years (Hancock et al., 2019). Thus, the roughly year separation between epochs in the GLEAM SGP region made it a fitting choice for a commensal survey of spectral variability at megahertz frequencies. Furthermore, the low frequencies of the GLEAM Survey make it an optimal opportunity to probe the variability of PS sources in the optically thick regime (at frequencies below their spectral turnover).

## 2.2 Implications

As this survey covered a broad spectral range, it was able to distinguish between sources that showed a variable spectral shape and sources that maintained spectral shape but varied in overall flux density, by introducing robust and reproducible statistics. A statistical approach is vital for upcoming future spectral variability surveys where populations, temporal coverage and spectral coverage are all set to increase.

From a population of of over $21,000$ sources, we find 323 variable sources ($\sim$1.5%) corresponding to $\lesssim$1 variable source per square degree. This fraction of variable sources is consistent with previous sources, however, the hard quality cuts implemented in this study suggest the fraction of variability should be considered a lower limit estimation. We also investigate the variability of sources identified as PS in our observations (which had $\nu_p$ between $72\,\mathrm{MHz}$ and $1.4\,\mathrm{GHz}$) independently, and identify them as an intrinsically variable population when compared to the overall AGN population. Furthermore, around 30% of PS sources lose their PS classification entirely, suggesting catalogues of PS sources are contaminated by a large fraction on temporarily peaked sources.

With the broad spectral coverage of this survey, we are able to begin to unravel the likely origins of the variability. The vast majority of variable sources (84%) show a consistent spectral shape, entirely consistent with refractive interstellar scintillation (RISS) inferring the presence of a compact feature $\lesssim 25\,$mas in these variable sources. However, RISS is unable to explain the changes in spectral shape within the MWA bandwidth. We suggest the sources showing a variable spectral shape are likely blazars, caught flaring in either year.

The broad range of variability found in this survey has highlighted the current insufficient understanding of emission mechanisms at low frequencies and AGN evolution.

## 2.3 Spectral variability of radio sources at low frequencies

The contents of this chapter have been published as "Spectral variability of radio sources at low frequencies" (2021) in the Monthly Notices of the Royal Astronomical Society, volume 501, `doi:10.1093/mnras/staa3795` (Ross et al., 2021). The accepted manuscript is re-produced, with permission, in full in this Chapter. Minor typographical and grammatical changes have been make to ensure consistency with the rest of the Thesis and minor additional comments have been added to clarify statements in the context of this Thesis.

# Spectral Variability of Radio Sources at Low Frequencies

K. Ross[1]⋆, J. R. Callingham[2,3], N. Hurley-Walker[1], N. Seymour[1],
P. Hancock[1], T. M. O. Franzen[3], J. Morgan [1], S. V. White[1,4],
M. E. Bell[7], P. Patil[5,6]

[1] *International Centre for Radio Astronomy Research, Curtin University, Bentley, WA 6102, Australia*

[2] *Leiden Observatory, Leiden University, PO Box 9513, Leiden, 2300 RA, The Netherlands*

[3] *ASTRON, Netherlands Institute for Radio Astronomy, Oude Hoogeveensedijk 4, Dwingeloo, 7991 PD, The Netherlands*

[4] *Department of Physics and Electronics, Rhodes University, PO Box 94, Makhanda, 6140, South Africa*

[5] *Department of Astronomy, University of Virginia, 530 McCormick Road, Charlottesville, VA 22903, USA*

[6] *National Radio Astronomy Observatory, 520 Edgemont Road, Charlottesville, VA 22903, USA*

[7] *University of Technology Sydney, 15 Broadway, Ultimo NSW, 2007, Australia*

## ABSTRACT

Spectral variability of radio sources encodes information about the conditions of intervening media, source structure, and emission processes. With new low-frequency radio interferometers observing over wide fractional bandwidths, studies of spectral variability for a large population of extragalactic radio sources are now possible. Using two epochs of observations from the GaLactic and Extragalactic All-sky Murchison Widefield Array (GLEAM) survey that were taken one year apart, we search for spectral variability across 100–230 MHz for 21,558 sources. We present methodologies for detecting variability in the spectrum between epochs and for classifying the type of variability: either as a change in spectral shape or as a uniform change in flux density across the bandwidth. We identify 323 sources with significant spectral variability over a year-long timescale. Of the 323 variable sources, we classify

51 of these as showing a significant change in spectral shape. Variability is more prevalent in peaked-spectrum sources, analogous to gigahertz-peaked spectrum and compact steep-spectrum sources, compared to typical radio galaxies. We discuss the viability of several potential explanations of the observed spectral variability, such as interstellar scintillation and jet evolution. Our results suggest that the radio sky in the megahertz regime is more dynamic than previously suggested.

**Key words:**  galaxies: active, radio continuum: galaxies, radio continuum: general

# 1   INTRODUCTION

Radio source variability is a powerful resource for studying extragalactic source structure and the physics of the environmental interaction of a radio galaxy. The two main categories of variability, intrinsic and extrinsic, provide information about the source itself or the intervening media along the line of sight, respectively. For example, radio variability can inform us about adiabatic expansion from changes in optical depth with time (Tingay et al. 2015) or changes in accretion state and jet evolution (Tetarenko et al. 2019). Extrinsic variability induced by scintillation provides information about the electron density variations between the source and observer. It can also give detailed information on the instrnsic structure of the source, particularly on the smallest angular scales (e.g. Macquart & de Bruyn 2007). The majority of previous studies of spectral variability have been conducted at gigahertz frequencies, which have shown to be dominated by the contributions from the core and jets (Hardcastle & Looney 2008), and thus detections of variability in the gigahertz regime have been common (e.g. Quirrenbach et al. 1989, 1992; Fan, J. H. et al. 2007; Bower et al. 2011).

Intrinsic variability of synchrotron radiation allows an observer to place a

⋆ E-mail: kathryn.ross@icrar.org

strict upper limit on the brightness temperature of the emission (e.g. Miller-Jones et al. 2008). Brightness temperatures for all sources emitting synchrotron radiation are subject to the strict upper limit of $10^{12}$ K due to the Compton scattering limit (Kellermann & Pauliny-Toth 1969). Sources with temperatures which exceed this limit indicate that their emission is coherent, as in the case of pulsars, or beamed towards the observer, as in the case of blazars.

The magnitude of the brightness modulation and timescales of extrinsic variability are dependent on which intervening medium is causing the scintillation (Hancock et al. 2019) and the source size (Narayan 1992). Depending on the frequency of the radiation, interstellar scintillation (ISS) typically varies source brightness on timescales of months to years (Coles et al. 1987), and is a result of the intervening electron density in the interstellar medium (ISM). ISS has two subcategories, refractive and diffractive, which produce slow (months–years) and short (days–weeks) timescale variability, respectively (Rickett 1986). Interplanetary scintillation (IPS) occurs when radio waves are distorted as they travel through the Solar wind (Clarke 1964; Hewish & Burnell 1970). Typically IPS has timescales of seconds or shorter, and sources with a larger angular size can vary due to IPS compared to ISS.

Previous studies of variability and transients at low frequencies ($< 1$ GHz) have searched a wide range of timescales and types of radio sources since the first discovery of variability due to refractive interstellar scintillation (RISS; Hunstead 1972; Rickett 1986; Fanti et al. 1990; Riley 1993; Hancock et al. 2019). However, such searches have only identified a small population. Chhetri et al. (2018) searched for variability in a sample of compact 37 extragalactic radio sources and identified only one source as showing significant variability; J013243-165444, a known blazar with a peaked radio spectrum.

A comparison of Tata Institute of Fundamental Research (TIFR) GMRT 150 MHz Sky Survey Alternative Data Release 1 (TGSS-ADR1; Intema, H. T. et al. 2017) and the GaLactic and Extragalactic All-Sky Murchison Widefield

Array (GLEAM; Wayth et al. 2015; Hurley-Walker et al. 2017b) surveys at
$\sim 150\,\text{MHz}$ to search for transients between the two surveys yielded only one
candidate that had no detectable spectral curvature (Murphy et al. 2016). Stew-
art et al. (2015) conducted a search for transients at $60\,\text{MHz}$ using the Low-
Frequency Array (LOFAR; van Haarlem et al. 2013) and also found only one
candidate, showing that bright transient radio sources at low frequencies are
fairly uncommon. The Murchison Widefield Array Transients Survey (MWATS;
Bell et al. 2019) surveyed ~1,000 sources for almost three years at a cadence of
≈3 months. MWATS found 15 variable sources with significant flux-density mod-
ulation at $154\,\text{MHz}$, seven of which were identified as having a curved spectrum
by Callingham et al. (2017), and detected no transients.

Previously, it has been suggested that surveys of variability at low frequencies
($\leq 500\,\text{MHz}$) have found few variable extragalactic sources because emission at
megahertz frequencies is expected to be dominated by the emission from the
lobes of the radio galaxies (Bell et al. 2019). Such radio lobes are $\sim$10–1000 kpc
in size (Hardcastle & Looney 2008), and thus are often too large for ISS to be
significant, which requires angular sizes $\lesssim 5$ milliarcseconds. However, the radio
sources that have previously been identified as low-frequency variables are more
likely to also have a peaked spectrum (Bell et al. 2019; Chhetri et al. 2018). It still
remains unclear whether peaked-spectrum sources dominate the low-frequency
variable population due to intrinsic effects, such as source evolution, or due to
their potentially small spatial structures causing them to be more susceptible to
scintillation.

Peaked spectrum sources (PSS), analogous to gigahertz-peaked spectrum (GPS),
high-frequency peaked (HFP) and compact steep-spectrum (CSS) sources (O'Dea
1998; Kunert-Bajraszewska et al. 2010; O'Dea & Saikia 2020), are a unique sub-
set of AGN that can display far more compact double-lobe morphology than
typical radio-loud AGN (Phillips & Mutel 1982; Tzioumis et al. 2010). GPS and
HFP radio sources are categorised by their notable peak at gigahertz frequen-

cies, and CSS radio sources are expected have a peak at a lower radio frequency (< 200 MHz) and display a compact double structure. A subclass of PSS were identified by Callingham et al. (2017) that display the same identifiable peak but in the megahertz regime that are believed to be the same class of object as GPS and HFP sources (Callingham et al. 2015; Coppejans et al. 2015, 2016).

Previous studies of the variability of PSS at gigahertz frequencies have yielded several sources that show flux density variability across their radio spectra while maintaining their PSS classification (i.e., retain a clear peak in their radio spectra at each epoch). However, it has also been observed that some sources can lose their PSS classification over time (Torniainen et al. 2005). Several sources displayed a temporary peaked spectrum which over time smoothed to a flat spectrum. Such sources with a temporary peaked spectrum at gigahertz frequencies are believed to be blazars (Tinti et al. 2005), where the features in the small core-jet structure are likely also scintillating at gigahertz frequencies. In contrast, one known peaked-spectrum source, PKS B1718-649, which has a double-lobe morphology on parsec scales, has been observed to show variability both above and below the spectral peak at gigahertz frequencies over an approximately two-year period (Tingay et al. 2015). The spectral variability of the spectral energy distribution (SED) of PKS B1718–649 was best modelled by variations in the optical depth and adiabatic expansion of the source.

Despite the plethora of radio frequency variability research, the majority of previous studies have been limited to identifying variability at a single frequency (Stewart et al. 2015; Murphy et al. 2016; Chhetri et al. 2018; Bell et al. 2019), small sample size (Tingay et al. 2015), or spectral variability at gigahertz-frequencies formed from non-contemporaneous data (Torniainen et al. 2005). Such shortcomings have limited our understanding about the cause of the identified variability since, for example, scintillation is a broadband effect producing unique variability across the entire radio spectrum. Likewise, intrinsic variability produces frequency-dependent effects depending on the emission or absorption

mechanism. Distinguishing between intrinsic or extrinsic processes as the cause of variability requires simultaneous multi-frequency spectral coverage, but this has been hard to achieve.

Large population studies with significant spectral and temporal coverage have only recently become available with the development of radio telescopes like the Murchison Widefield Array (MWA; Tingay et al. 2013) and LOFAR (van Haarlem et al. 2013). The MWA has a large field of view ($\sim 600\,\mathrm{deg}^2$) and operates over a wide frequency range ($\sim$80-300 MHz) with an instantaneous bandwidth of 30.72 MHz. As we move into the Square Kilometre Array (SKA) era, low-frequency surveys with wide spectral coverage of large populations will become more readily available, permitting us to discern the origins of radio variability. Consequently, it is imperative that we derive appropriate methodologies and robust statistical techniques in order to produce insightful results from these future surveys.

This paper presents the first large population survey of low-frequency spectral variability using two epochs of the GLEAM survey. In Section 2 we outline the sample selection process and data used in this analysis. Section 3 describes the methodology for detecting and classifying spectral variability. We present the catalogue of variable candidates in Section 4, in particular the sources with persistent PSS in Section 4.0.1 and variable spectral shape in Section 4.0.2. The potential mechanisms for the observed variability of each class are discussed in Section 5. We adopt the standard $\Lambda$-cold dark matter cosmological model, with $\Omega_\mathrm{M} = 0.286$, $\Omega_\Lambda = 0.714$, and the Hubble constant $H_0 = 69.6\,\mathrm{km\,s^{-1}\,Mpc^{-1}}$ (Hinshaw et al. 2013).

## 2  DATA

### 2.1  GLEAM Year 1 and Year 2

In the first year of GLEAM observations ('Year 1': Aug 2013 – Jun 2014), the entire sky south of Dec +30 deg was surveyed at 72–231 MHz using meridian drift scan observations at different declination stripes, taken at night in week-long runs spaced about three months apart. Due to the observing strategy, 8–10 hour scans taken at night, there is little crossover in surveyed sky area in the observations separated by three months, making a variability search on a three month timescale feasible only for small areas of sky. Quasi-simultaneous spectral coverage was ensured by cycling through a sequence of two minute scans in five frequency bands; the frequency bands covered 72–103, 103–134, 139–170, 170–200, 200–231 MHz. Hurley-Walker et al. (2017b) published the GLEAM Extragalactic Catalogue, which excludes Galactic latitudes, $|b| < |10°|$, and a few areas around bright sources, based on these observations. The catalogue provides 20 almost independent flux density measurements across 72–231 MHz and covers $24,000 \, \mathrm{deg}^2$ of sky, making it the widest fractional bandwidth radio survey to date.

An additional epoch ('Year 2', Aug to Dec 2014) was conducted with minimal changes to the observing strategy. In Year 2 the observations of year one were repeated twice with hour angles of $\pm 1$ hour. This second epoch of GLEAM provides a unique opportunity to search for low-frequency variability in the flux density over a large fractional bandwidth over a one year timescale (hereafter referred to as Year 1 and Year 2 observations).

We independently processed a subset of the Year 1 and Year 2 data from the highest four frequency bands over an $\sim 8000 \, \mathrm{deg}^2$ region of sky centred on the South Galactic Pole and covering $300° \leq \mathrm{RA} \leq 100°$ and $0° \leq \mathrm{Dec.} \leq -60°$. In this region of sky, the Year 1 data were taken almost entirely over the period Aug–Nov 2013 and the Year 2 data were taken over the period Aug–Dec 2014. We

used an improved pipeline and beam model for the MWA, and used the published GLEAM catalogue as a sky model for calibration.

The lowest MWA sub-band (72–103 MHz) was not used as the presence of the bright sources Fornax A and Pictor A in the sidelobes of the primary beam prevented maps with sufficient quality being produced for the Year 2 data. A more detailed explanation of this enhanced processing is provided by Franzen (2020). We use these two epochs of data, each composed of sixteen 7.68 MHz mosaics spanning 103–231 MHz and a wide-band mosaic covering 200–231 MHz, to search for variability.

## 2.2    Source Extraction

We used Aegean[1], a source finding algorithm (Hancock et al. 2012, 2018), to create the catalogue of sources for each epoch. Firstly, Aegean was run blindly (i.e. without prior positional constraints) over the most sensitive and highest resolution mosaic, the 200–231 MHz mosaic for the Year 2 data. The background and noise mosaics were generated using the Background and Noise Estimation tool (BANE). The resulting catalogue was used to provide the positions for a priorized fit measurement in each of the other mosaics. Aegean also used the point spread function (PSF) maps as well as the background and noise images for source characterisation.

Aegean measures the peak flux density of a source by a Gaussian fit to its brightness distribution, with the reported total flux density representing the integrated flux density under the fit. We used the priorized fitting mode of Aegean, which took the known position and size of the source and only fit for the flux density. Since we are only investigating high signal-to-noise sources, small variations induced by the fitting algorithm have a negligible impact on the spectra of the sources and were accurately captured in our flux density uncertainties.

---

[1] https://github.com/PaulHancock/Aegean

For thoroughness, we checked for any significant changes in source shapes or the PSF between epochs and found no such changes. Consequently, by assuming a consistent shape and position and by using the priorized mode to fit the flux, we reduced the possibility of induced artificial variability due to differences in the source finder fitting.

An accurate estimate of the uncertainty for individual flux density measurements for each source at each frequency is necessary to evaluate the reliability of any observed variability. For sources detected above $100\,\sigma$ in the 200–231 MHz Year 1 mosaic and 200–231 MHz Year 2 mosaic, we examined the distribution of the flux density ratios of the Year 1 to Year 2 integrated flux densities. Note that since the variability is rare, the width of the distribution is dominated by systematic and random noise. We used this distribution to confirm that the flux density scales are consistent. The measured FWHM of this distribution was used to determine the random flux density uncertainty at each frequency. The percentage uncertainty for each of the 16 frequency bands was found to be $\sim 0.5$–1%, consistent with the internal uncertainties reported by Hurley-Walker et al. (2017b).

Near the edges of the mosaic there is correlated noise in some bands. As a result, we increased the error for sources within roughly five degrees of the edge of the mosaics by $\sim 3\%$. Likewise, in several regions, poor calibration due to bright sources in the sidelobe of the MWA or bright nearby sources could result in correlated variability. The sources we account for are Pictor A (both for nearby sources and when Pictor A is in the sidelobe), Fornax A, Cassiopeia A in the sidelobe and the Crab nebula in the sidelobe. We increased the error in these regions to $\sim 2$–5% to account for this. The percentage increase for the error was calculated to ensure there was no structure in the variability index parameter (VIP), discussed further in Section 3.1, according to RA or Dec. Firstly, regions with a higher density of sources with large values for the VIP were identified. The error was increased in these regions until there was no discernible structure in the VIP across the entire mosaic. The central coordinates of these regions

| Source Name | Coordinates, RA, Dec (deg) |
|---|---|
| Pictor A | 80, −46 |
| Pictor A sidelobe | 62, −15 |
| Fornax A | 51, −37 |
| Cassiopeia A sidelobe | 350, −25 |
| Crab Nebula sidelobe | 31, −42 |

**Table 1.** Bright sources where correlated variability was noticed. We assign higher error when calculating the VIP and MOSS to reduce the measured variability making it in line with other regions.

are presented in Table 1. Furthermore, any sources with $18° \leq$ RA $\leq 36°$ and $-35° \leq$ Dec $\leq -20°$ or $54° \leq$ RA $\leq 95°$ and $-35° \leq$ Dec $\leq -22°$ were excluded entirely as the quality of the mosaics was lower in these sky regions due to issues with calibration or bright sources in the primary beam in the Year 2 data.

The final catalogue used for this project contains 93,928 sources (selected from the Year 2 200–231 MHz mosaic). Each source has 16 individual flux density measurements across 103–231 MHz, and a wide-band (200–231 MHz) flux density for both Year 1 and Year 2. Noise levels were measured from the local root-mean-squared (rms) of the initial mosaics. For the 200–231 MHz wide-band mosaics, the mean and standard deviation of the rms noise was found to be $7 \pm 5$ mJy beam$^{-1}$.

### 2.3 Sample Selection

Several quality cuts were applied to the catalogue to select reliable sources. These cuts are based on those outlined by Callingham et al. (2017). In summary, the quality cuts ensure that unresolved GLEAM sources are bright enough to form high signal-to-noise spectra to reliably search for spectral variability. The selection criteria, applied to both years, are presented in Table 2. Sources that met the first five criteria in Table 2 (in both years) are classified as the "master sample", which is composed of a total of 21,558 sources.

## 2.4   Description of Additional Radio Data

We use the Sydney University Molonglo Sky Survey (SUMSS; Mauch et al. 2003) and the NRAO VLA Sky Survey (NVSS;  Condon et al. 1998), as part of our spectral modelling to estimate the spectral index for the high frequency section of the SED (180 MHz – 843 MHz/1.4 GHz). We considered the possibility that the higher resolution of SUMSS and NVSS would mean some of our MWA sources are resolved into multiple components. After visually inspecting the NVSS and SUMSS counterparts to our PSS candidates, no source was found to be heavily resolved. We also note that the SUMSS and NVSS data is only used in the PSS classification, not in the variability analysis. Furthermore, it is worth noting, by using non contemporaneous measurements for the PS source classification, there is a possibility that variability could influence the measured spectral index and classification of PS sources. This highlights the need for simultaneous broadband spectral coverage to classify PS sources confidently. We recommend a further follow-up of all PS sources in this study to confirm the classification.

The Australia Telescope 20 GHz (AT20G) Survey was used to test if there was the presence of compact features and the detections of core components (Murphy et al. 2010), see Section 4.1 for more details. All other radio surveys used in this paper were not explicitly used in any analysis, but are included in the SEDs for completeness. The additional radio surveys are the Very Large Array Low-frequency Sky Survey Redux (VLSSr;  Lane et al. 2014), TIFR GMRT 150 MHz Sky Survey Alternative Data Release 1 (TGSS-ADR1;  Intema, H. T. et al. 2017), and the Molonglo Reference Catalogue (MRC:  Large et al. 1981, 1991). All catalogues were cross-matched using Topcat's (Taylor 2005) nearest neighbour routine with a 2 arcmin radius. A 2 arcmin radius was chosen as it is comparable to the resolution of GLEAM. Despite the low resolution of GLEAM, and large crossmatch radius used, sources in GLEAM are sufficiently sparse that misidentification is unlikely.

*2.4.1 SUMSS*

SUMSS is a continuum survey at 843 GHz with observations taken between 1997 and 2003 (Mauch et al. 2003). SUMSS was conducted by the Molonglo Observatory Synthesis Telescope (MOST; Mills 1981; Robertson 1991) covering the southern sky up to a declination of $-30°$, excluding Galactic latitudes below $10°$. The published catalogue has a total of 211,063 sources and the resolution of the survey varied with declination $\delta$ as $45'' \times 45'' \operatorname{cosec}|\delta|$. SUMSS is 100% complete above $\approx 8$ mJy south of a declination of $-50°$, and above $\approx 18$ mJy for sources with a declination between $-50°$ and $-30°$.

*2.4.2 NVSS*

NVSS is a continuum survey at 1.4 GHz with observations taken between 1993 and 1996 (Condon et al. 1998). NVSS was conducted by the Very Large Array (VLA) covering the northern sky down to a declination of $-40°$ with a resolution of $\approx 45$ arcseconds. The published catalogue has a total of 1,810,672 sources, and is 100% complete above 4 mJy.

*2.4.3 AT20G*

AT20G is a blind search for radio sources at 20 GHz with observations taken between 2004 and 2008 (Murphy et al. 2010). AT20G was conducted by the Australia Telescope Compact Array (ATCA) covering the southern sky up to a declination of $0°$ with a resolution of $\approx 10$ arcseconds. The published catalogue has a total of 5,890 sources, and is 91% complete above 100 mJy in regions south of declination $-15°$.

# 3 VARIABILITY ANALYSIS

In this section, we present methods to determine if a source is variable and if it changes spectral shape. The classification steps are presented in Table 2.

| | Step | Criteria | Number of Sources |
|---|------|----------|-------------------|
| 0 | Total Sources in Field | | 93,928 |
| 1 | Unresolved in wide-band mosaic | $\frac{ab}{a_{\mathrm{psf}} b_{\mathrm{psf}}} \leq 1.1$ | 77,916 |
| 2 | Bright in wide-band mosaic | $S_{200-231\mathrm{MHz}} \geq 160\,\mathrm{mJy}$ | 24,089 |
| 3 | High signal-to-noise (S/N) | eight or more flux density measurements with S/N $\geq$ 3 | 24,624 |
| 4 | NVSS and/or SUMSS counterparts | Cross-match within 2 arcmin counterpart | 24,619 |
| 5 | Cut bad RA and Dec regions | Source outside regions with $18° \leq$ RA $\leq 36°$ and $-35° \leq$ Dec $\leq -20°$ or $54° \leq$ RA $\leq 95°$ and $-35° \leq$ Dec $\leq -22°$ | 21,558 |
| | *Total Master Population* | *Sources that passed steps 0–5* | *21,558* |
| 6 | Variable | VIP $\geq 58.3$ | 340 |
| 7 | Manual Check | Pass manual inspection | 323 |
| 8 | Uniform Spectral Change | MOSS $< 36.7$ | 272 |
| 9 | Changing Spectral Shape | MOSS $\geq 36.7$ | 51 |

**Table 2.** Quality cuts (from Section 2.3) applied to the catalogue of sources to derive the master population and the criteria for variability classification. Any source that did not pass criteria 1–5 in each year of data was discarded. $a$, $b$, $a_{\mathrm{psf}}$ and $b_{\mathrm{psf}}$ are the semi-major and semi minor axes of the source and the point spread function, respectively. $S_{200-231\mathrm{MHz}}$ is the measured flux density in the wide band mosaic covering 200–231 MHz. NVSS is the NRAO VLA Sky Survey (Condon et al. 1998) and SUMSS is the Sydney University Molonglo Sky Survey (Mauch et al. 2003). These quality cuts are identical to those implemented by Callingham et al. (2017). Sources which pass steps 1–5, in both years, are classified as the "master population". Variable sources are selected as described in Section 3. The VIP is a measure of variability and is calculated according to Equation 1. The MOSS parameter is presented in Equation 2 and measures the change in spectral shape.

## 3.1 Variability Index Parameter

In order to identify true source variability, instead of instrumental noise, we define the variability index parameter (VIP). The VIP is adopted from the $\chi^2$ statistic,

$$\text{VIP} = \sum_{i=1}^{n} \frac{\left(S_{\text{yr1}}(i) - S_{\text{yr2}}(i)\right)^2}{\sigma_i^2}, \tag{1}$$

where $S_{\text{yr1}}(i)$ and $S_{\text{yr2}}(i)$ are the flux densities in Year 1 and Year 2, respectively, in a given sub-band, $i$. $\sigma_i$ is the combined uncertainty of each flux density added in quadrature. The uncertainties for each flux density also incorporate systematic errors. The VIP is calculated entirely from the raw flux density measurements to avoid biasing variability estimates induced when fitting spectral models to the data.

The VIP was calculated for each source in the master sample, including the 422 sources previously identified as a PSS by Callingham et al. (2017).

We plotted a $\chi^2$ probability density function (pdf) with 15 degrees of freedom using SCIPY.STATS.CHI2 (Virtanen et al. 2019). The pdf and histogram are presented in Figure 1. We observe that the shape of the VIP distribution for the master population is what we would expect for an intrinsically non-variable population, with the variation largely produced by noise in the flux density measurements. Such an interpretation is supported by the fact the vast majority of sources in the master population have a VIP within 0–16, suggesting any change from Year 1 to Year 2 is entirely within 68 per cent confidence limit for all 16 flux density measurements. Furthermore, the agreement with a theoretical $\chi^2$ distribution with 15 dof is consistent with a largely non-variable population.

We chose to prioritise the reliability of the selected variable sources over completeness of the sample as we are investigating an unexplored parameter space for variability. Therefore, we have implemented a conservative cut to the VIP of $\geq 58.3$ (equivalent to a confidence level of true variability of 99.99994%, i.e. $5\sigma$). All sources with a VIP$\geq$58.3 also had a visual inspection of the SEDs to ensure the variability was reliable. 17 sources with a VIP$\geq$58.3 were flagged as non-variable; their apparent variability is likely due to calibration errors or bright nearby sources, and is characterised by large, non-physical steps in the SED.

We also compare the master population distribution of VIP with that of the PSS population (in Figure 1). Unlike the master population, the PSS population is not well defined by a $\chi^2$ distribution. There is an excess of sources identified as a PSS with VIP $\geq$ 16. This result suggests that variability is a more prominent feature of the PSS population compared to the general radio source population. To ensure this bulk property of the PSS population is not due to this population having a larger signal-to-noise ratio (S/N), we demonstrate how the VIP of the master population and PSS sources varies as a function of S/N in Figure 2. The PSS population relative to the master population does not have completeness issues at S/N$\geq$ 50, as shown in the top panel of Figure 2 as the PSS S/N population closely matches that of the master population. However, we find the distribution of the VIP of the PSS population much wider than the master population (for sources with S/N$\geq$ 50), with a larger tail towards a higher VIP, as shown in the histogram in the right panel of Figure 2.

We take this as evidence that the PSS source *population* is more variable, on average, than the general radio source population.

## 3.2   Measure of Spectral Shape

The large fractional bandwidth of this study enables us to detect changes in spectral shape between epochs. We classified the variable population into two classes of spectral variability:

(i) Uniform change: all 16 flux density measurements increase or decrease by the same absolute amount (within uncertainty);

(ii) Changing shape: the shape of the spectrum has changed between epochs.

To distinguish between these two categories, we define the measure of spectral shape (MOSS) parameter. The MOSS parameter uses the flux density measurements directly to detect changes in spectral shape in order to reduce uncertainties
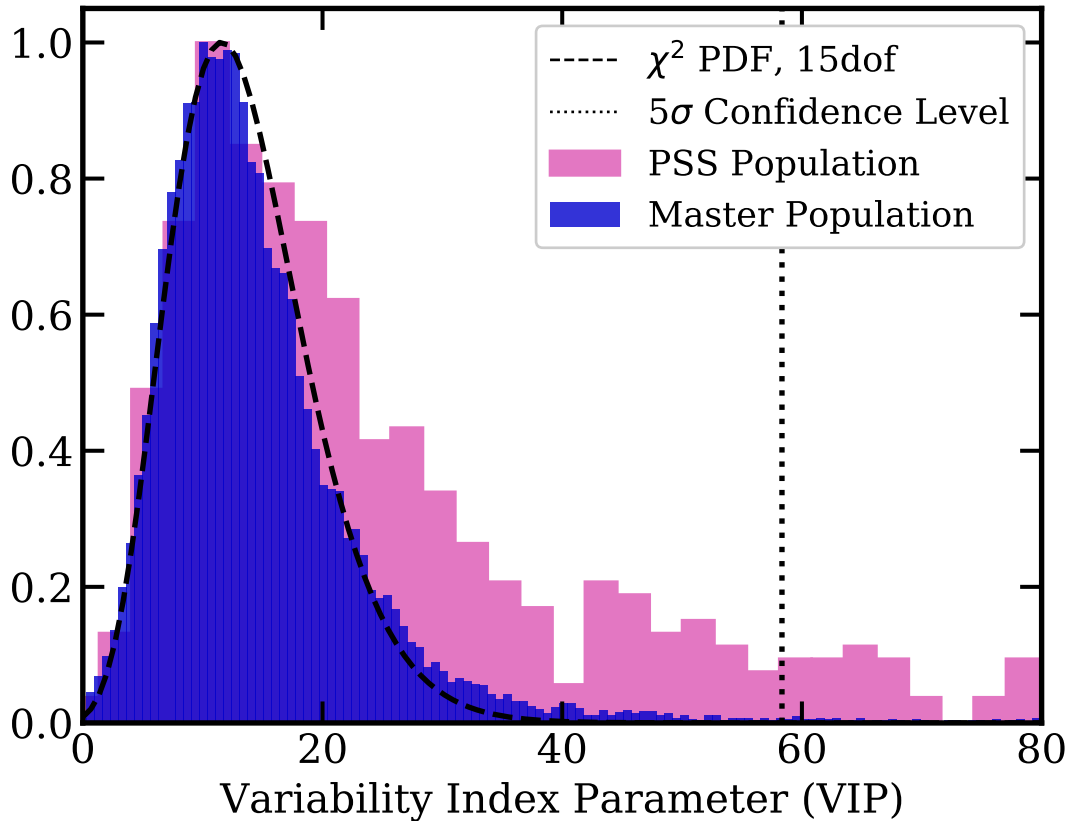
**Figure 1.** Histogram of the VIP as a measure of spectral variability for both the master population (blue) and the PSS population (pink) normalised to a maximum of one. The master population was modelled with a $\chi^2$ probability density function with 15 degrees of freedom and is consistent with a population which is mostly non-varying. Using this distribution a 99.99994% confidence level, corresponding to a VIP of 58.3, was used to determine whether a source was variable. The PSS population is not well defined by a $\chi^2$ distribution, implying it is likely a more intrinsically variable population.

that accompany fitting spectral models. The MOSS parameter is also a variation of the $\chi^2$ statistic, namely:

$$\text{MOSS} = \sum_{i=1}^{n} \frac{(\widetilde{\text{diff}} - \text{diff}(i))^2}{\sigma_i^2} \tag{2}$$

where $\widetilde{\text{diff}}$ is the median of the differences between the flux density over all frequencies, $\text{diff}(i)$ is the difference of the flux densities between the two epochs at frequency $i$, and $\sigma_i$ is the combined uncertainty of each flux density added in quadrature. Unlike the VIP, the MOSS parameter measures how many flux density points are greater than $1\sigma$ away from the median difference value. A larger

**Figure 2.** Distribution of the VIP as a function of the signal-to-noise ratio (S/N) in the 200–231 MHz wide band mosaic. The grey hexagons represent the density of the master population (as indicated by the colour-bar). Pink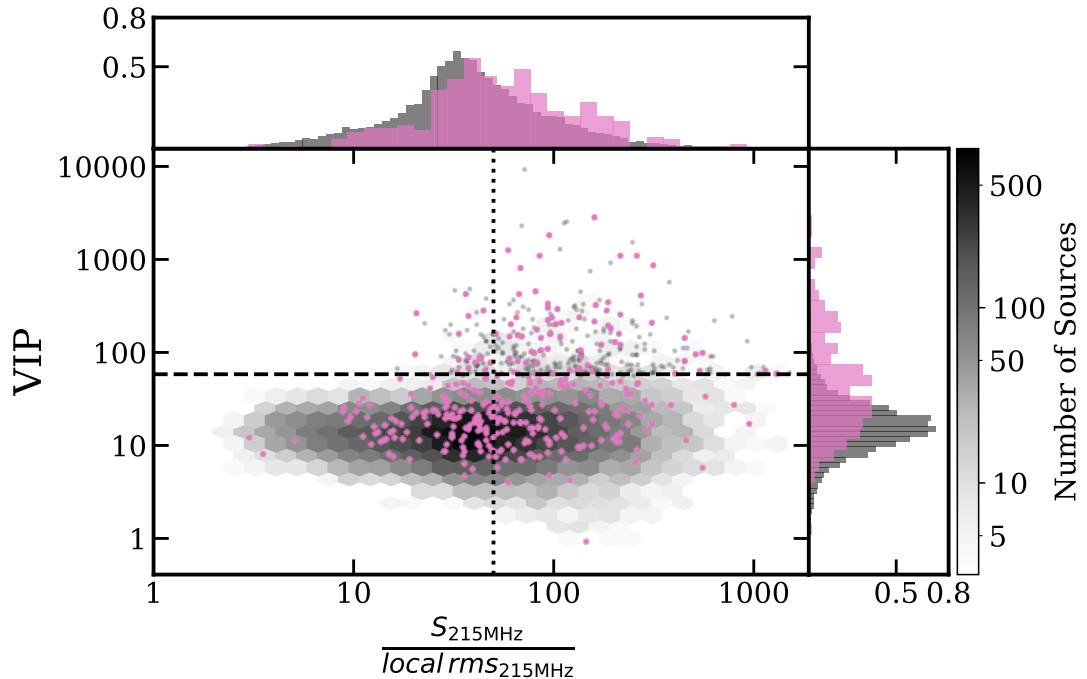 dots are sources identified as persistent PSS and grey points are all other variable sources. The dashed horizontal line is the 99.99994% VIP confidence level of 58.3 (equivalent to $5\sigma$): sources with a VIP$\geq$58.3 are classified as variable. The distribution of the S/N for the master population and PSS population is shown in the grey and pink histograms in the top panel. The dotted vertical line denotes a S/N cut of 50 where the PSS population is complete, relative to the master population. The grey and pink histograms in the right panel represent the VIP distributions for the master population and PSS population respectively for sources with a S/N above 50. The PSS VIP histogram shows a significantly different distribution to that of the master population with a peak at higher VIP, a wider distribution, and longer tail towards higher VIP.

MOSS value suggests a larger spread of the difference in measurements from the median value between the two epochs and hence a change in spectral shape.

The distribution of the MOSS parameter for the non-variable population is most consistent with a $\chi^2$ probability density function with 12 dof, as shown in Figure 3. Hurley-Walker et al. (2017a) noted that the errors within the 30 MHz bands of GLEAM are correlated. Since we are measuring correlated change away from a central point, this has a stronger effect on the MOSS parameter than the VIP. We hypothesise that this is the cause of the reduced number of de-

grees of freedom of the optimal PDF distribution, given we expect 14 dof. Using the distribution of the non-variable population a value of 36.7 and above for the MOSS parameter was chosen to select sources that are 99.99994% likely to be truly changing shape (equivalent to a $5\sigma$ confidence level). We define the *uniform change population* as variable sources with no significant change in spectral shape according to the MOSS parameter (with a MOSS parameter below 36.7). Likewise we define the *changing spectral shape population* as variable sources with a significant change in spectral shape according to the MOSS parameter (with a MOSS parameter $\geq 36.7$).

The spectra of two example sources that are classified as changing spectral shape according to the MOSS parameter are presented in Figure 4.

We note that the MOSS parameter could potentially miss truly changing spectral shape sources if the difference between the two epochs are symmetric around the mean frequency. For example, GLEAM J234312–480659 (Figure 5) shows a "tick" shape in its difference spectra. Therefore, it is classified as uniform change rather than changing shape. Furthermore, it is harder to detect a change in spectral shape for sources with lower S/N. After careful testing to balance a reliable changing shape population with completeness, sources with a MOSS > 36.7 are classified as changing spectral shape, corresponding to a confidence level of $5\sigma$.

### 3.3  Spectral Modelling

Following the spectral modelling outlined by Callingham et al. (2017), the flux density measurements for each source for both years were fit with two different models using the non-linear least squares python SCIPY module, `curve_fit` (Virtanen et al. 2019):
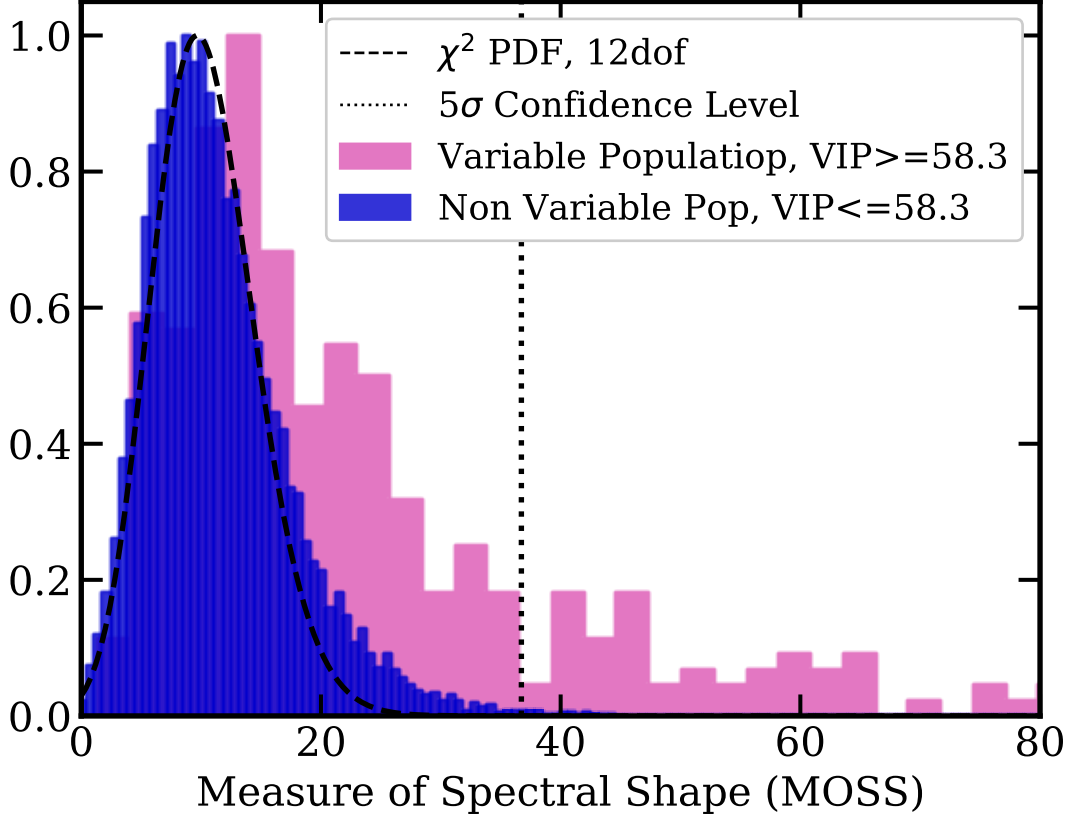
**Figure 3.** Histogram of the MOSS parameter, a measure of the variability of spectral shape, for the non-variable master population (blue) and the 323 variable sources (sources with a VIP$\geq$ 58.3) (pink) both normalised to have the max number of sources in a bin as 1. This distribution was fit with a $\chi^2$ probability density function and is consistent with the majority of variable sources not displaying changing spectral shape. Using this distribution, a 99.99994% confidence level, corresponding to a MOSS parameter $> 36.7$, was used to determine a significant change in spectral shape between Year 1 and Year 2.

(i) Power-law: A model that fits the flux density distribution of sources whose emission is primarily non-thermal:

$$S_\nu = a\nu^\alpha, \tag{3}$$

where $S_\nu$ is the flux density at frequency $\nu$ and $a$ is the amplitude of the spectrum. This model was fit to two datasets: (1) the 16-band MWA data (100–231 MHz) to measure the spectral index for the low frequency section of the SED, $\alpha_{\text{low}}$, and; (2) two MWA flux density measurements (189 and 212 MHz) and the

**Figure 4.** Examples of radio spectra of two variable sources showing a significant change in spectral shape between Years 1 and 2. One was found to be have a peaked spectrum in Year 1 and then flattened in Year 2 (GLEAM J225641–201140, left panel) and the other (GLEAM J032237–482010, right panel) showed the reverse. The points represent the following data: GLEAM low frequency (72–100 MHz) (grey circles), Year 1 (pink circles), Year 2 (blue circles), TGSS (b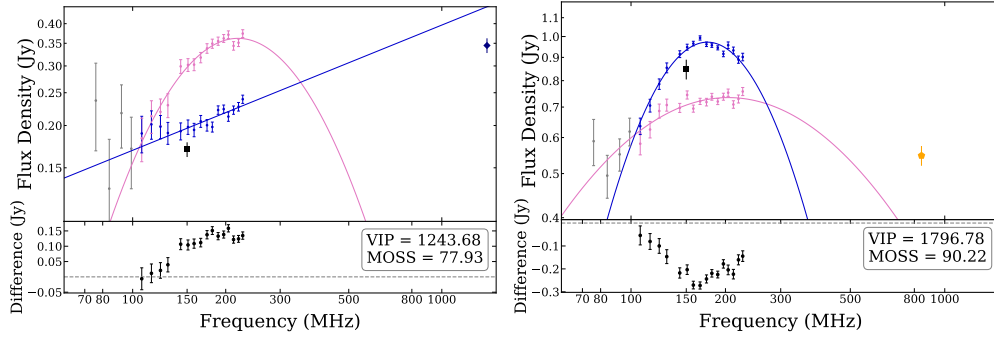lack square), SUMSS (yellow pentagon), and NVSS (navy diamond). The difference of the flux densities in Year 1 and 2 are plotted below. Models plotted for each year are determined by the PSS classification only. A source classified with a peak within the observed MWA band, which also satisfied the PSS criteria presented by Callingham et al. (2017), was modelled by a quadratic according to Equation 4. Remaining sources were modelled by a power-law according to Equation 3, see Section 3.3 for details.

flux density of the SUMSS and/or NVSS counterpart to measure the spectral index for the high frequency section of the SED, $\alpha_{\text{high}}$.

(ii) Quadratic: A non-physical model to detect any spectral curvature within the MWA band. This is only fit to the 16-band MWA data (100–231 MHz):

$$S_\nu = a\nu^\alpha \exp^{q(\ln \nu)^2},$$ (4)

where $q$ represents the spectral curvature and the other parameters are as defined in Equation 3.

It is worth noting, when classifying PSS using observations at different frequencies taken at different times, it is possible to over-estimate or under-estimate the spectral indices due to variation in fluxes (e.g. due to scintillation or Doppler boosting at higher frequencies, i.e. the peak may seem more pronounced when combining different epochs of observation). Consequently, the best way to detect and classify PSS is with simultaneous megahertz and gigahertz-frequency spectral coverage of the SED with monitoring of a least a year to determine if the source maintains its PSS classification. In common with all other searches
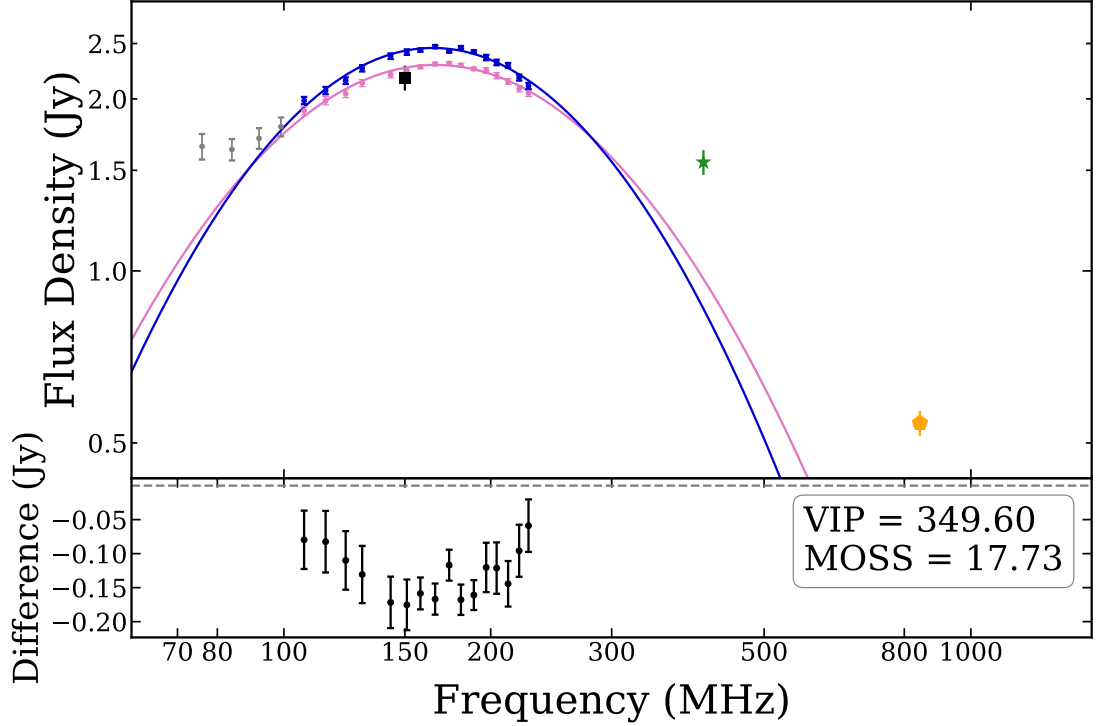
**Figure 5.** Example of a source for which there is insignificant change in spectral shape according to the MOSS parameter $5\sigma$ confidence level cut despite the sharper peak in the spectra for Year 2. The data points represent the following data: GLEAM low frequency (72–100 MHz) (grey circles), Year 1 (pink circles), Year 2 (blue circles), TIFR GMRT 150 MHz Sky Survey Alternative Data Release 1 (TGSS) (black square), MRC (green star), and SUMSS (yellow pentagon). Residuals are calculated by differencing the flux density measurements of the two epochs of observations. The models for each year are determined by the classification of the source; We identify a peak within the observed bandwidth that is well modelled by a quadratic according to Equation 4 for both years.

in the literature so far, our PSS classifications rely on measurements taken over different epochs (i.e. SUMSS/NVSS), implying there will be false positives in the population.

## 4 RESULTS

Firstly, we compare the distributions of $\alpha_{\mathrm{low}}$, $\alpha_{\mathrm{high}}$ and $q$ with those presented by Callingham et al. (2017). In both the Year 1 and 2 data, the majority of sources lie close to a $\alpha_{\mathrm{high}} = \alpha_{\mathrm{low}}$ line, consistent with no change of spectral index across the full frequency. The median and standard deviation for $\alpha_{\mathrm{low}}$ and $\alpha_{\mathrm{high}}$ are

$-0.82 \pm 0.28$ and $-0.76 \pm 0.24$ in Year 1, and $-0.81 \pm 0.28$ and $-0.76 \pm 0.22$ in Year 2.

The curvature parameter distributions for Year 1 and Year 2 are both consistent with those found by Callingham et al. (2017) with the median curvature, $q$, and standard deviation for Year 1 and Year 2 found to be $-0.12 \pm 0.50$ and $-0.12 \pm 0.41$ respectively. We compared distributions for $\alpha_{\mathrm{low}}$, $\alpha_{\mathrm{high}}$ and $q$ with those presented by Callingham et al. (2017) and find no significant differences from visual inspection or between the reported median and standard deviations.

From the 21,558 sources of the master population, we have identified 323 sources that have VIP$\geq 58.3$ and classified them as variable. The majority of sources in this variable population show no significant change in spectral shape between the two MWA epochs, with 272 sources ($\sim 84$ per cent) showing a uniform spectral change across the observed bandwidth. The other 51 sources ($\sim 16$ per cent) are classified as changing spectral shape, since their spectral shapes change significantly from Year 1 to Year 2 as their MOSS parameter was $\geq 36.7$.

Of the variable population, 91 sources ($\sim 28\%$) were identified as PSS by Callingham et al. (2017). We also classified sources in the master population as PSS according to the same criteria outlined by Callingham et al. (2017), and find 123 sources identified as PSS in either year in the variable population ($\sim 38$ per cent). We find 83 PSS in the variable population maintain a PSS classification in both years (67 per cent of sources identified as PSS in either year).

One variable source, GLEAM J043715–471506, shows extreme variability (with a VIP of 9,124); see Figure B1 in Appendix B for the SED. GLEAM J043715–471506 is a known pulsar, PSR J0437–47. Other known pulsars in the field are not included in the master population as they fail to meet the brightness cut, see step 2 in Table 2.

We identify six sources – GLEAM J001942–303118, GLEAM J010626–271803, GLEAM J033112–430208, GLEAM J033412–400823, GLEAM J041636–185102, GLEAM J215155-302751 – which were classified as potential restarted galaxies

by Callingham et al. (2017) due to their "upturned" SEDs, each with a VIP$\geq$ 64. We conclude that these sources were misclassified and are likely not restarted galaxies but variable quasars with flat spectra. Of the 25 sources identified as "upturned" SEDs by Callingham et al. (2017), 19 sources (76 per cent) are not identified as variable.

Mid infra-red colour selection techniques using Wide-field Infrared Survey Explorer (*WISE,* Wright et al. 2010) are widely used to distinguish between AGN and star-forming galaxies (e.g., Lacy et al. 2004; Stern et al. 2005; Wu et al. 2012; Assef et al. 2013). We compare our variable population with the *WISE* infra-red colours and find all variable sources are consistent with AGN/quasar classifications, as expected based on the flux density limit of our sample. Furthermore, we searched for any trend in VIP or MOSS with Galactic latitude and find none.

### 4.0.1 *Variable Persistent PSS Population*

Of the persistent PSS in the variable population, 11 sources ($\sim$13%) are classified as showing a change in spectral shape between epochs according to the MOSS parameter, while still maintaining a PSS classification. For example, some persistent PSS may have a positive spectral index, $\alpha_{\mathrm{low}}$, in each year but the steepness changes significantly according to the MOSS parameter. The other 72 sources are classified as showing a uniform change across the MWA bandwidth.

There are four sources that are classified as variable persistent PSS but are not classified as PSS by Callingham et al. (2017). The inconsistency in classification is likely due to the lack of the lowest band in this study, which prevented a robust fit in the optically thick region of the SED, making their peaked-spectrum classification less certain. These four sources are GLEAM J020903–495243, GLEAM J041913–142024, GLEAM J042140–152734 and GLEAM J234625–073042.

### *4.0.2   Changing Spectral Shape*

We detect 51 variable sources that have a MOSS parameter $> 36.7$, and are thus classified as showing a significant change in their spectral shape between epochs. Of these changing spectral shape sources, 18 (20 per cent) were selected as PSS by Callingham et al. (2017). The significant change in spectral shape suggests even if these sources maintain PSS classification in Year 1 and 2, it is possible this is only temporary and they will lose their peaked-spectrum classification over time.

A change in spectral shape may allow more accurate identification of the astrophysics of sources. For instance, GLEAM J033023–074052 was classified peaked-spectrum by Callingham et al. (2017) but is classified as changing spectral shape between epochs. VLBI observations of GLEAM J033023–074052 found it was unresolved on milliarcssecond-scales, and constrained its projected linear size to be $< 45\,\mathrm{pc}$ (Keim et al. 2019). After reexamination of the optical spectral for GLEAM J033023–074052, we find the MgII line was a misidentified Lyman-$\alpha$ line (Wolf et al. 2018; Onken et al. 2019)[2], thus the redshift is likely 2.85 rather than 0.67 as previously reported by the 6df Galaxy Survey (Jones et al. 2009) and used by Keim et al. (2019). Using the updated redshift, we recalculated the upper limit for the projected linear size of J033023–074052, and the limit increases to $< 50\,\mathrm{pc}$[3].

The compact linear size and changing spectral shape over a year-long period is consistent with the jets from the AGN being oriented towards the observer (i.e.f a blazar), as opposed to a small double source that would be expected for a young AGN. The radio SED for GLEAM J033023–074052 is shown in Figure 6.

---

[2]  The SkyMapper ID is 21523027 and details of the object can be found here: `http://skymapper.anu.edu.au/object-viewer/dr3/21523027/#` and the spectra can be analysed here: `http://skymapper.anu.edu.au/static/sm_asvo/marz/index.html#detailed`

[3]  The small change in limit is due to the two redshifts having nearly identical angular diameter distances in the $\Lambda$-CDM cosmology.
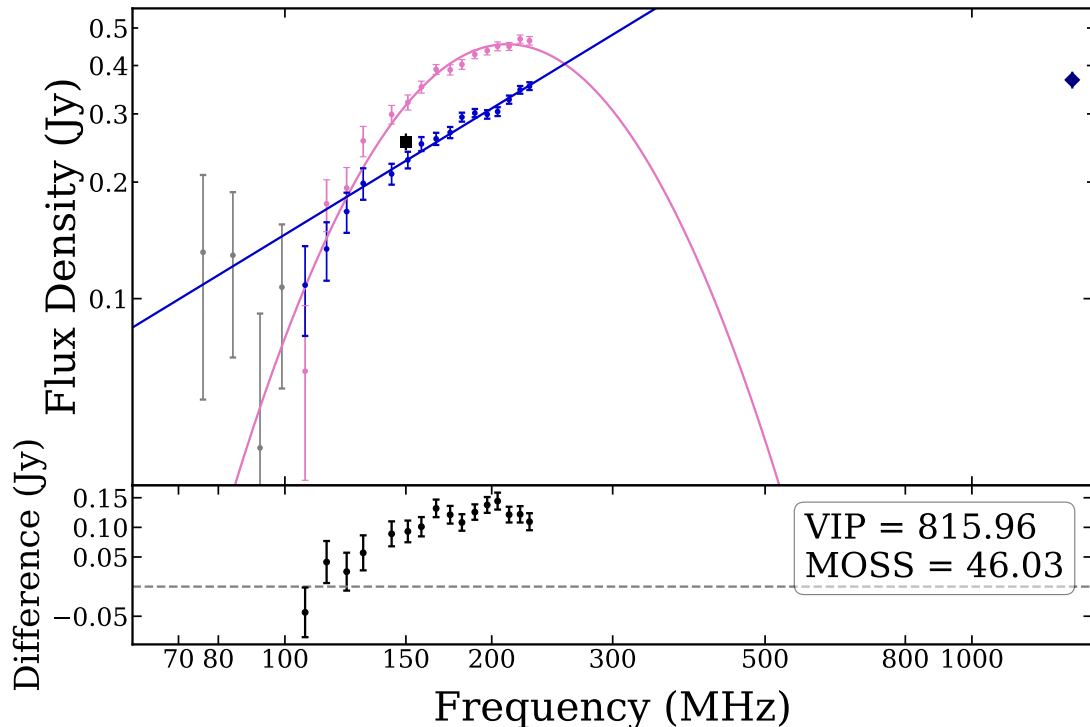
**Figure 6.** GLEAM J033023–074052, classified as changing spectral shape in this paper according to the MOSS. This source has also been found to be unresolved with VLBI with an upper limit on the projected linear size of 50 pc (from the new redshift presented here and the angular size reported in Keim et al. 2019). The points represent the following data: GLEAM low frequency (72–100 MHz) (grey circles), Year 1 (pink circles), Year 2 (blue circles), TGSS (black square), and NVSS (navy diamond). In Year 1 the spectrum is classified with a peak within the observed band and was modelled by a quadratic according to Equation 4, and the Year 2 spectrum was modelled by a power-law according to Equation 3.

## 4.1 AT20G Counterparts

Murphy et al. (2010) present a blind search for radio sources using the Australia Telescope Compact Array (ATCA) at 20 GHz. At 20 GHz, the brightness of radio galaxies is more likely to be core-dominated. We cross-matched our master population with the AT20G survey to identify sources that are dominated by their core flux density and/or are more likely to be blazars. Of the 1020 sources in our master population that have a counterpart in AT20G, 116 sources are classified as variable (11 per cent).

This result contrasts with just ∼1.6% of the total master population being

variable and therefore supports the idea that core-dominated radio sources are more likely to be variable. Furthermore, of the variable sources with AT20G counterparts, we identify 24 sources (21 per cent) as changing spectral shape, larger than the 16 per cent of the total variable population showing significant change in spectral shape.

We note one source in particular, GLEAM J032237–482010, has a significant change in spectral shape (MOSS≈90) yet has no AT20G counterpart. GLEAM J032237–482010 does have a flux density of ∼ 0.5 Jy at 840 MHz according to SUMSS. If GLEAM J032237–482010 is a quasar with a flat spectrum around 0.5 Jy or a blazar with a temporary peak in the SED, the core should be bright enough for an AT20G detection. The non-detection of AT20G suggests this source is not core dominated, contradictory to what the variability suggests. The SED for GLEAM J032237–482010 is presented in Figure 4.

## 4.2   Known blazars in the variable population

Massaro et al. (2015) combined optical spectra and absorption lines with the radio spectra to identify blazars, which they present in the Roma-BZCAT catalogue. We cross-match our master population with Roma-BZCAT and find 295 sources with a BZCAT counterpart. Of these sources, 64 are classified as variable by the VIP (22 per cent), 18 of which (28 per cent) are classified as changing spectral shape according to the MOSS parameter. This is a larger proportion of sources classified as changing spectral shape compared to the total variable population of which the changing spectral shape sources make up 16 per cent.

## 4.3   Comparison to literature 150 MHz variability studies

### 4.3.1   MWA Transients Survey

The MWA Transients Survey (Bell et al. 2019, MWATS;) was a blind search for variable sources at 150 MHz over 3–4 years. We compare our variable popula-

tion with the sources identified by the single frequency variability identified by MWATS and find no overlap. Of the 15 variable sources identified by MWATS, seven were in our field and no source had a VIP≥23.

By considering the light curves presented by Bell et al. (2019) for the seven sources in our field, it appears MWATS is more sensitive to changes in flux density over 3–4 years, while this work considers only two epochs one year apart. The different parameter spaces each survey explores suggest different astrophysical explanations are driving the observed variability. MWATS predominantly attributes their observed variability to RISS. We explore the viability of RISS as the cause for the observed variability of this survey in Section 5.1.

### 4.3.2   *Interplanetary Scintillation with the MWA*

We performed a cross-match of the master population with the catalogue of sources displaying IPS from Chhetri et al. (2018) and found 1,873 sources in our field, only 40 of which had a VIP≥ 58.3. Of the variable sources presented in the IPS catalogue, only four are reported as non-scintillating while 28 are reported as highly scintillating with a normalised scintillation index above 0.9. We note, Chhetri et al. (2018) report 12 per cent of their total population were strongly scintillating due to IPS while 90 per cent of the variable sources in the field are at least moderately scintillating.

Chhetri et al. (2018) identify 37 compact sources according to IPS and search for variability at 150 MHz within this sample. The one source identified as variable, GLEAM J013243–165444, is also in our master population. We also classify GLEAM J013243–165444 as a variable source with significant change in spectral shape with a VIP of $\sim$ 122 and a MOSS parameter of $\sim$ 85. Despite its blazar identification and variability in both surveys, GLEAM J013243–165444 maintains a peaked spectrum in both years of GLEAM observations with a peak at $\sim$150 MHz. There are several sources within the changing spectral shape population that temporarily display a peaked-spectrum classification. Such temporary

spectral peaks have also been identified by Torniainen et al. (2005). It is thus possible that the PSS classification of GLEAM J013243–165444 is also temporary. The SED for GLEAM J013243–165444 is presented in Figure B1 in Appendix B.

### 4.4    GMRT Search for Transients

The VIP is calculated using only two epochs but takes advantage of the 16 individual flux density measurements. Hajela et al. (2019) present a statistical method which compares two epochs on over four different timescales (4 hours, 1 day, 1 month and 4 years) but only uses one flux density measurement for each epoch. We apply the methodology presented by Hajela et al. (2019) to our master population to probe variability over one year at a single frequency, and compare this to the VIP. Such a comparison helps us put our methodology of identifying variability in the context of the literature.

We calculate their variability statistic, $V_s$, at 150 MHz:

$$V_s = \frac{(S_1 - S_2)}{\sqrt{\sigma_1^2 + \sigma_2^2}}, \tag{5}$$

and the modulation index, $m$:

$$m = 2 \times \frac{S_1 - S_2}{S_1 + S_2}, \tag{6}$$

where $S_1$ and $S_2$ are the flux densities in the first and second epoch, respectively. $\sigma_1$ and $\sigma_2$ are the uncertainties on the measurements. Hajela et al. (2019) state a source is *truly variable* if the $V_s$ is more than four times the standard deviation of $V_s$ and $|m| > 0.26$. Using this classification of variability on our MWA master sample at the 150 MHz, we find 13 sources which would be what Hajela et al. (2019) define as *truly variable*. Of these 13 sources, 12 are selected by the VIP as showing significant variability as shown in Figure 7, all of which have a VIP≥85. Additionally, of these 13 sources, only two are classified as having a change in shape, and 11 are classified as having a uniform change across the band. The VIP takes full advantage of the multiple flux density measurements and is thus more robust to single frequency random fluctuations. The $V_s$ and $m$ presented by
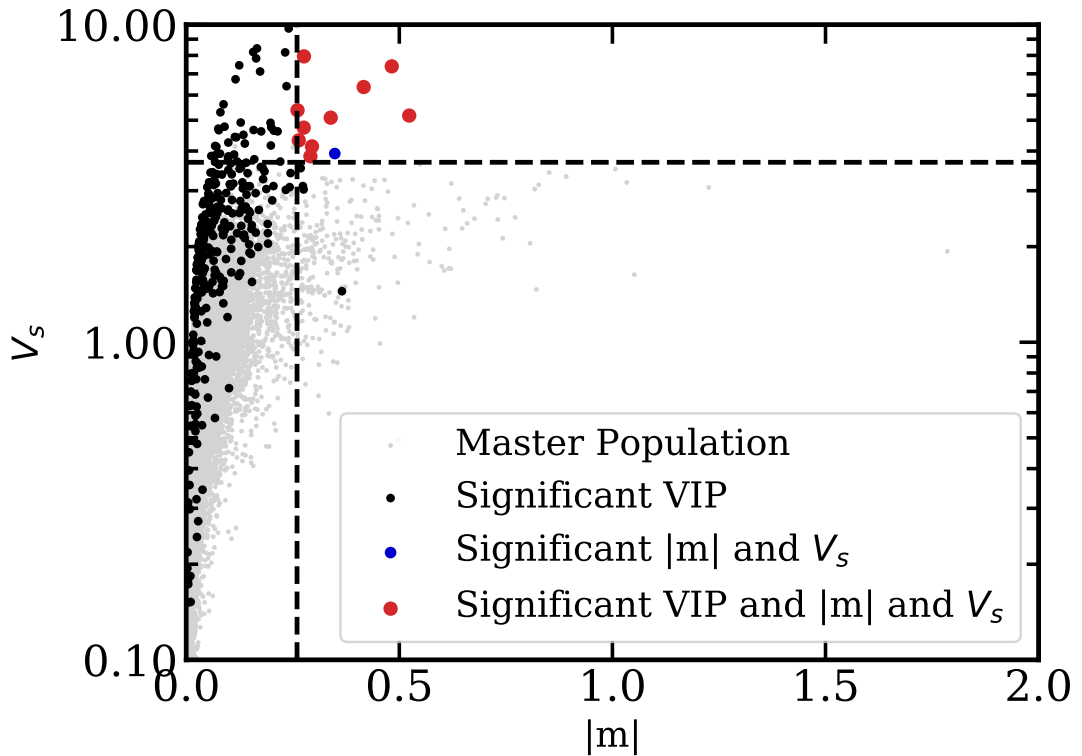
**Figure 7.** The distribution of the variability statistics defined by Hajela et al. (2019) for our master sample; the y-axis shows $V_s$ (Equation 5), as a function of the modulus of the modulation index, $m$ at 150 MHz (Equation 6). The different populations are listed in the legend. Many sources that are variable according to the VIP are missed by the $V_s$ and $m$. Using single-frequency variability statistics seems to cause low completeness.

Hajela et al. (2019) has a high reliability, but a low completeness, missing a large fraction of variable sources at low frequencies, shown by black dots in Figure 7.

Separately, we cross-match our variable population with that presented by Hajela et al. (2019) and find only one common source. GLEAM J012528–000557 (referred to as J012528+000505 in Hajela et al. 2019), is found to be variable in this work and by Hajela et al. (2019). This source is a known blazar (Section 4.2) and thus variability at these frequencies on timescales of years is not unexpected.

## 5 DISCUSSION

As we have classified the observed variability according to the *type* of variability observed, and compared it to other low-frequency variability studies, we now

discuss the potential physical mechanisms that could drive each variability classification.

## 5.1 Extrinsic Variability

Scintillation can cause radio sources to vary in brightness over several different timescales depending on the scattering regime. The mosaics used in this study are composed of multiple 2 minute snapshots, and IPS and ionosphere scintillation timescales are short enough that the variations will be smoothed over in the mosaics. Likewise the high Galactic latitude of our survey area places the transition frequency from weak scattering to the strong scattering at $\gtrsim 1\,\mathrm{GHz}$. Therefore, variability identified in our survey is probing the strong scattering regime (Walker 1998).

Refractive interstellar scintillation (RISS) in the strong regime can cause variability at megahertz frequencies on year-long timescales. In comparison, diffractive interstellar scintillation (DISS) occurs on shorter timescales (seconds to minutes) and with a larger amplitude of modulation (Narayan 1992). Furthermore, DISS requires much smaller limits on source size than RISS, so more strongly influences light from extremely compact sources such as pulsars and fast radio bursts, and is a narrow band effect (with the fractional decorrelation bandwidth $\ll 1$ Narayan 1992). We thus attribute the observed variability of the known pulsar GLEAM J043715–471506 (PSR J0437-47) to DISS, further supported by the irregularity of the SED suggesting significant frequency dependence on the modulation within the MWA bandwidth. We focus on RISS in the following sections when considering scintillation as the cause for the observed variability.

Extended sources can still scintillate if they have point-like components embedded within the extended structure, such as hotspots in the lobe of a radio galaxy. However, for sources with an angular size far larger than the scintillation angle, and with no such compact features, the combined modulation of the smaller regions averages to a negligible total modulation. Thus, if we assume the source is

point-like and find the spectral variability consistent with scintillation, it is also consistent with a point-like structure embedded within an extended source. However, for an extended structure, the point-like region is a fraction $f$ of the total flux density. The point-like region will still scintillate while the extended structure will not. Consequently, for extended sources, we measure the modulation index reduced by a factor $1 - f$, (Hancock et al. 2019). Hence, the compact region needs to dominate the emission from the lobes of a radio galaxy for scintillation to produce the observed variability. Furthermore, if the scintillating component is larger than the Fresnel angle, the scintillation timescale increases (Narayan 1992).

We also consider the possibility that extreme scattering events (ESEs) could cause some of the observed variability (e.g. Bannister et al. 2016). While the features of some of the observed variability are consistent with an ESE, current confirmed detections of ESEs suggest they are rare events. Lazio et al. (2001) only report finding 15 events in a survey of almost 150 sources monitored roughly once every two days for up to 15 years). We thus discount ESEs as a likely explanation for the variability observed, but suggest a third epoch of observations on our sample is required to test the validity of this assertion.

We outline below the feasibility of RISS as the mechanism behind the observed variability for each class of variable source we observe. We note, however, that we have made several necessary assumptions regarding scintillation that may not be valid for all of the sources. For example, it is possible the transition frequency for weak scattering by refractive scintillation may be much lower than expected. Consequently, this survey may be probing a transition space where many assumptions are no longer viable. However, given this study is at low (megahertz) frequencies and probing timescales of around a year, it is reasonable to assume we are well within the strong scattering regime since the transition frequency is $\gtrsim 1\,\mathrm{GHz}$.

### 5.1.1 *Non-PSS Uniform Change Population*

While scintillation strength is dependent on wavelength, RISS is a broadband effect at megahertz frequencies (with the fractional decorrelation bandwidth $\sim 1$; Narayan 1992). Thus, we expect any variability due to RISS to be approximately uniform across the $\sim$100–230 MHz bandwidth of this study (Narayan 1992; Hancock et al. 2019).

Variable sources that are classified as having a uniform spectral change may have bright embedded compact features that can scintillate within their extended radio lobes, including but not limited to knots, jets, and hot spots. For such sources where the compact scintillating feature is embedded, the timescales are longer and the amount of modulation decreases as the observed scintillation is a combined average of individual regions scintillating. Sources with spectra which change uniformly can be interpreted as being compact (or their brightness being dominated by compact components) and undergoing RISS. Using estimates of the RISS of compact sources based on distribution of H$\alpha$ within the Galaxy (Hancock et al. 2019) we confirm the observed variability of sources showing a uniform change can be explained by scintillation. Scintillation on year long timescales at megahertz frequencies requires a compact component or hot spot of size $\lesssim$5 milliarcseconds, assuming a (Galactic) scattering screen at $D = 1$ kpc and Kolmogorov turbulence (Narayan 1992; Walker 1998). The preponderance of our detected variable sources having a AT20G counterpart implies that many of our sources likely have small, compact features in their morphology.

To provide confirmation of the possibility of RISS as the cause of the observed variability, we propose a long-term monitoring of these sources at centimetre wavelengths (where interstellar scintillation is negligible for sources with an angular size greater than tens of microarcseconds). Likewise, a comparison of the distributions of variable sources with a uniform spectral change with the H$\alpha$ line-of-sight intensities (for example, the Wisconsin H-Alpha Mapper, WHAM,

survey ([Tufte et al. 1998](#))) to search for a correlation could confirm the Hα as the likely scintillating screen. VLBI observations to obtain high resolution morphologies of these sources could search for a compact features small enough to scintillate. VLBI is performed at ∼gigahertz frequencies where different features may contribute more to the integrated flux density than at megahertz frequencies. Assumptions of how the morphology changes with respect to frequency would be necessary in order to estimate the morphology at megahertz frequencies. Alternatively, IPS at megahertz frequencies could be a way to confirm the presence of a compact component without the need for VLBI.

The morphology of the sources at different frequencies also significantly impacts the modulation due to scintillation. Megahertz frequencies are more dominated by older, likely large structures, such as radio lobes. These structures have a much larger angular size than the core or jets of an AGN. A knot or hot-spot in the lobe may not contribute as much to the overall flux density at megahertz frequencies as it does at gigahertz frequencies. Thus at low frequencies only a fraction of the flux density may be compact enough to scintillate while at higher frequencies a larger proportion (if not all) may scintillate. Long-term, multi-epoch monitoring of the entire SED paired with high resolution maps of the morphology (ideally at several frequencies) would be needed to confirm RISS as the mechanism behind the observed variability in this study. We have begun such a monitoring campaign combining roughly simultaneous observations (within a week) with the MWA and the ATCA with multiple epochs over a year long timescale[4].

### 5.1.2 Persistent PSS Uniform Change Population

As PSS are a subset of AGN, all possible explanations of variability for the non-PSS uniform change population, outlined in Section [5.1.1](#), are applicable to the persistent PSS uniform change population. However, we note that hot spots do

---

[4] ATCA project code, C3333 and MWA project codes are D0025 and G0067

not appear to be a dominant feature of PSS at gigahertz-frequencies (Keim et al. 2019). Sources larger than the source size limit of $\sim$5 mas[5] can scintillate but have a reduced modulation index, and increased timescale of variability. If all the observed variability for the persistent PSS uniform change population is due to scintillation, at least 6% of PSS may be dominated by core-jet structures, or have a compact component in their morphology. If confirmed, the variability due to scintillation can help provide milliarcsecond resolution of structures of persistent PSS at redshifts $\gtrsim 0.5$ without the requirement of high resolution imaging using VLBI.

In order to confirm scintillation as the mechanism behind the detected variability of persistent PSS, similar follow-up campaigns for the non-PSS uniform change sources are recommended. SED coverage would need to be simultaneous (within a few days) to ensure accurate estimation of the spectral peak and spectral indices.

### 5.1.3 Changing Spectral Shape Population

As mentioned previously, both a point-like source and an extended source with an embedded compact feature can scintillate. In this section, we calculate the feasibility of RISS as the driving mechanism behind the observed variability for sources with a changing spectral shape.

According to Walker (1998) the modulation scales with $\left(\frac{\nu}{\nu_0}\right)^{\frac{17}{30}}$, where $\nu$ is the observed frequency and the transition frequency is denoted by $\nu_0$. We note $\nu_0 \gtrsim 1$ GHz, thus placing this survey well into the strong regime and RISS is a broadband effect at the frequencies probed by our survey (Narayan 1992; Walker 1998). At megahertz frequencies and high galactic latitudes, the expected modulation is fairly constant across the 100-230 MHz band. Furthermore, if the source is scintillating, while scintillation strength does scale with frequency, the differ-

---

[5] at $z = 0.5$, 5 mas is equivalent to 30 pc and at $z \approx 1$, 5 mas is equivalent to 40 pc

ence in the observed effect across 130 MHz bandwidth is negligible according to the decoherence bandwidth for RISS ($\delta\nu_{\mathrm{dc}} \approx 1$). Therefore, scintillation cannot be the sole explanation for those sources that show significant changes in their spectral shape.

## 5.2   Intrinsic Variability

The observed variability is consistent with several mechanisms of intrinsic evolutions or changes. Causes of intrinsic variability include evolution of knots in core/jet structures and changes in the immediate environment surrounding radio lobes. The megahertz frequencies of this study are probing the large scale structure and are dominated by the lobes of AGN. Hardcastle & Looney (2008) report the cores of typical AGN being four orders of magnitude fainter than the lobes at low frequencies, although it is unknown whether this holds true for compact AGN. We find it unlikely the lobes for any AGN are $\leq 1$ ly ($\sim 0.3$ pc) across, which would be necessary for light travel time to explain variability on year-long timescales. We largely focus on more plausible solutions relating to interactions within the jet/lobes and nearby surrounding absorbing media:

(i) Internal shocks, where shells of plasma within lobes interact and can cause a re-energisation of the electrons;

(ii) Knots in the jet that are being ejected from the central core and travelling to the lobes;

(iii) Changes in optical depth due to a fast-moving clumpy cloud of surrounding media;

(iv) Core or jet structures being oriented towards the observer, i.e. the possibility of all sources being blazars

As with extrinsic variability discussed in Section 5.1, we will outline the feasibility of intrinsic variability per variable class: non-PSS uniform change sources, persistent PSS, and variable spectral shape sources.

### 5.2.1 *Non-PSS Uniform Change Population*

As AGN with no detectable peak in their spectra are often significantly larger than PSS, there are some intrinsic mechanisms we can eliminate as explanations for the observed variability. For example, we can rule out variability due to the evolution of a knot travelling from the core to the lobes on a year long timescale as this is unfeasible on these timescales.

However, if the core or jet were to vary (due to changes in accretion rate, for example) we could expect to see significant changes on much shorter timescales. At low frequencies we would normally expect the lobe emission to dominate, so such variation would require either:

(i) The feature varying is not travelling across the entire source: this would reduce travel time to the lobes;

(ii) The component of the total flux density determined by the core is greater than expected: this could result in short timescale variability from the core itself, which may be detected at low frequencies.

In the first scenario, the timescale of variability can be reduced by introducing interaction of the plasma within the jets/lobes. This interaction creates shells of energised plasma which merge and increase the lobe brightness on much shorter timescales than energy travelling from the core (Jamil et al. 2010)

Similarly in the second scenario, if the flux density is dominated by the core, we could detect the variability we observe via standard core or jet fuelling. This would suggest that for a small fraction of radio galaxies (and in particular PSS), current estimates of the relative brightness of the core to the lobes, ranging from $10^{-1}$–$10^{-4}$ (Hardcastle & Looney 2008), is massively underestimated at low frequencies.

Furthermore, it is worth noting that 38 of the non-PSS uniform change sources are known blazars (of a total 175 non-PSS uniform change sources in the field). It is thus not unreasonable to see variability on short timescales from the core or jet which is oriented towards the observer providing an additional beaming effect

(Madau et al. 1987). Any slight change of the source may be Doppler Boosted and variability on year long timescales due to the flaring or changing state of a blazar could explain the observed spectral variability of these sources. However, blazars are generally compact enough to scintillate, thus disentangling whether the observed variability is due to the intrinsic variable nature of the blazar or from scintillation in the interstellar medium is challenging. Comprehensive monitoring with high time resolution of both low frequency (radio) with high frequency (X-ray and/or Gamma) follow up is required, or VLBI observations tracing the evolution of the jet.

### 5.2.2   Persistent PSS Uniform Change Population

Given PSS are a sub-population of typical AGN, all mechanisms explained in Section 5.2.1 are also plausible for the PSS population. But there are potentially unique intrinsic mechanisms due to the typically more compact morphologies of PSS and their interactions with the warm ISM (Bicknell et al. 2018a).

Firstly, a subset of PSSs may have a core-jet prominence more typically associated with AGN that have a flat spectrum, even at megahertz frequencies. As such, this core variability may arise from changes in accretion rate or flaring state. If we assume an impulsive change at the core to be the cause of the variability, we would expect a uniform decrease across the entire SED of the source if the material is adiabatically expanding. In this case, the cause of the overall persistent peak in the SED remains the same. As outlined in Section 5.2.1, current estimates of the core prominence place core flux density at $10^{-1}$–$10^{-4}$ times fainter than the lobes at low frequencies ($\sim$150 MHz) for typical AGN. However, measurements of the core dominance for PSS have yet to be reliably measured at megahertz-frequencies. Furthermore, for the PSS that have a compact double morphology, the core is hardly ever even detected (Orienti 2016). Thus, the identified variable PSS in this study may have an inherently different core prominence. If a multi-epoch follow up with simultaneous observations of the broad band SED

($\sim 70\,\mathrm{MHz}$–$\geq 10\,\mathrm{GHz}$) showed a flare typical of a changing state in the core and/or jet, we could surmise a larger component of the flux density measured at megahertz frequencies is due to the core. Intrinsic variability due to the core may signify persistent PSS have a vastly different core prominence than their non-peaked counterparts. Only LOFAR will have the resolution in the coming decades to potentially resolve some of these sources at megahertz-frequencies.

Secondly, similar temporary peaks in radio spectra have been observed in X-ray binary systems where ejecta from the jet has been observed (Fender et al. 2009; Tetarenko et al. 2019). Radio monitoring for Cygnus X-1 detected a lag of the radio flare from higher radio frequency to lower radio frequency (11 GHz down to 2 GHz Tetarenko et al. 2019). Furthermore, Tetarenko et al. (2019) report a decreased amplitude of modulation and increased width of the timescale of the flare at lower frequencies ($\sim 2$–$3\,\mathrm{GHz}$). Tetarenko et al. (2019) suggest this delay is due to the different frequencies probing further along the jet away from the core, with higher frequency observations probing younger, faster-evolving material. While black hole X-ray binary systems are orders of magnitude more compact than AGN, varying on the timescales of weeks, a similar mechanism could explain the observed variability of the persistent PSS but on year long timescales, given the typically compact ($\leq 20\,\mathrm{kpc}$) morphology of PSS. Observing the light curves at multiple radio frequencies over year long timescales for the persistent PSS may show a delay in the flare from higher frequencies to lower as the ejection from the jet travels further from the core. Furthermore, given it is not unreasonable to expect ejecta from the jets being detected on these timescales for PSS, it is also justifiable to explain the observed variability with interacting shells (Jamil et al. 2010), which theoretically occur on shorter timescales.

Thirdly, one potential cause of the variability below the spectral turnover could be due to changes in the free-free optical depth along the line of sight (e.g. Tingay et al. 2015). The free-free absorption (FFA) model has been considered as the cause of absorption in the optically thick region for at least some PSS

(Peck et al. 1999; Kameno et al. 2000; Tremblay et al. 2008; Marr et al. 2014; Callingham et al. 2015; Tingay et al. 2015). Attributing the variability to changes in optical depth would be evidence to support the FFA model for these sources. Recent simulations have also proposed GPS and CSS are the result of relativistic jet feedback and interactions with the surrounding warm ISM (Bicknell et al. 2018b). Several observations of absorption features linked with dust surrounding AGN have also found a strong connection with PSS (Grasha et al. 2019; Glowacki et al. 2019; Jarvis et al. 2019). However, as several studies have noted (O'Dea 1998; Callingham et al. 2017; Bicknell et al. 2018a), distinguishing between synchrotron self absorption (SSA) and FFA for the PSS population as a whole has thus far yielded inconclusive results as both SSA and FFA spectral models are consistent with current observations for most PSSs. Testing for prominent HI gas via upcoming surveys such as the ASKAP First Large Absorption Survey in HI (FLASH; Allison et al. 2022), would help identify galaxies that likely have a lot of intervening media between us and the radio lobes (Callingham et al. 2015).

We note it is entirely possible that the majority of the persistent PSS population may be entirely composed of flaring blazars that are observed at both epochs with a peaked spectrum. While only 25 per cent of the persistent PSS population were known blazars, as selected based on X-ray, optical and gigahertz-frequency characteristics, it is possible other members of the persistent PSS population happen to have a jet orientation relative to our line-of-sight that ensures it is not X-ray- or optically-bright relative to its radio luminosity. Blazars are also known to display a peaked spectrum over a prolonged period, even at gigahertz-frequencies (Chhetri et al. 2018). For example, we find known blazar GLEAM J013243–165444 to be classified as a PSS in both years of observation. We thus suggest long-term observations of the light curves of the persistent PSS population at either gigahertz frequencies or, if the sources are bright enough, follow up with $\gamma$- or X–ray telescopes, like the extended ROentgen Survey with an Imaging Telescope Array (eROSITA; Predehl et al. 2016). Furthermore, follow up with multi-frequency

VLBI would be critical to determine if these sources are core-jet or double-lobed objects.

### 5.2.3    *Changing Spectral Shape Population*

For intrinsic variability of a source emitting synchrotron radiation, the brightness temperature $(T_b)$ has an upper limit of $10^{12}$ K, as determined by the inverse-Compton losses. We reproduce the calculation used by Bell et al. (2019) to estimate if changes in the flux density are within expectations for intrinsic variability using the following equation:

$$\Delta S \leq \frac{2k_B\nu^2\tau^2 T_b b^3}{D^2}, \tag{7}$$

where $\Delta S$ is the change in flux density, $\tau$ is the timescale (here 1 yr), $T_b$ is the brightness temperature (set as the upper limit, $10^{12}$ K), $b^3$ is a beaming factor for emission directed towards the observer (we assumed an upper limit of 10, a typical value for blazars (Lahteenmaki & Valtaoja 1999)), and $D$ is the distance to the source (set as 10 Gpc, equivalent to roughly $z = 1$). Using Equation 7 we find that sources can not exceed 0.68 Jy for $\Delta S$ at 150 MHz when no beaming factor is used. By introducing the beaming factor for incoherent emission, all the observed variability for these sources can be explained via intrinsic mechanisms. We thus suggest that sources where we observe a variable spectral shape between epochs as beamed AGN. 24 of the 51 (47 per cent) changing spectral shape sources have AT20G counterparts (Murphy et al. 2010), suggesting core-dominance. Additionally, 18 sources (35 per cent) are known blazars already from BZCAT (Massaro et al. 2015).

However, it is worth noting that if these sources are indeed heavily beamed, their morphology will likely be compact enough that they may also scintillate. Furthermore, Koay et al. (2018) find a correlation between sources showing intrinsic variability and scintillation, suggesting any sources that are compact enough to scintillate also tend to be more variable intrinsically. Therefore, it is possible

the observed variability is a combination of both intrinsic blazar flares and scintillation. Finally, we note that we assumed a timescale of one year due to the rough timescale of this work in searching for variability but it is likely these sources have variability that will occur on longer timescale than observed. Increasing the timescale of variability increases the $\Delta S$ limit, according to Equation 7, for these sources to be intrinsically variable. Thus, further long-term monitoring over several years with wide spectral coverage is necessary to estimate the true timescale more accurately as well as determine the role of scintillation.

If confirmed, spectral shape variability at low frequencies ($< 1\,\mathrm{GHz}$) has the ability to detect and classify blazars on relatively short timescales, even if they are too faint to observe at higher frequencies.

## 5.3  Summary of plausible causes of the observed variability

Considering causes for intrinsic or extrinsic variability, we determined the most likely causes for the observed spectral variability for the different classes of sources. For non-PSS and PSS sources that show a uniform change in their SED between epochs, scintillation can easily explain the observed low-frequency variability. If confirmed, observing the variability due to scintillation could be paired with observations of pulsars to increase the resolution of maps of the electron column density to test models that aim to predict scintillation, such as RISS19[6]. In contrast, the sources in which we observe a changing spectral shape between epochs are more likely explained as a blazar with changing flaring states. While scintillation may be a component of the observed variability it is unlikely the sole mechanism to explain the spectral shape variability due to the wide bandwidth of RISS. We therefore present the changing spectral shape variable population as blazar candidates requiring a follow-up campaign for confirmation, for example a search for X-ray counterparts with *eROSITA* (Predehl et al. 2016).

---

[6]  RISS19 can be downloaded here: `https://github.com/PaulHancock/RISS19`

## 6   CONCLUSIONS AND OUTLOOK

We have conducted a study of low-frequency spectral variability and devised a methodology for detecting, measuring, and classifying spectral variability using the variability index parameter (VIP) and the measure of spectral shape (MOSS) parameter. This study uses two epochs of the GLEAM survey, producing a data set that contains over 21,000 sources. Therefore, our study represents the largest survey of low-frequency spectral variability, particularly of spectra formed from contemporaneous flux density measurements over a large fractional bandwidth.

We present 323 sources that show significant spectral variability according to the VIP, 51 of which display a significant change in shape of their spectra according to the MOSS parameter. We find that the variable sources are more likely to have a peaked spectrum, consistent with results from the MWATS and IPS surveys with the MWA. We compare the variable population with the *WISE* infrared survey to determine the classification of galaxy and find no variable sources to be classified as star forming. Furthermore, we conclude many of the variable sources are consistent with quasar and blazar classifications. We also compare the variable population with BZCAT to find known blazars. There is a larger proportion of variable sources that are known blazars (22 per cent) compared to the master population ($\sim$1 per cent), with many of the remaining variable population possessing characteristics similar to the identified blazars. Likewise, we find a larger proportion of variable sources with AT20G counterparts (11 per cent) when compared to the master population (1 per cent). One source in particular, GLEAM J 032237–482010, shows a significant change in spectral shape, suggesting it is a core-dominated source or a blazar, yet has no AT20G counterpart.

We discuss several sources that have particular interesting features. For reported restarted radio galaxy candidates, we find that six are variable and conclude they are misclassified quasars with a flat spectra. We compare our variable sources with several notable single frequency variability surveys conducted around

150 MHz and only find two sources which are classified as variable in each, both of which are known blazars: GLEAM J012528–000557 and GLEAM J013243-165444. We also find one known pulsar, PSR J0437–47, to show significant variability and conclude this is likely due to diffractive interstellar scintillation.

We argue that the observed variability of the persistent PSS and uniform change sources are entirely consistent with refractive interstellar scintillation. The sources which show a changing spectral shape according to the MOSS parameter cannot be explained by ISS and we thus present this population as blazar candidates requiring further confirmation.

While we suggest likely causes for each category of spectral variability, it is worth noting this is based on only two epochs of observation. Long term monitoring and specific follow up campaigns are recommended to test the presented hypotheses. Furthermore, in all cases having more epochs of observation with greater spectral coverage from megahertz to gigahertz frequencies would increase the reliability of detected variability. Thus a lower level of significance cut off for the VIP could be used to detect variability. More epochs of observation on a range of timescales could allow for the timescale of variability to be accurately estimated, this can refine viable variability mechanisms.

## 6.1 SKA Era Implications

In the SKA era, as we gain the capability to perform large scale variability surveys with large spectral and temporal coverage, understanding how prevalent variability is at low frequencies is crucial. This paper outlines a methodology to begin dissecting this variability by detecting and classifying the low-frequency spectral variability with rigorous and reproducible statistical methods. MWATS place an upper limit prediction on the expected number of variable source at low frequencies ($\sim$150 MHz) of 6,000 sources for a given sample of 350,000 sources. Following this trend, we would expect fewer than 400 variable sources in this study. Our results are consistent with this expectation numerically, however, the nature of

spectral variability detected suggests our current understanding of low-frequency variability is not yet complete. These results highlight the insufficient understanding of the emission mechanisms at low frequencies, and AGN evolutionary scenarios. As many PSS are used for calibrators of high-frequency (gigahertz) radio telescopes, understanding the short-timescale ($\sim$years) evolution and variability of their SEDs is critical. Despite this variability being observed at low frequencies, it is important to see how this variability relates to the gigahertz regime. Furthermore, SKA_LOW will be able to detect fainter PSS. An understanding of the current known PSS population is critical if we are to investigate the fainter population. We encourage careful monitoring of the presented sources in this paper in order to understand how they may change within the span of future surveys and studies.

## 7  DATA AVAILABILITY

The data underlying this article are available in the article and in its online supplementary material

## REFERENCES

Allison J. R., et al., 2022, Publ. Astron. Soc. Australia, 39, e010

Assef R. J., et al., 2013, ApJ, 772, 26

Astropy Collaboration et al., 2013, A&A, 558, A33

Bannister K. W., Stevens J., Tuntsov A. V., Walker M. A., Johnston S., Reynolds C., Bignall H., 2016, Science, 351, 354

Bell M. E., et al., 2019, MNRAS, 482, 2484

Bicknell G. V., Mukherjee D., Wagner A. Y., Sutherland R. S., Nesvadba N. P. H., 2018a, Monthly Notices of the Royal Astronomical Society, 475, 3493

---

[7] http://ds9.si.edu/site/Home.html

Bicknell G. V., Mukherjee D., Wagner A. Y., Sutherland R. S., Nesvadba N. P. H., 2018b, Monthly Notices of the Royal Astronomical Society, 475, 3493

Bower G. C., Whysong D., Blair S., Croft S., Keating G., Law C., Williams P. K. G., Wright M. C. H., 2011, The Astrophysical Journal, 739, 76

Callingham J. R., et al., 2015, ApJ, 809, 168

Callingham J. R., et al., 2017, The Astrophysical Journal, 836, 174

Chhetri R., Morgan J., Ekers R. D., Macquart J. P., Sadler E. M., Giroletti M., Callingham J. R., Tingay S. J., 2018, MNRAS, 474, 4937

Clarke M., 1964, PhD thesis, Cambridge University

Coles W. A., Frehlich R. G., Rickett B. J., Codona J. L., 1987, ApJ, 315, 666

Condon J. J., Cotton W. D., Greisen E. W., Yin Q. F., Perley R. A., Taylor G. B., Broderick J. J., 1998, AJ, 115, 1693

Coppejans R., Cseh D., Williams W. L., van Velzen S., Falcke H., 2015, MNRAS, 450, 1477

Coppejans R., et al., 2016, MNRAS, 459, 2455

Fan, J. H. et al., 2007, A&A, 462, 547

Fanti R., Fanti C., Schilizzi R. T., Spencer R. E., Nan Rendong Parma P., van Breugel W. J. M., Venturi T., 1990, A&A, 231, 333

Fender R. P., Homan J., Belloni T. M., 2009, MNRAS, 396, 1370

Franzen T. e., 2020, Publ. Astron. Soc. Australia, Submitted

Glowacki M., et al., 2019, Monthly Notices of the Royal Astronomical Society, 489, 4926

Grasha K., Darling J., Bolatto A., Leroy A. K., Stocke J. T., 2019, The Astrophysical Journal Supplement Series, 245, 3

Hajela A., Mooley K. P., Intema H. T., Frail D. A., 2019, Monthly Notices of the Royal Astronomical Society, 490, 4898

Hancock P. J., Murphy T., Gaensler B. M., Hopkins A., Curran J. R., 2012, MNRAS, 422, 1812

Hancock P. J., Trott C. M., Hurley-Walker N., 2018, Publ. Astron. Soc. Australia, 35, e011

Hancock P., Charlton E., Maquart J., Hurley-Walker N., 2019, arXiv preprint arXiv:1907.08395

Hardcastle M. J., Looney L. W., 2008, Monthly Notices of the Royal Astronomical Society, 388, 176

Hewish A., Burnell S. J., 1970, Monthly Notices of the Royal Astronomical Society, 150, 141

Hinshaw G., et al., 2013, ApJS, 208, 19

Hunstead R. W., 1972, Astrophys. Lett., 12, 193

Hunter J. D., 2007, Computing in Science & Engineering, 9, 90

Hurley-Walker N., Seymour N., Staveley-Smith L., Johnston-Hollitt M., Kapinska A., McKinley B., 2017a, GaLactic and Extragalactic All-Sky MWA-eXtended (GLEAM-X) survey: Pilot observations, MWA Proposal id.2017A-1

Hurley-Walker N., et al., 2017b, MNRAS, 464, 1146

Intema, H. T. Jagannathan, P. Mooley, K. P. Frail, D. A. 2017, A&A, 598, A78

Jamil O., Fender R. P., Kaiser C. R., 2010, Monthly Notices of the Royal Astronomical Society, 401, 394–404

Jarvis M. E., et al., 2019, Monthly Notices of the Royal Astronomical Society, 485, 2710

Jones D. H., et al., 2009, MNRAS, 399, 683

Kameno S., Horiuchi S., Shen Z.-Q., Inoue M., Kobayashi H., Hirabayashi H., Murata Y., 2000, Publications of the Astronomical Society of Japan, 52, 209

Keim M. A., Callingham J. R., Röttgering H. J. A., 2019, A&A, 628, A56

Kellermann K. I., Pauliny-Toth I. I. K., 1969, ApJ, 155, L71

Koay J. Y., et al., 2018, MNRAS, 474, 4396

Kunert-Bajraszewska M., Gawroński M. P., Labiano A., Siemiginowska A., 2010, MNRAS, 408, 2261

Lacy M., et al., 2004, The Astrophysical Journal Supplement Series, 154, 166

Lahteenmaki A., Valtaoja E., 1999, The Astrophysical Journal, 521, 493

Lane W. M., Cotton W. D., van Velzen S., Clarke T. E., Kassim N. E., Helmboldt J. F., Lazio T. J. W., Cohen A. S., 2014, MNRAS, 440, 327

Large M. I., Mills B. Y., Little A. G., Crawford D. F., Sutton J. M., 1981, MNRAS, 194, 693

Large M. I., Cram L. E., Burgess A. M., 1991, The Observatory, 111, 72

Lazio T. J. W., Waltman E. B., Ghigo F. D., Fiedler R. L., Foster R. S., Johnston K. J., 2001, The Astrophysical Journal Supplement Series, 136, 265

Macquart J. P., de Bruyn A. G., 2007, MNRAS, 380, L20

Madau P., Ghisellini G., Persic M., 1987, Monthly Notices of the Royal Astronomical Society, 224, 257

Marr J. M., Perry T. M., Read J., Taylor G. B., Morris A. O., 2014, ApJ, 780, 178

Massaro E., Maselli A., Leto C., Marchegiani P., Perri M., Giommi P., Piranomonte S., 2015, Astrophysics and Space Science, 357, 75

Mauch T., Murphy T., Buttery H. J., Curran J., Hunstead R. W., Piestrzynski B., Robertson J. G., Sadler E. M., 2003, MNRAS, 342, 1117

Miller-Jones J. C. A., Gallo E., Rupen M. P., Mioduszewski A. J., Brisken W., Fender R. P., Jonker P. G., Maccarone T. J., 2008, Monthly Notices of the Royal Astronomical Society, 388, 1751

Mills B. Y., 1981, Proceedings of the Astronomical Society of Australia, 4, 156

Murphy T., et al., 2010, MNRAS, 402, 2403

Murphy T., et al., 2016, Monthly Notices of the Royal Astronomical Society, 466, 1944

Narayan R., 1992, Philosophical Transactions of the Royal Society of London Series A, 341, 151

O'Dea C. P., 1998, PASP, 110, 493

O'Dea C. P., Saikia D. J., 2020, arXiv e-prints, p. arXiv:2009.02750

Onken C. A., et al., 2019, Publ. Astron. Soc. Australia, 36, e033

Orienti M., 2016, Astronomische Nachrichten, 337, 9

Peck A. B., Taylor G. B., Conway J. E., 1999, The Astrophysical Journal, 521, 103

Pérez F., Granger B. E., 2007, Computing in Science and Engineering, 9, 21

Phillips R. B., Mutel R. L., 1982, A&A, 106, 21

Predehl P., et al., 2016, in Space Telescopes and Instrumentation 2016: Ultraviolet to Gamma Ray. p. 99051K, doi:10.1117/12.2235092

Price-Whelan A. M., et al., 2018, AJ, 156, 123

Quirrenbach A., Witzel A., Krichbaum T., Hummel C. A., Alberdi A., 1989, Nature, 337, 442

Quirrenbach A., et al., 1992, A&A, 258, 279

Rickett B. J., 1986, ApJ, 307, 564

Riley J. M., 1993, Monthly Notices of the Royal Astronomical Society, 260, 893

Robertson J. G., 1991, Australian Journal of Physics, 44, 729

Stern D., et al., 2005, ApJ, 631, 163

Stewart A. J., et al., 2015, Monthly Notices of the Royal Astronomical Society, 456, 2321

Taylor M. B., 2005, TOPCAT &amp; STIL: Starlink Table/VOTable Processing Software. p. 29

Tetarenko A. J., Casella P., Miller-Jones J. C. A., Sivakoff G. R., Tetarenko B. E., Maccarone T. J., Gandhi P.,

Eikenberry S., 2019, Monthly Notices of the Royal Astronomical Society, 484, 2987

Tingay S. J., et al., 2013, Publications of the Astronomical Society of Australia, 30, e007

Tingay S. J., et al., 2015, The Astronomical Journal, 149, 74

Tinti S., Dallacasa D., de Zotti G., Celotti A., Stanghellini C., 2005, A&A, 432, 31

Torniainen I., Tornikoski M., Teräsranta H., Aller M. F., Aller H. D., 2005, A&A, 435, 839

Tremblay S. E., Taylor G. B., Helmboldt J. F., Fassnacht C. D., Pearson T. J., 2008, The Astrophysical Journal, 684, 153

Tufte S. L., Reynolds R. J., Haffner L. M., 1998, in Novak G., Landsberg R., eds, Astronomical Society of the Pacific Conference Series Vol. 141, Astrophysics From Antarctica. p. 169

Tzioumis A. K., et al., 2010, The Astronomical Journal, 140, 1506

Virtanen P., et al., 2019, Nature Methods, p. arXiv:1907.10121

Virtanen P., et al., 2020, Nature Methods, 17, 261

Walker M. A., 1998, MNRAS, 294, 307

Wayth R., et al., 2015, Publications of the Astronomical Society of Australia, 32

Wes McKinney 2010, in Stéfan van der Walt Jarrod Millman eds, Proceedings of the 9th Python in Science Conference. pp 56 – 61, doi:10.25080/Majora-92bf1922-00a

Wolf C., et al., 2018, Publ. Astron. Soc. Australia, 35, e010

Wright E. L., et al., 2010, AJ, 140, 1868

Wu X.-B., Hao G., Jia Z., Zhang Y., Peng N., 2012, AJ, 144, 49

pandas development team T., 2020, pandas-dev/pandas: Pandas, doi:10.5281/zenodo.3509134, https://doi.org/10.5281/zenodo.3509134

van Haarlem M. P., et al., 2013, A&A, 556, A2

van der Walt S., Colbert S. C., Varoquaux G., 2011, Computing in Science Engineering, 13, 22

# APPENDIX A: SUPPLEMENTARY ONLINE CATALOGUE DESCRIPTION

Column numbers, names, units and description for the supplementary online catalogue. This table contains the first 10 lines of the description table, the full table is available in the online materials. Source names follow International Astronomical Union naming conventions for co-ordinate-based naming. Background and RMS measurements were performed by BANE; the fitted spectral index parameters were derived as described in Section 3.3; other measurements were made using AEGEAN or measurements from additional surveys, as mentioned in Section 2.4. AEGEAN incorporates a constrained fitting algorithm. The columns with the subscript "wide" are derived from the 200–230 MHz wide-band image. Subsequently, the subscript indicates the central frequency of the measurement,

in MHz. These sub-band measurements are made using the priorised fitting mode of AEGEAN, where the position and shape of the source are determined from the year 2 wide-band image, and only the flux density is fitted.

| Number | Name | Unit | Description |
|--------|------|------|-------------|
| 1 | GLEAM Name | hh:mm:ss+dd:mm:ss | Name of the source in the GLEAM extragalactic catalogue |
| 2 | RA_hms | hh:mm:ss | Right ascension |
| 3 | Dec_dms | dd:mm:ss | Declination |
| 4 | RA | ° | Right ascension |
| 5 | err_ra | ° | Error on RA |
| 6 | Dec | ° | Declination |
| 7 | err_dec | ° | Error on Dec |
| 8 | int_flux_wide_yr1 | Jy | Integrated flux density in year 1 wideband image |
| 9 | err_int_flux_wide_yr1 | Jy | Error on integrated flux density in year 1 wideband image |
| 10 | local_rms_wide_yr1 | Jy beam$^{-1}$ | Local RMS in year 1 wideband image |

# APPENDIX B: SPECTRAL ENERGY DISTRIBUTIONS (SEDS)

SEDs for 15 sources classified as variable according to the VIP presented in order of Right Ascension. SEDs for all variable sources can be found in the online materials. Models were included to assist with visual interpretation. However, models plotted for each year are dictated by their PSS classification only. A source classified with a peak within the observed MWA band, which also satisfied the PSS criteria presented by Callingham et al. (2017), was modelled by a quadratic according to Equation 4. Remaining sources were modelled by a power-law according to Equation 3.

This paper has been typeset from a TeX/LaTeX file prepared by the author.
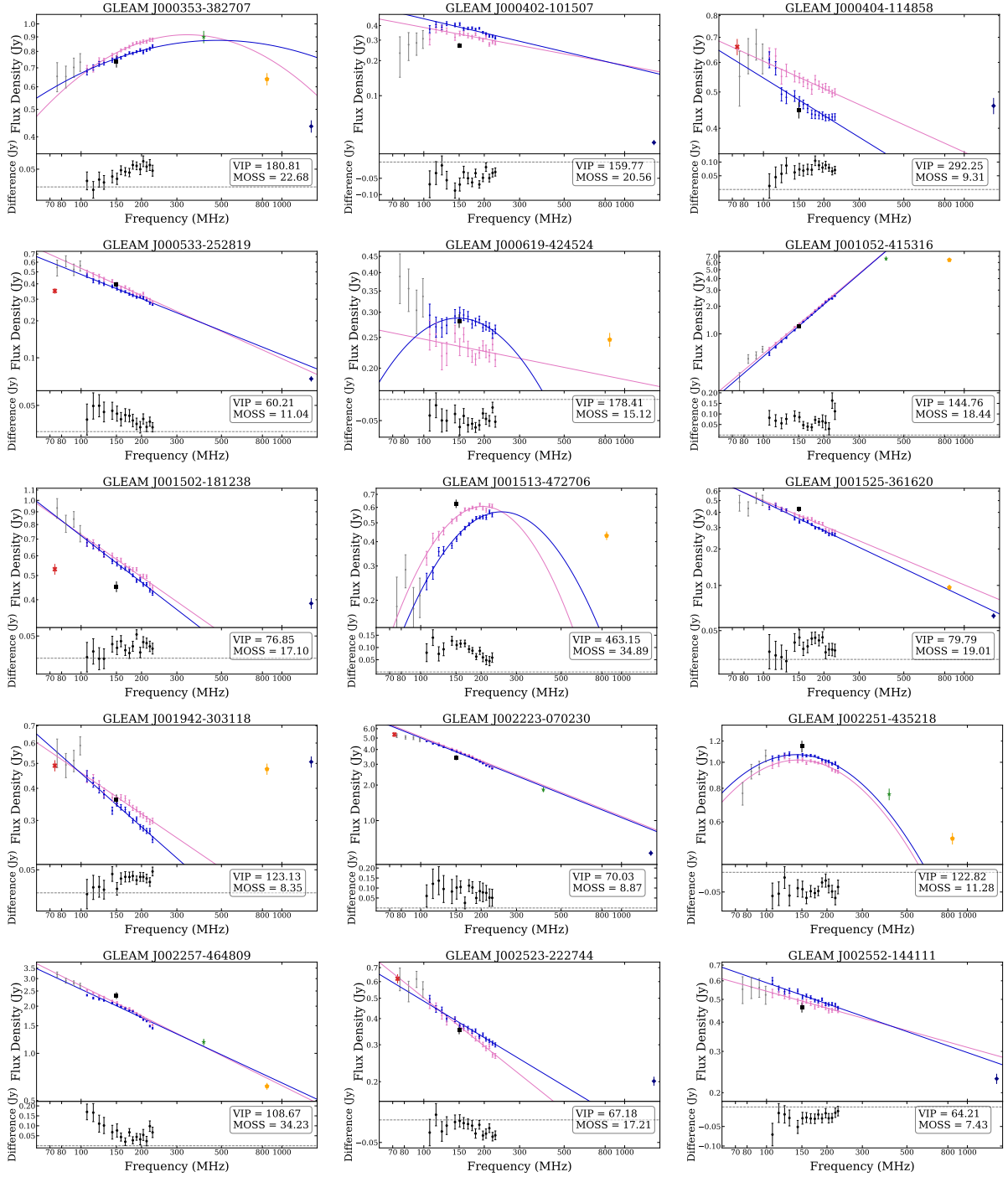
**Figure B1.** SEDs for all sources classified as variable according to the VIP. For each source the points represent the following data: GLEAM low frequency (72–100 MHz) (grey circles), Year 1 (pink circles), Year 2 (blue circles), VLSSr (red cross), TGSS (black square), MRC (green star), SUMSS (yellow pentagon), and NVSS (navy diamond). The models for each year are determined by their classification; a source classified with a peak within the observed band was modelled by a quadratic according to Equation 4, remaining sources were modelled by a power-law according to Equation 3.

# Chapter 3

# A Targeted Broadband Spectral Variability Survey

## 3.1 Context

Spectral variability can inform on details of the source itself and the intervening media but is limited by the quality and sampling of the SED and temporal coverage. As discussed in Section 1.3, a single physical origin of variability can produce vastly different effects over a range of timescales and frequencies. In particular, for PS sources, the optically thin and optically thick regimes of the SED (above and below the spectral peak respectively), can vary independently due to entirely separate processes. To confidently determine the physical origins of variability, one must have large spectral coverage to characterise the variability and regular time sampling to measure the timescale and amplitude of modulation accurately.

Historically, variability surveys often involved combining observations taken from a range of instruments for spectral coverage and/or searching in archival data. Combining several instruments for spectral coverage can induce variability from instrumental differences reducing confidence in the level of variability. Furthermore, the use of searching archival data limits the time cadence sampling, thus calculating accurate estimates for the variability timescale are limited by

availability.

The design of a targeted spectral variability survey is vital to ensure desired frequency and time cadences are sampled while minimising the number of instruments used. Both the MWA and ATCA have a large fractional bandwidth, allowing for a broad spectral coverage 72 MHz to 10 GHz with just two instruments. By selecting PS sources with a peak within or above the MWA frequency range, a spectral variability survey using these two instruments samples both the optically thin and optically thick regimes, crucial for determining the origins of variability. Furthermore, a targeted approach ensures sufficient sampling of the time cadences expected for specific physical processes.

## 3.2   Implications

This targeted spectral variability survey selected 15 PS sources of the 91 identified as variable in Ross et al. (2021) and found 13 to still be showing significant short duration (∼months) variability at MHz frequencies. Furthermore, RISS was found to explain at least some (if not all) of this variability.

From a sample of just 16% of variable PS sources from Ross et al. (2021), over 85% continued to display significant variability likely due in part to RISS. This is an incredibly high fraction of sources continuing to show variability from a blind spectral variability survey with just two epochs at MHz frequencies. Given the expected timescale of modulation due to weak RISS is of the order of several hours at GHz frequencies (see Section 1.2.1), it is reasonable to expect the variable PS sources of this study would also exhibit intraday variability (IDV) at GHz frequencies due to weak RISS.

The fast survey speed of the MWA due to its large field-of-view makes it the perfect instrument for blind surveys to search for variability. The results of this Chapter suggest that from a blind survey with just two epochs (as conducted in Chapter 2), it is possible to identify candidates for IDV. This Chapter builds on the blind survey conducted in Chapter 2 and confirms IDV for several sources

presented as source showing variability due to scintillation in Ross et al. (2021). Characterising the IDV, and its annual cycle due to the orbit of the Earth, can inform on the kinematics, distance and composition of the intervening screen (see Section 1.2.1). Likewise, tentative links between the refracting screen and nearby hot stars have been made but the confidence of such connections is hindered by small populations. We present blind spectral variability surveys at MHz frequencies as a methodology for identifying IDV candidates to investigate this link. Unfortunately, none of the targets in this Chapter had known spectroscopic redshifts at the time of publication. This had minimal impact on estimates for scintillation which depends on the angular size and relative size of the source compared to the scattering screen, or the spectral fitting which was predominantly used to determine the best spectral model and variations in the peak frequency. However, follow up investigations of the variable targets showing variability due to processes other than scintillation would benefit from high resolution imaging and accurate redshift estimates in order to determine the rest frame peak frequency and linear size.

## 3.3  Wide-band spectral variability of peaked spectrum sources

The contents of this chapter have been published as *"Wide-band spectral variability of peaked spectrum sources"* (2022) in the Monthly Notices of the Royal Astronomical Society, volume **512**, `10.1093/mnras/stac819` (Ross et al., 2022). The accepted manuscript is re-produced, with permission, in full in this Chapter. Minor typographical and grammatical changes have been made to ensure consistency with the rest of the Thesis.

# Wide-band Spectral Variability of Peaked Spectrum Sources

K. Ross[1*], N. Hurley-Walker[1], N. Seymour[1], J. R. Callingham[2,3],
T. J. Galvin[1], M. Johnston-Hollitt[4]

[1] *International Centre for Radio Astronomy Research, Curtin University, Bentley, WA 6102, Australia*

[2] *Leiden Observatory, Leiden University, PO Box 9513, Leiden, 2300 RA, The Netherlands*

[3] *ASTRON, Netherlands Institute for Radio Astronomy, Oude Hoogeveensedijk 4, Dwingeloo, 7991 PD, The Netherlands*

[4] *Curtin Institute for Computation, Curtin University, GPO Box U1987, Perth WA 6845*

## ABSTRACT

Characterising spectral variability of radio sources is a technique that offers the ability to determine the astrophysics of the intervening media, source structure, emission and absorption processes. We present broadband (0.072–10 GHz) spectral variability of 15 peaked-spectrum (PS) sources with the Australia Telescope Compact Array (ATCA) and the Murchison Widefield Array (MWA). These 15 PS sources were observed quasi-contemporaneously with ATCA and the MWA four to six times during 2020 with approximately a monthly cadence. Variability was not detected at 1–10 GHz frequencies but 13 of the 15 targets show significant variability with the MWA at megahertz frequencies. We conclude the majority of variability seen at megahertz frequencies is due to refractive interstellar scintillation of a compact component $\sim 25$ mas across. We also identify four PS sources that show a change in their spectral shape at megahertz frequencies. Three of these sources are consistent with a variable optical depth from an inhomogeneous free-free absorbing cloud around the source. One PS source with a variable spectral shape at megahertz frequencies is consistent with an ejection travelling along the jet. We present spectral variability as a method for determining the physical origins of observed variability and for providing further evidence to support absorption models for PS sources where spectral modelling alone is insufficient.

# 1   INTRODUCTION

Variability at radio wavelengths of active galactic nuclei (AGN) has the potential to reveal their radio structures, astrophysical properties, and the medium between the observer and the source. Long-duration variability at radio wavelengths has previously been shown to provide insight into a range of intrinsic phenomena including young jets (Patil et al. 2020; Nyland et al. 2020), jet interactions or shocks (Jamil et al. 2010), flare events and adiabatic expansion (Hovatta et al. 2008), oscillating jet orientation (Kudryavtseva et al. 2011), or the nature of a surrounding ionized medium (Tingay et al. 2015; Bicknell et al. 2018).

Short duration (hours to days) variability in the gigahertz regime is largely attributed to extrinsic propagation effects such as interstellar scintillation (ISS; Lovell et al. 2008; Koay et al. 2018). Characterising the timescales and size of modulation due to ISS can provide information on source morphologies on micro-arcsecond ($\mu$as) scales (Narayan 1992; Walker 1998). Furthermore, variability at low frequencies ($< 1\,\mathrm{GHz}$) has also been attributed to ISS, particularly refractive ISS (RISS; Hunstead 1972; Rickett 1986; Bell et al. 2019; Hancock et al. 2019).

Previously, Ross et al. (2021, hereafter R21), conducted one of the largest searches for spectral variability at radio frequencies to date. R21 surveyed over 21,000 sources with the Murchison Widefield Array (MWA; Tingay et al. 2013) over 100–231 MHz with a two epochs separated by roughly one year. R21 introduced the variability index parameter (VIP) to detect variability across a wide spectral range, and the measure of spectral shape (MOSS) parameter to classify the type of variability. R21 found a range of spectral variability, from uniform

$^\star$ E-mail: kathryn.ross@icrar.org

increases in flux density across the observing band to various changes in spectral shape. Furthermore, R21 also found that AGN with a peak in their spectral energy distributions (SEDs) appear to be more variable than typical power-law AGN. These peaked-spectrum (PS) sources are typically also compact ($\leq$20 kpc); see O'Dea & Saikia (2021) for a comprehensive review. PS sources have been shown to have a higher scintillation index for interplanetary scintillation (IPS) with the MWA (Chhetri et al. 2018). Likewise, high-resolution imaging with VLBI found that sources with compact morphologies also had high scintillation indices (Jaiswal et al. 2021). PS sources have also been shown to vary significantly on decade-long timescales attributed to renewed AGN activity and young, evolving jets (Wołowska et al. 2017; Nyland et al. 2020).

The cause of the low-frequency absorption producing the spectral peak of PS sources is still largely debated between two competing theories: synchrotron self-absorption (SSA) or free-free absorption (FFA). The first case, often considered the 'youth' scenario (O'Dea & Baum 1997), suggests their compact size is likely due to the jets being young and having formed within the past $\sim$10$^5$ years (Owsianik & Conway 1998) and that SSA occurs due to high brightness temperatures at low frequencies. Alternatively, the FFA case, often referred to as the 'frustration' scenario (van Breugel et al. 1984), suggests the radio jet/lobe is prevented from growing due to a surrounding cloud of dense ionized plasma (Bicknell et al. 1997). Unfortunately, distinguishing between these two scenarios requires large spectral coverage in the optically-thick regime (below the spectral turnover), and complex (often inconclusive) spectral modelling (Tingay & de Kool 2003; Callingham et al. 2015). Furthermore, previous variability monitoring of PS sources found many displayed a temporary peak in their SED and lost their PS source classification (Torniainen et al. 2005, R21). Such temporary PS sources were considered likely to be blazars (i.e. a radio source with one jet pointed towards the observer), rather than compact symmetric objects (Taylor et al. 1996).

One of the key issues in radio variability, at all frequencies, is distinguishing between intrinsic and extrinsic origins (Lovell et al. 2008). Once the origin of variability is determined, it can be used to inform the physical properties of the source itself. Given recent findings that PS sources appear to be a more variable population compared to typical AGN (Chhetri et al. 2018, R21), this population provides a unique opportunity to study variability mechanisms. Furthermore, the variability above and below the spectral peak (in the optically thin and optically thick regimes respectively) may be due to separate physical mechanisms. Tingay et al. (2015) monitored the nearby PS source, PKS B1718–649, with the ATCA for almost two years, with a large spectral coverage of 1–10 GHz. The vast spectral coverage was able to cover the optically thick and optically thin regimes as well as the spectral turnover at $\sim 3$ GHz, which allowed for confident spectral modelling of both SSA and FFA spectral models. Tingay et al. (2015) also detected variability across the entire sampled spectrum of PKS B1718–649. By combining low- and high-frequency observations to search for spectral variability, Tingay et al. were able to refine the causes of variability below and above the spectral turnover as being due to different physical processes. Furthermore, low-frequency variability was found to be caused by changes in the free-free optical depth, as the magnitude of variability across the spectrum was inconsistent with SSA. While the spectral modelling provided tentative evidence for an FFA spectral model over an SSA spectral model, the cause of the low-frequency variability being due to variations in the free-free optical depth added further evidence in support of a FFA spectral model.

Spectral variability, therefore, has the potential to distinguish between intrinsic and extrinsic origins of variability. Until recently, surveys of spectral variability have been limited by single/small sample sizes (Tingay et al. 2015), narrow spectral coverage (Hunstead 1972; Fanti et al. 1979; Bell et al. 2019), only gigahertz frequency coverage (Nyland et al. 2020; Wołowska et al. 2021) or combining non-simultaneous spectral coverage (Torniainen et al. 2005). Furthermore, the

low-frequency spectral variability (in the optically thick regime of PS sources) appears to have distinct properties and origins compared to variability at gigahertz frequencies. With the development of the MWA, and leading into the next generation of telescopes such as the Square Kilometre Array low frequency array (SKA_LOW), surveys of large spatial regions/population sizes with significant temporal and spectral coverage are now becoming achievable.

In this paper, we build on the work of R21 to study the spectral variability (0.07–10 GHz) of 15 PS sources to determine the origins of their variability and absorption at megahertz frequencies. The combined simultaneous observations from the MWA (0.07-0.23 GHz) and the Australia Telescope Compact Array (ATCA, 1-10.GHz) over one year make this survey a unique study of broad spectral variability. Section 2 outlines the selection process of the 15 PS sources in this study. The observational and data reduction strategies for the MWA and the ATCA are described in Section 3.1 and Section 3.2 respectively. The spectral models and fitting routines are described in Section 4. The results are summarised in Section 5 and detailed analysis and discussion of individual sources is presented in Section 6. All coordinates are in J2000.

## 2 SOURCE SELECTION

The main goal of this variability monitoring campaign was large quasi-contemporaneous spectral coverage using the ATCA and the MWA for a small number of targets.

The sample of sources were selected for follow up monitoring according to several criteria:

(i) classified as a PS source by Callingham et al. (2017);

(ii) predicted flux density $\geq 10$ mJy at 9 GHz;

(iii) observed to show spectral variability in R21 with a variability index parameter (VIP) $\geq 58.3$ according to Equation 1.

We selected PS source targets based on criteria (i) for a reliable PS source

classification. Callingham et al. combined flux density measurements from the GaLactic and Extragalactic All-Sky MWA (GLEAM; Wayth et al. 2015) ExGal data release (Hurley-Walker et al. 2017) with flux density measurements from either the Sydney University Molonglo Sky Survey (SUMSS; Mauch et al. 2003) or the NRAO VLA Sky Survey (NVSS; Condon et al. 1998) to identify PS sources with an observed spectral peak between 72 MHz and 1.4 GHz. Sources were classified as a PS source if they either showed a spectral peak or curvature within the GLEAM band (72 – 231 MHZ), or a power-law spectrum with a positive spectral index. As the frequencies of spectral peaks of the PS sources presented by Callingham et al. are below 1.4 GHz, our monitoring with the MWA and the ATCA with a spectral coverage of 0.072–10 GHz covers both the optically thin and optically thick regimes of each of our targets.

For criterion (ii), we calculated the spectral index of a power-law spectral model and predicted the flux densities at 9 GHz. The power-law was fit using the GLEAM flux density measurement at 220 MHz and the flux density at either 843 MHz or 1.4 GHz, based on the availability of either SUMSS or NVSS. This criterion ensures we have enough signal-to-noise in the ATCA data to probe variability at $< 10\%$ level.

We selected the 15 most promising targets that satisfied all three criteria as the sources for this study. Initial results of variability for R21 identified 15 targets that satisfied all three criteria. Criterion (iii) used the variability index parameter (VIP) according to:

$$\mathrm{VIP} = \sum_{i=1}^{n} \frac{\left(S_1(i) - S_2(i)\right)^2}{\sigma_i^2}, \tag{1}$$

where $S_1(i)$ and $S_2(i)$ are the flux densities in the first and second epoch in a given sub-band $i$, respectively, and $\sigma_i$ is the combined uncertainty of each flux density added in quadrature. The VIP is a measure of how many flux density measurements in the second epoch differ from those in the first epoch, and by how

much. As part of our initial results for R21, we identified 15 targets that satisfied criteria (i) and (ii) and had a VIP that implied they were variable. However, five of our proposed PS targets were later excluded from the final catalogue of variable sources in R21 due to lower mosaic quality and higher median VIP in those regions. Despite the lower mosaic quality, these five targets were included in this variability study as their measured VIP was at least two times greater than the significance cut off used for the other areas of the mosaic and significantly larger than the median value in the poor quality regions. As such, the variability of these five targets were considered more significant than the variability due to the poorer mosaic quality. The measure of spectral shape (MOSS) parameter for these targets was also calculated according to:

$$\mathrm{MOSS} = \sum_{i=1}^{n} \frac{(\widetilde{\mathrm{diff}} - \mathrm{diff}(i))^2}{\sigma_i^2} \tag{2}$$

where $\widetilde{\mathrm{diff}}$ is the median of the differences between the flux density over all frequencies, $\mathrm{diff}(i)$ is the difference of the flux densities between the two epochs at frequency $i$, and $\sigma_i$ is the combined uncertainty of each flux density added in quadrature. The calculated VIP and MOSS for all 15 PS targets are presented in Table 1.

Only 10 of our original 15 targets were classified as variable in R21 but all have a VIP>58.3. Furthermore, all 15 satisfied criteria (i) and (ii). All 15 targets were included in this study. A summary of the 15 targets monitored in this study and the observations used in the analysis can be found in Table 1.

## 3 OBSERVATIONS

Each target was observed six separate times during 2020. However, due to some observational difficulties, discussed in detail in Sections 3.1 and 3.2, some epochs were discarded from analysis for both the ATCA and the MWA. Table 2 summarises the telescope configurations and observation information for each epoch, we also include the two original GLEAM epochs (MWA Phase I from R21).

| GLEAM Name | $S_{151\mathrm{MHz}}$ (Jy) | VIP | MOSS |
|---|---|---|---|
| J001513-472706 | 0.50 | 463 | 35 |
| J015445-232950 | 0.65 | 331* | 11* |
| J020507-110922 | 1.36 | 1092 | 48 |
| J021246-305454 | 0.29 | 125* | 11* |
| J022744-062106 | 0.48 | 431 | 8 |
| J024838-321336 | 0.41 | 264 | 38 |
| J032213-462646 | 0.42 | 336 | 26 |
| J032836-202138 | 0.55 | 290 | 25 |
| J033023-074052 | 0.33 | 816 | 46 |
| J042502-245129 | 0.63 | 431* | 76* |
| J044033-422918 | 1.86 | 1095 | 15 |
| J044737-220335 | 2.67 | 767* | 104* |
| J052824-331104 | 0.64 | 173* | 38* |
| J223933-451414 | 1.43 | 2796 | 95 |
| J224408-202719 | 0.39 | 226 | 19 |

**Table 1.** Targets chosen for monitoring. $S_{151\mathrm{MHz}}$ is as reported in the GLEAM catalogue (Hurley-Walker et al. 2017). All sources are compact within GLEAM, thus the GLEAM names are also accurate coordinates to $\sim 2'$. We present the corresponding variability index parameter (VIP) and measure of spectral shape (MOSS) parameter. A VIP$\geq$ 58.3 was classified as variable and a MOSS$\geq$ 36.7 was classified as changing spectral shape, according to R21. Five targets did not meet criteria (iii) as they were cut from the final catalogue of variable sources presented by R21, as discussed in Section 2. The presented VIP and MOSS values for these targets are denoted with a $*$ and has been calculated as part of this work.

| Epoch | Notes on MWA Observations | Notes on contemporaneous ATCA Observations |
|---|---|---|
| August to September 2013 | GLEAM Year 1, MWA Phase I | No Data |
| August to December 2014 | GLEAM Year 2, MWA Phase I | No Data |
| January 2020 | No Data | 6A configuration, 2.1, 5.5 and 9 GHz observed |
| March 2020 | No Data | 6D configuration, incorrect central frequency for X-band, 9 GHz data omitted for GLEAM J001513−472706, GLEAM J223933−451414 and GLEAM J224408−202719 |
| April 2020 | Extended Phase II configuration, Daytime observations, omitted for GLEAM J020507−110922, GLEAM J024838−321336 | 6A configuration, 2.1, 5.5 and 9 GHz observed |
| May 2020 | Extended Phase II configuration | 6A configuration, 2.1, 5.5 and 9 GHz observed |
| July 2020 | Extended Phase II configuration | No Data |
| September 2020 | Extended Phase II configuration | No Data |
| October 2021 | No Data | H168 configuration, 5.5 and 9 GHz observed for GLEAM J001513−472706 and GLEAM J020507−110922 |

**Table 2.** The dates of each epoch used for the variability analysis, details of the telescope configuration for both MWA and the ATCA and any relevant notes on the observations or data omitted.

## 3.1   MWA

The MWA observations were scheduled to match the awarded ATCA observations[1]. Unfortunately, the MWA Phase II was in the compact configuration during the January and March 2020 ATCA observations[2]. As such, these observations were omitted from our analysis. All subsequent MWA observations were obtained with the MWA in the extended Phase II configuration. Two further epochs were observed with the MWA in July and September 2020 without contemporaneous ATCA observations. Thus there are a total of four usable MWA epochs over six months of 2020 with two taken within 48 hours of the ATCA observations in April and May 2020. Furthermore, the GLEAM South Galactic Pole observations from 2013 and 2014 (Franzen et al. 2021), used by R21, were also considered to make a roughly six year time baseline.

The observational strategy for the MWA relied on targeted two-minute snapshots with the target source approximately centred in the primary beam. Due to the large field of view of the MWA, the sensitivity is fairly consistent within ∼5 degrees of the pointing centre. These targeted snapshots were taken at five different frequency bands of 30.72 MHz bandwidth and centred at 87.7, 118.4, 154.2, 185.0, and 215.7 MHz to match the frequencies used in GLEAM survey (Wayth et al. 2015). High elevations were required for good sensitivity, so the April and May 2020 observations were taken during the day. Where possible, the Sun was placed in a null of the primary beam to reduce its effect on the observations. In the April observations, each target had three snapshots for each frequency band; for subsequent epochs, each target had six snapshots.

We employed a similar strategy as used for the GLEAM-X survey reduction[3]. No calibration scans were taken, instead the latest sky model, GLEAM

---

[1] The project code for MWA observations is G0067, PI: Ross.

[2] The side-lobe confusion of the MWA in the compact configuration is often large enough that the scientific use of the final image is limited. For details of the configurations of MWA Phase II, see (Wayth et al. 2018)

[3] The GLEAM-X pipeline can be found and downloaded here: `https://github.com/tjgalvin/GLEAM-X-pipeline`

Global Sky Model (GGSM), was used to calculate calibration solutions for each snapshot (Hurley-Walker et al. submitted). For the region containing all 15 of our targets, this model is largely derived from GLEAM ExGal (Wayth et al. 2015; Hurley-Walker et al. 2017). Following the same reduction strategy as GLEAM-X, any known bad tiles were flagged before initial calibration solutions were calculated with respect to the GGSM. These solutions were inspected and any further bad tiles were flagged before applying the solutions. If the calibration was unable to converge on solutions, solutions from an observation taken around a similar time with a similar pointing were applied.

Initial images were made using WSCLEAN (Offringa et al. 2014) with a Briggs weighting of robust weighting of +0.5 (Duchesne et al. 2021). Images were visually inspected to ensure calibration was appropriate and assess the effects of the Sun for any day-time observations or bright sources known to reduce image quality[4]. In the April observations, despite placing the Sun in a null of the primary beam where possible, due to the frequency dependence of the primary beam, some pointings resulted with the Sun within the images. This significantly increased the noise in the images and large scale artefacts across the entire image.

For GLEAM J020507–110922 and GLEAM J024838–321336, the location of the Sun resulted in at least twice the local root-mean-squared (RMS) noise in snapshot images for each frequency compared to other targets. As a result, this epoch for these targets was emitted. For remaining day-time observations, imaging parameters were adjusted to reduce the power of the Sun. Since the Sun is resolved and this study was only interested in unresolved (with the MWA) bright sources, short baselines of the MWA were removed when producing images that contained the Sun in the primary beam. The short baselines were tapered out using the `minuv-l` and `taper-inner-tukey` options of WSCLEAN to create a gradual taper of shorter baselines rather than a sharp cut. Both the `minuv-l` and `taper-inner-`

---

[4] A list of these sources can be found in Table 2 of Hurley-Walker et al. (2017).

`tukey` were set to $50\,\lambda$ to cut baselines less than $50\,\lambda$ and minimise baselines between $50$ and $100\,\lambda$. The *uv*-taper also reduced the effect of bright, resolved galaxies, like Fornax-A, which were also occasionally in the field of view.

Once satisfactory images were produced, the flux density scale and position shifting were corrected, to account for miscalculations of the primary beam and effects from the ionosphere, respectively. A correction was derived and applied using FLUX_WARP (Duchesne et al. 2020) and FITS_WARP (Hurley-Walker & Hancock 2018), both of which use a subset of the Global GLEAM Sky Model (GGSM). Only unresolved (according to GLEAM), bright (signal to noise ratio $\geq 10$) and isolated (to within $5\,\mathrm{arcminutes}$) sources were considered in the reference catalogue to ensure a reliable model of the flux density scale and compared to the GGSM catalogue (Hurley-Walker et al. submitted). Corrected images were stacked together to create a small mosaic of 5,000 by 5,000 pixels with the target at the centre. Images were stacked using SWARP (Bertin et al. 2002) and coadded with inverse-variance weighting using the RMS noise of the images. Due to the large field of view of the MWA, some observations covered multiple targets. To decrease the overall RMS of stacked images, any observations where the target was within the field of view of the MWA were included in the stacking, even if it was not a targeted observation.

The variable ionospheric conditions during the observations can result in a residual blurring effect. To correct for this, a blur correction was applied to the resampled, coadded mosaics by generating point-spread-function (PSF) maps. Firstly, the background and noise maps of the mosaics were generated using the Background and Noise Estimation tool (BANE). An initial shallow source finding was run on the resultant mosaics using AEGEAN[5] (Hancock et al. 2012, 2018). For this shallow source finding, the "seed" clip was set to 10, i.e. only pixels with a flux density 10 times the local RMS noise were used as initial source positions.

---

[5] https://github.com/PaulHancock/Aegean

The output catalogue from the shallow run of Aegean was cut to only include unresolved sources. This catalogue was then used to produce a measured PSF map for the mosaic. The measured PSF map was used as input for a further run of Aegean to account for the variable PSF of the mosaic. The generated catalogue of sources from the second run of Aegean was used to generate a new PSF map with the right blur correction, which we applied to the mosaic to correct for the ionosphere. Resolved sources were excluded from the catalogue for this blur correction.

A final correction for any large scale flux density variations across the blur corrected mosaic was applied using FLUX_WARP again. This correction was of the order of 2%–10% depending on the frequency and whether the observations were taken during the day. As with the first run of FLUX_WARP, a reference catalogue of bright, unresolved and isolated sources was used to ensure a reliable model of the flux density scale and compared to the GGSM catalogue. The GGSM catalogue was used as a prior catalogue for source positions for Aegean's priorised fitting. Furthermore, any sources that were previously classified as variable by R21 were excluded from the reference catalogue.

A final source-finding of the blur and flux density scale corrected mosaics using BANE and Aegean produced the catalogue used in variability analysis.

## 3.2 ATCA

In 2020, four observations of the 15 targets were taken in January, March, April and May. Observations were taken at L-band (central frequency 2.1 GHz), and C/X-band (central frequencies 5.5 GHz and 9.5 GHz). The bandwidth in all cases was 2 GHz (Wilson et al. 2011). For the January and March epochs, the observing strategy was two 12-hour blocks on consecutive days, each of which was devoted to a single ATCA band. The April and May epochs each had an 18 hour observing block, and frequency switching was used between the two bands. In all epochs, two-minute snapshots were taken of the target sources sandwiched between sec-

ondary phase calibrator observations. Secondary calibrators were shared between targets when both targets had an angular separation less than 10 degrees to the secondary calibrator in order to reduce slew overheads. The $(u, v)$-coverage was more complete in the April and May epochs compared to the January and March epochs as there was a larger time gap between snapshots due to the frequency switching. All epochs were observed in a 6-km array configuration; for specific array configurations in each epoch, see Table 2.

The same primary bandpass calibrator, PKS B1934–638, was observed for each epoch and used for estimates of the overall instrumental errors. Furthermore, we use the measured flux density of PKS B1934-638 in each epoch to compare with our sources to assess the variability of the target sources.

Due to an error in scheduling, GLEAM J001513–472706, GLEAM J223933–451414 and GLEAM J224408–202719 were observed at 9 GHz in March while PKS B1936–638 was observed at 9.5 GHz. As a result, the 9 GHz observations for the sources in March were discarded to avoid applying an inaccurate calibration solution and inducing artificial variability.

The majority of data reduction was completed using CASA 6.4 (McMullin et al. 2007) after first converting the data into a measurement set via the MIRIAD (Sault et al. 1995) task `atlod`. Data were processed using the same reduction procedure[6], which we briefly describe here. After initial flagging for radio frequency interference (RFI), observations were split into a separate measurement set with the primary bandpass calibrator and associated secondary calibrator. An initial round of bandpass and gain calibration solutions were calculated using just the primary calibrator. Then a second round of gain calibration solutions were calculated using the primary and secondary calibrators. The flux density scale was estimated using PKS B1934–638 as a flux density standard (Reynolds 1994). Further RFI flagging was performed on the calibrated measurement set

---

[6] The code used to process all the ATCA data can be found here: https://github.com/astrokatross/ATCA_datareduction

before an initial model image was created using the interactive `tclean` on a Multi-Frequency Synthesis (MFS) image of the entire bandwidth. Three rounds of phase self-calibration were performed on the target source using the created model image. For all targets, in the 5.5 GHz and 9.5 GHz bands, no other sources sources were detected in the field of view. However, the larger field-of-view for the 2.1 GHz band resulted in an occasional nearby source in the image field. Where appropriate, these other sources were included in the model used for self-calibration. Self-calibration solutions were calculated by combining the entire ATCA band to increase signal to noise, and applied without flagging any sections that were unable to converge on a solution. Targets were split into smaller spectral windows for imaging (to create the model) and flux density measurements. Observations at 2.1 GHz were split into eight spectral windows, 5.5 GHz into five and 9.5 GHz into four. Such binning ensured roughly equal fractional bandwidth per spectral band. The flux density for each spectral band was measured using the `uvmodelfit` function in CASA. A rough initial source position was given based on the MFS image but allowed to vary.

The flux densities of secondary calibrators and the primary bandpass calibrator were also measured using `uvmodelfit`. These measurements were used to estimate systematic errors on the flux density measurements of targets and assess the significance of any variability.

In October 2021, opportunistic follow-up observations with the ATCA at 5.5 GHz and 9 GHz during Director's Time were undertaken of GLEAM J001513–472706 and GLEAM J020507–110922 in the H168 configuration. The observational strategy differed slightly to the 2020 monitoring. Targets were observed with 10 minute scans over several hours.

## 4   SPECTRAL MODELLING

We fit spectral models to each source at each epoch to determine the underlying absorption mechanism. There are two main mechanisms for absorption at low frequencies: synchrotron self-absorption (SSA) or free-free absorption (FFA). The SSA model assumes the electron energy distribution for a single homogeneous synchrotron emitting region is described by a non-thermal power-law with index $\beta$. A spectral turnover occurs in a SSA model when the photons from the source are scattered by the relativistic electrons in the plasma. The low-energy photons are more likely to be scattered repeatedly resulting in them appearing to be "re-absorbed" by the plasma. The SSA model can be described according to Equation 3 of Kellermann (1966), where $\nu_p$ is the frequency where the source becomes optically thick (i.e. the optical depth, $\tau_\nu$, is unity). Namely,

$$S_\nu = S_{\mathrm{norm}} \left( \frac{\nu}{\nu_p} \right)^{\frac{\beta-1}{2}} \left[ \frac{1 - e^{-\tau_\nu}}{\tau_\nu} \right],$$

where                                                                                            (3)

$$\tau_\nu = \left( \frac{\nu}{\nu_p} \right)^{\frac{-(\beta+4)}{2}}.$$

Alternatively, the FFA model assumes a process of inverse bremsstrahlung or free-free absorption, where an ionized plasma screen is causing the absorption of the photons emitted by the relativistic electrons from the source (Bicknell et al. 1997; Tingay & de Kool 2003; Callingham et al. 2015). In this scenario, the electrons emit photons described by a non-thermal power-law distribution, using $\alpha$ as the spectral index of the synchrotron emission, where $\alpha = (\beta - 1)/2$ for the electron energy distribution as described by Equation 3. Several variations of FFA models exist that account for variations in screen morphology (either homogeneous or inhomogeneous) and whether the absorption is external or internal to the emitting electrons. In this work, we only consider FFA models with an external ionized screen that is either homogeneous or inhomogeneous since internal

free-free absorption has been shown to poorly replicate observed spectra of PS sources (e.g. Callingham et al. 2015).

The external homogeneous FFA model assumes a uniform ionized absorbing screen covers the entire emitting source. For a screen with optical depth $\tau_\nu$, the external homogeneous FFA model is written (Bicknell et al. 1997):

$$S_\nu = S_{\text{norm}} \nu^\alpha e^{-\tau_\nu},$$

where

$$\tau_\nu = \left(\frac{\nu}{\nu_p}\right)^{-2.1}$$

(4)

where $\nu_p$ is the frequency where the free-free optical depth equals unity.

The inhomogeneous FFA model is an external FFA model where the absorbing ionized cloud has a range of optical depths. The inhomogeneous FFA model was first presented by Bicknell et al. (1997), who modelled the interaction of the radio jets with the surrounding interstellar medium (ISM). Bicknell et al. (1997) proposed the jets create shocks in the ISM as they propagate from the AGN, producing regions of shocked gas with spatially variable optical thickness. To derive the spectral model of such a scenario, Bicknell et al. (1997) assumed the range of optical depths can be described by a power-law distribution with index $p$ according to:

$$\tau_{\text{ff}} \propto \int (n_e^2 T_e^{-1.35})^p dl,$$

(5)

where $n_e$ is the free electron density and $T_e$ is the electron temperature. We assume $p > -1$, otherwise as this model reduces to the homogeneous condition. By assuming the scale of the lobes is much larger than the scales of the inhomogeneities in the ISM and the shocks, Bicknell et al. (1997) represent the inhomogeneous FFA model as:

$$S_\nu = S_{\text{norm}}(p+1)\gamma\left[p+1, \left(\frac{\nu}{\nu_p}\right)^{-2.1}\right]\left(\frac{\nu}{\nu_p}\right)^{2.1(p+1)+\alpha}$$

(6)

where $\gamma$ is the lower incomplete gamma function of order $p+1$. In this model, the

spectral index of the optically thick regime is described by $\alpha_{\text{thick}} = \alpha - 2.1(p+1)$ (Bicknell et al. 1997).

Each of the SSA, FFA, and inhomogeneous FFA models assume a non-thermal synchrotron emission power-law distribution of the relativistic electrons. However, a continuous injection model (Kardashev 1962) predicts that the higher-energy electrons cool more quickly than the lower-energy electrons, presenting as a spectral steepening at frequencies higher than a break frequency, $\nu_{\text{break}}$. We introduce an exponential multiplicative factor, $e^{-\nu/\nu_{\text{break}}}$, into the SSA, homogeneous FFA and inhomogeneous FFA models to represent the spectral steepening (Callingham et al. 2015). We therefore fit a total of six spectral models: SSA, SSA with an exponential break, external homogeneous FFA, external homogeneous FFA with a spectral break, external inhomogeneous FFA and an external inhomogeneous FFA with a spectral break.

We fitted each spectral model using the `UltraNest` package[7] (Buchner 2021). `UltraNest` uses a nested sampling Monte Carlo algorithm MLFriends (Buchner 2017, 2016) to derive the Bayesian evidence and posterior probability distributions. We assumed a Gaussian distribution for the likelihood of each parameter and used a reactive nested sampler. As discussed in Section 5, we detected no significant variability with the ATCA across the 2, 5.5 or 9 GHz frequency sub-bands. As a result, ATCA flux densities were combined over time per sub-band to create an average flux density with 17 unique spectral points per source. This average ATCA spectrum was used to fit each MWA epoch over using individual ATCA epochs.

To compare spectral models, we calculate the Bayes factor, $K$:

$$K = e^{\log z_1 - \log z_2} \tag{7}$$

for each pair of models where $z_i$ is the maximum likelihood of the model $i$. Models with fewer parameters have a higher likelihood, thus the Bayes factor is robust

---

[7] https://johannesbuchner.github.io/UltraNest/

against preferring over-fitting. Assuming the physical mechanism causing the absorption in the SED is constant between epochs, we can determine the most likely spectral model based on all epochs. We calculate the average log likelihood of each model per source and conclude the most likely model is that with the largest average log likelihood. We calculate the Bayes factor, according to Equation 7, for the preferred model to the second most likely model to determine the significance of the likelihood. If $K \geq 100$, the likelihood of the first model is strongly more likely. If $K < 100$, the first model is more likely but there is less evidence of support. We present the average log likelihood (averaged over all the epochs), $\log(i)$ for each model in Table 3.

| GLEAM Name | $\log L_{\mathrm{SSA}}$ | $\log L_{\mathrm{FFA}}$ | $\log L_{\mathrm{inFFA}}$ | $\log L_{\mathrm{SSAb}}$ | $\log L_{\mathrm{FFAb}}$ | $\log L_{\mathrm{inFFAb}}$ | Best Model | Variability |
|---|---|---|---|---|---|---|---|---|
| J001513-472706 | 75 | 93.2 | 121.4 | 115.3 | 117.6 | 125.2 | inFFA(b) | Brightness change at $\leq$231 MHz |
| J015445-232950 | 30.5 | 61 | 107.6 | 98.5 | 105.9 | 120.6 | inFFAb | Variable spectral shape at $\leq$231 MHz |
| J020507-110922 | 19.0 | 47.7 | 84.6 | 74.6 | 82.6 | 99.9 | inFFAb | Variable spectral shape at $\leq$231 MHz |
| J021246-305454 | 113.8 | 40.9 | 148.2 | 154.3 | 152.9 | 156.0 | inFFAb* | Brightness change at $\leq$231 MHz |
| J022744-062106 | -38.4 | -20.4 | 98.7 | 76.2 | 77.1 | 98.0 | inFFA(b) | No variability detected |
| J024838-321336 | 65.0 | 76.6 | 87.5 | 119.8 | 116.3 | 115.3 | (SSA)b | Variable spectral shape at $\leq$231 MHz |
| J032213-462646 | -167.9 | -256.4 | 83.8 | 56.0 | 44.0 | 89.0 | inFFA(b) | Brightness change at $\leq$231 MHz |
| J032836-202138 | 12.3 | 62.9 | 131.4 | 124.2 | 136.3 | 151.7 | inFFAb | Brightness change at $\leq$231 MHz |
| J033023-074052 | 25.6 | 7.9 | 104.2 | 106.6 | 101.5 | 114.4 | inFFAb | Brightness change at $\leq$231 MHz |
| J042502-245129 | -291.7 | -287.3 | 76.9 | 49.7 | 27.2 | 102.4 | inFFAb | Brightness change at $\leq$231 MHz |
| J044033-422918 | -291.9 | -242.3 | 51.7 | -73.7 | -76.8 | 82.4 | inFFAb | Brightness change at $\leq$231 MHz |
| J044737-220335 | -1816.0 | -2351.6 | 29.8 | -876.2 | -1210.2 | 76.2 | inFFAb | Brightness change at $\leq$231 MHz |
| J052824-331104 | -71.8 | -78.7 | 90.9 | 74.2 | 50.5 | 104.7 | inFFAb | No variability detected |
| J223933-451414 | -87.3 | 64.8 | 99.1 | 78.0 | 125.3 | 132.5 | (in)FFAb | Variable spectral shape at $\leq$231 MHz |
| J224408-202719 | -9.5 | 10.1 | 92.1 | 110.8 | 100.9 | 119.4 | inFFAb | Brightness change at $\leq$231 MHz |

**Table 3.** The average log likelihoods for each spectral model for each source. For each source, the best model was determined using the average Bayes factor to determine the most likely model over all epochs. See Section 4 for details. Models are defined as: SSA, SSA with an exponential break (SSAb), external homogeneous FFA (FFA), external inhomogeneous FFA (inFFA), external homogeneous FFA with a spectral break (FFAb), external inhomogeneous FFA with a spectral break (inFFAb). A preferred model with an asterisk (*) next to it, indicates there was not strong evidence for this model compared to any other model (i.e. the Bayes factor was less than 100 for each pair of models). Preferred models with a (b) indicates that there is not strong evidence to support the presence of a high frequency spectral break over the absence of one but that the spectral model itself is preferred. Likewise, preferred models of (in)FFA indicate that an FFA model is preferred but there is not strong evidence of the FFA model over the inFFA model. Furthermore, a preferred model of (SSA)b indicates all spectral models with a high frequency spectral break are preferred but there is not strong evidence for the SSA model over any other spectral model.

## 5   RESULTS

We present the SEDs for each epoch of each source in Figure 1. We include flux density measurements from other radio surveys in the SEDs; these were not used in any fitting, but are included in the plots for completeness. The additional radio surveys are the Very Large Array Low-frequency Sky Survey Redux (VLSSr; Lane et al. 2014), Tata Institute for Fundamental Research Giant Metrewave Radio Telescope 150 MHz Sky Survey Alternative Data Release 1 (TGSS-ADR1; Intema, H. T. et al. 2017)[8], the Molonglo Reference Catalogue (MRC; Large et al. 1981, 1991), Sydney University Molonglo Sky Survey (SUMSS; Mauch et al. 2003), Rapid ASKAP Continuum Survey (RACS; Hale et al. 2021), NRAO VLA Sky Survey (NVSS; Condon et al. 1998), an the Australia Telescope 20 GHz Survey (AT20G; Murphy et al. 2010). All catalogues were cross-matched using TOPCAT's (Taylor 2005) nearest neighbour routine with a 2 arcmin radius. A 2 arcmin radius was chosen as it is comparable to the resolution of GLEAM. Table 3 presents the results of the spectral fitting, reporting the average log likelihoods to determine the most likely spectral model over all epochs, and observed variability.

We find each source shows a negative-slope power-law SED at frequencies $\geq 1$ GHz, which steepens at high frequency, consistent with synchrotron emission from a radio-loud AGN. We do not find any sources in our sample with a flat spectrum at gigahertz frequencies. Furthermore, we do not detect any significant variability with the ATCA in the 2020 monitoring, which sampled timescales of up to four months. The ATCA spectra of targets were compared to their secondary calibrators and the bandpass calibrator, PKS B1934–638, but no target showed significant variability or trends.

In contrast, there are several different behaviours of variability detected at megahertz frequencies. Most common are sources showing a consistent spectral shape with small variations with an overall trend over the epochs. However, some

---

[8] (We use the rescaled version of TGSS by Hurley-Walker 2017, to match the GLEAM flux density scale)
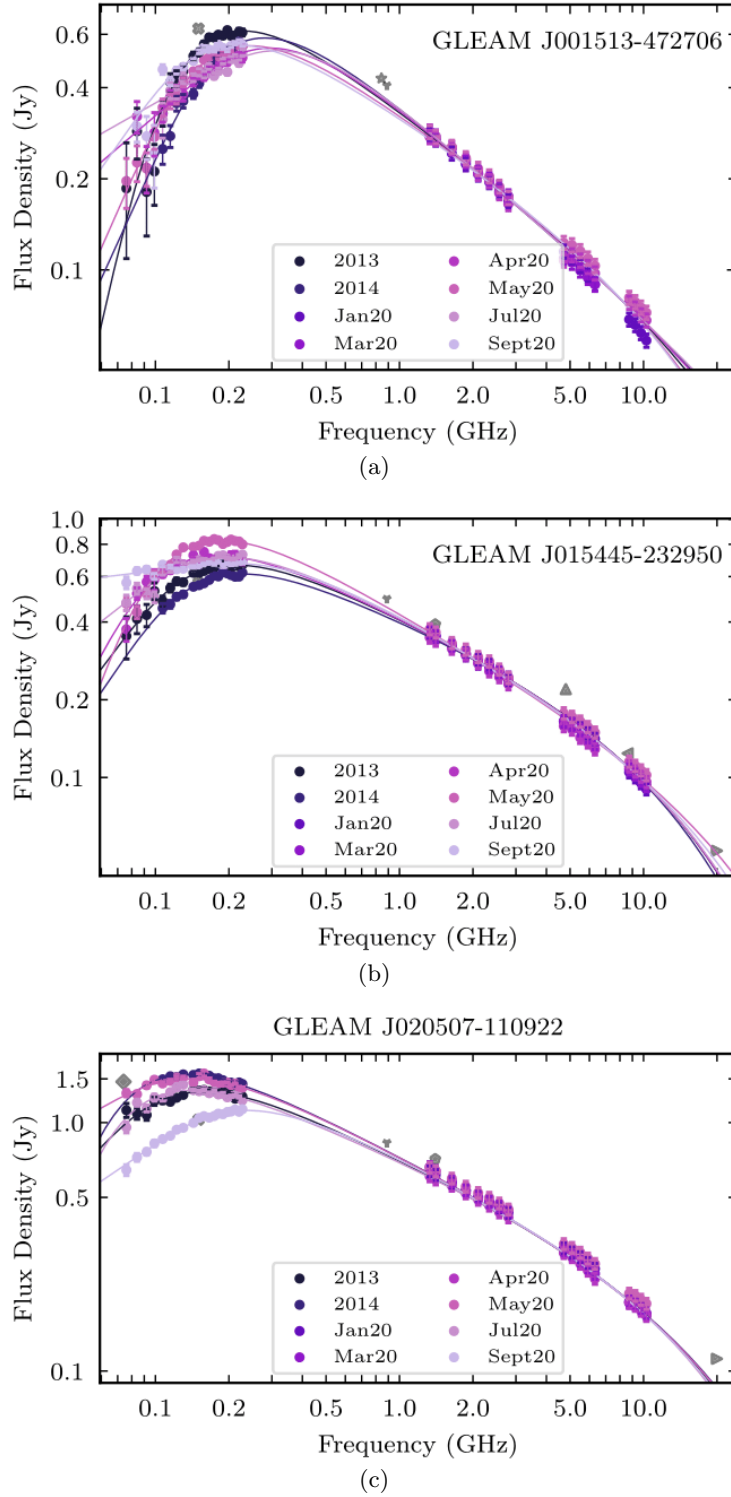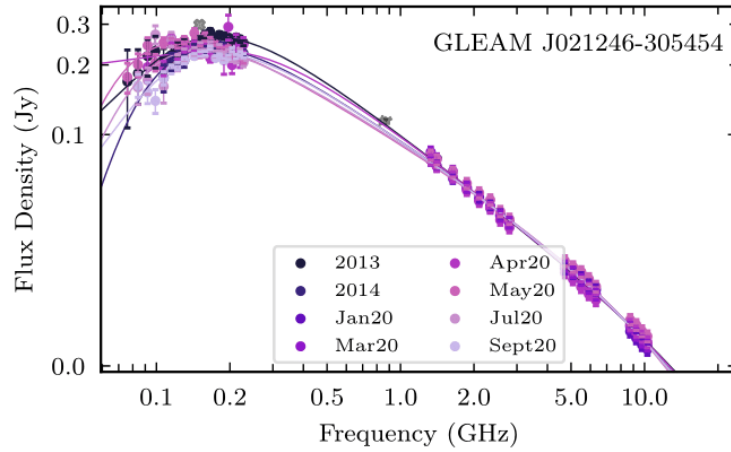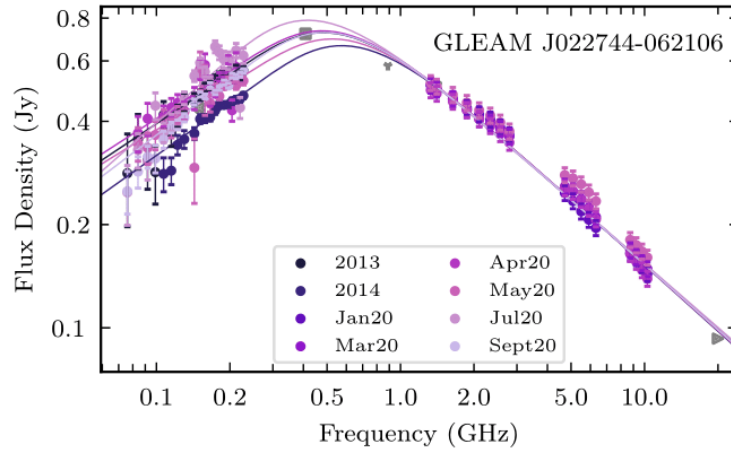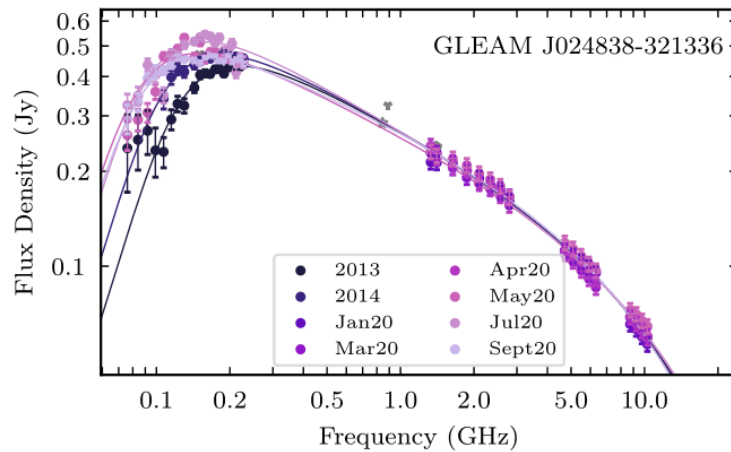
(a)



(b)



(c)

**Figure 1.** SEDs for all targets. ATCA and MWA data are plotted for each epoch with the best spectral model, according to the average Bayes Factor presented in Table 3, overlaid. Additional surveys are plotted in grey: VLSSr (diamond), TGSS-ADR1 (cross), MRC (square), SUMSS (star), RACS (Y), NVSS (pentagon), AT20G (20 GHz: left arrow, 8.6 GHz: right arrow, 4.8 GHz upwards arrow)

(d)



(e)



(f)

**Figure 1.** (continued) SEDs for all targets. Models plotted are the best spectral model according to the average Bayes Factor presented in Table 3. Additional surveys are plotted in grey: VLSSr (diamond), TGSS-ADR1 (cross), MRC (square), SUMSS (star), RACS (Y), NVSS (pentagon), AT20G (20 GHz: left arrow, 8.6 GHz: right arrow, 4.8 GHz upwards arrow)

(g)



(h)



(i)

**Figure 1.** (continued) SEDs for all targets. Models plotted are the best spectral model according to the average Bayes Factor presented in Table 3. Additional surveys are plotted in grey: VLSSr (diamond), TGSS-ADR1 (cross), MRC (square), SUMSS (star), RACS (Y), NVSS (pentagon), AT20G (20 GHz: left arrow, 8.6 GHz: right arrow, 4.8 GHz upwards arrow)
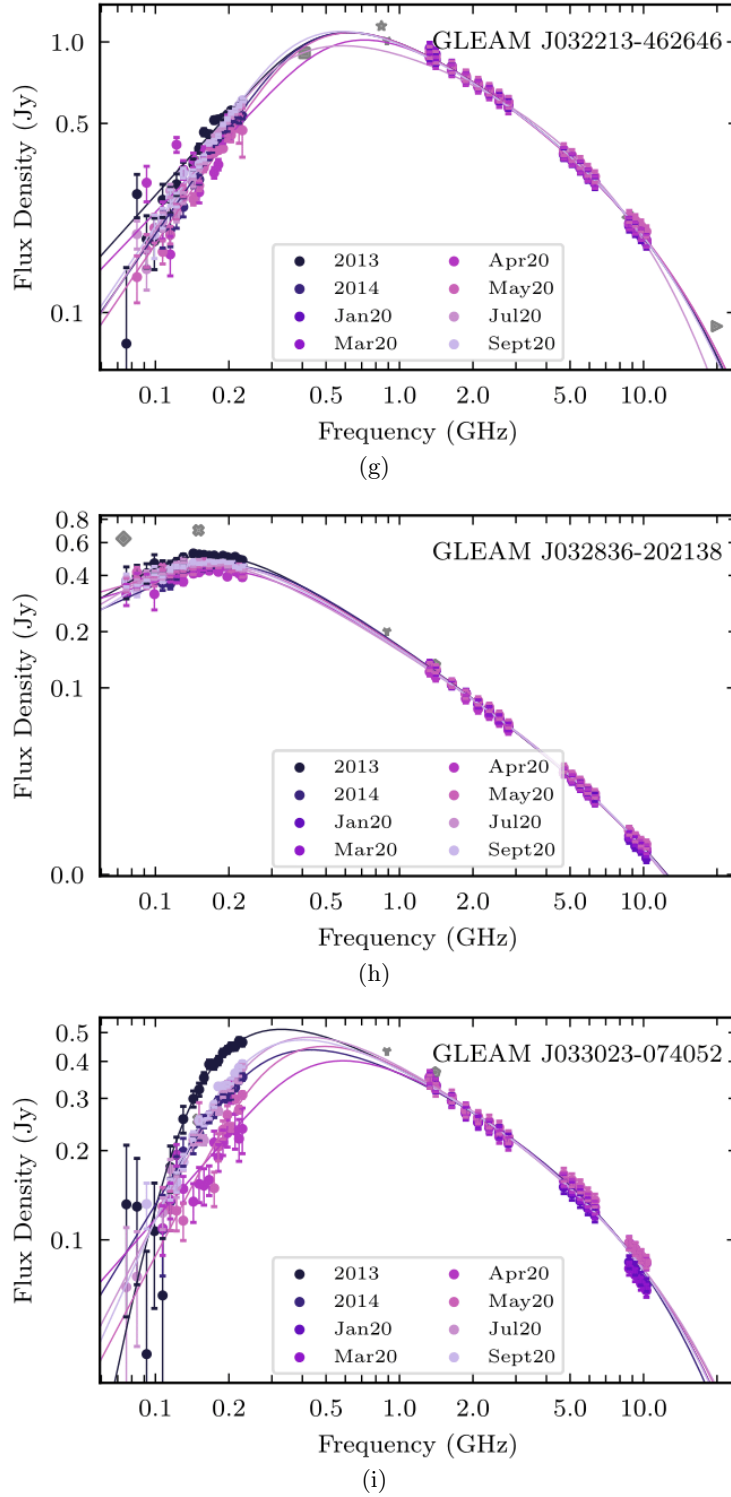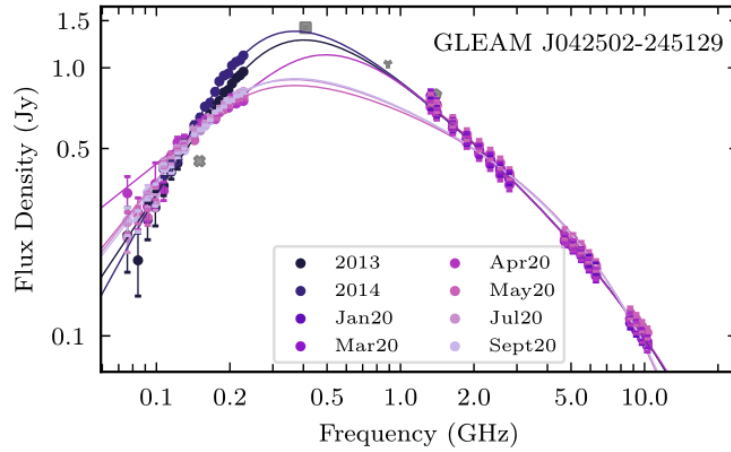
(j)



(k)



(l)

**Figure 1.** (continued) SEDs for all targets. Models plotted are the best spectral model according to the average Bayes Factor presented in Table 3. Additional surveys are plotted in grey: VLSSr (diamond), TGSS-ADR1 (cross), MRC (square), SUMSS (star), RACS (Y), NVSS (pentagon), AT20G (20 GHz: left arrow, 8.6 GHz: right arrow, 4.8 GHz upwards arrow)
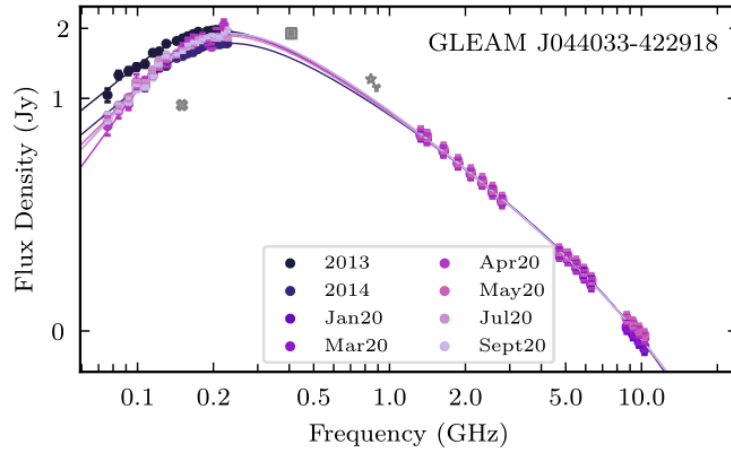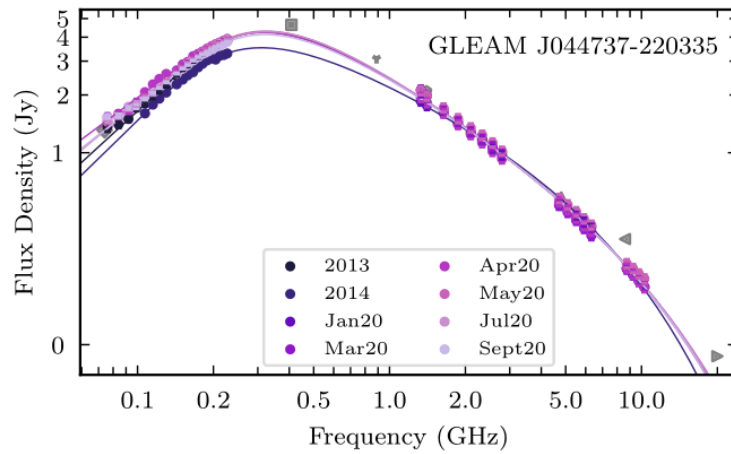
(m)



(n)



(o)

**Figure 1.** (continued) SEDs for all targets. Models plotted are the best spectral model according to the average Bayes Factor presented in Table 3. Additional surveys are plotted in grey: VLSSr (diamond), TGSS-ADR1 (cross), MRC (square), SUMSS (star), RACS (Y), NVSS (pentagon), AT20G (20 GHz: left arrow, 8.6 GHz: right arrow, 4.8 GHz upwards arrow)
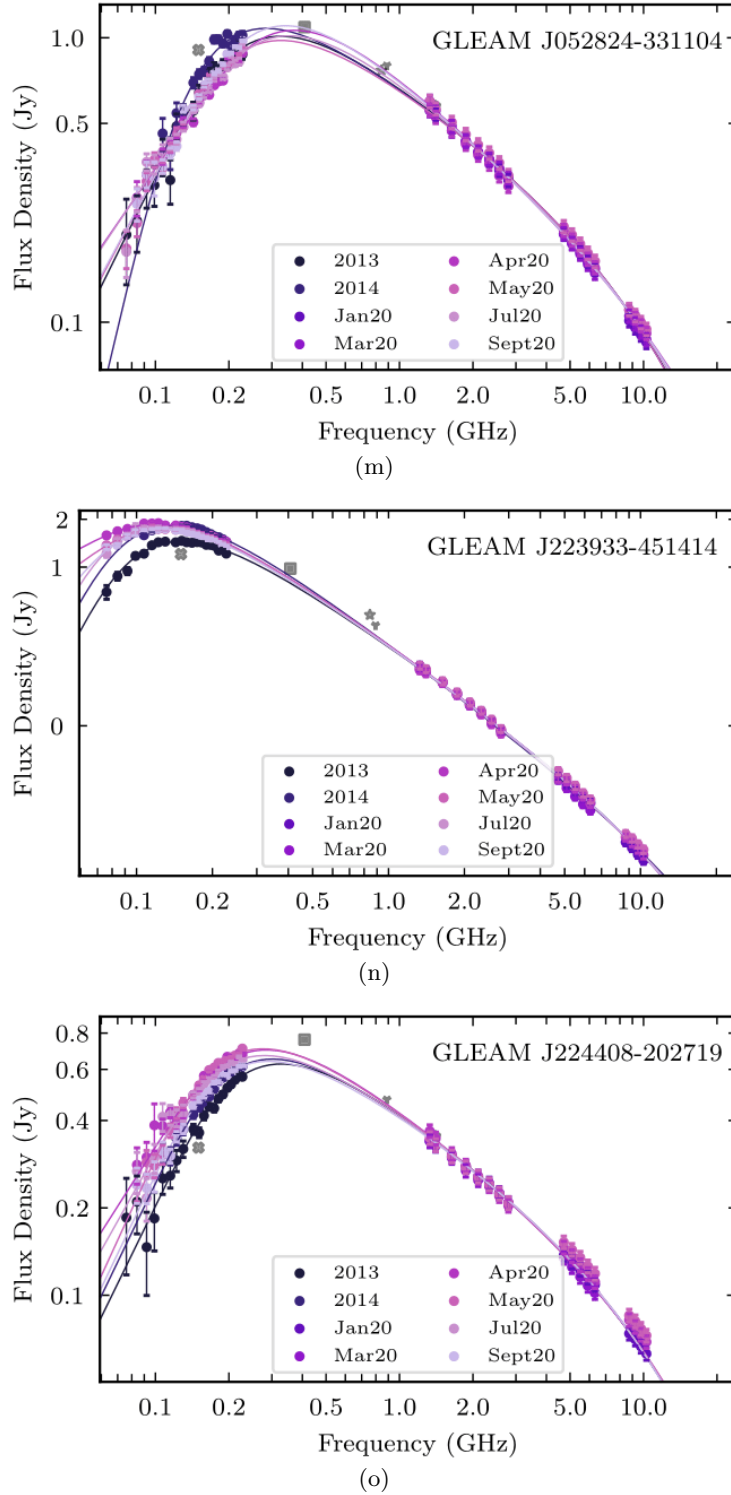
appear to change their spectral shape significantly, for example GLEAM J020507–110922 shown in Figure 1c. For each source, we check for significant variability with the MWA by comparing to nearby ($\lesssim 1\,\mathrm{deg}$) sources. In each case, we find no significant variability or common behaviours between our targets and nearby sources. The SEDs of nearby targets can be found in the online supplementary materials.

There is no significant variability at any frequency or timescale for GLEAM J052824–331104 (Figure 1m) or GLEAM J022744–062106 (Figure 1e). We do not detect any greater difference in flux densities for either source compared to any nearby source in the MWA images. GLEAM J052824–331104 was in the region of the SGP mosaics that R21 deemed too poor quality to detect variability (see Section 2 for details). We therefore conclude any difference observed between 2013 and 2014 for GLEAM J052824–331104 is not physical. It is possible the initial variability of GLEAM J022744–062106 detected by R21 was genuine and not due to introduced instrumentation errors, and it was still variable in 2020. However, the noise of the images created in 2020 were of too low quality to detect any significant changes in flux density as the Sun was in the primary beam for several images.

The SSA model with a spectral break was the most likely model for only one source, GLEAM J024838–321336 (Figure 1f). However, the Bayes factors for the SSAb model compared to the next most likely models, the FFAb and inFFAb, are 33 and 90, respectively. Consequently, there is not strong evidence to support the SSAb spectral model over either the FFAb or inFFAb, given a $K > 100$ is considered strong evidence. A higher frequency spectral break is more likely in each case, but there is low evidence for distinguishing between the spectral models: SSA, FFA or inFFA. This is likely due to the shifting peak frequency (shown in Figure 7 and discussed further in Section 6.3) and insufficient sampling below the spectral peak (since $\nu_p \leq 140\,\mathrm{MHz}$ in all epochs).

The other 14 sources were best fit with an inhomogeneous FFA spectral model

with a spectral break. For GLEAM J001513–472706 (Figure 1a), the Bayes factor for inFFAb compared to the second most likely model, inFFA, is 82. This also suggests there is not enough strong evidence to support the inFFAb model, however, the Bayes factor for either inhomogeneous FFA model compared to either the FFA or SSA models is ≫100. We therefore conclude that the spectrum of GLEAM J001513–472706 is best fit by an inhomogeneous FFA model but the presence of a exponential break is uncertain. This is likely due to the lack of higher frequency flux densities at 9 GHz in March 2020, which is roughly the frequency where we could expect a spectral break.

Lastly, we note GLEAM J021246–305454 (Figure 1d) has a Bayes factor of 5.7 when comparing the inFFAb model with the SSAb model (the second most likely spectral model). This is not decisive evidence, so we cannot confidently say the inFFAb spectral model is the most appropriate. Comparing the log likelihoods for each model presented in Table 3, there is strong evidence GLEAM J021246–305454 has an exponential spectral break. However, similar to GLEAM J024838–321336 (Figure 1f), there is low evidence to distinguish between the spectral models. Again, it is likely this is due to insufficient sampling below the spectral turnover ($\approx$150 MHz).

## 6  DISCUSSION

In this section, we will discuss the likely physical mechanisms for any observed variability. The majority of sources appear to show slow trends of increasing or decreasing flux density across the MWA band throughout 2020 with no significant variability detected with the ATCA.

In Section 6.1, we present the sources that are likely showing variability due to interstellar scintillation and discuss the implications of such a mechanism. We focus on individual sources that show uncommon variability; GLEAM J020507–

110922, GLEAM J024838–321336, GLEAM J015445–232950 and GLEAM J223933–451414 in Sections 6.2, 6.3, 6.4 and 6.5, respectively.

## 6.1    Interstellar Scintillation

The large spectral coverage of these observations samples the two different regimes of scattering: weak and strong. The electron column density along the line of sight and observing frequency determine which scattering regime is applicable (Narayan 1992; Walker 1998). The electron column density is largely related to the Galactic latitude. All our sources are far away from the Galactic plane, thus the transition frequency, $\nu_0$, from strong to weak scattering is $\sim 8\,\text{GHz}$ and the angular size limit at the transition frequency, $\theta_{F0}$, is $4\,\mu\text{as}$ (Walker 1998). Continuing under this assumption, all our calculations for ISS at $2.1\,\text{GHz}$, $5.5\,\text{GHz}$ and megahertz frequencies will be using the strong scattering regime, while the $9\,\text{GHz}$ calculations will be using the weak scattering regime. Furthermore, we eliminate the possibility of diffractive ISS in the strong regime, as the fractional bandwidth of variations is predicted to be $\sim 1.4 \times 10^{-5}$, but the smooth SED for all sources at frequencies $< 8\,\text{GHz}$, in each epoch suggests the fractional bandwidth is closer to unity.

### 6.1.1    Weak Scattering

First, we consider the modulation and timescales of variability due to weak scattering at $9\,\text{GHz}$ for a compact source. A compact source is defined as having angular size $\leq \theta_F$ where:

$$\theta_F = \theta_{F0}\sqrt{\frac{\nu_0}{\nu}}, \tag{8}$$

resulting in a timescale of scintillation according to:

$$t_{\text{compact}} \approx 2\sqrt{\frac{\nu_0}{\nu}}, \tag{9}$$

where $\theta_{F0}$ is the angular size limit of a source at an observation frequency, $\nu$ that equals the transition frequency, $\nu_0 \approx 8\,\text{GHz}$ at our Galactic latitude (Walker 1998).

Using Equation 9, for observations observed at frequency, $\nu$, of 9 GHz, the timescale of modulation due to ISS, $t_{\mathrm{compact}}$, would be of the order of 1.9 hours. Any observations over several hours would therefore average over the variability due to ISS. All our observations for ATCA were taken over observations blocks of $\sim 18$ hours, thus our measured flux densities average over any hourly variability. Thus, no significant variability would be detected in our observations at these short timescales.

To test this hypothesis, we analyse the ATCA Director's Time data collected hourly in October 2021, see Section 3.2. The October 2021 follow-up observations with the ATCA were taken using a different observing technique to the original 2020 monitoring. These observations consisted of multiple 10 minute scans separated by a couple of hours. Let us take GLEAM J001513–472705 as an example source for future calculations. In the October 2021 epoch, we observed GLEAM J001513–472705 twice with 10 minute scans separated by $\sim 1.5$ hours, which is slightly below the expected timescale of 1.9 hours. Figure 2 presents the light-curves of GLEAM J001513–472705 in October 2021 at 5 and 9 GHz. Flux density measurements were taken at 30 second intervals in $(u, v)$ space using the `uvmodelfit` module in CASA and the percentage offset is calculated from a median flux density value[9].

Within the 10 minute scans, there may be modulation (seen as rising in the first scan and then decreasing in the second) but it is likely this is sampling a small fraction of the longer-term (hourly) modulation. In the 2021 observations we see an overall modulation of $\approx 0.15$ at 9 GHz. We can calculate the expected modulation using:

$$m_{\mathrm{compact}} = \left(\frac{\nu_0}{\nu}\right)^{17/12}, \tag{10}$$

which suggests $m_{\mathrm{compact}} \approx 0.85$. It is worth noting, Equation 10 applies for a well sampled light-curve, since we only have poor time sampling, this calculated mod-

---

[9] In each case, our target dominates the visibilities ensuring such model fitting is appropriate.
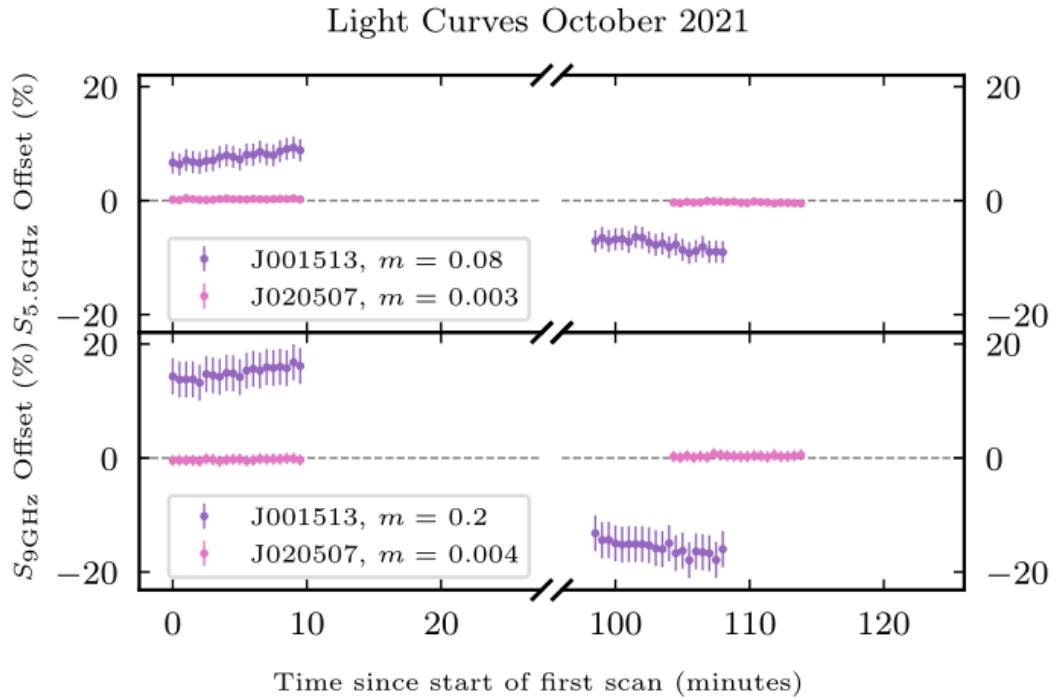
**Figure 2.** Light curves of flux density variance for GLEAM J001513–472705 (purple) and GLEAM J020507–110922 (pink) in October 2021 at 5 GHz (top) and 9 GHz (bottom). Flux densities were measured using the `uvmodelfit` function of CASA for 30 second time intervals. The fractional flux density percentage offset (or modulation, $m$) was calculated as the difference of each 30 second flux density measurement from the median flux density of the entire light curve for each source. The errors on the flux density are the local rms of the images for each source only, as any systematic errors do not influence the fractional flux density offset.

ulation has a large margin of error. The smaller measured modulation could be due to a number of factors: we are not sampling the entire timescale or modulation of variability, and/or the source is slightly resolved compared to the angular size limit, $\theta_{F0}$. The October 2021 observations only consisted of two 10 minute scans, hence it is likely that the modulation and timescale is not sampled sufficiently. Further observations of GLEAM J001513–472705 at 9 GHz with continued monitoring over timescales of hours to days would increase the likelihood of sampling the entire timescale of variability and converging on the modulation.

Alternatively, if GLEAM J001513–472705 has a compact component that is slightly resolved compared to the angular size of the scattering screen, the mod-

ulation decreases and timescale increases according to:

$$m_{\text{observed}} = m_{\text{compact}} \left( \frac{\theta_F}{\theta_S} \right)^{7/6}, \tag{11}$$

$$t_{\text{observed}} = t_{\text{compact}} \left( \frac{\theta_S}{\theta_F} \right), \tag{12}$$

where $\theta_F$ is defined by Equation 8 and is the angular scale of the scattering screen and $\theta_S$ is the angular size of the compact component (Walker 1998). If we have sampled the timescale and modulation sufficiently, GLEAM J001513–472705 must have a compact component $\approx 17\,\mu$as. This would correspond to a timescale of scintillation of roughly 8.5 hours. It is likely we overestimated the modulation and underestimated the timescale based on our poor sampling, as such, this compact component size estimate should be considered as a lower limit.

These caveats to the weak scattering are reasonable assumptions to explain the variability of GLEAM J001513–472705 measured at 9 GHz. This would imply that GLEAM J001513–472705 is an intra-day variable source with a compact feature on $\mu$as scales. Further monitoring at 9 GHz would be required to sample the modulation more thoroughly and estimate the timescales of ISS more accurately.

### 6.1.2   Strong Scattering

Let us now consider whether any variability at frequencies $< \nu_0$ are also consistent with interstellar scintillation but in the strong regime, in particular due to refractive interstellar scintillation (RISS). In the strong regime, we have:

$$\theta_r = \theta_{F0} \left( \frac{\nu_0}{\nu} \right)^{11/5}, \tag{13}$$

$$m_{\text{compact}} = \left( \frac{\nu}{\nu_0} \right)^{17/30}, m_{\text{observed}} = m_{\text{compact}} \left( \frac{\theta_r}{\theta_S} \right)^{7/6} \tag{14}$$

$$t_{\text{compact}} = 2 \left( \frac{\nu}{\nu_0} \right)^{11/5}, t_{\text{observed}} = t_{\text{compact}} \left( \frac{\theta_S}{\theta_r} \right) \tag{15}$$

following Walker (1998), where a compact source is defined as $\leq \theta_r$.

At 5 GHz, we would expect a modulation of $\sim$0.77 on timescales of $\sim$6 hours with a angular screen size, i.e. the angular size of a compact component, of $\sim$11.2 $\mu$as. Considering GLEAM J001513–472705 as an example again, we measure a modulation at 5 GHz of $\sim$0.086 across approximately two hours. Consistent with the results of the 9 GHz variability, this calculation suggests that the compact feature of GLEAM J001513–472705 is likely resolved compared to the scattering screen and/or we have not sampled the timescale and modulation sufficiently.

Furthermore, at 150 MHz, using Equation 15, the timescale of variability is expected to be 1.4 years with a modulation of 0.1 (using Equation 14) and a scattering screen angular size $\approx$ 25 mas (using Equation 13). Our observations during 2020 cover a timescale of six months with four epochs. Thus, we should be able to detect a small level of variability as a slow shift in flux density across the entire MWA band over the course of the observations. For GLEAM J001513–472705, we see a modulation of 0.1 over the 6 month monitoring period with a constant trend of the flux density increasing across the entire MWA band. Several other sources also display slow trends of increasing/decreasing flux density across the entire MWA band in the 2020 observations: GLEAM J021246–305454, GLEAM J032213–462646, GLEAM J032836–202138, GLEAM J033023–074052, GLEAM J042502–245129, GLEAM J044033–422918, GLEAM J044737–220335, GLEAM J224408–202719. Since the variability detected for GLEAM J001513–472705 at each frequency band is consistent with ISS, it is likely the sources that show a similar variability trend at MHz frequencies are also variable due to ISS. GLEAM J015445–232950 and GLEAM J020507–110922 also show trends of variations in the flux density across the MWA band. However, both also display a change in their spectral shape within the MWA band in later epochs. We discuss the variability of GLEAM J020507–110922 and GLEAM J015445–232950 further in Section 6.2 and Section 6.4 respectively.

It is worth noting, R21 suggest sources with a low MOSS value ($<$ 36.7) are likely variable due to refractive ISS. In agreement with R21, of our 15 tar-

gets, we find all sources with a low MOSS value to be exhibiting variability consistent with ISS apart from one source which shows no significant variability (GLEAM J022744–062106). Inversely, inspecting the MOSS value of the 9 sources we claim are exhibiting ISS, all bar one (GLEAM J033023–074052) have a low MOSS value consistent with ISS according to R21.

We would thus expect these sources to show intra-day variability at higher frequencies $> 1\,\mathrm{GHz}$. While it is uncommon for PS sources to have hot-spots or compact features in their morphologies (Keim et al. 2019), 9 of our 15 PS sources show variability entirely consistent with scintillation due to such a compact feature. High-resolution imaging would determine the presence of a compact feature on $\mu$as to mas scales.

## 6.2    GLEAM J020507–110922

Due to the unique and extreme nature of the variability exhibited by GLEAM J020507–110922, we discuss several plausible explanations: intrinsic variability due to SSA, ISS, and variations in the free-free opacity. A close-up of variability observed at megahertz-frequencies for GLEAM J020507–110922 is presented in Figure 3.

### 6.2.1    *Synchrotron Self Absorption*

Firstly, we assume that the mechanism for the turnover in GLEAM J020507–110922 is due to SSA. Any changes in flux density below or around the turnover would be due to changes in the synchrotron absorption. Using a synchrotron model, with $m_e$ and $e$ the electron mass and electron charge respectively, we have (in the observed frame of reference),

$$S_{\nu_p} = \left( \frac{\pi^3 m_e^3 \nu_p^5 \theta_S^4}{0.94 e B \sin(\theta)} \right)^{\frac{1}{2}}, \tag{16}$$

where $\theta_S$ is the angular source size, and the magnetic field, $B$, is at an angle $\theta$ to the line of sight (Tingay et al. 2015). Thus, changes in the peak frequency, $\nu_p$, would result in changes to the flux density at the peak frequency, $S_{\nu_p}, \propto \nu_p^{5/2}$.
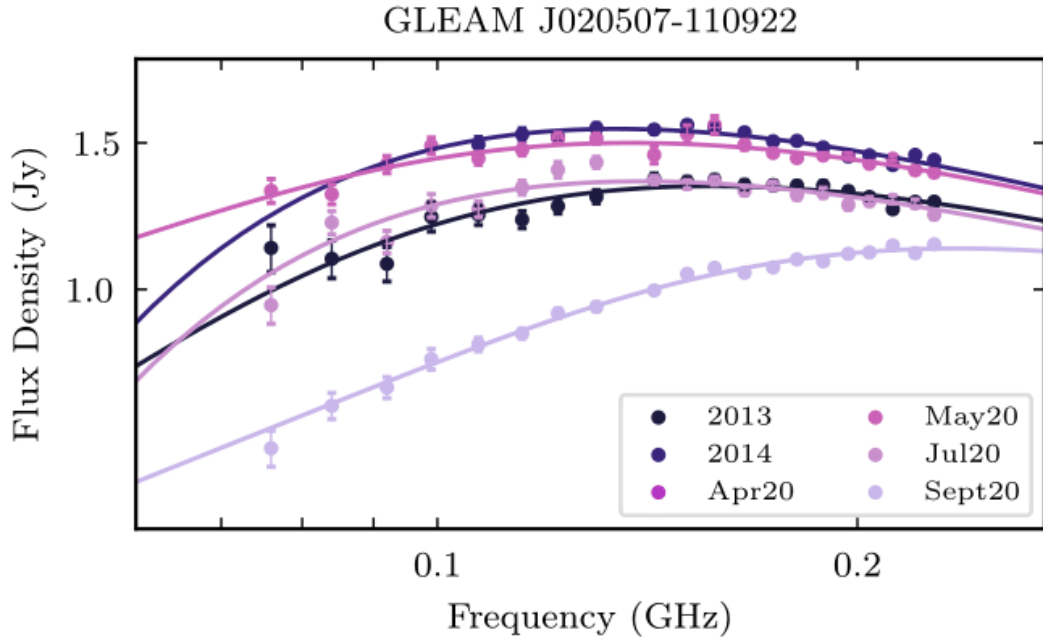
**Figure 3.** SED of only MWA flux densities for GLEAM J020507–110922. The spectral shape in September 2020 (lavender) is significantly different to all previous epochs.

Using the best model fit for each epoch, Figure 4 shows the change in $\nu_p$ with time. Therefore, assuming a constant $\theta_S$, $B$ and $\sin(\theta)$, the measured change in $\nu_p$ of 0.1 GHz would correspond to $S_{\nu_p}$ increasing by $\approx 4$ mJy. However, we detect a *decrease* in $S_{\nu_p}$ of $\approx 0.5$ Jy. Either the magnetic field would need to increase by several orders of magnitude, or the source size would need to contract significantly ($\sim 10\%$); both scenarios are physically improbable. Consequently, we can eliminate the possibility that the variability is due to variations of the synchrotron emission.

### 6.2.2  *Interstellar Scintillation*

Secondly, we consider the possibility of ISS following the same calculations described in Section 6.1. As the 9 GHz data is the only frequency in the weak regime, we start by examining these data. We do not detect any modulation at 9 GHz on timescales of months or years, however, as described in Section 6.1, we would
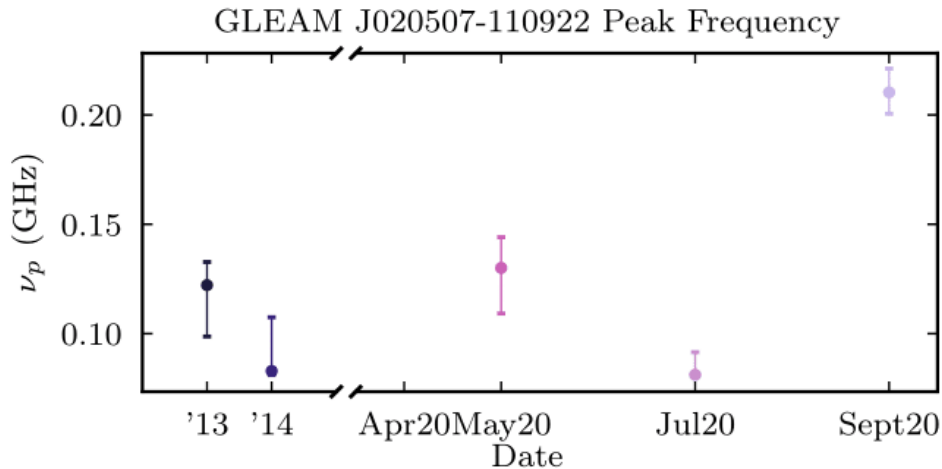
**Figure 4.** The measured peak frequency ($\nu_p$) from the fitted spectral model (inFFAb) of GLEAM J020507–110922 for each epoch. $\nu_p$ is consistent from 2013 to July 2020 and then significantly increases in September 2020.

expect weak scattering on the timescale of $\sim$1.9 hours for compact sources where $\theta_{\mathrm{src}} < \theta_{\mathrm{F}}$. The October 2021 observations of GLEAM J020507–110922 consisted of two 10 minute scans separated by $\sim$2 hours. Thus, we can expect any modulations we detect between the scans to be due to weak scattering. At 9 GHz, we measure a modulation of $\approx$ 0.0063, which is two orders of magnitude smaller than the expected modulation of 0.85 at 9 GHz. There is no variability detected by eye in the light curve for GLEAM J020507–110922 presented in Figure 2. Consequently, GLEAM J020507–110922 would have to be resolved compared to the scattering screen. If the variability observed at 9 GHz between the 10 minute scans is due to weak scattering, GLEAM J020507–110922 must have a compact component of the scale 0.3 mas. Furthermore, it would increase the timescale of observed variability to five days. While it is unlikely GLEAM J020507–110922 has a compact feature $< 1$ mas, we recommend monitoring over the course of several consecutive days at 9 GHz to confirm.

Next, we consider the variability in the strong regime at 5 GHz. We detect no significant variability by eye at 5 GHz in the October 2021 observations and calculate a modulation of only 0.0025 at 5 GHz between the 10 minute scans in

October 2021. Again, this significantly smaller modulation at 5 GHz could be explained by GLEAM J020507–110922 being slightly resolved compared to the refracting scintillating screen, but there is still a constraint on the compact component of ≤1.5 mas. This is perhaps not surprising, given most compact flat spectrum sources are typically at least partially resolved compared to the constraints of the scattering screen. The typical power-law spectrum of GLEAM J020507–110922 above the turnover suggests it is unlikely there is a compact component contributing a large fraction of the flux density at 5 GHz and 9 GHz that is smaller than 2 mas. Furthermore, this modulation is well within the $1\sigma$ flux density errors of GLEAM J020507–110922: thus, no significant modulation is detected between the 10-minute scans.

Continuing with considering the strong regime but now at 150 MHz, we find there is a noticeably different spectral shape in September 2020 compared to previous epochs, see Figure 3. Such a change in spectral shape would require small scale structures within the refracting screen creating a frequency dependence smaller than the bandwidth of the MWA. While it is not impossible, it is unlikely that such small scale structures only appeared between July and September 2020. The constant spectral shape until the September 2020 epoch suggests a different physical mechanism may have caused the observed variability between July and September 2020. We will therefore consider the variability of the other epochs and exclude September 2020 first.

At 150 MHz, the timescale of variability is expected to be $\sim 1.4$ years according to Equation 15. We see consistent variability between the epochs of observation on scales of months, suggesting that GLEAM J020507–110922 must be entirely compact compared to the refracting plasma at 150 MHz. As shown in Section 6.1, the scale of the scattering disc is $\approx 25$ mas at 150 MHz. It is possible GLEAM J020507–110922 has a compact component $\sim$25 mas in size that is dominating the flux density measured at 150 MHz; i.e. that the resolved lobes are contributing a small, almost negligible, portion of the flux density at MHz frequencies

or that GLEAM J020507–110922 is extremely compact. Therefore, the variability observed by the MWA is possibly due to RISS, provided GLEAM J020507–110922 is ∼25 mas. Furthermore, there would need to be small-scale structures ($< \theta_r = 25$ mas) in the scintillating screen inducing strong frequency dependence between July and September 2020. Such small structures in the plasma would be comparable to the scales of plasma required for an extreme scattering event (ESE). ESEs are rare events and high-quality dynamic radio spectra are required to characterise the features of the plasma causing such an event (Bannister et al. 2016; Tuntsov et al. 2016).

High resolution images using VLBI would be able to confirm or deny the presence of a scintillating compact feature. The high resolution images paired with continued monitoring at MHz frequencies (on timescales of ∼years) and GHz frequencies (on timescales of ∼days) would be able to determine the dominance of the compact feature and morphology at multiple frequencies.

### 6.2.3   *Variable Optical Depth*

Lastly, we consider the possibility that the variability is due to variations in the optical depth of an ionised plasma screen. If we assume all the variability seen at 100 MHz is due to variations in this optical depth, we can scale the variations up to 5 GHz and 9 GHz as the free-free opacity, $\tau_{\mathrm{ff}}$, scales according to $\nu^{-2.1}$ (Lang 2013). We see a flux density change at 100 MHz of 0.7 Jy, which would scale to variations of 0.2 mJy at 5 GHz and 0.05 mJy at 9 GHz. Both these are well within the measurement error on the flux density measurements of GLEAM J020507–110922 at 5 GHz and 9 GHz, suggesting inhomogeneities in the free-free absorbing media are consistent with the variability seen at all frequencies. Continuing under this assumption, we can calculate the opacity change, $\Delta\tau_{\mathrm{ff}}$, according to:

$$\Delta\tau_{\mathrm{ff}} = -\ln\left[1 - \frac{\Delta S}{S_0 e^{-\tau_{\mathrm{ff}}}}\right], \tag{17}$$

where $\Delta S$ is the change in flux density, and $S_0$ is the flux density of the compact region (Tingay et al. 2015). We calculate an upper limit on the opacity variation (by setting $\tau_{ff}$ to 0), using the median flux density at $100\,\text{MHz}$ of $1.2\,\text{Jy}$ as $S_0$, of $\Delta\tau_{ff} < 0.88$. This suggests a large density gradient within the free-free cloud. The optical depth due to FFA is proportional to the electron temperature and free electron density, thus changes in either would result in changes to the overall absorption (Bicknell et al. 1997). It is possible a region in the free-free absorbing cloud with a higher density of free electrons or a "clump" with a lower electron temperature moved into the line of sight between July 2020 and September 2020. As the optical depth is proportional to the emission measure, $EM$, and electron temperature, $T_e$ according to $EM \times T_e^{-1.35}$ (Mezger & Henderson 1967), we can calculate the ratio of the optical depth in September 2020 to July 2020. We find the $EM \times T_e^{-1.35}$ in September 2020 is $\sim 7.42$ times that of July 2020. This would explain the significant change in spectral shape from July to September 2020. It is also worth noting the September 2020 epoch is inconsistent with all spectral models except an inhomogeneous free-free absorbing model with an exponential break at higher frequencies, shown in Figure 5. The consistency with an inhomogeneous free-free absorbing model is consistent with the explanation of a denser or cooler region in the inhomogeneous surrounding cloud changing the optical depth at megahertz frequencies.

To summarise, the variability of GLEAM J020507–110922 is inconsistent with changes in the synchrotron emission and DISS. While it is possible to explain the majority of variability with ISS, it requires extreme constraints on the source size of $< 2\,\text{mas}$ above $5\,\text{GHz}$ and $< 25\,\text{mas}$ at $150\,\text{MHz}$ and small scale structures within the scattering screen. Changes in the optical depth can explain all of the variability seen at MHz frequencies and the insignificant variability seen in the GHz regime, as well as the change in spectral shape between July and September 2020. Furthermore, the spectral SED of GLEAM J020507–110922 in September 2020 is best described by an inhomogeneous free-free absorbing model,
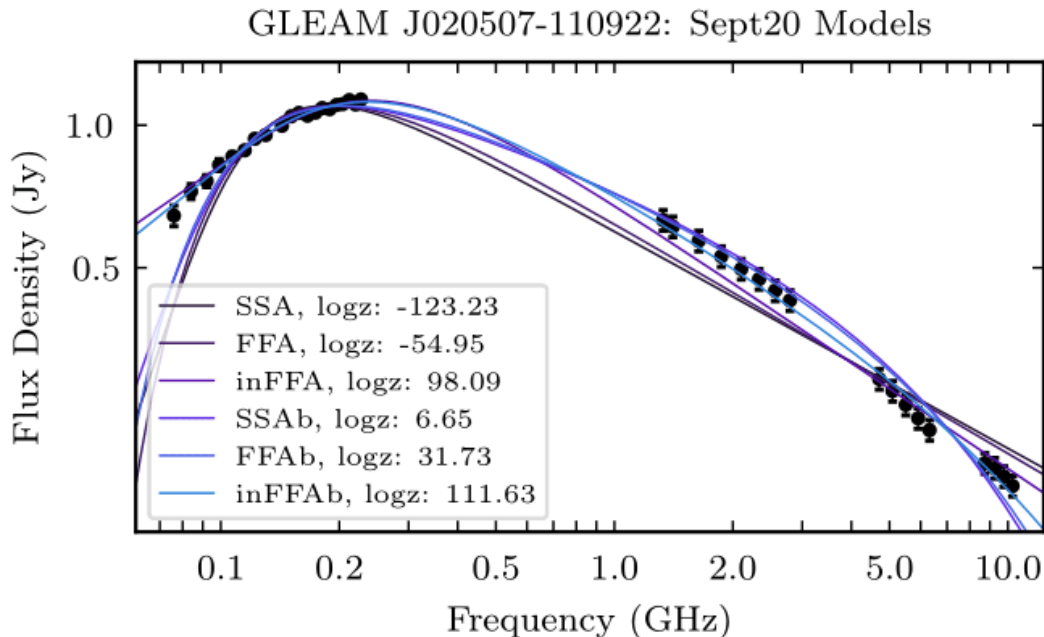
**Figure 5.** SED for GLEAM J020507–110922 using the MWA September 2020 epoch and the average ATCA flux densities used for spectral fitting. The models plotted are the six spectral models fitted to the September 2020 flux densities. The log likelihood of each spectral model is presented in the legend, a higher log likelihood suggests more evidence for the spectral model. All spectral models other than an inhomogenenous free-free absorption spectral model are inadequate at explaining the flux densities below the spectral turnover.

consistent with the variability being explained by inhomogeneities in the free-free absorbing media.

### 6.3   GLEAM J024838–321336

GLEAM J024838–321336 showed variability during the 2020 monitoring unlike any other source; the SED for just the MWA frequency range is presented in Figure 6. Most notable is the variability in the peak frequency, $\nu_p$, and flux density at the peak frequency, $S_{\nu_p}$. It appears $\nu_p$ shows a general trend of decreasing from 2013 right through to September 2020, shown in Figure 7. Additionally, $S_{\nu_p}$ increases until July 2020 and then is stable with the September 2020 SED. The odd behaviour of GLEAM J024838–321336 suggests a complex system or combination of mechanisms behind the variability.
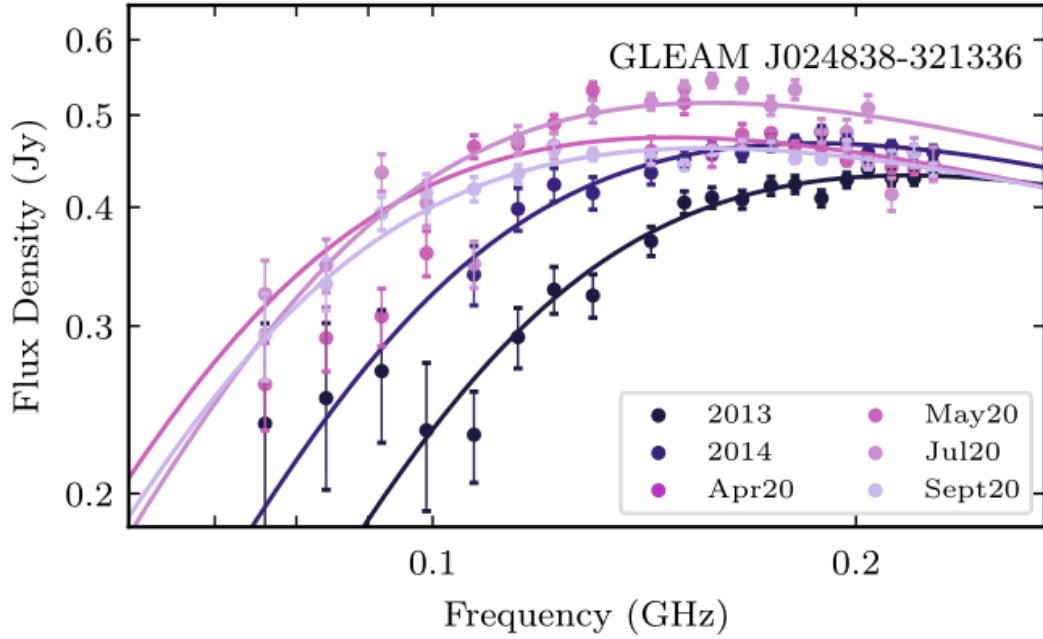
**Figure 6.** SED of only MWA flux densities for GLEAM J024838–321336. The similar spectral shape but shifting peak frequency to lower frequencies is consistent with an ejection cooling and adiabatically expanding as it travels across the jet.
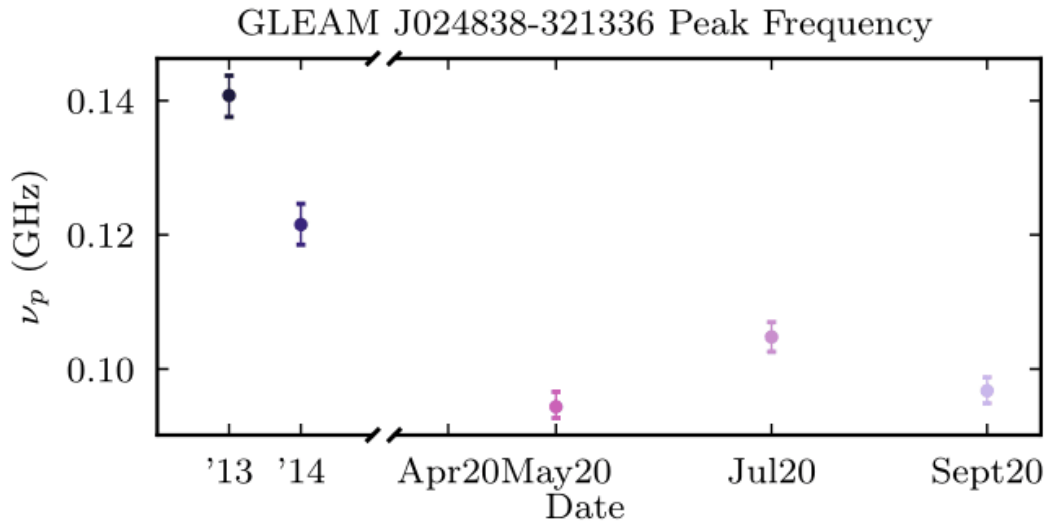


**Figure 7.** The measured peak frequency ($\nu_{\mathrm{p}}$) from the fitted spectral model of GLEAM J024838–321336 for each epoch. The decreasing $\nu_{\mathrm{p}}$ from 2013 to September 2020 is consistent with an ejecta from the core traversing the jet.

The first section of variability with an increasing $S_{\nu_p}$ and decreasing $\nu_p$ is consistent with an ejecta from the core cooling and expanding. Such an ejection would be emitting due to synchrotron radiation. Rearranging the equation for synchrotron emission, shown in Equation 16, we can relate the energy of the emitting particles to the rest-frame brightness temperature of the emission. Therefore, as the temperature of the ejecta, $T_B$ decreases so too does the peak frequency according to:

$$k_B T_B \approx m_e c^2 \left( \frac{2\pi m_e \nu_p}{0.47 e B \sin\theta} \right)^{1/2} , \tag{18}$$

where $k_B$ is the Boltzmann constant and $m_e$, $e$ and $B \sin\theta$ were defined earlier by Equation 16 (Tingay et al. 2015).

Such a region slowly expanding and cooling would also be compact enough for ISS to be a dominant feature of the detected variability. The SEDs in July 2020 and September 2020 are fairly constant in shape with a decrease in $S_{\nu_p}$; this behaviour is consistent with RISS, as discussed in Section 6.1. We suggest the variability of GLEAM J024838–321336 is due to both RISS and the cooling and expanding of a compact synchrotron-emitting region ejected from the core. Such a system would show a combination of increasing/decreasing flux density across the MWA band due to RISS with a slowly decreasing $\nu_p$.

We note observations of X-ray binary systems, which can be considered analogous to AGN but on smaller scales, have detected ejecta from the core at multiple frequencies (Fender et al. 2009; Tetarenko et al. 2019). Lower frequencies detect emission further along the jets, away from the core. Monitoring of X-ray binary flares shows a lag in flares at lower frequencies consistent with the ejecta travelling along the jet. If the variability of GLEAM J024838–321336 is partly due to an ejection from the core slowly cooling and expanding, it is possible archival observations at higher frequencies ($\geq 1\,\mathrm{GHz}$) prior to the initial 2013 observations may have detected the initial ejection event from the core. Furthermore, follow-

up high resolution imaging using VLBI would potentially be able to resolve such compact structures and test this interpretation.

### 6.4 GLEAM J015445–232950

Similar to GLEAM J020507–110922, GLEAM J015445–232950 shows two distinct forms of variability: a shift in flux density across the entire MWA spectra from 2013 to May 2020 (consistent with RISS), then an evolving spectral shape in July and September 2020. The SED of the MWA flux densities for GLEAM J015445–239250 are presented in Figure 8. Interestingly, the spectral shape of GLEAM J015445–232950 in July and September appears to flatten rather than steepen like GLEAM J020507–110922.

Following the same logic described in Section 6.2, we consider changes in the synchrotron emission first. Figure 9 presents the variation of $\nu_p$ with time showing that the value of $\nu_p$ increased in September 2020 whilst $S_{\nu_p}$ decreases. This would require a significant *decrease* in the size of the synchrotron emitting region, which is nonphysical. Furthermore, the changes in spectral shape would require improbably small-scale ($< 25\,\mathrm{mas}$) structures within the plasma for the variability to be due to scintillation.

Lastly, we consider variations in the optical depth, $\tau_{\mathrm{ff}}$. Using Equation 17, we calculate an upper limit for the opacity variation of 0.35 at 200 MHz. While less than the opacity variation calculated for GLEAM J020507–110922, $\tau_{\mathrm{ff}} < 0.35$ still suggests a significant gradient of varying optical depths in the absorbing ionized plasma. As noted in Section 4, $\tau_{\mathrm{ff}}$ is described by a power-law distribution with index $p$ and the spectral index in the optically thick regime $\alpha_{\mathrm{thick}}$, is proportional to $p$. A decrease in $\alpha_{\mathrm{thick}}$ is consistent with a decrease in $p$, or equivalently, a decrease in the optical depth. The spectral flattening of GLEAM J015445–232950 in July and September 2020 is consistent with a decrease in the optical depth suggesting GLEAM J015445–232950 is surrounded by an inhomogeneous free-free absorbing cloud. This is consistent with the results of spectral mod-
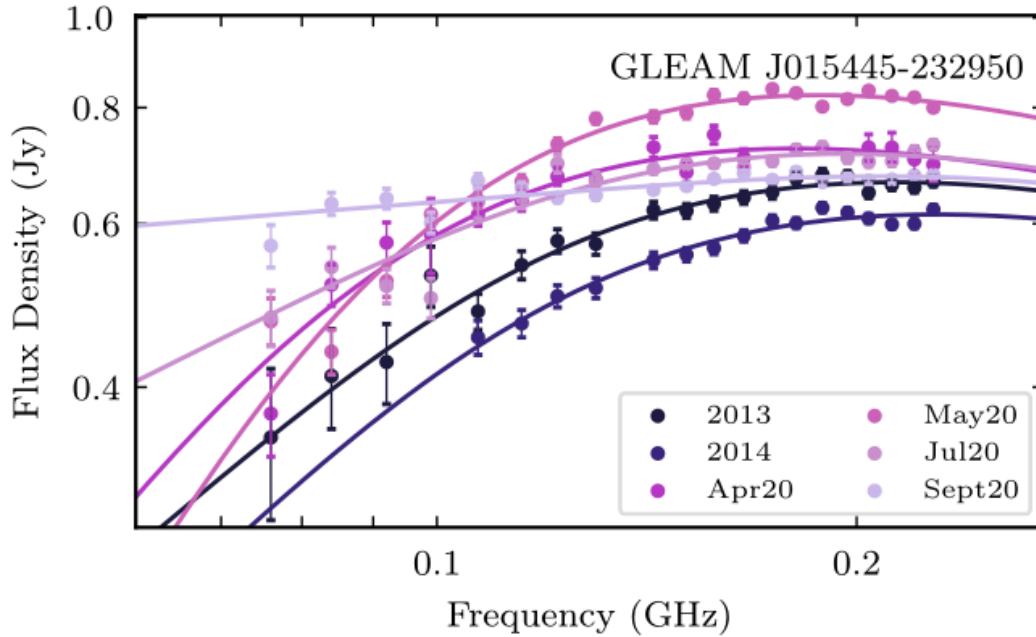
**Figure 8.** SED of only MWA flux densities for GLEAM J015445–232950. The constant spectral shape until May 2020 is consistent with interstellar scintillation. The changing spectral shape and spectral flattening in July and September 2020 is consistent with variations in the optical depth.

elling, where GLEAM J015445-232950 is best explained by an inhomogeneous FFA model in five of the six epochs of MWA observations. The overall variability of GLEAM J015445–232950 can therefore be explained by a combination of RISS and a varying optical depth.

## 6.5   GLEAM J223933–451414

GLEAM J223933–451414 showed variability consistent with sources discussed in Section 6.1, as presented in Figure 1n. The similar variability suggests it is varying due to RISS at MHz frequencies. However, there is also a notable steepening below the spectral turnover of  130 MHz, see Figure 10. Similar to GLEAM J020507–110922 and GLEAM J015445–232950, it is unlikely the variability below the turnover is due to synchrotron emission as the increased absorption would require decreases in the source size or an increase in the magnetic field. The larger modulation in the optically thick region suggests there are changes in the op-
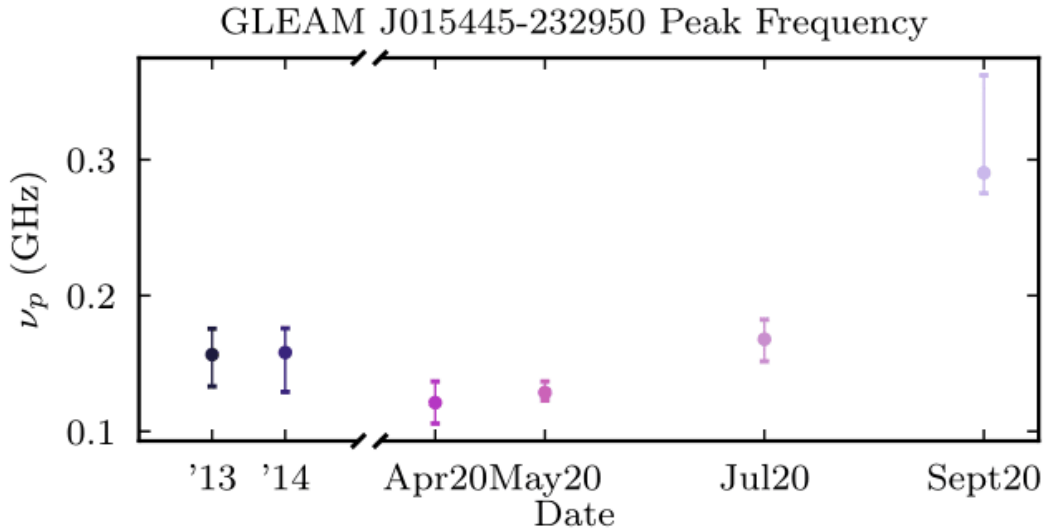
**Figure 9.** The measured peak frequency ($\nu_{\mathrm{p}}$) from the fitted spectral model of GLEAM J015445-232950 for each epoch. Similar to GLEAM J020507–110922, synchrotron emission can only explain the increasing $\nu_{\mathrm{p}}$, provided the source contract by $\leq 10\%$ (according to Equation 16).

tical depth of GLEAM J223933–451414 due to an free-free absorbing medium. Using Equation 17, we calculate a change in the free-free opacity of $\Delta\tau_{\mathrm{ff}} \lesssim 0.45$ within the 2020 observations at 70 MHz. Variability due to a changing free-free opacity suggests the physical mechanism producing the spectral turnover for GLEAM J223933–451414 is also due to free-free absorption. This interpretation is consistent with the spectral modelling. For each epoch, GLEAM J223933–451414 is best described by either a homogeneous or inhomogeneous free-free absorbing model with an exponential break.

We therefore suggest that the variability of GLEAM J223933–451414 is due to two physical mechanisms: RISS, which produced a slow decrease in flux density across the MWA band during 2020; and changes in the optical depth due to an inhomogeneous free-free absorbing cloud surrounding GLEAM J223933–451414. High resolution images on mas scales could search for the presence of a feature compact enough for variability due to ISS. Previous detections of dust surrounding AGN have been made via observations of absorption features in the
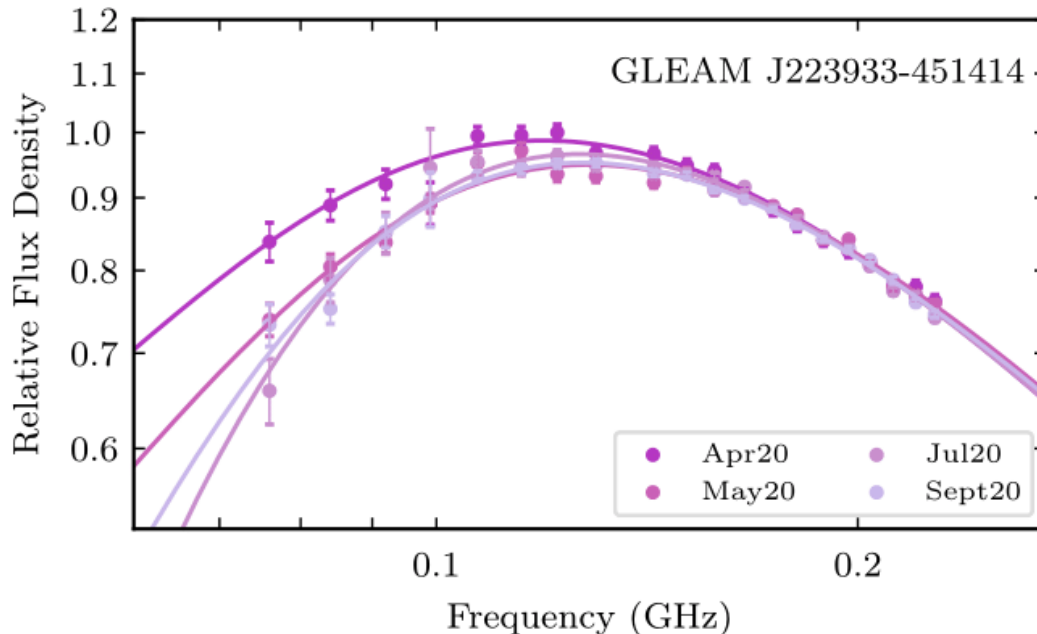
**Figure 10.** SED of only MWA flux densities and spectral models for GLEAM J223933–451414 in the 2020 epochs. May, July and September 2020 have had a constant factor added to the model and raw flux densities so each SED is similar in the optically thin region of the SED. The variability present below the spectral turnover despite the consistent flux densities in the optically-thin regime suggests some variability is due to changes in the absorption mechanism.

infrared spectra (Zhang 2021; Mason 2015). Testing for prominent HI gas and other absorption features would determine whether the variability is caused by variations in the optical depth. Furthermore, we recommend continued monitoring of GLEAM J223933–451414, particularly below the spectral turnover, to detect and characterise any variability in the absorption that could be attributed to variations in the optical depth.

## 7   CONCLUSIONS

R21 identified variable sources using two epochs of MWA observations separated by approximately one year. Subsequently, we have monitored 15 PS sources during 2020 with the MWA and the ATCA to search for and characterise spectral variability across $72\,\mathrm{MHz}$ – $10\,\mathrm{GHz}$. We found 13 of the 15 targets continued to

show variability at MHz frequencies. We detect no significant variability at GHz frequencies for any source on timescales of weeks to months.

We discussed the nature of ISS and the spectral variations it can produce. We determine it is unlikely to create changes in spectral shape, particularly on month long timescales at MHz frequencies unless there are small structures within the ISM on scales of ∼AU. We find nine sources show slow trends of either increasing or decreasing flux densities across the entire MWA bandwidth with a constant spectral shape. Slow variable trends at 150 MHz over the course of ∼1 year is consistent with a compact feature approximately 25 mas in size scintillating due to ISS. We therefore attribute this variability entirely to ISS. To confirm, we detect intra-day variability of GLEAM J001513–472706 at 5 and 9 GHz with the ATCA, also consistent with ISS. The short snapshot observations of targets in the 2020 monitoring meant there was insufficient sampling for searching for hourly variability in these epochs.

We discuss GLEAM J020507–110922 in detail due to the sudden change in spectral shape in September 2020 and the increase in peak frequency by ∼100 MHz. We consider variability due to changes in the synchrotron emission/absorption, ISS, an ESE and variations in the optical depth. We determine two likely origins for the variability of GLEAM J020507–110922: ISS and changes in the optical depth. The variability of GLEAM J020507–110922 prior to September 2020 is consistent with ISS, however the change in spectral shape from July to September suggests either small structures within the scintillating screen comparable to the structures that would produce an ESE. The lack of intra-day variability at 5 and 9 GHz and the increase in peak frequency supports the conclusion of a second origin of variability. The change in spectral shape of GLEAM J020507–110922 from July to September 2020 is consistent with a varying optical depth due to an inhomogeneous free-free absorbing cloud, where a 'clump' of either higher electron density or cooler electron temperature has moved into the line of sight. We conclude the origins of spectral variability for GLEAM J020507–110922

are due to both ISS and an inhomogeneous ionized cloud surrounding the source. We combine the evidence of the most likely spectral model, an inhomogeneous FFA model with an exponential break, with the origins of spectral variability to determine the cause of the spectral turnover as an inhomogeneous FFA model.

We find GLEAM J015445-232950 and GLEAM J223933–451414 show similar variability to GLEAM J020507–110922. GLEAM J015445–232950 shows variability consistent with ISS until July 2020 then a flattening of the spectral shape below the spectral turnover in July and September 2020. As with GLEAM J020507–110922, we conclude the origins of the spectral variability is most likely due to a combination of ISS and variations in the optical depth from an inhomogeneous free-free absorbing cloud. However, as the absorption decreases, it is likely either a 'clump' of hotter temperature electrons with a lower electron density has moved into the line of sight. Similarly, GLEAM J223933–451414 shows a constant spectral shape above the turnover frequency but a steepening below the spectral turnover. We conclude, both GLEAM J015445–232950 and GLEAM J223933–4511414 are best explained by an inhomogeneous FFA spectral model with an exponential break based on their spectral fitting and spectral variability.

We investigate the variable peak frequency of GLEAM J024838–321336. The decreasing peak frequency is consistent with a cooling ejecta travelling along the jet, which is also compact enough to scintillate due to ISS. Due to the likely origins of the spectral variability and the spectral fitting finding an SSA model as the most likely, we determine the most likely explanation for the absorption of GLEAM J024838–321336 is due to synchrotron self absorption.

The results of this variability study show the large spectral coverage, particularly at MHz frequencies, is key to determining the origins of the variability. Furthermore, PS sources continue to be a rich source of variability, particularly showing distinct forms of variability in the optically thick and thin regimes. We show that combining spectral modelling with spectral variability is a novel and powerful tool to determine the likely cause of absorption of PS sources. We rec-

ommend future observations of spectral variability of PS sources, particularly in the optically thick regime, to determine the absorption mechanism.

In the SKA era, as large-scale surveys become feasible, it is crucial we design surveys with large spectral and temporal coverage in order to adequately sample spectral variability. In particular, we should design surveys with cadences that probe timescales relating to specific types of variability paired with complementary spectral coverage. In particular, for scintillation monitoring on six monthly to yearly cadences at megahertz frequencies compared to hour to day cadences at gigahertz frequencies. Likewise, monitoring on monthly cadences at megahertz frequencies for variability due to free-free absorption. This paper highlights the value of low (MHz) frequency spectral coverage over month-year-decade long timescales with high (GHz) frequency observations on minutes-hours-days (ideally simultaneously) in distinguishing the origins of variability.

and Australian Governments. This research made use of NASA's Astrophysics Data System, the VizieR catalog access tool, CDS, Strasbourg, France. We also make use of the IPython package (Pérez & Granger 2007); SciPy (Virtanen et al. 2020); Matplotlib, a Python library for publication quality graphics (Hunter 2007); Astropy, a community-developed core Python package for astronomy (Astropy Collaboration et al. 2013; Price-Whelan et al. 2018); pandas, a data analysis and manipulation Python module (pandas development team 2020; Wes McKinney 2010); and NumPy (van der Walt et al. 2011). We also made extensive use of the visualisation and analysis packages DS9[10] and Topcat (Taylor 2005). This work was compiled in the useful online LATEX editor Overleaf.

## DATA AVAILABILITY

The raw data underlying this article are available in the ATCA Online Archive (ATOA) for project code C3333 and the MWA All-Sky Virtual Observatory (ASVO) for project code G0067. Derived and processed data products, including fits images and measured flux densities, are available upon request.

## REFERENCES

Astropy Collaboration et al., 2013, A&A, 558, A33
Bannister K. W., Stevens J., Tuntsov A. V., Walker M. A., Johnston S., Reynolds C., Bignall H., 2016, Science, 351, 354
Bell M. E., et al., 2019, MNRAS, 482, 2484
Bertin E., Mellier Y., Radovich M., Missonnier G., Didelon P., Morin B., 2002, in Bohlender D. A., Durand D., Handley T. H., eds, Astronomical Society of the Pacific Conference Series Vol. 281, Astronomical Data Analysis Software and Systems XI. p. 228
Bicknell G. V., Dopita M. A., O'Dea C. P. O., 1997, ApJ, 485, 112
Bicknell G. V., Mukherjee D., Wagner A. Y., Sutherland R. S., Nesvadba N. P. H., 2018, MNRAS, 475, 3493
Buchner J., 2016, Statistics and Computing, 26, 383
Buchner J., 2017, arXiv e-prints, p. arXiv:1707.04476
Buchner J., 2021, The Journal of Open Source Software, 6, 3001
Callingham J. R., et al., 2015, ApJ, 809, 168

[10] http://ds9.si.edu/site/Home.html

Callingham J. R., et al., 2017, The Astrophysical Journal, 836, 174

Chhetri R., Morgan J., Ekers R. D., Macquart J. P., Sadler E. M., Giroletti M., Callingham J. R., Tingay S. J., 2018, MNRAS, 474, 4937

Condon J. J., Cotton W. D., Greisen E. W., Yin Q. F., Perley R. A., Taylor G. B., Broderick J. J., 1998, AJ, 115, 1693

Duchesne S. W., Johnston-Hollitt M., Zhu Z., Wayth R. B., Line J. L. B., 2020, Publ. Astron. Soc. Australia, 37, e037

Duchesne S. W., Johnston-Hollitt M., Bartalucci I., 2021, Publ. Astron. Soc. Australia, 38, e053

Fanti R., Ficarra A., Mantovani F., Padrielli L., Weiler K., 1979, A&AS, 36, 359

Fender R. P., Homan J., Belloni T. M., 2009, MNRAS, 396, 1370

Franzen T. M. O., Hurley-Walker N., White S. V., Hancock P. J., Seymour N., Kapińska A. D., Staveley-Smith L., Wayth R. B., 2021, Publ. Astron. Soc. Australia, 38, e014

Hale C. L., et al., 2021, Publ. Astron. Soc. Australia, 38, e058

Hancock P. J., Murphy T., Gaensler B. M., Hopkins A., Curran J. R., 2012, MNRAS, 422, 1812

Hancock P. J., Trott C. M., Hurley-Walker N., 2018, Publ. Astron. Soc. Australia, 35, e011

Hancock P., Charlton E., Maquart J., Hurley-Walker N., 2019, arXiv preprint arXiv:1907.08395

Hovatta T., Nieppola E., Tornikoski M., Valtaoja E., Aller M. F., Aller H. D., 2008, A&A, 485, 51

Hunstead R. W., 1972, Astrophys. Lett., 12, 193

Hunter J. D., 2007, Computing in Science & Engineering, 9, 90

Hurley-Walker N., 2017, arXiv e-prints, p. arXiv:1703.06635

Hurley-Walker N., Hancock P. J., 2018, Astronomy and Computing, 25, 94

Hurley-Walker N., et al., 2017, MNRAS, 464, 1146

Intema, H. T. Jagannathan, P. Mooley, K. P. Frail, D. A. 2017, A&A, 598, A78

Jaiswal S., An T., Wang A., Tingay S., 2021, MNRAS, 509, 2122

Jamil O., Fender R. P., Kaiser C. R., 2010, Monthly Notices of the Royal Astronomical Society, 401, 394–404

Kardashev N. S., 1962, Soviet Ast., 6, 317

Keim M. A., Callingham J. R., Röttgering H. J. A., 2019, A&A, 628, A56

Kellermann K. I., 1966, ApJ, 146, 621

Koay J. Y., et al., 2018, MNRAS, 474, 4396

Kudryavtseva N. A., et al., 2011, A&A, 526, A51

Lane W. M., Cotton W. D., van Velzen S., Clarke T. E., Kassim N. E., Helmboldt J. F., Lazio T. J. W., Cohen A. S., 2014, MNRAS, 440, 327

Lang K. R., 2013, Astrophysical Formulae: Space, time, matter and cosmology. Springer

Large M. I., Mills B. Y., Little A. G., Crawford D. F., Sutton J. M., 1981, MNRAS, 194, 693

Large M. I., Cram L. E., Burgess A. M., 1991, The Observatory, 111, 72

Lovell J. E. J., et al., 2008, ApJ, 689, 108

Mason R. E., 2015, Planet. Space Sci., 116, 97

Mauch T., Murphy T., Buttery H. J., Curran J., Hunstead R. W., Piestrzynski B., Robertson J. G., Sadler E. M., 2003, MNRAS, 342, 1117

McMullin J. P., Waters B., Schiebel D., Young W., Golap K., 2007, in Shaw R. A., Hill F., Bell D. J., eds, Astronomical Society of the Pacific Conference Series Vol. 376, Astronomical Data Analysis Software and Systems XVI. p. 127

Mezger P. G., Henderson A. P., 1967, ApJ, 147, 471

Murphy T., et al., 2010, MNRAS, 402, 2403

Narayan R., 1992, Philosophical Transactions of the Royal Society of London Series A, 341, 151

Nyland K., et al., 2020, ApJ, 905, 74

O'Dea C. P., Baum S. A., 1997, AJ, 113, 148

O'Dea C. P., Saikia D. J., 2021, A&ARv, 29, 3

Offringa A. R., et al., 2014, MNRAS, 444, 606

Owsianik I., Conway J. E., 1998, A&A, 337, 69

Patil P., et al., 2020, ApJ, 896, 18

Pérez F., Granger B. E., 2007, Computing in Science and Engineering, 9, 21

Price-Whelan A. M., et al., 2018, AJ, 156, 123

Reynolds J., 1994, Technical report, A revised flux scale for the AT Compact Array. AT Memo 39.3/040

Rickett B. J., 1986, ApJ, 307, 564

Ross K., et al., 2021, MNRAS, 501, 6139

Sault R. J., Teuben P. J., Wright M. C. H., 1995, in Shaw R. A., Payne H. E., Hayes J. J. E., eds, Astronomical Society of the Pacific Conference Series Vol. 77, Astronomical Data Analysis Software and Systems IV. p. 433 (arXiv:astro-ph/0612759)

Taylor M. B., 2005, TOPCAT &amp; STIL: Starlink Table/VOTable Processing Software. p. 29

Taylor G. B., Readhead A. C. S., Pearson T. J., 1996, ApJ, 463, 95

Tetarenko A. J., Casella P., Miller-Jones J. C. A., Sivakoff G. R., Tetarenko B. E., Maccarone T. J., Gandhi P., Eikenberry S., 2019, Monthly Notices of the Royal Astronomical Society, 484, 2987

Tingay S. J., de Kool M., 2003, AJ, 126, 723

Tingay S. J., et al., 2013, Publ. Astron. Soc. Australia, 30, e007

Tingay S. J., et al., 2015, The Astronomical Journal, 149, 74

Torniainen I., Tornikoski M., Teräsranta H., Aller M. F., Aller H. D., 2005, A&A, 435, 839

Tuntsov A. V., Walker M. A., Koopmans L. V. E., Bannister K. W., Stevens J., Johnston S., Reynolds C., Bignall H. E., 2016, ApJ, 817, 176

Virtanen P., et al., 2020, Nature Methods, 17, 261

Walker M. A., 1998, MNRAS, 294, 307

Wayth R., et al., 2015, Publications of the Astronomical Society of Australia, 32

Wayth R. B., et al., 2018, Publ. Astron. Soc. Australia, 35, e033

Wes McKinney 2010, in Stéfan van der Walt Jarrod Millman eds, Proceedings of the 9th Python in Science Conference. pp 56 – 61, doi:10.25080/Majora-92bf1922-00a

Wilson W. E., et al., 2011, MNRAS, 416, 832

Wołowska A., Kunert-Bajraszewska M., Mooley K., Hallinan G., 2017, Frontiers in Astronomy and Space Sciences, 4, 38

Wołowska A., et al., 2021, Astronomische Nachrichten, 342, 1212

Zhang X.-G., 2021, MNRAS, 502, 2508

pandas development team T., 2020, pandas-dev/pandas: Pandas, doi:10.5281/zenodo.3509134, https://doi.org/10.5281/zenodo.3509134

van Breugel W., Miley G., Heckman T., 1984, AJ, 89, 5

van der Walt S., Colbert S. C., Varoquaux G., 2011, Computing in Science Engineering, 13, 22

# APPENDIX A: SUPPLEMENTARY SPECTRAL ENERGY DISTRIBUTIONS (SEDS)

The SEDs for the 15 sources nearby ($\leq 1$ degree) the targets of interest can be found in the supplementary online materials. Nearby sources were used to confirm that the variability observed was unique to the source and not due to the data processing. Several nearby sources were inspected and these 15 nearby sources are included as examples. Uncertainties are calculated from the flux density uncertainties estimated from the Background And Noise Estimation Tool (BANE) plus a 2% flux density error added in quadrature. The 2% flux density measurement error was used to account for the systematic and random noise of the images across the MWA band and is the internal uncertainty on the GLEAM flux density measurements.

This paper has been typeset from a TEX/LATEX file prepared by the author.

# Chapter 4

# Milliarcsecond Structures in Variable Peaked-Spectrum Sources

*The contents of this Chapter have been accepted as "Milliarcsecond Structures of Variable Peaked-Spectrum Sources" in Publications of the Astronomical Society of Australia (PASA). The accepted version of this paper is presented in Appendix C.*

## 4.1 Context

Imaging of PS sources using VLBI to obtain the small scale (mas) structures and morphology has traditionally been used to differentiate between young and frustrated sources. PS sources with extremely asymmetrical mas structures are considered likely amorphous due to large interactions with their surrounding environment, compared with a fairly symmetrical morphology associated with young AGN with minor asymmetries likely coming from orientation effects. Relying on a purely visual inspection of VLBI images without detailed spectral analysis to distinguish between young or frustrated sources has several limitations. It can result in a population of PS sources that are misclassified as many young sources

165

may appear frustrated and vice versa. Consequently, populations of PS sources may be a combination of temporarily peaked sources, young AGN and frustrated AGN, limiting the reliability of population studies for any of these individual populations.

In Chapter 2 and Chapter 3, we present blind and targeted spectral variability surveys as a new methodology to differentiate between these sub-populations of PS sources. Most importantly, we identify sources that show a changing spectral shape suggesting they are only temporarily classified as PS sources and thus are unlikely to be either young or frustrated sources, but instead blazars. If confirmed, it suggests any sources showing a changing spectral shape in our initial blind search should be excluded from any population studies of PS sources. Furthermore, we used spectral variability to infer the small scale morphology of several PS sources, in particular, we identify MRC 0225–065 (PKS J0227-0621, GLEAM J022744–062106) as likely having a partially resolved structure on mas scales, but do not identify any variability that would suggest it has a variable optical depth consistent with FFA. If confirmed, spectral variability thus has the potential to identify AGN that are only temporarily peaked or frustrated and to infer the compact morphology from already planned and existing surveys, without the need for observationally expensive targeted VLBI imaging. This Chapter seeks to confirm the predictions of small scale morphology from the previous spectral variability surveys using LBA observations. If confirmed, future spectral variability surveys can potentially be used to produce a reliable and large population of young AGN, as well as frustrated AGN for investigations of these individual sources.

## 4.2  Target Selection

Targets were selected for LBA imaging with the goal of comparing direct imaging of milliarcsecond structures with predicted morphologies based on their variability. Three targets were selected for based on the previous variability detected

in Ross et al. (2021, 2022). MRC 0225–065 (GLEAM J022744-062106) was initially identified as showing variability in Ross et al. (2021) but further monitoring over a year found no evidence of variability (Ross et al., 2022). As such, it was predicted MRC 0225–065 would have resolved structures on milliarcsecond scales with a compact feature $\lesssim 25\,\text{mas}$, resulting in variability from RISS on a longer timescale with a dampened modulation index due to the extended structure. Conversely, PMN J0322–4820 (GLEAM J032237–482010) was selected due to the variable spectral shape identified in Ross et al. (2021). To explain the variable spectral shape, Ross et al. (2021) concluded PMN J0322–4820 was likely a blazar caught flaring in 2014. As such, it was predicted to show a compact morphology even on milliarcsecond scales. Finally, MRC 2236-454 (GLEAM J223933–451414) was identified as the only PS source in Ross et al. (2021) that showed significant variability but maintained a constant peak frequency below $231\,\text{MHz}$. A low peak frequency is typically associated with PS sources that are of the order of tens of kilo-parsecs across, but the RISS detected in Ross et al. (2022) suggested MRC 2236-454 is dominated by a compact feature, and showed variability due to a surrounding inhomogeneous environment. As such, it was predicted MRC 2236-454 may be resolved on milliarcsecond scales and show an asymmetrical morphology, often associated with frustrated sources in an inhomogeneous surrounding environment (Orienti et al., 2006).

## 4.3 LBA Observations and Data Reduction

### 4.3.1 Observations

LBA observations were taken on November 23, 2020 and February 17, 2021 as part of project V600. The November observation was centered at $2.4\,\text{GHz}$ and the February observation was centered at $8.3\,\text{GHz}$ and both utilised $128\,\text{MHz}$ of bandwidth in dual polarizations. Stations used in each observation and their diameter is listed in Table 4.1. Both observations cycled through phase calibra-

tor scans and target scans of lengths 2 min and 5 min, respectively. However, the spatial separation of each target and their respective phase calibrator meant each target had a different number of scans. A summary of the targets, phase calibrators and number of scans each is presented in Table 4.2.

Parkes at 2.4 GHz, and Katherine at both frequencies, observed using their native linear feeds. These were converted to a circular polarization basis post-correlation using the PolConvert software (Martí-Vidal et al., 2016)

| Name | Code | Diameter (m) | Nov20 | Feb21 |
|---|---|---|---|---|
| ATCA, phased up | At | 5×22 | Y | Y |
| Mopra | Mp | 22 | Y | Y |
| Parkes | Pa | 64 | Y | Y |
| Hobart | Ho | 26 | Y | Y |
| Ceduna | Cd | 30 | Y | Y |
| Yarragadee | Yg | 12 | Y | Y |
| Warkworth | Ww | 12 | Y | Y |
| Hartebeesthoek | Hh | 26 | Y | Y |
| Katherine | Ke | 12 | Y | Y |
| Tidbinbilla | Td | 34 | Y | N |

Table 4.1: LBA stations included in observations

| Name | Calibrator | Number of scans |
|---|---|---|
| MRC 0225–065 | PKS J0217+0144 | 27 |
| PMN J0322–4820 | PMN J0335-4837 | 40 |
| MRC 2236–454 | QSO B2227–445 | 48 |

Table 4.2: Targets, associated calibrators and number of LBA scans for each target source.

### 4.3.2 Data Processing and Calibration

After correlation, data calibration and processing were done using the NRAO's Astronomical Imaging Processing System (AIPS) (Wells, 1985). The calibration and flagging followed the general procedure outlined in the AIPS cookbook[1] and was implemented in a semi-automated script with the ParselTongue interface

---

[1]The AIPS cookbook can be found here http://www.aips.nrao.edu/cook.html

(Kettenis et al., 2006). Initial flagging of edge channels and RFI was done using UVFLG. Auto-correlations were scaled to unity across the band using ACCOR before removing gross residual instrumental delays using FRING on a short scan of a bright calibrator. Complex bandpass corrections were derived using BPASS. The system temperature and gain calibration were applied using APCAL. Delay, rate and phase calibrations were determined from fringe fitting using FRING from each target's respective phase calibrator. A phase referenced image was created for all targets except for MRC 0225–065, as a first pass detection of the targets to determine if a phase shift was needed. Lastly, UVFIX was used to apply a phase shift to the data for any sources that were ∼arcsecond away from the phase centre used in correlation. MRC 0225–065 had accurate VLBI coordinates and thus did not require a phase shift. The calibrated and phase shifted data were exported to be imaged using CASA.

### 4.3.3   Imaging and Self-Calibration

Initial Stokes-I images were made with a quasi-natural weighting with robust parameter set to +1 (Briggs, 1995) using the `tclean` function in CASA (McMullin et al., 2007). Clean boxes were used but were tightly restricted for the models used for self-calibration to avoid inducing artificial structure from the complex point-spread-function. For each image, phase only self calibration was performed and applied using the `gaincal` and `applycal` functions respectively. Due to the sparse $(u, v)$-coverage and low signal-to-noise (SNR), calibration solutions were inspected and applied without flagging solutions that had insufficient SNR. The slow rate of improvement necessitated several (∼9) rounds of self-calibration. The SNR of the main component and the root-mean-squared (rms) noise of the image were inspected after each self calibration iteration to ensure each round improved the overall image quality. For each source the initial model assumed for the self-calibration was an unresolved point source to avoid inducing any morphological features. Any resolved components were included in subsequent rounds of imaging

clean components and kept in the model for self-calibration if this reduced the rms noise of the image. The initial solution interval for the self calibration was set to the scan length and decreased in further rounds of self calibration. Phase only self calibration rounds were continued until the rms noise of the image increased. A final round of both phase and amplitude self calibration was then performed (provided it reduced the rms of the final image) with the solution interval set to the scan length. For MRC 0225–065, an amplitude self-calibration was applied to both frequencies, but no amplitude self-calibration was applied to the 2.4 GHz image of PMN J0322–4820.

## 4.4    Results

Images of MRC 0225–065 at both 2.4 and 8.3 GHz are presented in Figure 4.3, and an image of PMN J0322–4820 at 2.4 GHz, presented in Figure 4.6a. Unfortunately, due to large phase errors from a pointing offset, we were unable to recover images for MRC 2236–454 at either frequency, or for PMN J0322–4820 at 8.3 GHz, this was because the source positions were beyond the observed correlated field of view for recovery in each case. For MRC 2236–454, the pointing offset was over 11 arcseconds for both the 2.4 GHz and 8.3 GHz observations, thus the phase errors from this pointing offset was beyond recovery. PMN J0322–4820 also had a pointing offset of $\approx 11.5$ arcseconds, however, given it was bright ($\sim 0.2$ Jy), there was sufficient sensitivity using a subset of antennas (flagging the Harte-beesthoek antenna), and a phase shift combined with self calibration to recover and image at 2.4 GHz. However, this method was not possible at 8.3 GHz due to the smaller field-of-view and decreased sensitivity. Henceforth, we will only discuss the results for MRC 0225–065 and PMN J0322–4820.

170
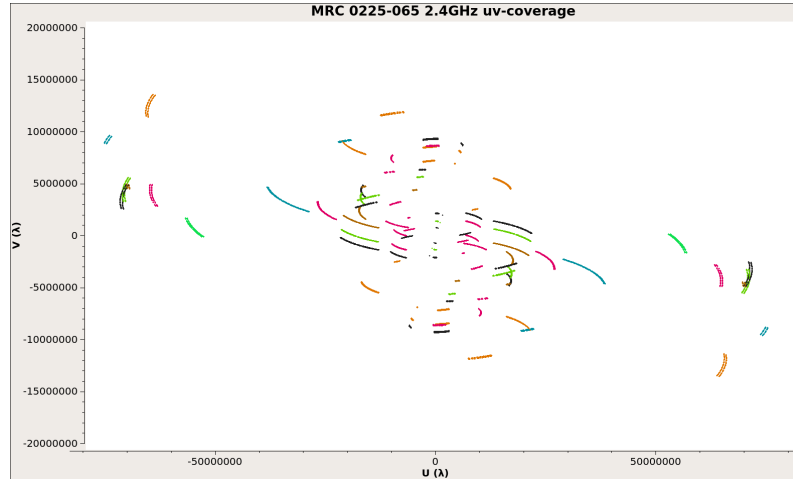
(a)
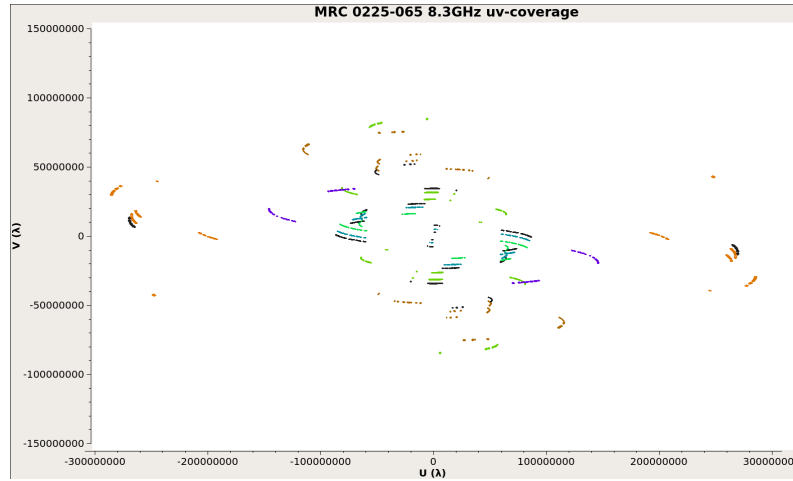


(b)

Figure 4.1: $(u, v)$-coverage for MRC 0225–065 at a) 2.4 GHz and b) 8.3 GHz from the LBA observations. Colours are based on antennas. $u$ and $v$ are in units of wavelengths ($\lambda$). Figures produced using CASA.

| Source, Frequency (GHz) | rms (mJy/beam) | $\theta_{\text{beam,maj}}$ (mas) | $\theta_{\text{beam,min}}$ (mas) | PA (deg) |
|---|---|---|---|---|
| MRC 0225–065, 2.4 | 2.7 | 9.5 | 3.2 | 7.0 |
| MRC 0225–065, 8.3 | 1.2 | 3.3 | 1.6 | 14 |
| PMN J0322–4820, 2.4 | 1.0 | 30 | 17 | -54 |

Table 4.3: Properties for each LBA image. Synthesised beam size and rms noise.
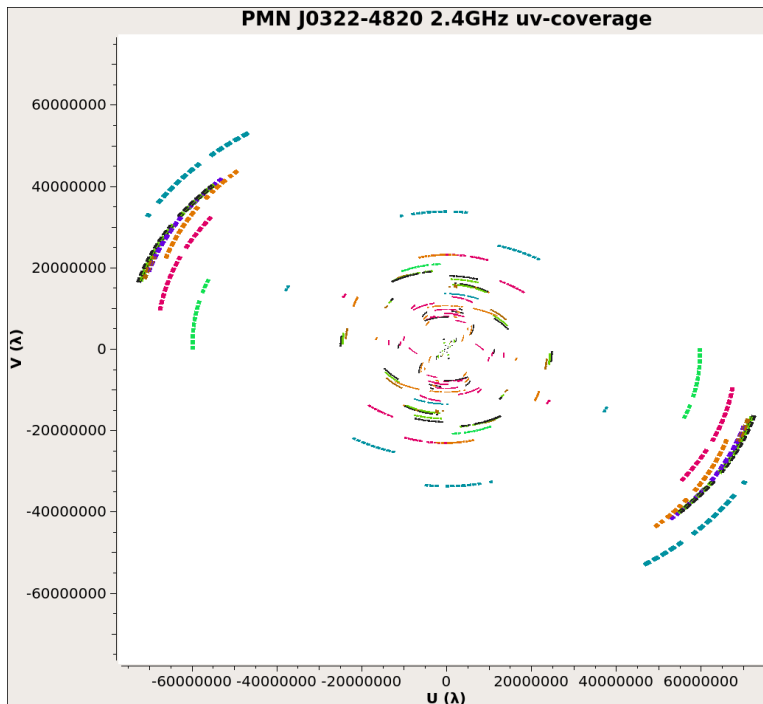
Figure 4.2: $(u, v)$-coverage for PMN J0322–4820 at 2.4 GHz from the LBA observations. Colours are based on antennas. $u$ and $v$ are in units of wavelengths ($\lambda$). Figure produced using CASA.

### 4.4.1 MRC 0225–065

MRC 0225–065 was resolved into three components morphology at both 2.4 GHz and 8.3 GHz, as shown in Figure 4.3. The final image was made with a robust parameter of -1 at 2.4 GHz and -0.5 at 8.3 GHz (Briggs, 1995). MRC 0225–065 is resolved into 3 regions: a bright, unresolved central component, with an upper limit of source size of $2.5 \times 4$ mas assuming the beam size at 8.3 GHz (labelled C in Figure 4.3), a fainter $16 \times 11$ mas Western region (L1) and even fainter $14 \times 10$ mas Eastern component (L2). All three components were found at the same coordinates for both 2.4 GHz and 8.3 GHz and did not coincide with the side-lobes in the point spread function (PSF), as evident by the PSF images with contours from the source overlaid presented in Figure 4.4. Thus, each component is likely a genuine component rather than an artefact induced by the self-calibration. The sizes of L1 and L2 are measured using the contours in the 2.4 GHz image. The triple morphology is roughly symmetrical with the distance between the C to L1

and L2 being $\sim 40\,\mathrm{mas}$ each. Since it appears the components of MRC 0225–065 may be resolved, we measured their flux density over an irregular polygon[2] for each component.

We recovered all the flux density predictions from the spectral fit to the R22 ATCA observations at 2.4 GHz, but found that $\sim 35\%$ of the flux density was lost at 8.3 GHz, likely due to being resolved out. The flux densities for each component and their spectral index are presented in Table 4.4. The irregular polygon was shaped based on contour levels to ensure only real flux was included in the final measurement. However, the missing flux density at 8.3 GHz may be due to extended structure being resolved out. Consequently, the estimates for the spectral index presented in Table 4.4 should be considered lower limits.

| Component | $S_{2.4\mathrm{GHz}}$ (mJy) | $S_{8.3\mathrm{GHz}}$ (mJy) | $\alpha$ |
|---|---|---|---|
| C | 270±10 | 56±13 | -1.2±0.2 |
| L1 | 121±8 | 23±14 | -1.33±0.5 |
| L2 | 56±7 | 22±14 | -0.7±0.5 |
| Integrated LBA | 447±14 | 100±24 | -1.1±0.2 |
| Model Prediction | 400 | 195 | N/A |

Table 4.4: Flux densities and spectral index for each component of MRC 0225–065 found in the LBA images. The uncertainties for the flux densities are measured calculated using the measured uncertainty from polygon flux and the rms noise of the image. The uncertainty for $\alpha$ is calculated using standard propagation of errors. The model prediction is calculated from the best spectral fit, a double SSAb spectral model[3].

The symmetrical triple morphology suggests MRC 0225–065 is a CSO candidate with a core (C) and two lobes (L1 and L2). The spectral index of the central component is $\alpha_\mathrm{C} = -0.95 \pm 0.08$, which is far steeper than expected for a typical AGN "core", generally expected to have a $\alpha \geq -0.5$ (Orienti et al., 2006; Hardcastle & Looney, 2008). However, on rare occasions, components have previously been identified as cores with spectral indices as steep as $-0.7$ (Orienti et al., 2006). We present the SED for MRC 0225–065 in Figure 4.5 including the MWA flux densities from R22 as well as the flux densities and power-law spectral

---

[2]using https://github.com/nhurleywalker/polygon-flux, (Hurley-Walker et al., 2019)

Figure 4.3: LBA images of MRC 0225–065 at 2.4 GHz (a) and 8.3 GHz (b). Beam sizes are shown with a white ellipse in the bottom left corner of each image and dimensions are specified in Table 4.3. Contours are placed at (-3, 3, 4, 5, 6, 7, 10, 20, 50, 100, 200, 400, 800, 1600) times the rms noise of the image, also specified in Table 4.3. Pixel brightness is plotted in a linear scale following the colour-bars to the right of each image. The resolved regions are labelled C, L1, L2 and properties of each region are outlined in Table 4.4. Relative R.A and Dec are calculated from the central coordinate: J2000 02h27m44.5s -06d21m06.7s.
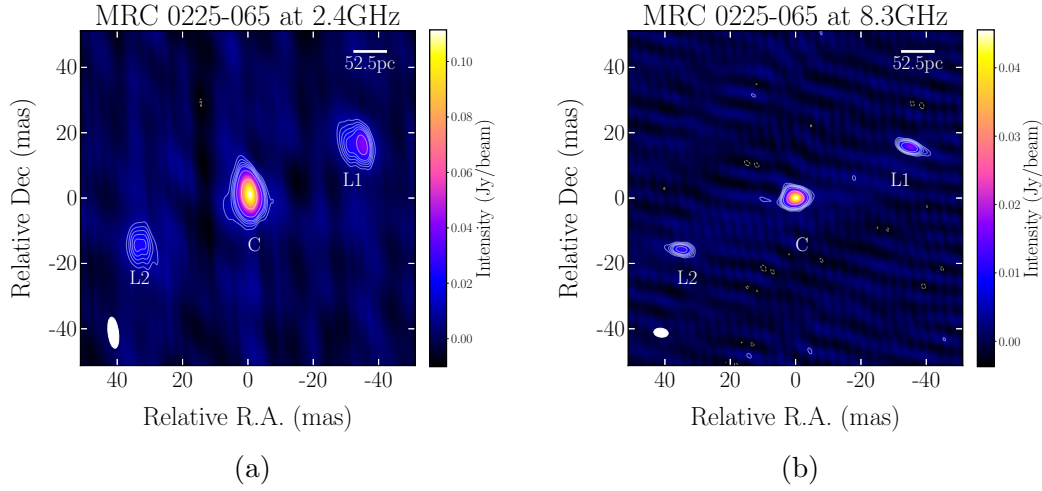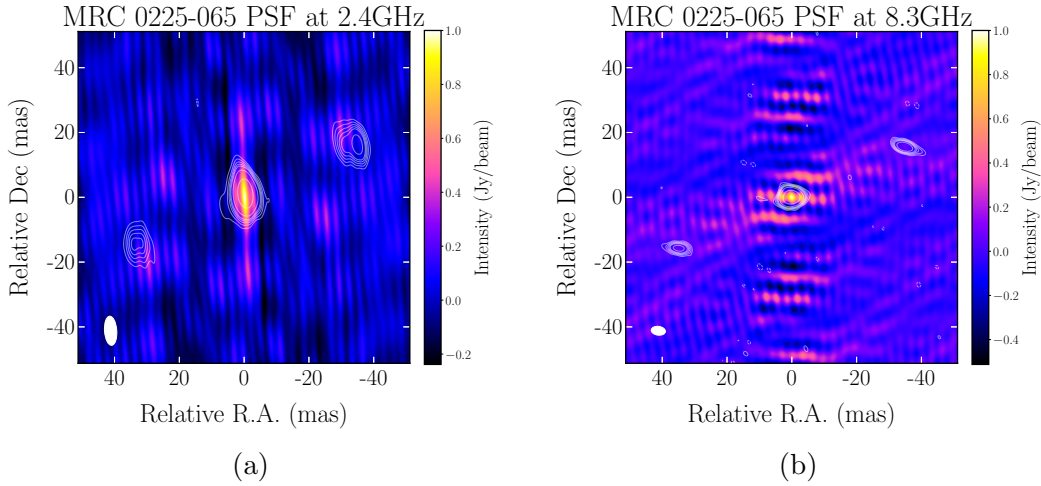


Figure 4.4: PSF images of MRC 0225–065 at 2.4 GHz (a) and 8.3 GHz (b). Beam sizes are shown with a white ellipse in the bottom left corner of each image and dimensions are specified in Table 4.3. Contours are the same as those in Figure 4.3 and placed at (-3, 3, 4, 5, 6, 7, 10, 20, 50, 100, 200, 400, 800, 1600) times the rms noise of the source image, also specified in Table 4.3. Pixel brightness is plotted in a linear scale following the colour-bars to the right of each image. Relative R.A and Dec are calculated from the central coordinate: J2000 02h27m44.5s -06d21m06.7s.

174

model for each LBA component. The entire SED is fit, using the most recent MWA epoch (2020-09), with a double SSA model with an exponential break, which assumes two synchrotron emitting regions that are self-absorbed and ageing producing the exponential break, $\nu_b$, separate from the peak frequency. The break frequency is the frequency where the spectrum begins to steepen as the electrons are ageing and experiencing energy losses (Turner et al., 2018). We fit the spectral model using the `UltraNest` package[4] (Buchner, 2021), which uses a nested sampling Monte Carlo algorithm. From the double SSA spectral model, we find the peak frequencies for the two SSA components to be $\nu_{p,1}$ =400±100 MHz and $\nu_{p,2}$=112±90 MHz, and find $\nu_b$ =14.3±2.7 GHz.

MRC 0225–065 has a spectroscopic redshift of 0.445 (Albareti et al., 2017); thus, 1 mas corresponds to a linear scale of 5.25 pc. Using this redshift, we find the projected linear size of MRC 0225–065 (from L1 to L2) to be ∼430 pc, the linear distance from the core to either lobe to be ∼210 pc and place an upper limit on the size of component C to be ≤26 pc.

### 4.4.2 PMN J0322–4820

Due to difficulties in the phase calibration, we were only able to produce a high quality image of J0322–483 at 2.4 GHz, shown in Figure 4.6a. We do not resolve PMN J0322–4820 and it is confined to the size of the beam: $56 \times 40$ mas. The final image was made using a robust parameter of +0.5, and by flagging the Hartebeesthoek antenna, thus the beam size for PMN 0322–4820 compared to MRC 0225–065 for the same frequency is much larger. Details of the image properties are presented in Table 4.3. Compared to the spectral model fit to the ATCA and 2014 MWA observations, 18% of the flux density was missing. We used a reported photometric redshift for PMN J0322–4820 of 0.16 (Bilicki et al., 2014), thus 1 mas corresponds to a linear size of 2.650 pc. We place an upper limit on the source size of 148 pc.

---

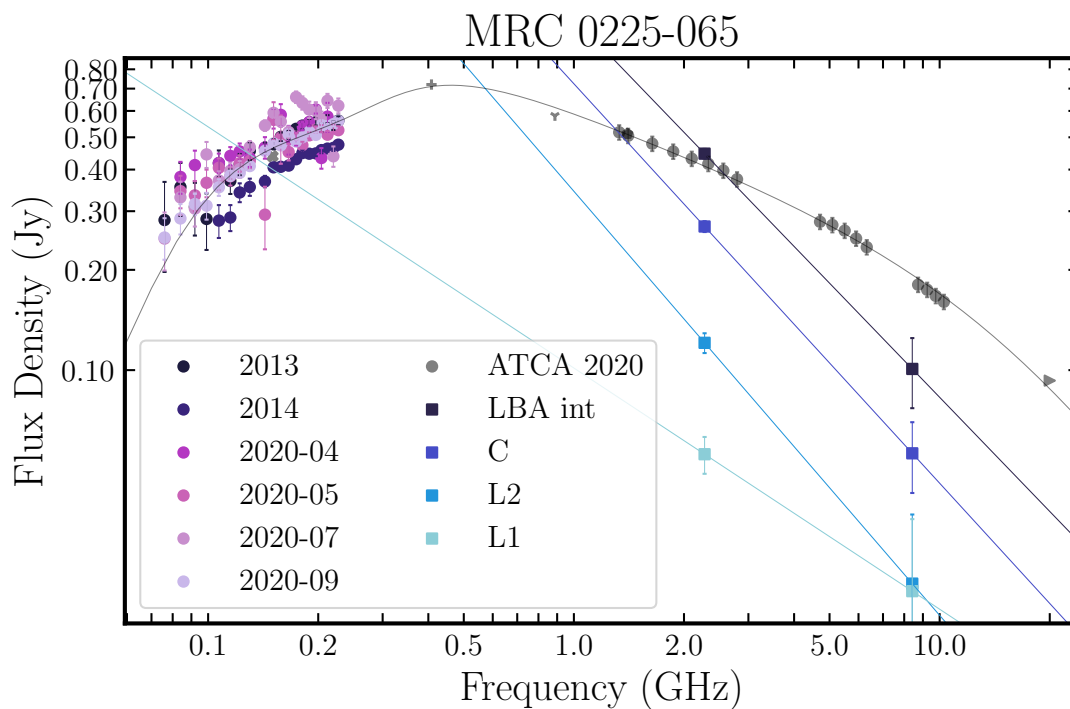[4] https://johannesbuchner.github.io/UltraNest/

Figure 4.5: Spectral energy distribution (SED) for MRC 0225–065. Data included is from R21 and R22 monitoring (circles) and coloured according to epoch. LBA flux densities are plotted as squares with the integrated flux density of LBA plotted as black squares. The spectral fit to each LBA point is a power-law with spectral index presented in Table 4.4. The grey spectral model to the entire SED is a double SSA model with an exponential break. Supplementary data included is: TIFR GMRT 150 MHz Sky Survey Alternative Data Release 1 (TGSS-ADR1; Intema et al., 2017) (grey cross), Molonglo Reference Catalogue (MRC; Large et al., 1981, 1991) (grey +), Rapid ASKAP Continuum Survey (RACS; Mc-Connell et al., 2020; Hale et al., 2021) (grey 'Y'), NRAO VLA Sky Survey (NVSS; Condon et al., 1998), Australia Telescope 20 GHz (AT20G; Murphy et al., 2010) (grey right arrow).
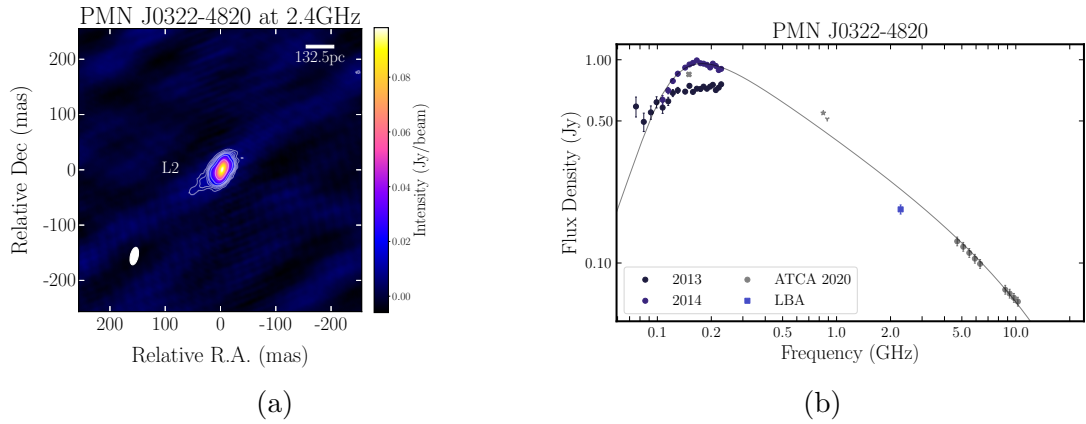
Figure 4.6: LBA image for PMN J0322–4820 at 2.4 GHz (left) and associated SED (right). The beam size is shown with a white ellipse in the bottom left corner and dimensions are specified in Table 4.3. Contours are placed at (-3, 3, 4, 5, 6, 7, 10, 20, 50, 100, 200, 400, 800, 1600) times the rms noise of the image, also specified in Table 4.3. Pixel brightness is plotted in a linear scale following the colour-bars to the right of the image. Relative R.A and Dec are calculated from the central coordinate: J2000 03h22m38.0s -48d20m16.2s. Data included in SED is from R21 and R22 (circles) and coloured according to epoch. LBA flux density is plotted as a blue square. The grey spectral model to the entire SED is a single SSA model with an exponential break. Supplementary data included is: TIFR GMRT 150 MHz Sky Survey Alternative Data Release 1 (TGSS-ADR1; Intema et al., 2017) (grey cross), Sydney University Molonglo Sky Survey (SUMSS; Mauch et al., 2003) (grey star), Rapid ASKAP Continuum Survey (RACS; McConnell et al., 2020; Hale et al., 2021) (grey 'Y').

## 4.5 Discussion

In this section, we will present a comprehensive analysis of both MRC 0225–065 and PMN J0322–4820 to produce a unified perspective of these two sources with the aim of concluding whether they are young or frustrated PS sources. In Section 4.5.1, we present our two sources in the linear size and turnover relation, in Section 4.5.2, we discuss the host galaxy properties according to mid-infrared, optical observations and radio properties. Lastly, in Section 4.5.4, we predict the expected scintillation based on the morphology revealed in our LBA images, and conclude with the the limitations of future observations for detecting such scintillation.

### 4.5.1 Linear Size and Turnover Relation

PS sources follow an inverse relation between their linear size and intrinsic turnover frequency, often referred to as the linear size turnover relation, first presented by O'Dea (1998). This relation is directly predicted from the youth scenario (O'Dea, 1998) where the peak frequency is due to SSA and thus the linear size is directly related to the peak frequency (Kellermann & Pauliny-Toth, 1981). While modifications to models in the frustration scenario can reproduce this relation (Bicknell et al., 2018), it is generally understood that PS sources that fall below the linear size-turnover relation are likely compact beyond what is expected for a young source and are thus assumed to be frustrated. We plot both MRC 0225–065 and PMN J0322–4820 on the linear size-turnover relation in Figure 4.7, along with other known PS sources, details of which are discussed by Keim et al. (2019). It is evident from Figure 4.7, that MRC 0225–065 is entirely consistent with the relation whereas PMN J0322–4820 sits somewhat below the relation, particularly since the linear size is an upper limit. This would suggest MRC 0225–065 is consistent with the youth scenario whereas PMN J0322–4820 may be frustrated. However, it is worth nothing, R21 identified PMN J0322–4820 as a variable PS source with a changing spectral shape, and thus concluded it was likely a blazar.

Furthermore, R21 found the peak frequency changed from ~320 MHz in 2013 to ~145 MHz in 2014. As the peak frequency is variable and PMN J0322–4820 is known to exhibit a changing spectral shape, its position on the linear size-turnover relation will also vary, shown by the error bar in Figure 4.7 corresponding to the range of the peak frequency from 2013 to 2014. Most likely, PMN J0322–4820 is only a temporary PS source and thus should not be included in this relation nor when considering the PS population at large.
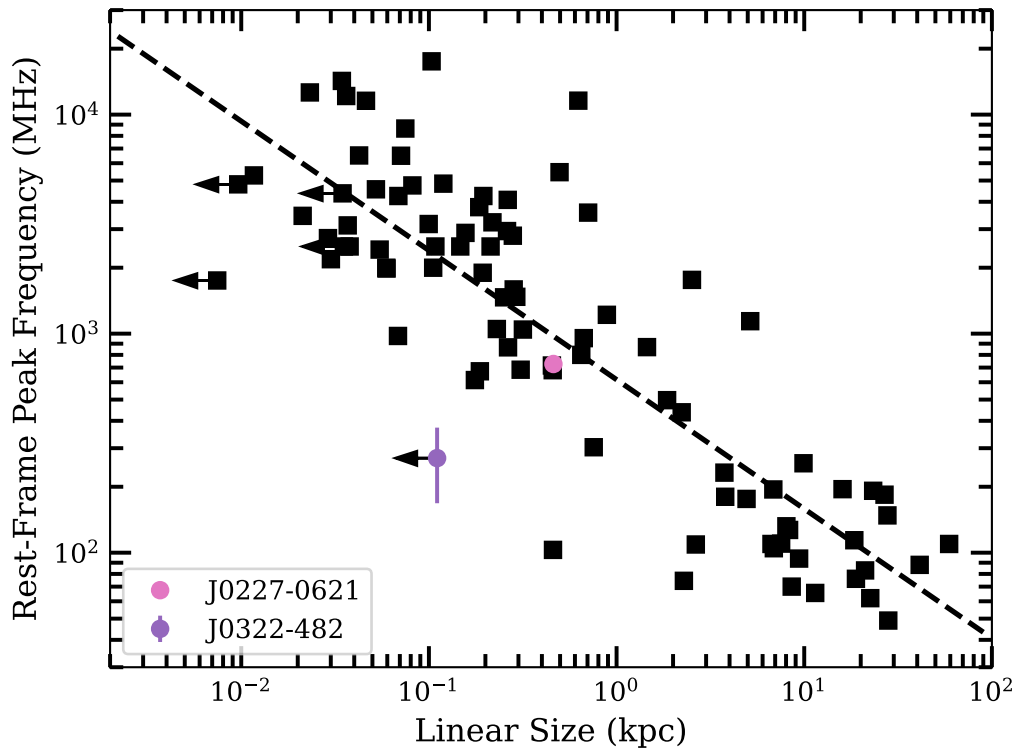


Figure 4.7: Rest frame peak frequency versus linear size. Sources in black are described in Keim et al. (2019). The dashed line is the fit to the relation found by Orienti & Dallacasa (2014). Arrows indicate maximum linear sizes for unresolved sources. MRC 0225–065 (pink circle) and PMN J0322–4820 (purple circle) are plotted with linear sizes calculated from LBA images. The error bars for MRC 0225–065 represent the range for peak frequencies calculated in R21.

### 4.5.2 Host Galaxy Properties

#### 4.5.2.1 *WISE* Colours

Mid infra-red (MIR) colour selection techniques using the *Wide-Field Infrared Survey Explorer* (*WISE* Wright et al., 2010) and the *Spitzer Space Telescope* (Werner et al., 2004) are widely used to efficiently distinguish between AGN and star-forming galaxies.

*WISE* is a MIR all sky survey covering four photometric bands: 3.4, 4.6, 12, and 22 $\mu$m referred to as W1, W2, W3, and W4 respectively. The MIR wavelengths are sensitive to the emission from hot dust in the torus of the AGN, allowing for the identification of AGN where X-ray and optical emission may be obscured by intervening gas and dust. Hence, AGN stand out from starbursting galaxies or stars due to incredibly red MIR emission (Lonsdale et al., 2015). Obscured AGN with red MIR emission have been identified by their MIR colours, often by their place in a colour-colour diagram (Jarrett et al., 2011; Stern et al., 2012; Lonsdale et al., 2015). In Figure 4.8 we present the *WISE* colourcolour diagram, in Vega magnitudes, for the radio sources in our total population presented in Chapter 2 with clearly identified *WISE* counterparts. The bulk of sources centred around $W1 - W2 = 1.2$ and $W2 - W3 = 3$ correspond to the region typically associated with quasars and AGN, with $W1 - W2 > 0.8$ typically indicative of hot AGN dust rather than star formation.

The tail towards the bottom left of Figure 4.8 is associated with emission from star formation or stellar emission, with increasing star formation towards the lower right. MRC 0225–065 is in the spiral regime, however, there is evidence for moderate star formation. As we know MRC 0225–065 is an AGN, it is possible that the emission at MIR is a combination of these two processes, this conclusion is supported by the spectrum presented in Figure 4.9 that shows evidence of ongoing accretion. Conversely, PMN J0322–4820 is well within the elliptical regime, thus has low emission from star formation and no evidence of hot AGN dust. Blazars are typically found to dominate the top right region of the *WISE* colour-

colour plot as the MIR emission is dominated by the emission of the blazar jet over the galaxy (and associated stellar emission). As discussed in Section 4.5.1, the compact morphology and variable spectral shape suggest PMN J0322–4820 is a blazar. However, we find the *WISE* colours of PMN J0322–4820 suggest the host galaxy is an elliptical with predominantly red optical emission but the emission from the radio blazar is not dominating in the MIR, which would increase the emission at W2 and W3 bands. While it is more common to find blazars in the top right region of the *WISE* colour-colour plot, the MIR colours suggesting the host galaxy for PMN J0322–4820 is an elliptical is still consistent with a blazar classification (Yang et al., 2015; D'Abrusco et al., 2019), often previously referred to as BL Lacs and LERGs (see Section 1.1.2 for descriptions of blazar sub-classifications).

#### 4.5.2.2 Optical Spectra

MRC 0225–065 has an optical spectrum from the $13^{\text{th}}$ data release of the Sloan Digital Sky Survey (Albareti et al., 2017, SDSS). From the fitted spectrum, Albareti et al. (2017) report a spectroscopic redshift for MRC 0225–065 of $z = 0.445$ and classify it as a broad-line, starburst quasar. The spectrum additionally has low-ionisation nuclear emission-line region (LINER) properties, evident from the strong NII, SiII and OI lines. A LINER has a high energy radiation field. There is still debate about whether this is AGN emission or star formation, but likely the combination of the broad lines, strong OIII emission and radio-loudness of MRC 0225–065 is evidence of AGN. From the broad H$\alpha$, we can calculate the velocity dispersion according to:

$$d(\text{velocity}) = c\frac{d(\lambda)}{\lambda_0}, \tag{4.1}$$

where $c$ is the speed of light, $d(\lambda)$ is the wavelength dispersion from the spectral fit, and $\lambda_0$ is the rest-frame wavelength of H$\alpha$. Using the reported fit to the broad H$\alpha$ from SDSS where $\lambda_{\text{observed}} = 9486\,\text{Å}$, we use the equivalent width,
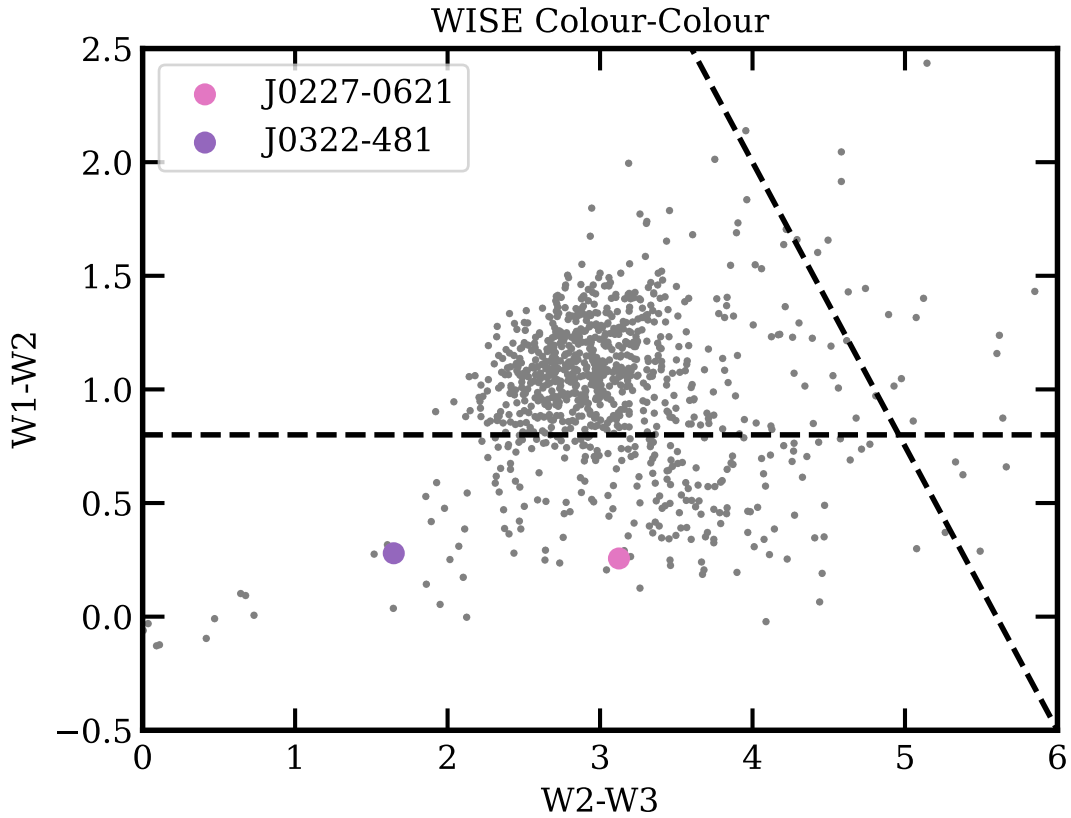
Figure 4.8: *WISE* $W1 - W2$ vs $W2 - W3$ colour-colour plot with targets from the total population of radio sources presented in R21, MRC 0225–065 (pink) and PMN J0322–4820 (purple). There is a smaller number of sources (including PMN J0322–4820) within the regions typically associated with elliptical, spiral, starburst galaxies or luminous infrared galaxies (Wright et al., 2010), the branch to the lower left. The horizontal dashed line is the AGN colour selection defined by Stern et al. (2012), *WISE* colours above this line are indicative of hot AGN dust. The dashed diagonal line is the AGN colour selection used by Lonsdale et al. (2015) to identify extremely red, radio-loud quasars.

EW= $30 \pm 4$ Å, and find the velocity dispersion to be $900 \pm 100$ km/s. This large velocity dispersion may be from an extreme star formation wind but it is also indicative of the broad-line regions from an AGN, which is more consistent given our radio observations identify MRC 0225–065 as an AGN. The broad H$\alpha$, and large velocity dispersion, is consistent with an AGN that is quite obscured, as reported by Albareti et al. (2017) who classify it as a broad-line quasar. Perhaps of more interest are the starburst properties of MRC 0225–065, namely OII and OIII emission lines, identified by Albareti et al. (2017). Both OII and OIII are forbidden lines with different origins: OII is mostly due to star formation and thus is often used as an indicator for star formation in galaxies; OIII is due to an AGN and can be used as a proxy for the AGN bolometric luminosity. This is also consistent with the *WISE* colours shown in Figure 4.8 discussed in Section 4.5.2.1, which find MRC 0225–065 consistent with a galaxy with emission coming from both the AGN and star formation. Combining the radio, MIR and optical properties of MRC 0225–065, it is likely this galaxy has moderate star formation with an obscured AGN.

### 4.5.3   Radio Properties of MRC 0225–065

Combining the spectral information and high resolution resolved structure of MRC 0225–065, we are able to determine several intrinsic properties that can help differentiate between SSA and FFA models. In this section, we estimate the magnetic field strength and spectral ages to assess whether MRC 0225–065 is consistent with the youth scenario. We do not focus on PMN J0322–4820 in this section due to its unresolved morphology (even on mas scales) and since the radio variability suggests it is a blazar with an added beaming effect producing Doppler boosting and thus many of the assumptions required for these calculations no longer hold.
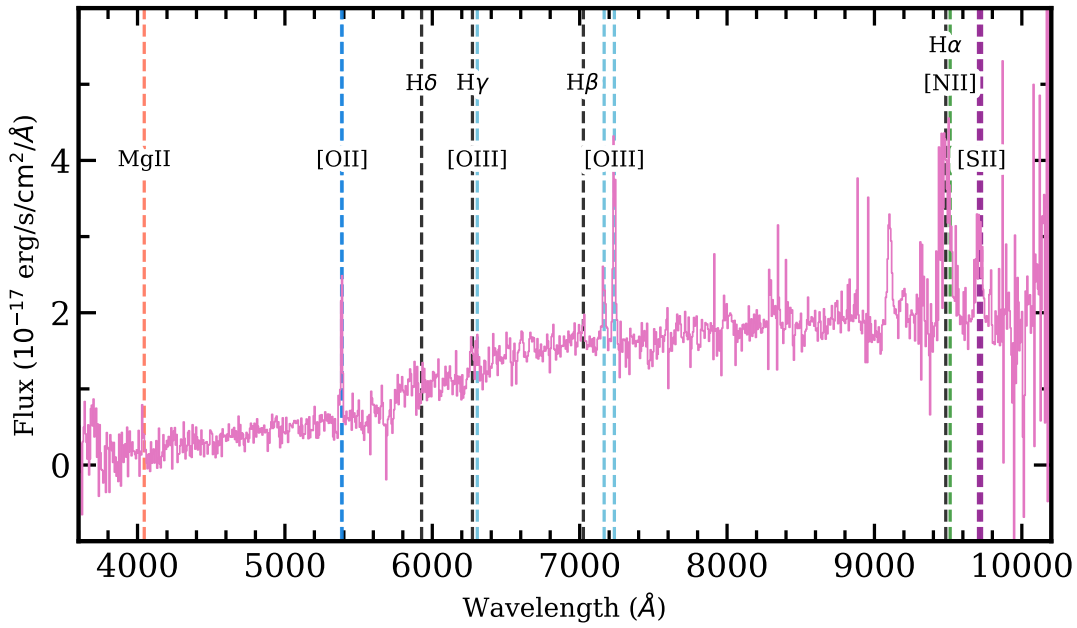
Figure 4.9: SDSS optical spectrum for MRC 0225–065 (GAMA J022744.46-062106.7), data from (Albareti et al., 2017). The fitted spectral lines report a spectroscopic redshift of 0.445. Hydrogen lines are marked with a grey dashed line, MgII marked with an orange dashed line, OII and OIII lines marked with blue lines, NII marked with a green dashed line, and SII marked with purple dashed lines.

#### 4.5.3.1 Magnetic Field

As a means of evaluating the validity of SSA compared to an FFA, we can calculate the magnetic field estimates based on a pure SSA model and on equipartition. Equipartition assumes there is equal energy between the radiating particles and the magnetic field. The comparison between magnetic field estimates based on an SSA model and equipartition has been used as evidence both for the SSA model (when the estimates are in agreement; Orienti & Dallacasa, 2008) and against (when there is a clear disparity; Keim et al., 2019). In this section, we will first estimate the magnetic field assuming a purely SSA model, then assuming equipartition and compare these to determine whether SSA is a reasonable model for MRC 0225–065.

We can estimate the magnetic field strength, in Gauss, based on a purely SSA spectral model, $B_{\mathrm{SSA}}$, according to:

$$B_{\mathrm{SSA}} \approx \frac{(\nu_{\mathrm{peak}}/f(\alpha_{\mathrm{thin}}))^5 \theta_{\mathrm{src,min}}{}^2 \theta_{\mathrm{src,max}}{}^2}{S_{\mathrm{peak}}{}^2(1+z)} \tag{4.2}$$

where $\nu_{\mathrm{peak}}$ is the observed peak frequency in GHz, $S_{\mathrm{peak}}$ is the flux density in Jy at the peak frequency for the source at redshift $z$ with angular minor and major component axis, $\theta_{\mathrm{src,min}}$ and $\theta_{\mathrm{src,max}}$, in mas (Kellermann & Pauliny-Toth, 1981). We note, $f(\alpha_{\mathrm{thin}})$ is as defined by Kellermann & Pauliny-Toth (1981) and can take values typically $\sim$7–9, where it is loosely related to $\alpha_{\mathrm{thin}}$. We take $f(\alpha_{\mathrm{thin}}) = 8$ based on values from Marscher (1983); Orienti & Dallacasa (2008).

Now, assuming equipartition, we calculate the magnetic field strength, in

Gauss, according to (Miley, 1980):

$$B_{\text{equi}} \approx 5.69 \times 10^{-5} \left[ \frac{(1+k)}{\eta} (1+z)^{(3-\alpha_{\text{thin}})} \frac{1}{\theta_{\text{src,min}}\theta_{\text{src,max}}^2} \frac{S_0}{\nu_0^{\alpha_{\text{thin}}}} \chi(\alpha_{\text{thin}}) \right]^{\frac{2}{7}}$$

where

$$\chi(\alpha_{\text{thin}}) = \frac{\nu_2^{\alpha_{\text{thin}}+1/2} - \nu_1^{\alpha_{\text{thin}}+1/2}}{\alpha_{\text{thin}} + \frac{1}{2}}$$

(4.3)

where $S_0$ is the flux density in Jy at frequency $\nu_0$, $\eta$ is the filling factor of the emitting region, $k$ is the ratio of energy of the heavy particles to the electrons, and $\theta$ is as defined above. In this case, we have assumed the component has cylindrical symmetry such that the width of the source on the sky is equivalent to the line of sight path-length. The factor $\chi(\alpha)$ is equivalent to an integration over the optically thin frequency range we probe, from $\nu_1 = \nu_{\text{peak}}$ to $\nu_2 = 10\,\text{GHz}$. Furthermore, we calculate using a flux density and frequency lower than the high frequency spectral break.

For both calculations, we calculate $B_{\text{SSA}}$ and $B_{\text{equi}}$ for the compact core region rather than the total source, to ensure we are comparing a homogeneous region (Orienti & Dallacasa, 2008; Keim et al., 2019). For MRC 0225–065, using Equation 4.2, we estimate the magnetic field strength for a purely SSA model to be $B_{\text{SSA}} \approx 6 \pm 7\,\text{mG}$ for the core region where $\theta_{\text{src}} = 2.5 \times 4\,\text{mas}$. Using Equation 4.3, we assume a filling factor $\eta = 1$ and set $k = 1$[5] to estimate $B_{\text{equi}} \approx 7 \pm 2\,\text{mG}$. As $B_{\text{SSA}}$ is within the uncertainties of $B_{\text{equi}}$, it suggests the core region of MRC 0225–065 is in equipartition and consistent with a pure SSA model. While this does not exclude the FFA model, it does provide supportive evidence for the SSA model. Furthermore, it may not be a valid assumption that MRC 0225–065 is in equipartition, thus Equation 4.3 would not be a reasonable estimate of the magnetic field strength.

---

[5]$k = 1$ is equivalent to the minimum energy condition, however values for $k$ have ranged from 1 to 100, where $k = 100$ produces an order of magnitude difference in $B_{\text{equi}}$ (Pacholczyk, 1970; Miley, 1980)

We can also use the estimated magnetic field to calculate the age of the electron population as a proxy for the age of the jets/lobes. Calculating the spectral age of the electron population requires an accurate estimate of the break frequency, $\nu_b$, separate from the peak frequency. The break frequency is the frequency where the spectrum begins to steepen as the electrons are ageing and experiencing losses (Turner et al., 2018). We can thus calculate the spectral age, $\tau_{\mathrm{spec}}$, according to:

$$\tau_{\mathrm{spec}} = \frac{aB^{1/2}}{B^2 + B_{\mathrm{iC}}{}^2} \left[\nu_b(1+z)\right]^{-1/2}$$

where

$$B_{\mathrm{iC}} = 0.318(1+z)^2$$

$$a = \left(\frac{243\pi m_e{}^5 c^2}{4\mu_0{}^2 e^7}\right)^{1/2}$$

(4.4)

where $B_{\mathrm{iC}}$ is the magnitude of the microwave background magnetic field in nT, $B$ is the magnetic field of the source in nT, $\nu_b$ is the break frequency in GHz, and the constants $m_e$, $c$, $\mu_0$, and $e$ are the mass of an electron, speed of light, magnetic permeability of free space, and charge of an electron, respectively.

It is possible the core is actually an unresolved double of more recent AGN activity than the outer lobes, producing the steep ($\alpha \lesssim -1$, see Table 4.4) spectral index. We assume a constant expansion speed, $v$, and use the linear sizes to estimate the dynamical age, $\tau_{\mathrm{dyn}}$, of the core and outer lobes. Using the magnetic field calculated for the core region assuming equipartition, i.e. setting $B = B_{\mathrm{equi}} = 6 \pm 2\,\mathrm{mG}$, and determining a break frequency, we can estimate the spectral age of the core. Using a break frequency of $\nu_b = 14.3 \pm 2.7\,\mathrm{GHz}$, calculated from the double SSA spectral model fit, we estimate the spectral age of the core to be $\tau_{\mathrm{spec}} \approx 700 \pm 100\,\mathrm{years}$. We then calculate an upper limit on the expected expansion velocity of $v \leq 0.13\,c$ (using simple speed = distance/time arguments) for the core using the upper limit for the linear source size of $\theta_{\mathrm{src}} \leq 26\,\mathrm{pc}$, as outlined in Section 4.4.1. An expansion velocity of $v = 0.13\,c$ is

187

well within previous measurements of the expansion speeds for compact AGN that have been found to range from $0.1\,c$ up to $0.7\,c$ (Polatidis & Conway, 2003; An & Baan, 2012; Orienti & Dallacasa, 2020). The range of expansion velocities would correspond to a range in dynamical ages for the core of $100 \lesssim \tau_{\mathrm{dyn}} \lesssim 900$ years. If we assume the expansion velocity of the core of "inner lobes" is roughly equal to that of the outer lobes from a previous epoch of activity, we can place an upper limit on the dynamical ages of the outer lobes. We calculate the distance between the core and L1 as $\sim 210\,\mathrm{pc}$, which corresponds to a dynamical age of $5000$ years for an expansion velocity of $0.13\,c$. For the range of dynamical ages for typical PS sources, we expect the age of the outer lobes to be $1000 \lesssim \tau_{\mathrm{dyn}} \lesssim 7000$ years. Previous estimates for the ages of PS sources using similar assumptions have estimated ages from $\sim 10^1$ to $\sim 10^5$ years (Orienti et al., 2010), which is entirely consistent with our age estimates for both the inner core and outer lobes.

As the ages, expansion velocities, and magnetic fields that we calculate are all consistent with the SSA model and a youth scenario, it appears MRC 0225–065 is more consistent with a young CSO rather than a frustrated compact AGN. However, there are several caveats and assumptions made in these calculations. Thus, while these results are consistent with the evolutionary scenario of MRC 0225–065 being the youth model, it is not sufficient for excluding the frustration scenario entirely.

### 4.5.4 Predicted Scintillation

In Chapter 2 and Chapter 3, we were able to infer morphologies based on the scintillation properties. In this Chapter, having now retrieved small scale ($\sim$mas) structures for both MRC 0225–065 and PMN J0322–4820, we are able to predict the scintillation that would be observed based on this morphology. As outlined in Section 1.2.1, the timescale and amplitude of modulation due to ISS depends on the angular size of the source, $\theta_{\mathrm{src}}$, compared to the angular size of the scintillation screen, $\theta_{\mathrm{screen}}$. Furthermore, the timescales are also influenced by the observed

frequency, $\nu$, compared to the transition frequency between scintillation regimes, $\nu_0$. For the purpose of this discussion, we use the assumptions and estimates of scintillation parameters from Walker (1998) and Rickett et al. (1995) and find for our Galactic Latitude, $\nu_0 = 8\,\mathrm{GHz}$[6].

Firstly, we note there are two relevant scenarios of scintillation for an extended source:

1. a compact component embedded in an overall larger extended structure (e.g. a hot spot embedded within a diffuse lobe) and

2. multiple individual components separated by a small angle.

In each case, the produced observed scintillation will be the combined effect of the overall structure and thus the different morphologies will produce different effects in the observed scintillation. In Appendix B, we derive mathematical expressions for the predicted scintillation in each scenario stated above. In this section, we use the scintillation theorised according to Appendix B to predict the likely future scintillation of MRC 0225–065 and PMN J0322–4820.

### 4.5.4.1 PMN J0322–4820

As PMN J0322–4820 is unresolved in the LBA 2.4 GHz image, we use the upper limit of the angular size, $\theta_\mathrm{src} = 40\,\mathrm{mas}$. We note however, since PMN J0322–4820 appears to be a blazar (see Section 4.6), it is likely that PMN J0322–4820 is far smaller than 40 mas at 2.4 GHz. Furthermore, considering the flux density and morphology of PMN J0322–4820 at 150 MHz, it seems likely that it is also dominated by a compact region on angular scales of 10's mas, with only a small fraction of extended emission.

At 150 MHz (well into the strong regime), we calculate the angular size of the scattering disk to be $\theta_\mathrm{screen} = 25\,\mathrm{mas}$, according to Equation 1.26. As stated

---

[6]We assume a thin screen at a distance of $\sim 0.3\,\mathrm{kpc}$ with a velocity of $v = 50\,\mathrm{km s^{-1}}$ with Kolmogorov turbulence.

above, it is likely that the vast majority of the flux density at 150 MHz is dominated by a region that is compact compared to $\theta_{\mathrm{screen}}$, given the angular size is an upper limit of PMN J0322–4820. We thus continue under the assumption PMN J0322–4820 is a point source relative to the scintillation screen for both RISS and WISS. Using Equation 1.24, we estimate the modulation index to be $m_p \approx 10\%$ on a timescale of $t_p \approx 1.4$ years at 150 MHz. It is, therefore, likely that monitoring of PMN J0322–4820 at 150 MHz, over several years with a time cadence sampling roughly monthly would detect this slow variability due to RISS.

At higher frequencies in the weak regime, $\theta_{\mathrm{screen}}$ corresponds to the Fresnel scale which gets smaller towards higher frequencies by $\sqrt{\nu}$, according to Equation 1.10. If we consider the expected scintillation at 9 GHz (given it is the central frequency of the ATCA X band), we find $\theta_{\mathrm{screen}} \approx 4\,\mu$as and $t_p \approx 2$ hours. Evidently, the angular size limit in the weak regime is several orders of magnitude smaller than the resolution of our LBA image. However, as source sizes typically scale as $\nu^{-1}$, despite the decreasing Fresnel scale, it is still likely PMN J0322–4820 will be compact enough to scintillate. However, the modulation index will decrease with increasing frequency, by $\nu^{-17/12}$ according to Equation 1.12. If this is the case, one can then expect to detect variability at higher (GHz) frequencies on timescales of hours to days (with an increase in the timescale if PMN J0322–4820 is partially resolved relative to $\theta_{\mathrm{screen}}$). In summary, we expect PMN J0322–4820 to show scintillation at frequencies from $\sim 150$ MHz to $\sim 10$ GHz consistent with a compact source on scales $\mu$as, and potentially exhibiting IDV at gigahertz frequencies.

We have conducted a follow up observation of PMN J0322–4820 with the ATCA at 5.5 and 9 GHz on IDV timescales. The lightcurves for these initial observations are presented in Figure 4.10. From these lightcurves, it is clear PMN J0322–4820 is exhibiting variability on $\sim$hourly timescales, consistent with our scintillation predictions. We present PMN J0322–4820 as an IDV source, where the modulation is potentially significant enough to measure an annual

cycle. We therefore recommend further monitoring of PMN J0322–4820 with the ATCA to obtain sufficient time sampling to measure the scintillation timescales and annual cycle to constrain properties of the ISM turbulence and velocity, and determine further details of the source structure on $\mu$as scales (Bignall et al., 2003; Said et al., 2020). With further multi-frequency monitoring, it may be possible to detect a time delay in the IDV lightcurves between frequencies, suggesting a slight shift in the position of the scintillating component, revealing further insight into the structure of the unresolved component.
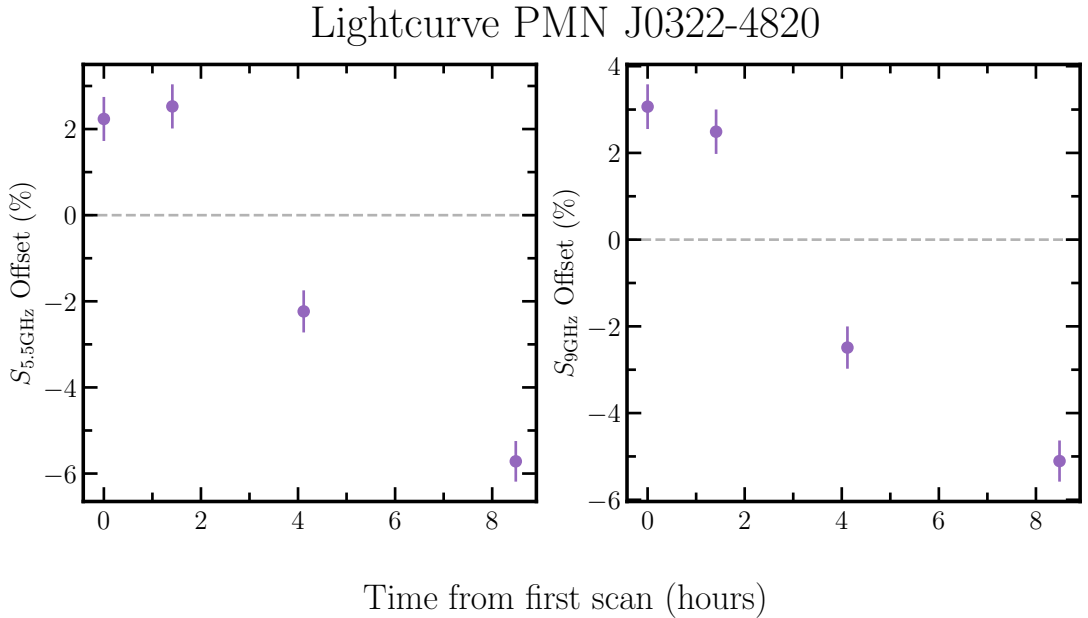


Figure 4.10: Lightcurves of the flux density variance for PMN J0322–4820 from 02 May 2022 at 5.5 GHz and 9 GHz. Flux densities were measured using the `uvmodelfit` function of CASA for 5 minute time intervals. The fractional flux density percentage offset (or modulation, $m$) was calculated as the difference of each 5 minute flux density measurement from the median flux density of the entire light curve for each source. The errors on the flux density are calculated from the systematic error for measuring the flux.

### 4.5.4.2  MRC 0225–065

As MRC 0225–065 is resolved into multiple components, the prediction of scintillation becomes more complicated. At low-frequencies in the strong regime, the

constraint for a source to be considered compact relative to the scintillation screen is less restrictive. Thus in this regime, the individual components of MRC 0225–065 can be treated as point sources, i.e. $\theta_{\text{component}} < \theta_{\text{screen}}$. As discussed in Appendix B, the overall observed variation is a superposition of the flux density variations for the individual components. As MRC 0225–065 is resolved into three compact (in this regime) regions, we can therefore define the overall flux variations of MRC 0225–065 using Equation B1 as:

$$S_{\text{J0227}-0621}(t) = s_C(t) + s_{L1}(t) + s_{L2}(t)$$
$$\text{where} \tag{4.5}$$
$$s_i(t) = A_i(t) \sin \omega_i t + \eta(t)$$

where $s_C(t)$, $s_{L1}(t)$ and $s_{L2}(t)$ are the flux variations for the components C, L1 and L2 respectively, according to the labelled regions in Figure 4.3. According to Equation B2, we can simplify the overall flux variations of MRC 0225–065 according to:

$$\begin{aligned} S_{\text{J0227}-0621}(t) = {} & A_C(t) \sin(\omega t) + \eta_C(t) \\ & + A_{L1}(t) \sin(\omega t + \phi_{L1}) + \eta_{L1}(t) \\ & + A_{L2}(t) \sin(\omega t + \phi_{L2}) + \eta_{L2}(t) \end{aligned} \tag{4.6}$$

where $\phi_{L1}$ and $\phi_{L2}$ are the angular separation between the core and regions L1 and L2 respectively. Since each component is modelled with a sinusoidal function, we can combine these into a third sinusoidal function representing the overall flux variations of MRC 0225–065:

$$S_{\text{J0227}-0621}(t) = A_{\text{J0227}-0621}(t) \sin(\omega t + \phi_{\text{J0227}-0621}) + \eta_{\text{J0227}-0621}(t) \tag{4.7}$$

where the amplitude of the flux variations, $A_{\text{J0227}-0621}$, and the phase, $\phi_{\text{j0227}-0621}$ are determined in terms of $A_{L1}$, $A_{L2}$, $A_C$, $\phi_{L1}$ and $\phi_{L2}$. Likewise, the noise and measurement error for each component is combined into an overall noise and

measurement error, $\eta_{\mathrm{J0227-0621}}$. In this case, the frequency of the flux variations, $\omega$, is analogous to the timescale of scintillation, and the amplitude of the flux variations, $A_{\mathrm{J0227-0621}}$, is analogous to the modulation index.

It is worth noting, the flux density of the core component, $S_C$, is $\sim 50\%$ of the overall flux density of MRC 0225–065 at both 2.4 GHz and 8.3 GHz. Assuming a similar flux density distribution across the components at 150 MHz, the overall modulation of MRC 0225–065 due to RISS would be dominated by the flux variations of the core component. However, as MRC 0225–065 has a spectral peak at $\sim 500$ MHz, the core component is most likely self-absorbed at lower frequencies. Thus, the flux density at 150 MHz may be dominated by the other components, L1 and L2. Further VLBI observations of MRC 0225–065 at megahertz frequencies would provide the flux density of each component in the RISS regime. Currently, the highest resolution attained at megahertz frequencies is with the LOw Frequency ARray (LOFAR) at 0.3 arcseconds (Harwood et al., 2022).

Using the source sizes determined from our LBA images, at 150 MHz, each component is compact relative to $\theta_{\mathrm{screen}} \approx 25$ mas. Thus, each component will be scintillating with a timescale $t_p \approx 1.4$ years and modulation index $m_p \approx 10\%$. According to Equation 4.7, we can expect the timescale of the combined flux variations to also be $\sim 1.4$ years. While the timescale of scintillation would remain constant, the phase shifts between the components can reduce the amplitude of the modulation, potentially below a detection threshold. For the combined modulation to be detected, the components need to be at least partially in-phase (resulting in an additive effect to the flux density variations). As discussed in Appendix B, the phase shift between components would likely translate to periods of "activity" and "inactivity" in the scintillation, as the component flux variations move through constructive and destructive periods. However, since we can assume the timescale of scintillation will be $\sim 1.4$ years, it is possible to schedule long term monitoring on a cadence with the largest probability of

sufficiently sampling this timescale. While not impossible, this does present as a significant observational limitation. Ideally, VLBI monitoring of the flux densities of each component individually would be ideal and solve this issue. However, the frequencies required by VLBI to achieve the resolution needed to resolve the structures (e.g. in this study, $2.4\,$GHz) are also the frequencies where the scintillation timescale is too short for VLBI to obtain sufficient $u - v$-coverage.

At higher frequencies, where the condition $\theta_{\text{component}} < \theta_{\text{screen}}$ no longer holds, recovering the timescale and modulation of scintillation for MRC 0225–065 becomes even more arduous. Considering higher frequencies, for example $5\,$GHz or $9\,$GHz (the central frequencies of ATCA bands C and X respectively), the individual components of MRC 0225–065 no longer satisfy the compact criteria. As summarised in Appendix B, in the case of a resolved source, Narayan (1992) assume the source can be modelled as a Gaussian intensity profile with a width $\theta_{\text{src}} > \theta_{\text{screen}}$. The Gaussian profile produces a dampening effect on the modulation index and increases the timescale of modulation. In the case of MRC 0225–065, the modulation index for each component would be dampened by their resolved structure and their timescale would also be increased. We can thus no longer assume the timescale of modulation for each component would be the same. Consequently, Equation 4.7 is no longer applicable, since $\omega_C \neq \omega_{L1} \neq \omega_{L2}$. As with the RISS regime, it is theoretically possible to recover the timescale of the combined scintillation of MRC 0225–065, provided there is sufficient discrete time sampling over periods where the scintillation is "active". However, as the timescales of modulation of the individual components is unknown (and thus the combined timescale), scheduling observations that would sufficiently sample the scintillation becomes far less achievable. However, from the LBA images, it appears that both L1 and L2 have extended structure, with a fairly even distribution of flux density across this structure. It is thus unlikely that any component other than the core will show scintillation at higher frequencies. If true, it would then be possible to detect ISS of MRC 0225–065 at higher frequencies.

194

## 4.6 A Unified Perspective of MRC 0225–065 and PMN J0322–4820

Combining all the information we have obtained about MRC 0225–065, we begin to create a unified perspective that suggests MRC 0225–065 is a CSO with a peaked spectrum best explained by SSA and recent jet activity over the last $10^2$–$10^3$ years. A summary of the evidence in support of this conclusion are as follows:

- **Variability:** R21 identified spectral variability of MRC 0225–065 with a constant spectral shape, consistent with variability due to RISS. Further spectral variability monitoring by R22 detected no further variability, suggesting a resolved structure but consistent PS source classification. This observation suggests it is unlikely MRC 0225–065 is a contaminating blazar or source with only a temporary PS source classification, such as frustrated sources with an inhomogeneous surrounding medium.

- **Radio morphology:** Previously, it has been suggested frustrated PS sources are more likely to show an asymmetrical morphology due to the asymmetrical environment confining the growth of the lobes. Inversely, this suggests young PS sources that are not frustrated may be more likely to show a symmetrical morphology like that of a CSO. MRC 0225–065 has a very symmetrical morphology according to our LBA images, suggesting it may not be interacting with its surrounding environment.

- **Linear size and turnover relation:** We find MRC 0225–065 is entirely consistent with the linear size turnover relation, a natural product of the youth scenario. Although, it can be reproduced in certain frustration models.

- **Host galaxy:** Using the MIR colours reported in by *WISE* and the optical spectrum from SDSS, we identify the MRC 0225–065 as having an obscured

AGN with moderate star formation. Since the AGN does not dominate the entire MIR and optical emission, and there is still star formation present, it is possible the AGN has only recently been switched on and thus has not yet quenched all star formation in the galaxy, which is not surprising given the compact size of MRC 0225–065. It is also possible the AGN is temporarily frustrated by a thick obscuring material (consistent with the frustrated model) where the host galaxy has plenty of cold gas for star formation to occur.

- **Magnetic field:** Estimating the magnetic field using a purely SSA model and comparing it to the magnetic field calculated assuming equipartition are entirely consistent, suggesting the SSA model is a reasonable model for MRC 0225–065. It's worth noting, in Chapter 3, we found an FFA model was a better fit. This is likely due to the complex, multi-component nature of MRC 0225–065. Future detailed spectral modelling of the individual components with sufficient spectral coverage below the peak frequency ($\sim$ 400 MHz) would be insightful regarding the best spectral model for the overall source as well as individual components.

- **Spectral ages:** Using spectral modelling of the break frequency, we estimate the age of the radio emission (from the core and lobes) to be roughly 700 years, consistent with estimates of the age of PS sources in the youth scenario.

- **Dynamical ages:** Using the linear size from our LBA images and previous measurements of expansion velocity we estimate MRC 0225–065 has two major epochs of activity, one between 1000 to 7000 years ago and another more recently from 100 to 900 years ago. This is also consistent with previous estimates of the ages for young PS sources. Furthermore, due to the missing flux density at 8.3 GHz, this estimate should be considered an upper limit as the spectral indices for each component may be artificially

steepened by the missing flux density.

We therefore conclude, MRC 0225–065 is likely a young AGN and with the peak occurring due to SSA.

Likewise, combining all information of PMN J0322–4820, we can also begin to create a unified picture that PMN J0322–4820 is a blazar. A summary of the evidence for this conclusion are:

- **Spectral variability:** R21 identified PMN J0322–4820 as a variable source in and classified it as showing a changing spectral shape. The dramatic change in spectral shape in the megahertz regime on a timescale of $\sim 1\,\mathrm{year}$ is inconsistent with evolutionary models for PS sources and predicted variability due to RISS. The changing spectral shape is most easily explained by the dynamical nature of blazars.

- **Radio morphology:** The high resolution image of PMN J0322–4820 using the LBA found it was still compact on mas scales. This is also entirely consistent with a blazar morphology, which appears compact due to orientation effects.

- **Linear size and turnover relation:** PMN J0322–4820 sits well below the linear size and turnover relation typically associated with PS sources. This could either be because it is a frustrated source and is thus more compact than expected for it's predicted age. However, more likely, is that the temporary peak detected with the MWA in 2014 was a result of the variability of a blazar with effects like Doppler boosting influencing measurements and thus the spectral peak is unrelated to the source age or absorption mechanisms.

- **WISE MIR Colours:** PMN J0322–4820 has *WISE* colours typically associated with elliptical galaxies and/or LERGs/BL Lac blazars.

We therefore identify PMN J0322–4820 as a new blazar where the jets are oriented along the line-of-sight. However, PMN J0322–4820 was not in the ROMA-bzcat

catalogue of $\gamma$-ray emitting blazars. This is potentially due to the steep spectrum at frequencies over 1 GHz where PMN J0322–4820 is too faint to be detected by traditional blazar searches. We suggest further observations using higher frequency observations in the X-ray or $\gamma$ regimes to search for any high frequency counterpart (Massaro et al., 2009, 2015). We conclude PMN J0322–4820 should not be included in any future population studies of PS sources as it is a contaminating blazar and not a genuine PS source. Furthermore, this highlights the possibility of a population of blazars with steep spectra at high frequencies ($\nu \geq 1$ GHz) that aren't detected in traditional blazar searches and thus may be contaminating populations of PS sources. Low-frequency spectral variability thus presents as a new method for identifying blazar candidates.

## 4.7 Conclusion

We have sought to link our detections of spectral variability for two PS sources with small scale ($\sim$mas) morphology and structures. The images produced using observations with the LBA have identified one resolved and one unresolved PS source. We have also combined our observations with archival observations of the host galaxies of our sources to provide evidence for either the youth or frustration scenario. In this section, we shall focus on each source, and summarise the results of this Chapter and conclude the likely evolutionary scenario or classification for these source.

In Chapter 2, we identified PMN J0322–4820 as a variable PS source with a changing spectral shape, where the peak became more pronounced in 2014. We concluded sources showing a variable spectral shape were likely blazars, thus would likely only have a temporary PS source classification and would likely continue to show variability on most timescales and frequencies. In this Chapter, we have produced a high resolution image of PMN J0322–4820 at 2.4 GHz using the LBA and find it is still unresolved on mas scales. We place an upper limit of the source size to be 14 pc, using a photometric redshift of 0.16. This

incredibly compact morphology is consistent with a blazar classification as the line-of-sight is along the jets thus the blazar appears compact due to projection effects. In Section 4.5.4, we discussed the predicted variability due to ISS, given the unresolved morphology. We find PMN J0322–4820 is highly likely to exhibit IDV, testable by hourly monitoring with the ATCA. Furthermore, we also predict continued monitoring of PMN J0322–4820 at megahertz frequencies would reveal further ISS, as well as a variable spectral shape due to the dynamic nature of blazars. We also suggest follow up observations at higher frequencies (X-ray or Gamma) to confirm our blazar classification. if confirmed, PMN J0322–4820 may hint to a new class of steep-spectrum blazars identifiable by their low-frequency spectral variability.

In Chapter 2, we identified MRC 0225–065 as a variable PS source with a consistent spectral shape. However, in Chapter 3, monitoring with the MWA and ATCA over 2020 revealed no further significant variability. We concluded it was likely MRC 0225–065 was variable due to ISS but likely partially resolved on the $\sim 25$ mas, resulting in the significant initial variability, but overall having a longer timescale of variability with a dampened modulation index and thus showing undetected variability in the 2020 monitoring. Our LBA images reveal MRC 0225–065 is resolved into three regions, a bright central region containing $\sim 50\%$ of the total flux, and two fainter regions roughly equal distance from the central region. This is consistent with our prediction that MRC 0225–065 has resolved structures on mas scales. However, as the morphology of MRC 0225–065 is three individual components, the scintillation can be considered individually for each region. In Section 4.5.4, we predict MRC 0225–065 would show periods of significant modulation at megahertz frequencies as the modulation due to ISS for the individual components goes into and out of phase. Furthermore, we predict detection of ISS at gigahertz frequencies would be unattainable as the individual components are resolved compared to the scintillation screen. Thus, without high resolution observations to resolve the individual components, it is unlikely

the modulation would be significant enough to detect.

We also investigate the viability of SSA and FFA models for MRC 0225–065 by combining our LBA images, spectral variability, spectral modelling and archival observations of the host galaxy. In both optical and mid-infrared observations, MRC 0225–065 is consistent with a star bursting quasar, i.e. while it is clearly an AGN, there is some emission that suggests the host galaxy of MRC 0225–065 has some residual star formation occurring. This is slightly unusual for the host galaxy of an AGN (most typically low-luminosity AGN), which are typically associated with red galaxies with no star formation, but not unheard of. We also investigated the *WISE* colours and find the host galaxy of MRC 0225–065 is again consistent with emission from both an AGN and star formation. This suggests the AGN itself is not dominating the emission at optical and infrared wavelengths and may be heavily obscured. Furthermore, the potential emission from star formation in both the optical and infrared spectra suggests the AGN of MRC 0225–065 may still be quite young and has not yet quenched all star formation in the galaxy, although there may be several other factors producing emission consistent with both AGN and star formation. With further optical and infrared observations and detailed spectral modelling it is possible that we could disentangle the contributions of the AGN and the host galaxy to the overall spectrum and thus determine the star formation rate of MRC 0225–065. Likewise, additional constraints on the star formation rate can be obtained from observations with Atacama Large Millimeter Array (ALMA) at sub-millimeter wavelengths to measure sub-mm continuum, where the emission is contaminated less by the AGN, and CO observations.

Lastly, we analysed the radio SED and radio morphology from our LBA images to determine a likely dynamical and spectral age for MRC 0225–065. We find the magnetic field calculated from a purely SSA model and by assuming equipartition are consistent for the central core region, suggesting an SSA model is a reasonable model for this source. Given the steep spectrum of each component in the LBA

images, it is possible MRC 0225–065 is a double-double AGN, with the outer resolved lobes being the result of an earlier phase of activity, and the core being an unresolved double of recent activity. Assuming this, we can estimate the age of the electron population in the core of "inner lobes" using the calculated magnetic field for the core, $B_{\mathrm{equi}} = 7 \pm 2 \, \mathrm{mG}$, and measured break frequency, $v_b = 14.3 \pm 2.7 \, \mathrm{GHz}$. We found the core to have a spectral age of $\tau_{\mathrm{spec}} = 700 \pm 100 \, \mathrm{years}$, which is consistent with previous age estimates of young CSO sources of $10^1 - 10^5 \, \mathrm{years}$ (Orienti et al., 2010; Orienti & Dallacasa, 2020). Furthermore, we use the spectral age of the core and the upper limit of core size to calculate and expected expansion velocity (assuming the simple relation speed = distance/time), and place an upper limit on the expansion velocity of the lobes to be $v = 0.13c$, well within previous measurements of expansion velocities for PS sources of $0.1c \lesssim v \lesssim 0.7c$ (Orienti & Dallacasa, 2020). Lastly, we use this to estimate the dynamical age of the outer lobes and estimate their age to be $\tau_{\mathrm{dyn}} \approx 5000 \, \mathrm{years}$, again, well within previous estimates of ages for young PS sources.

In Chapter 2 and Chapter 3, we demonstrated the importance of spectral coverage in variability surveys in order to distinguish between the different physical mechanisms producing the variability. Furthermore, the previous Chapters highlight the importance of spectral variability in identifying PS sources that are frustrated or contaminating blazars with a temporary peak. This Chapter has used high resolution imaging to confirm the conclusions made from the spectral variability. We thus highlight the use of spectral variability as a means of identifying and excluding polluting temporary PS sources in populations attempting to study young AGN. Previous attempts to do this relied on the observationally expensive option of VLBI imaging to estimate source ages, often with insufficient data to draw decisive conclusions. Here we show how the combination of blind spectral variability searches followed by targeted spectral variability monitoring can replace these previous methods to identify a reliable population of young AGN.

# Chapter 5

# Discussion, Conclusions, and Future Directions

## 5.1 Discussion

In this Thesis, we have investigated PS sources by measuring spectral variability. We developed the statistical analysis to identify variable sources and categorise them according to their variability in the largest spectral variability survey to date, (Ross et al., 2021, Chapter 2). We have demonstrated that with a large spectral coverage, distinguishing between intrinsic and extrinsic origins of variability is possible. This means we can ascertain detailed information on both the source and intervening media. We have applied this strategy to PS sources and used the spectral variability to identify frustrated PS sources and young PS sources. In this Section, we will discuss the implications of the results of this Thesis as a whole, outline some limitations of the current research, and finally, discuss the future prospects of spectral variability surveys and studies of PS sources.

This work has also highlighted the particular advantage of spectral coverage at megahertz frequencies. The complimentary timescales between RISS and survey speeds at megahertz frequencies allows for the detection of RISS as a natural by-product for such surveys. However, this does raise concerns for calibration

using sky models that include compact sources likely scintillating. The catalogue of variable sources identified as part of this work (Ross et al., 2021, Chapter 2) should be used with caution in sky models used for calibration. For most MWA observations, given the large field of view (610 sq. deg at 150 MHz) likely only one source showing extreme scintillation (i.e. sources showing large amplitude variations on the scale of $\sim 20\%$) will be covered in any given pointing. The accuracy of the sky model and thus accuracy of the calibration will depend on the percentage of extreme scintillators in the field as well as their fractional flux density variation compared to the sky model. Given the low fraction of the extreme scintillators relative to the number of sources in a given MWA pointing, such effects on the calibration will be minimal ($\lesssim 1\%$). However, for other instruments with a smaller field of view (e.g. LOFAR) or for science goals that require a high calibration accuracy (e.g. Epoch of Re-ionisation, EOR), consideration must be given to the benefit vs the hindrance of including variable sources in sky models used for calibration.

### 5.1.1 PS Source Evolution: Youth vs Frustration

Several key questions still remain regarding PS source origins and evolution, namely, the debate between youth and frustration, the mechanism producing the spectral turnover, and the implications for AGN feedback and duty cycles (O'Dea & Saikia, 2021, and references therein). This Thesis has demonstrated the critical importance of spectral coverage, particularly below the spectral turnover, and the value of combining this coverage with variability in working to resolve these issues. Furthermore, we have shown that characterising spectral variability offers a novel and robust methodology for identifying frustrated PS sources by their rapidly variable optical depths. Current methods to date (prior to this work), have often still had ambiguous conclusions regarding youth vs frustration (Saikia & Gupta, 2003; Callingham et al., 2015). In this Thesis, our targeted follow up of a subset of 15 PS sources (Chapter 3 Ross et al., 2022) was able to confidently characterise

three frustrated PS sources and one evolving SSA PS source from the spectral variability alone, with confirmation from detailed spectral modelling. While this is only identifying young and frustrated sources with ∼30% efficiency, the large population (123 sources) of variable PS sources identified in our blind survey presents the possibility for increasing the populations of confidently identified SSA and FFA PS sources significantly. With the next generation of instruments (in particular Australian SKA Pathfinder (ASKAP) and Square Kilometre Array (SKA)), surveying large sky areas with large spectral coverage will become more feasible and rapid. Thus future surveys of spectral variability that focus on PS sources could potentially increase populations of both frustrated and young PS sources by an order of magnitude at least. We thus present spectral variability as a promising and confident approach to distinguish between SSA and FFA absorption models.

In particular, the design of future spectral variability surveys can help to probe specific variable processes, discussed further in Section 5.3. To help resolve the debate between youth and frustration origins, we recommend future spectral variability surveys target PS sources at specific time cadences to extract populations of each. Based on the results of this Thesis, at ∼150 MHz, we suggest cadences of weeks to months (to probe a variable opacity) and cadences of years (to probe source evolution at jet propagation). The megahertz spectral coverage is particularly useful in sampling the optically thick region of PS sources, particularly those with a peak frequency below ∼1 GHz (Callingham et al., 2017). Upcoming variability surveys at higher frequencies (e.g. ASKAP variables and slow transients (VAST) survey, VLA Sky Survey (VLASS)) have the potential to investigate the optically thick region of PS sources that peak at higher frequencies. At these higher frequencies, the variability timescales of ISS compared to a variable opacity is likely very different. In particular, timescales of variability due to ISS is typically hours to weeks (Wang et al., 2021), while the opacity variations are still of the order months (Tingay et al., 2015). These future surveys present

a unique opportunity to probe PS sources with a variable opacity without the contamination of variability from ISS.

With the next generation of surveys, we are now uniquely placed to conduct large scale spectral variability surveys to distinguish between SSA and FFA PS sources for a large population. For example, the capabilities of ASKAP to survey the sky at record speeds (e.g. the Rapid ASKAP Continuum Survey (RACS) mapped over 2 million galaxies in just 300 hours of observations, Hale et al., 2021) and the large frequency coverage (700–1, 800 MHz) and instantaneous coverage (300 MHz) is perfectly placed to explore the spectral variability of PS sources. Furthermore, the variables and slow transients (VAST) survey probes timescales ranging from as short as 5 seconds up to 5 years at 888 MHz (Murphy et al., 2021), therefore exploring a broad range of physical origins of variability. As a pathfinder to the SKA, the preliminary results of ASKAP surveys highlights the calibre of future surveys that will be possible with the SKA, particularly with the synergy of SKA-Low and SKA-Mid covering frequencies between 50 MHz and 14 GHz.

Future investigations can therefore target specifically young and/or frustrated sources with more confidence that the selection of sources for each population is reliable, and thus these different classes of PS sources can be individually explored and compared. Furthermore, this Thesis builds on previous studies that identified several contaminating sources that show only a temporary peaked spectrum (e.g. Torniainen et al., 2005). We identified 33% of variable PS sources ($\lesssim$10% of the total PS population) lost their PS classification in just one year, consistent with previous estimates (Torniainen et al., 2007), and also conclude there are likely contaminating blazars. From a blind survey, we find $\lesssim$10% of PS sources lose their PS classification this fraction suggests current catalogues of PS sources (e.g. Orienti & Dallacasa, 2014; Callingham et al., 2017) need to be re-examined to ensure a reliable consistent population of PS sources. Likewise, our targeted spectral variability survey, which was biased towards selecting PS sources showing variability due to RISS, still identified three of the 15 PS sources as showing

a variable opacity on timescales of months, suggesting potentially a further 20% of variable PS sources will also lose their PS classification with further monitoring. The prevalence of temporary PS sources and frustrated sources suggests a high fraction (potentially from 10% to 35% Torniainen et al., 2005, 2007; Mingaliev et al., 2012) of known PS sources are not young SSA sources, and/or may not maintain a consistent PS classification. While these temporarily PS sources pose an interesting population in their own right, regular monitoring with broad spectral coverage is needed to ensure such contaminating sources with temporary spectral peaks are excluded from future evolutionary studies of PS sources and AGN.

While a large focus of the temporary PS sources has been to identify them with the intention of exclusion in future studies, this population does pose an interesting opportunity themselves. Sources displaying a temporary peaked spectrum have previously been presented as blazars (Tinti et al., 2005). This work has provided further evidence to confirm such classification via VLBI imaging of a variable PS sources showing a dramatic change in spectral shape, see PMN J0322–48200 (GLEAM J032237–482010), Chapter 4. Despite PMN J0322–4820 showing characteristics consistent with a blazar, it has not previously been identified as one, and not has it been detected in higher frequency surveys (e.g. AT20G Murphy et al., 2010), which are biased towards detecting blazars. This may be because the steep spectrum makes PMN J0322–4820 too faint to be detected at higher frequencies, which is unexpected for these sources, as discussed in Section 1.1.2. A follow up study of these blazar candidates to characterise any rapid scintillation (∼intra-hour to daily), large flux density modulation (∼20%) to potentially measure the Doppler factor, source size, and brightness temperatures, and thus potentially confirm the blazar classification is recommended. If confirmed, spectral variability at low frequencies presents a unique opportunity to identify blazars, producing a population of radio-selected blazars instead of relying on gamma- and X-ray selected populations. Exploration of such a pop-

ulation could help to understand the mechanism of jet formation, as well as the orientations and structure of the jet (Ostorero et al., 2004).

### 5.1.2   Scintillation

As discussed in Section 1.3.1, scintillation has been used to infer a range of properties both relating to the sources itself and the intervening media: from determining the size at which a component becomes optically thick to $\mu$as precision (Bignall et al., 2003) to detecting a $\sim$0.1 pc long filament in the ISM of the Milky Way (Wang et al., 2021). However, many scintillation surveys are limited to small populations due to the expensive amount of observing time required. In particular, scintillation candidates must first be identified (either by previously identified variability or by a SED suggesting it is variable), then regular follow-up observations made to accurately measure the scintillation timescale. Since gigahertz frequency ISS typically has timescales of hours to days, most scintillation surveys have been conducted at these frequencies where observing the variability is on manageable timescale. Furthermore, it is extreme scintillation that provides the most valuable information about the plasma in the scattering screen; e.g. extreme scattering events (ESEs), and IDV. Given only a handful of IDV sources are known (Kedziora-Chudczer et al., 1997; Dennett-Thorpe & de Bruyn, 2000; Bignall et al., 2003), a detailed understanding of the ISM for a large number of lines-of-sight is not currently feasible.

This work has used spectral variability at low-frequencies to present a population of IDV candidates (Ross et al., 2021, Chapter 2). Our work suggests the majority of variable sources in our blind spectral variability survey are showing RISS at 150 MHz and thus have compact features $\lesssim$25 mas, supported by the large fraction that continued to show RISS in our targeted monitoring (Ross et al., 2022, Chapter 3), and supported by high resolution imaging using the LBA (Chapter 4). Furthermore, for MRC 0225–065, we detected initial variability in Ross et al. (2021) but did not detect any further variability in Ross et al.

(2022). From this, we concluded it likely had a compact feature (which produced scintillation initially detected) but also had extended structure (increasing the timescale of modulation and dampening the amplitude). This was also confirmed by the high resolution imaging with the LBA. Thus we have demonstrated that by characterising the scintillation, we can infer the presence of a compact feature as well as extended structures. We therefore propose the use of RISS surveys to estimate source sizes for a large population of sources, in particular of PS sources. With many new/upgraded instruments and surveys upcoming (e.g. the SKA and ASKAP-VAST survey), there is large potential for multi-epoch and multi-frequency variability surveys from complimentary observations. Thus in this new observational era, obtaining estimates of source sizes of PS sources using scintillation offers a far cheaper alternative to VLBI for adding to the linear size-turnover relation, assuming redshifts can be obtained and survey timescales/frequencies are complimentary. A caveat is that the estimates of the source sizes obtained using scintillation will have large uncertainties due to the assumptions made regarding scattering screen distance, Kolmogorov turbulence and the fraction of flux density in the compact region scintillating. Such an approach is limited by the detection of scintillation and is sensitive to underestimating the source size if the flux is extremely dominated by a scintillating hot spot such that the dampening effect of the extended structure is below detection. Obtaining such redshifts is far more achievable with the development of instruments such as Dark Energy Spectroscopic Instrument (DESI; Abareshi et al., 2022) and WHT Enhanced Area Velocity Explorer (WEAVE) spectrograph (Agócs et al., 2012), and the upcoming Wise Area VISTA Extra-Galactic Survey (WAVES), which seeks to obtain $\sim 2$ million redshifts (Driver et al., 2016).

Furthermore, while the angular size limit of the scattering screen at 150 MHz is much larger than that at gigahertz frequencies, it is likely the majority of the sources showing RISS will show ISS at higher frequencies on timescales of hours to days, particularly those sources showing a constant spectral shape. Blind

low-frequency spectral variability surveys therefore have the potential to identify a large population of IDV candidates, which, if confirmed, could increase the number of known IDV sources by an order of magnitude.

Such a large population of scintillating sources offers a new strategy to characterise the properties of the ISM. Such observations have been used to characterise small-scale structures in the ISM (Wang et al., 2021; Bignall et al., 2022) but have relied on the extreme scintillation where the short timescale suggests nearby complex structures, potentially even from outflows of nearby hot stars (Walker et al., 2017). Increasing the population of sources showing extreme scintillation by an order of magnitude has the potential to understanding the small complex structures of the ISM with respect to Galactic latitude. In particular, since our population is around the SGP with ∼0.7 sources per sq. deg, larger populations with a higher density of variable sources and covering a larger range of Galactic latitudes will be an important development. Such trends would be complimentary to similar studies using pulsars which are generally at low Galactic latitudes. Similar strategies have been applied in the context of space weather; i.e. by using IPS to characterise the solar wind and its transverse velocity (Morgan et al., 2018; Iwai et al., 2021). As discussed in Section 1.2.1, sources that are compact enough to show ISS will also be compact enough to show IPS. One could thus also identify sources showing RISS to target in IPS surveys for heliospheric studies.

## 5.2 Conclusions

As discussed in Section 1.3.1, the physical origins of radio variability has mostly remained unclear for a large population. In this work, we have sought to demonstrate the value of spectral coverage in interpreting the cause of variability. In particular, we have focused on the unique and intriguing population of PS sources and used spectral variability to estimate PS source sizes and morphologies, evaluate the cause of absorption, distinguish between evolutionary scenarios for several

PS sources, and identify contaminating temporarily peaked sources. To do this, we have conducted an initial blind search for spectral variability to identifying a preliminary population of interest (Ross et al., 2021, Chapter 2), following by a targeted spectral variability survey carefully designed to detect the variability of interest (Ross et al., 2022, Chapter 3), and lastly, we have validated the inferred morphologies from scintillation using VLBI (Chapter 4). In this section, we outline the main results of each Chapter of this Thesis.

Firstly, we used the two epochs of observations for the GLEAM SGP data release to conduct an initial blind search for spectral variability at megahertz frequencies. The key results of this survey are as follows:

- We surveyed a population of $21,558$ sources with 16 individual flux density measurements across $100$–$230\,\mathrm{MHz}$, making this the largest spectral variability survey at publication.

- We classify 323 sources ($\sim 1.5\%$) as showing significant spectral variability, consistent with previous surveys of radio variability finding $\sim 2\%$ of the radio sky is variable. Of these 323 sources, 51 (16\%) were identified as showing changes in their spectral shape.

- The variability index parameter (VIP) was introduced to detect variable sources within the large population. The VIP is defined according to the equation:
$$\mathrm{VIP} = \sum_{i=1}^{n} \frac{\left(S_1(i) - S_2(i)\right)^2}{\sigma_i^2},\qquad(5.1)$$
where $S_1(i)$ and $S_2(i)$ are the flux densities in the first and second epoch in a given sub-band $i$, respectively, and $\sigma_i$ is the combined uncertainty of each flux density added in quadrature.

- The measure of spectral shape (MOSS) parameter was introduced to identify variable sources that exhibited a change in their spectral shape. The

MOSS parameter is defined according to the equation:

$$\text{MOSS} = \sum_{i=1}^{n} \frac{(\widetilde{\text{diff}} - \text{diff}(i))^2}{\sigma_i^2},$$  (5.2)

where $\widetilde{\text{diff}}$ is the median of the differences between the flux density over all frequencies, $\text{diff}(i)$ is the difference of the flux densities between the two epochs at frequency $i$, and $\sigma_i$ is the combined uncertainty of each flux density added in quadrature.

- PS sources were investigated separately and identified as an intrinsically more variable population when compared with the overall typical AGN population. Of the 323 variable sources, 91 ($\sim 28\%$) were known PS sources.

- Two main explanations were explored as potential physical origins for the different types of variability. However, with only two epochs of observations, ultimately resolving the physical origins of the variability was inconclusive. The two most plausible physical origins were:

  1. **Interstellar scintillation:** RISS was proposed as the most likely explanation for all sources that maintained their spectral shape. However, it was concluded to be insufficient at explaining any changes in spectral shape.

  2. **Blazars:** Sources showing a change in their spectral shape were proposed as most likely to be blazars and presented as candidates requiring follow-up confirmation. If confirmed, many of the sources identified in this work would be steep spectrum blazars and pose an interesting population for future investigations.

After identifying a variable population, we conducted a targeted spectral variability survey of 15 PS sources to determine the physical origins of the observed variability. These targets were monitored with roughly simultaneous observations

with the MWA and ATCA over 72 MHz to 10 GHz, throughout 2020 with approximately monthly cadence. The key results of this targeted survey are summarised as follows:

- No sources show any variability at gigahertz frequencies with the ATCA on time cadences of weeks to months. However, 13 of the 15 sources (87%) continued to show variability at megahertz frequencies, four of which showed a significant change in spectral shape on monthly timescales with the MWA.

- RISS was detected and characterised at megahertz frequencies and the presence of compact ($\lesssim 25$ mas) components for the 13 variable sources were inferred. We also predict most (if not all) of the 13 variable PS sources will also show IDV at higher frequencies.

- Three sources were identified as showing variability in the optically thick regime due to a variable optical depth. These sources showed no variability in the optically thin regime but displayed a noticeable increase or decrease in absorption on the timescales of months. This is inconsistent with the broadband effect of strong RISS at MHz frequencies. We concluded GLEAM J015445–232950, GLEAM J020507–110922 and GLEAM J223933–451414 are frustrated PS sources where a variable optical depth is the cause of spectral variability in the optically thick regime.

- We identified a decreasing peak frequency for GLEAM J024838–321336 and determined it is consistent with a recent ejected synchrotron component traversing the jet, slowly cooling and expanding.

Lastly, we compared the prediction of milliarcsecond structures from RISS at megahertz frequencies with direct imaging of compact structures using VLBI. The key results of Chapter 4 are as follows:

- We imaged two variable PS sources with the LBA: MRC 0225–065 (GLEAM J022744–062106) at 2.4 and 8.3 GHz; and PMN J0322–4820

213

(GLEAM J032237–482010) at 2.4 GHz. We resolved MRC 0225–065 into 3 compact components at both frequencies, while PMN J0322–4820 remains unresolved in the 2.4 GHz image.

- We concluded PMN J0322–4820 is likely a blazar due to the changing spectral shape identified in Ross et al. (2021, Chapter 2) and upper limit on source size of 148 pc.

- We concluded MRC 0225–065 is a young SSA PS source and estimated the spectral age to be $\sim$ 212 years for the central region consistent with an expansion velocity $v \leq 0.3\,c$, and a dynamical age of $\sim 2,643$ years to the outer lobes.

- We predicted MRC 0225–065 was partially resolved on milliarcsecond scales due to the variability identified in Ross et al. (2021, Chapter 2) and Ross et al. (2022, Chapter 3) and confirmed this using VLBI. We also used the direct imaging of milliarcsecond structures to predict the likely future scintillation of J0227–0621.

## 5.3   The Future of Low-Frequency Variability

The results from this Thesis has large implications on the strategies of future low-frequency variability surveys. As discussed in Section 1.3.1, previous variability surveys estimate roughly 2% of the radio sky is variable (Becker et al., 1995; Carilli et al., 2003; Ofek et al., 2011), which is also consistent with what we find in Ross et al. (2021, Chapter 2). However, these surveys search a variety of time cadences and frequencies, and thus a range of likely physical origins to the detected variability. This could mean either a consistent 2% of the radio sky shows variability at all frequencies and time cadences, or alternatively, different populations show variability at only specific cadences. While some sources are known to show variability across a broad range of timescales and frequencies

(e.g. blazars), it seems more likely that specific populations vary only at specific observational regimes. With improving instrument sensitivities and increasing spectral coverage, detecting lower significance variability will become possible. The 2% estimate of variability should thus be considered a lower limit of the fraction of variable sources when combining variable populations across all time cadences.

Designing blind spectral variability surveys to probe a time cadence sensitive to a variability mechanism of interest thus may bias the sources identified as variable. For example, in our blind spectral variability survey (Ross et al., 2021, Chapter 2), we used the VIP to identify a population of sources showing variability on a timescale of $\sim$1 year at 150 MHz. As the expected timescale for RISS at 150 MHz is $\sim$1.4 years (Walker, 1998; Hancock et al., 2019), this blind survey is sensitive to compact ($\lesssim$25 mas) sources. It is thus not surprising that we find PS sources as a more variable population compared to typical AGN in this search, given they often have compact morphologies. Alternatively, to identify sources likely showing variability due to adiabatic expansion and general source evolution, time cadences of several years at 150 MHz would be sensitive to this evolution; e.g. GLEAM J024838–321336 showed a decreasing peak frequency from GLEAM (2013, 2014) to our targeted monitoring (2020).

The approach of this Thesis to conduct a blind search for variability (Ross et al., 2021, Chapter 2), followed by a targeted monitoring of variable sources (Ross et al., 2022, Chapter 3), presents an opportunity to extract a population of sources of interest varying on the timescale of interest. In particular, the VIP identified just 1.5% of the population as showing significant variability and 28% of the PS sources were classified as variable, yet the targeted follow up of variable PS sources found over 85% continued to show variability. However, this can bias the population and reduces the completeness of the total variable population since only sources that were caught with significant variability between 2013 and 2014 were identified.

With upcoming surveys and in the SKA-era, surveys with large fraction bandwidth and several time cadences will become more common. We propose an extension of the VIP and MOSS statistics to extract variable populations and characterise the type of variability. In particular, one could use the VIP to identify variability between epochs for several epochs and produce a VIP lightcurve binned at time cadences of interest. The VIP in such a scenario could then be written as:

$$\text{VIP}(j) = \sum_{i=1}^{n} \frac{\left(S_j(i) - S_{j-1}(i)\right)^2}{\sigma_j(i)^2},$$ (5.3)

where $S_j(i)$ is the flux density in the sub-band $i$ in the epoch $j$, and $\sigma_j(i)$ is the combined uncertainty of the flux density at each frequency, $i$ added in quadrature for the epoch $j$. Likewise, the MOSS parameter could also be extended to be calculated per epoch according to:

$$\text{MOSS}(j) = \sum_{i=1}^{n} \frac{(\widetilde{\text{diff}_j} - \text{diff}_j(i))^2}{\sigma_j(i)^2},$$ (5.4)

where $\text{diff}_j(i)$ is the difference in flux density between the epoch $j$ and $j-1$ in the sub-band $i$, with a median value $\widetilde{\text{diff}_j}$, and $\sigma_j(i)$ is defined as above.

While the proposed multi-epoch VIP and MOSS parameters would need to be tested first, we expect they can be applied to large populations, with large spectral and temporal coverage. The multi-epoch VIP can be considered as a binned lightcurve of the variability where the bins are time cadences of interest. Likewise, the multi-epoch MOSS parameter can also be considered a binned lightcurve but sampling the spectral evolution across the time cadences probed. One could then change the bin sampling to probe different variability timescales (Driessen et al., 2022). Let us consider two scenarios:

1. the variability of a compact source due to RISS across the MWA bandwidth,

2. the variability of a PS source due to varying opacity.

In the first scenario, as discussed in Section 1.2.1, we do not expect the spectral

shape to change, but we do expect to see slow constant changes across the entire MWA bandwidth on timescales of roughly 1.5 years. In this case, to sample the variability due to RISS, we can bin our observations on timescales of ∼months over several years. In principle, the multi-epoch VIP should be significant between each epoch and roughly similar in magnitude as we probe the slow trend of variability. Conversely, the multi-epoch MOSS parameter should be small in each epoch as the spectral shape remains constant.

In the second scenario, as shown in Chapter 3 (Ross et al., 2022), a source with varying opacity is likely also compact enough to also show variability due to RISS. Identifying the variability due to the varying opacity is dependent on distinguishing it from RISS. As discussed above, the multi-epoch MOSS parameter should be fairly consistent (and small) across epochs for RISS. Alternatively, both the multi-epoch VIP and MOSS binned at a similar time cadence for RISS, should show a "flare" in the epoch where the spectral shape changes dramatically. Given in this Thesis we identify a dramatic change in spectral shape due to variable opacity in the MWA bandwidth due on timescales of ∼months, one could also bin the multi-epoch VIP and MOSS on shorter timescales. This would increase sensitivity to varying opacity while reducing the sensitivity to variability due to RISS.

To test this approach, we have calculated the multi-epoch VIP and MOSS for two sources from our targeted spectral variability survey which represent the two scenarios (Ross et al., 2022, Chapter 3): GLEAM J001513–472706 and GLEAM J020507–110922. We identified GLEAM J001513–472706 as a variable source entirely consistent with RISS, with a constant spectral shape and trend of variability across 2020. Conversely, GLEAM J020507–110922 showed a fairly consistent shape until the epoch in September 2020, where the spectral shape changed dramatically due to a variable opacity. In Figure 5.1 we present the binned multi-epoch VIP and MOSS for both sources. We can see that the multi-epoch VIP for GLEAM J001513–472706 is fairly large while the mutli-epoch MOSS remains

small with some scatter. Conversely, the multi-epoch VIP for GLEAM J020507–110922 shows a dramatic flare between July 2020 and September 2020, which coincides with the epoch we see a dramatic change in spectral shape. Furthermore, as expected the multi-epoch MOSS parameter also "flares" between July 2020 and September 2020 to a value orders of magnitude larger than all previous epochs, indicative of the change in spectral shape. While only a preliminary analysis, the difference between the multi-epoch VIP and MOSS for these two sources demonstrates the potential use of these statistics for large scale spectral variability surveys. Furthermore, as single frequency variability surveys rely on analysing lightcurves, similar analyses could be applied here, where instead of detecting varying flux density with time, one detects variations in the multi-epoch VIP and MOSS. This would be particularly useful in detecting "flares" with a dramatic change, as well as the overall trends of variability over long periods, while not becoming overwhelmed with increasing time sampling.

A possible extension of the multi-epoch VIP is the potential to investigate the variability of populations across a range of time cadences. For example, by measuring the multi-epoch VIP binned at a range of time cadences sensitive to various variability processes, one could investigate the variability of a single source (or specific population of sources) with respect to each cadence. This could be used to estimate the true prevalence of variability in the radio sky. Furthermore, it may be able to distinguish between different source populations by categorising populations based on the timescales they exhibit variability. For example, blazars would be expected to show variability across most (if not all) time cadences, while large AGN may only be expected to show variability due to RISS (assuming they have a bright, compact hot spot). This may also be helpful for identifying PS sources that are frustrated vs young. As young sources may show slow source evolution and the recent jet activity ages while frustrated PS sources may show dramatic changes in spectral shape due to the environmental interactions.

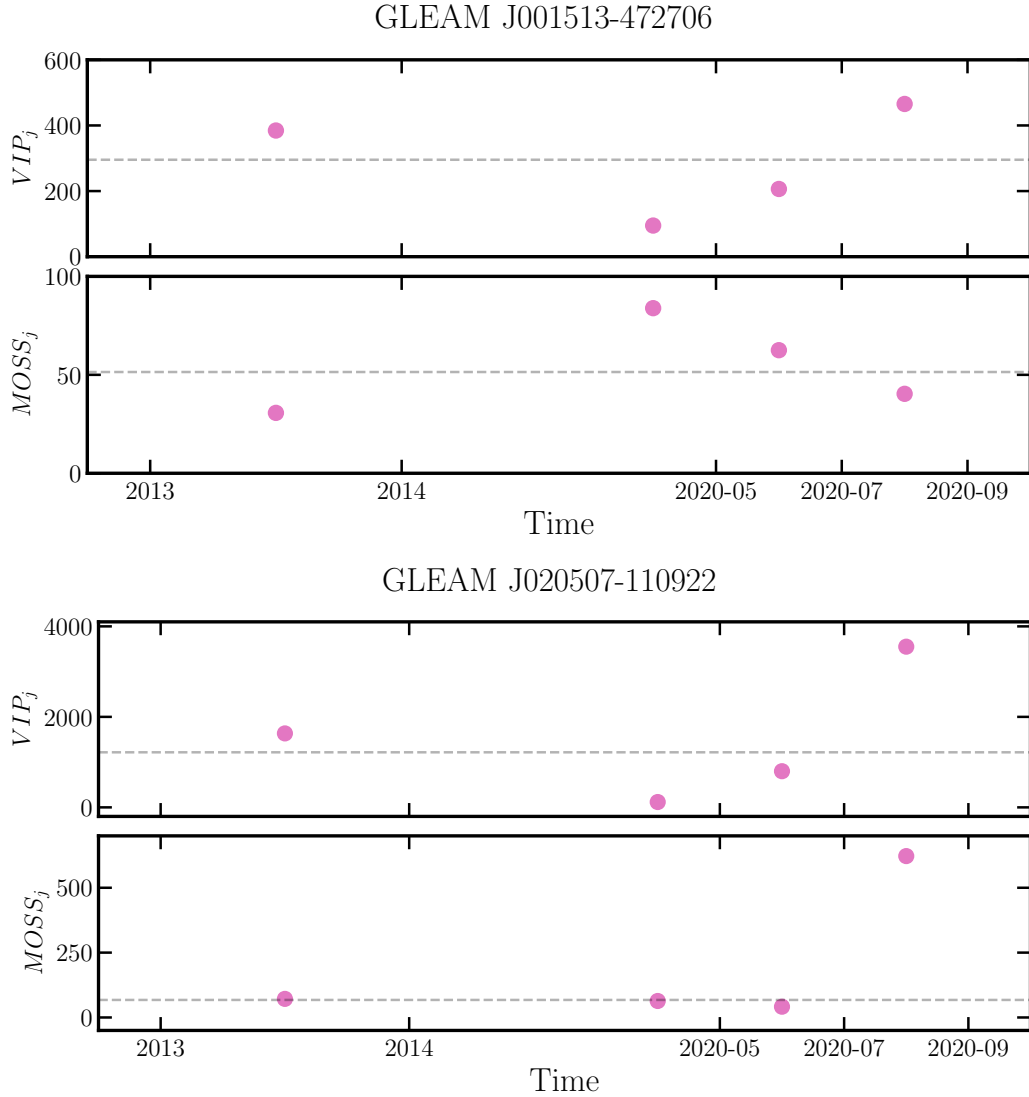Since its discovery in the 1950's, radio frequency variability has pushed the

Figure 5.1: The multi-epoch VIP and MOSS for GLEAM J001513–472706 (top) and GLEAM J020507–110922 (bottom). The VIP and MOSS are calculated for each epoch relative to the prior epoch according to Equation 5.3 and Equation 5.4 respectively. The magnitude of VIP for GLEAM J001513–472706 is large for each epoch, while the MOSS remains low. Conversely, the magnitude of the VIP for GLEAM J020507–110922 increases significantly in the last epoch, paired with an increase in the MOSS parameter in the same epoch, indicative of a dramatic change in spectral shape in this epoch.

limits of our understanding of radio sources (Slee, 1955; Hunstead, 1972). The results of this work highlight that low frequency spectral variability is still a largely unexplored parameter space, rich with possibilities. Recent upgrades and designs of next generation telescopes have placed a high value on sensitive, wide-field instruments to be used to conduct large surveys at rapid speeds; e.g. the Australian SKA Pathfinder (ASKAP), upgraded Giant Metrewave Radio Telescope (uGMRT), LOFAR and Karoo Array Telescope (MeerKAT). With upcoming surveys from these instruments and heading into the SKA-era, the immense volumes of data and vast populations mean it will be critical to design efficient spectral variability surveys. This Thesis presents a methodology for coping with the incoming data and presents a statistical approach to ensure detecting and classifying the low-frequency spectral variability is both rigorous and reproducible. By optimising the design of future spectral variability surveys to probe a range of cadences with large temporal and spectral coverage, it ensures the maximum opportunity to dissect physical origins of variability and determine their broad implications. In particular, we have highlighted the value of large spectral variability surveys in identifying absorption mechanisms for PS sources and inferring compact ($\lesssim 25\,\mathrm{mas}$) features without VLBI. Likewise, we have demonstrated the potential for using low-frequency spectral variability for identifying IDV candidates to characterise properties of the ISM.

# Bibliography

Abareshi B., et al., 2022, arXiv e-prints, p. arXiv:2205.10939

Agócs T., Abrams D. C., Cano Infantes D., O'Mahony N., Dee K., Daban J.-B., Gouvret C., Ottogalli S., 2012, in Stepp L. M., Gilmozzi R., Hall H. J., eds, Society of Photo-Optical Instrumentation Engineers (SPIE) Conference Series Vol. 8444, Ground-based and Airborne Telescopes IV. p. 84446J, doi:10.1117/12.925136

Albareti F. D., et al., 2017, The Astrophysical Journal Supplement Series, 233, 25

Alexander P., 2000, Monthly Notices of the Royal Astronomical Society, 319, 8

Alexander K. D., van Velzen S., Horesh A., Zauderer B. A., 2020, Space Science Reviews, 216, 81

An T., Baan W. A., 2012, The Astrophysical Journal, 760, 77

Armstrong J. W., Rickett B. J., Spangler S. R., 1995, The Astrophysical Journal, 443, 209

Astropy Collaboration et al., 2013, Astronomy and Astrophysics, 558, A33

Barthel P., Haas M., Leipski C., Wilkes B., 2012, The Astrophysical Journal Letters, 757, L26

Beaklini P. P. B., Abraham Z., 2014, Monthly Notices of the Royal Astronomical Society, 437, 489

Becker R. H., White R. L., Helfand D. J., 1995, The Astrophysical Journal, 450, 559

Bell M. E., et al., 2019, Monthly Notices of the Royal Astronomical Society, 482, 2484

Bicknell G. V., Dopita M. A., O'Dea C. P. O., 1997, The Astrophysical Journal, 485, 112

Bicknell G. V., Mukherjee D., Wagner A. Y., Sutherland R. S., Nesvadba N. P. H., 2018, Monthly Notices of the Royal Astronomical Society, 475, 3493

Bignall H. E., et al., 2003, The Astrophysical Journal, 585, 653

Bignall H. E., Tuntsov A. V., Stevens J., Bannister K., Walker M. A., Reynolds C., 2022, Monthly Notices of the Royal Astronomical Society, 513, 2770

Bilicki M., Jarrett T. H., Peacock J. A., Cluver M. E., Steward L., 2014, The Astrophysical Journal Supplement Series, 210, 9

Born M., Wolf E., 1980, Principles of Optics Electromagnetic Theory of Propagation, Interference and Diffraction of Light. Pergamon Press

Bower G. C., Whysong D., Blair S., Croft S., Keating G., Law C., Williams P. K. G., Wright M. C. H., 2011, The Astrophysical Journal, 739, 76

Briggs D. S., 1995, PhD thesis, New Mexico Institute of Mining and Technology

Buchner J., 2021, The Journal of Open Source Software, 6, 3001

Callingham J. R., et al., 2015, The Astrophysical Journal, 809, 168

Callingham J. R., et al., 2017, The Astrophysical Journal, 836, 174

Carilli C. L., Ivison R. J., Frail D. A., 2003, The Astrophysical Journal, 590, 192

Cheng Y. P., Kang S. J., Zheng Y. G., 2022, Monthly Notices of the Royal Astronomical Society, 515, 2215

Chhetri R., Morgan J., Ekers R. D., Macquart J. P., Sadler E. M., Giroletti M., Callingham J. R., Tingay S. J., 2018, Monthly Notices of the Royal Astronomical Society, 474, 4937

Clarke M., 1964, PhD thesis, Cambridge University

Condon J. J., Cotton W. D., Greisen E. W., Yin Q. F., Perley R. A., Taylor G. B., Broderick J. J., 1998, The Astronomical Journal, 115, 1693

D'Abrusco R., et al., 2019, The Astrophysical Journal Supplement Series, 242, 4

Dallacasa D., Orienti M., 2016, Astronomische Nachrichten, 337, 120

Deller A. T., Tingay S. J., Bailes M., West C., 2007, The Publications of the Astronomical Society of the Pacific, 119, 318

Deller A. T., et al., 2011, The Publications of the Astronomical Society of the Pacific, 123, 275

Dennett-Thorpe J., de Bruyn A. G., 2000, The Astrophysical Journal Letters, 529, L65

Driessen L. N., et al., 2022, Monthly Notices of the Royal Astronomical Society, 512, 5037

Driver S. P., Davies L. J., Meyer M., Power C., Robotham A. S. G., Baldry I. K., Liske J., Norberg P., 2016, in Napolitano N. R., Longo G., Marconi M., Paolillo M., Iodice E., eds, Astrophysics and Space Science Proceedings Vol. 42, The Universe of Digital Sky Surveys. p. 205 (arXiv:1507.00676), doi:10.1007/978-3-319-19330-4_32

Duffy P., Blundell K. M., 2012, Monthly Notices of the Royal Astronomical Society, 421, 108

Fan J. H., et al., 2007, Astronomy and Astrophysics, 462, 547

223

Fanaroff B. L., Riley J. M., 1974, Monthly Notices of the Royal Astronomical Society, 167, 31P

Fanti R., Ficarra A., Mantovani F., Padrielli L., Weiler K., 1979, Astronomy and Astrophysics Supplement Series, 36, 359

Fanti R., Fanti C., Schilizzi R. T., Spencer R. E., Nan Rendong Parma P., van Breugel W. J. M., Venturi T., 1990, Astronomy and Astrophysics, 231, 333

Franzen T. M. O., Hurley-Walker N., White S. V., Hancock P. J., Seymour N., Kapińska A. D., Staveley-Smith L., Wayth R. B., 2021, Publications of the Astronomical Society of Australia, 38, e014

Giommi P., Padovani P., Polenta G., Turriziani S., D'Elia V., Piranomonte S., 2012, Monthly Notices of the Royal Astronomical Society, 420, 2899

Gochelashvili K. S., Shishov V. I., 1975, Optical and Quantum Electronics, 7, 524

Goodwin A. J., et al., 2022, Monthly Notices of the Royal Astronomical Society, 511, 5328

Hale C. L., et al., 2021, Publications of the Astronomical Society of Australia, 38, e058

Hamacher D. W., Barsa J., Passi S., Tapim A., 2019, Proceedings of the Royal Society of Victoria, 131, 24

Hancock P. J., Charlton E. G., Macquart J.-P., Hurley-Walker N., 2019, arXiv e-prints, p. arXiv:1907.08395

Hardcastle M. J., Croston J. H., 2020, New Astronomy Reviews, 88, 101539

Hardcastle M. J., Looney L. W., 2008, Monthly Notices of the Royal Astronomical Society, 388, 176

Harwood J. J., et al., 2022, Astronomy and Astrophysics, 658, A8

Heeschen D. S., 1984, The Astronomical Journal, 89, 1111

Hernández-García L., et al., 2017, Astronomy and Astrophysics, 603, A131

Hewish A., Scott P. F., Wills D., 1964, Nature, 203, 1214

Hinshaw G., et al., 2013, The Astrophysical Journal Supplement Series, 208, 19

Hunstead R. W., 1972, Astrophysical Letters, 12, 193

Hunter J. D., 2007, Computing in Science & Engineering, 9, 90

Hurley-Walker N., et al., 2017, Monthly Notices of the Royal Astronomical Society, 464, 1146

Hurley-Walker N., et al., 2019, Publications of the Astronomical Society of Australia, 36, e048

Hurley-Walker N., et al., 2022, arXiv e-prints, p. arXiv:2204.12762

Intema H. T., Jagannathan P., Mooley K. P., Frail D. A., 2017, Astronomy and Astrophysics, 598, A78

Iwai K., Shiota D., Tokumaru M., Fujiki K., Den M., Kubo Y., 2021, Earth, Planets and Space, 73, 9

Jaffe W. J., Perola G. C., 1973, Astronomy and Astrophysics, 26, 423

Jamil O., Fender R. P., Kaiser C. R., 2010, Monthly Notices of the Royal Astronomical Society, 401, 394

Jarrett T. H., et al., 2011, The Astrophysical Journal, 735, 112

Jauncey D. L., et al., 2020, Advances in Space Research, 65, 756

Kameno S., Horiuchi S., Shen Z.-Q., Inoue M., Kobayashi H., Hirabayashi H., Murata Y., 2000, Publications of the Astronomical Society of Japan, 52, 209

Kameno S., Inoue M., Wajima K., Sawada-Satoh S., Shen Z.-Q., 2003, Publications of the Astronomical Society of Australia, 20, 134

Kedziora-Chudczer L., Jauncey D. L., Wieringa M. H., Walker M. A., Nicolson G. D., Reynolds J. E., Tzioumis A. K., 1997, The Astrophysical Journal Letters, 490, L9

Keim M. A., Callingham J. R., Röttgering H. J. A., 2019, Astronomy and Astrophysics, 628, A56

Kellermann K. I., 1966, The Astrophysical Journal, 146, 621

Kellermann K. I., Pauliny-Toth I. I. K., 1969, The Astrophysical Journal Letters, 155, L71

Kellermann K. I., Pauliny-Toth I. I. K., 1981, Annual Review of Astronomy and Astrophysics, 19, 373

Kettenis M., van Langevelde H. J., Reynolds C., Cotton B., 2006, in Gabriel C., Arviset C., Ponz D., Enrique S., eds, Astronomical Society of the Pacific Conference Series Vol. 351, Astronomical Data Analysis Software and Systems XV. p. 497

Koay J. Y., et al., 2018, Monthly Notices of the Royal Astronomical Society, 474, 4396

Koay J. Y., et al., 2019, Monthly Notices of the Royal Astronomical Society, 489, 5365

Komissarov S. S., Gubanov A. G., 1994, Astronomy and Astrophysics, 285, 27

Konar C., Hardcastle M. J., 2013, Monthly Notices of the Royal Astronomical Society, 436, 1595

Kudryavtseva N. A., et al., 2011, Astronomy and Astrophysics, 526, A51

Kunert-Bajraszewska M., Marecki A., Thomasson P., 2006, Astronomy and Astrophysics, 450, 945

Kunert-Bajraszewska M., Gawroński M. P., Labiano A., Siemiginowska A., 2010, Monthly Notices of the Royal Astronomical Society, 408, 2261

Lang K. R., 1980, Astrophysical Formulae. A Compendium for the Physicist and Astrophysicist.. Springer

Large M. I., Mills B. Y., Little A. G., Crawford D. F., Sutton J. M., 1981, Monthly Notices of the Royal Astronomical Society, 194, 693

Large M. I., Cram L. E., Burgess A. M., 1991, The Observatory, 111, 72

Liu X., et al., 2017, Monthly Notices of the Royal Astronomical Society, 469, 2457

Liu L.-J., et al., 2021, Monthly Notices of the Royal Astronomical Society, 504, 5437

Lonsdale C. J., et al., 2015, The Astrophysical Journal, 813, 45

Lovell J. E. J., Jauncey D. L., Bignall H. E., Kedziora-Chudczer L., Macquart J. P., Rickett B. J., Tzioumis A. K., 2003, The Astronomical Journal, 126, 1699

Lovell J. E. J., et al., 2008, The Astrophysical Journal, 689, 108

Madau P., Ghisellini G., Persic M., 1987, Monthly Notices of the Royal Astronomical Society, 224, 257

Malik Z., Shah Z., Sahayanathan S., Iqbal N., Manzoor A., 2022, Monthly Notices of the Royal Astronomical Society, 514, 4259

Manolakou K., Kirk J. G., 2002, Astronomy and Astrophysics, 391, 127

Marr J. M., Perry T. M., Read J., Taylor G. B., Morris A. O., 2014, The Astrophysical Journal, 780, 178

Marscher A. P., 1983, The Astrophysical Journal, 264, 296

Marscher A. P., Gear W. K., 1985, The Astrophysical Journal, 298, 114

Martí-Vidal I., Roy A., Conway J., Zensus A. J., 2016, Astronomy and Astrophysics, 587, A143

Massaro E., Giommi P., Leto C., Marchegiani P., Maselli A., Perri M., Piranomonte S., Sclavi S., 2009, Astronomy and Astrophysics, 495, 691

Massaro E., Maselli A., Leto C., Marchegiani P., Perri M., Giommi P., Piranomonte S., 2015, Astrophysics and Space Science, 357, 75

Mauch T., Murphy T., Buttery H. J., Curran J., Hunstead R. W., Piestrzynski B., Robertson J. G., Sadler E. M., 2003, Monthly Notices of the Royal Astronomical Society, 342, 1117

McConnell D., et al., 2020, Publications of the Astronomical Society of Australia, 37, e048

McKinley B., et al., 2022, Nature Astronomy, 6, 109

McMullin J. P., Waters B., Schiebel D., Young W., Golap K., 2007, in Shaw R. A., Hill F., Bell D. J., eds, Astronomical Society of the Pacific Conference Series Vol. 376, Astronomical Data Analysis Software and Systems XVI. p. 127

Middei R., Giommi P., Perri M., Turriziani S., Sahakyan N., Chang Y. L., Leto C., Verrecchia F., 2022, Monthly Notices of the Royal Astronomical Society, 514, 3179

Miley G., 1980, Annual Review of Astronomy and Astrophysics, 18, 165

Mingaliev M. G., Sotnikova Y. V., Torniainen I., Tornikoski M., Udovitskiy R. Y., 2012, Astronomy and Astrophysics, 544, A25

Mooley K. P., et al., 2016, The Astrophysical Journal, 818, 105

Morgan J. S., et al., 2018, Monthly Notices of the Royal Astronomical Society, 473, 2965

Morgan J. S., Macquart J. P., Chhetri R., Ekers R. D., Tingay S. J., Sadler E. M., 2019, Publications of the Astronomical Society of Australia, 36, e002

Murgia M., 2003, Publications of the Astronomical Society of Australia, 20, 19

Murphy T., et al., 2010, Monthly Notices of the Royal Astronomical Society, 402, 2403

Murphy T., et al., 2017, Monthly Notices of the Royal Astronomical Society, 466, 1944

Murphy T., et al., 2021, Publications of the Astronomical Society of Australia, 38, e054

Narayan R., 1992, Philosophical Transactions of the Royal Society of London Series A, 341, 151

Nyland K., et al., 2020, The Astrophysical Journal, 905, 74

Nyquist H., 1928, Transactions of the American Institute of Electrical Engineers, 47, 617

O'Dea C. P., 1998, The Publications of the Astronomical Society of the Pacific, 110, 493

O'Dea C. P., Baum S. A., 1997, The Astronomical Journal, 113, 148

O'Dea C. P., Saikia D. J., 2021, The Astronomy and Astrophysics Review, 29, 3

O'Dea C. P., Baum S. A., Stanghellini C., 1991, The Astrophysical Journal, 380, 66

Ochsenbein F., Bauer P., Marcout J., 2000, Astronomy and Astrophysics Supplement Series, 143, 23

Oei M. S. S. L., et al., 2022, Astronomy and Astrophysics, 660, A2

Ofek E. O., Frail D. A., Breslauer B., Kulkarni S. R., Chandra P., Gal-Yam A., Kasliwal M. M., Gehrels N., 2011, The Astrophysical Journal, 740, 65

Orienti M., Dallacasa D., 2008, Astronomy and Astrophysics, 487, 885

Orienti M., Dallacasa D., 2014, Monthly Notices of the Royal Astronomical Society, 438, 463

Orienti M., Dallacasa D., 2020, Monthly Notices of the Royal Astronomical Society, 499, 1340

Orienti M., Dallacasa D., Tinti S., Stanghellini C., 2006, Astronomy and Astrophysics, 450, 959

Orienti M., Murgia M., Dallacasa D., 2010, Monthly Notices of the Royal Astronomical Society, 402, 1892

Ostorero L., Villata M., Raiteri C. M., 2004, Astronomy and Astrophysics, 419, 913

Owsianik I., Conway J. E., 1998, Astronomy and Astrophysics, 337, 69

Pacholczyk A. G., 1970, Radio astrophysics. Nonthermal processes in galactic and extragalactic sources. W.H. Freeman & Co

Padovani P., Bonzini M., Kellermann K. I., Miller N., Mainieri V., Tozzi P., 2015, Monthly Notices of the Royal Astronomical Society, 452, 1263

Padovani P., et al., 2017, The Astronomy and Astrophysics Review, 25, 2

Pajdosz-Śmierciak U., Jamrozy M., Soida M., Stawarz Ł., 2018, The Astrophysical Journal, 868, 64

Pajdosz-Śmierciak U., Śmierciak B., Jamrozy M., 2022, Monthly Notices of the Royal Astronomical Society, 514, 2122

Payne-Scott R., 1949, Australian Journal of Scientific Research A Physical Sciences, 2, 214

Peck A. B., Taylor G. B., Conway J. E., 1999, The Astrophysical Journal, 521, 103

Pérez F., Granger B. E., 2007, Computing in Science and Engineering, 9, 21

Phillips R. B., Mutel R. L., 1982, Astronomy and Astrophysics, 106, 21

Polatidis A. G., Conway J. E., 2003, Publications of the Astronomical Society of Australia, 20, 69

Price-Whelan A. M., et al., 2018, The Astronomical Journal, 156, 123

Quici B., et al., 2021, Publications of the Astronomical Society of Australia, 38, e008

Quirrenbach A., Witzel A., Krichbaum T., Hummel C. A., Alberdi A., 1989, Nature, 337, 442

Quirrenbach A., et al., 1992, Astronomy and Astrophysics, 258, 279

Raiteri C. M., et al., 2017, Nature, 552, 374

Readhead A. C. S., Taylor G. B., Pearson T. J., Wilkinson P. N., 1996, The Astrophysical Journal, 460, 634

Richards J. L., et al., 2011, The Astrophysical Journal Supplement Series, 194, 29

Rickett B. J., 1990, Annual Review of Astronomy and Astrophysics, 28, 561

Rickett B. J., Quirrenbach A., Wegner R., Krichbaum T. P., Witzel A., 1995, Astronomy and Astrophysics, 293, 479

Rieger F. M., 2004, The Astrophysical Journal Letters, 615, L5

Rioul O., Vetterli M., 1991, IEEE Signal Processing Magazine, 8, 14

Ross K., et al., 2021, Monthly Notices of the Royal Astronomical Society, 501, 6139

Ross K., Hurley-Walker N., Seymour N., Callingham J. R., Galvin T. J., Johnston-Hollitt M., 2022, Monthly Notices of the Royal Astronomical Society, 512, 5358

Rossetti A., Fanti C., Fanti R., Dallacasa D., Stanghellini C., 2006, Astronomy and Astrophysics, 449, 49

Sadler E. M., 2016, Astronomische Nachrichten, 337, 105

Said N. M. M., Ellingsen S. P., Bignall H. E., Shabala S., McCallum J. N., Reynolds C., 2020, Monthly Notices of the Royal Astronomical Society, 498, 4615

Saikia D. J., Gupta N., 2003, Astronomy and Astrophysics, 405, 499

Sarbadhicary S. K., et al., 2021, The Astrophysical Journal, 923, 31

Shabala S. S., Jurlin N., Morganti R., Brienza M., Hardcastle M. J., Godfrey L. E. H., Krause M. G. H., Turner R. J., 2020, Monthly Notices of the Royal Astronomical Society, 496, 1706

Shannon C. E., 1949, IEEE Proceedings, 37, 10

Shklovskii I. S., 1960, Soviet Astronomy, 4, 243

Slee O. B., 1955, Australian Journal of Physics, 8, 498

Snellen I. A. G., Schilizzi R. T., de Bruyn A. G., Miley G. K., Rengelink R. B., Roettgering H. J., Bremer M. N., 1998, Astronomy and Astrophysics Supplement Series, 131, 435

Snellen I. A. G., Schilizzi R. T., Miley G. K., de Bruyn A. G., Bremer M. N., Röttgering H. J. A., 2000, Monthly Notices of the Royal Astronomical Society, 319, 445

Stern D., et al., 2012, The Astrophysical Journal, 753, 30

Sukharev A., et al., 2020, Astrophysics, 63, 32

Tadhunter C., Morganti R., Santoro F., Bernhard E., 2021, Astronomische Nachrichten, 342, 1200

Tary J. B., Herrera R. H., van der Baan M., 2018, Philosophical Transactions of the Royal Society of London Series A, 376, 20170254

Taylor M. B., 2005, TOPCAT &amp; STIL: Starlink Table/VOTable Processing Software. Shopbell, P. and Britton, M. and Ebert, R., p. 29

Thorne J., Robotham A., Davies L., Bellstedt S., 2022, AGN Unification Diagram, doi:10.5281/zenodo.6381013, https://doi.org/10.5281/zenodo.6381013

Tingay S. J., de Kool M., 2003, The Astronomical Journal, 126, 723

Tingay S. J., et al., 2013, Publications of the Astronomical Society of Australia, 30, e007

Tingay S. J., et al., 2015, The Astronomical Journal, 149, 74

Tinti S., de Zotti G., 2006, Astronomy and Astrophysics, 445, 889

Tinti S., Dallacasa D., de Zotti G., Celotti A., Stanghellini C., 2005, Astronomy and Astrophysics, 432, 31

Torniainen I., Tornikoski M., Teräsranta H., Aller M. F., Aller H. D., 2005, Astronomy and Astrophysics, 435, 839

Torniainen I., Tornikoski M., Lähteenmäki A., Aller M. F., Aller H. D., Mingaliev M. G., 2007, Astronomy and Astrophysics, 469, 451

Turner R. J., Shabala S. S., Krause M. G. H., 2018, Monthly Notices of the Royal Astronomical Society, 474, 3361

Tzioumis A. K., et al., 2010, The Astronomical Journal, 140, 1506

Virtanen P., et al., 2020, Nature Methods, 17, 261

Walker M. A., 1998, Monthly Notices of the Royal Astronomical Society, 294, 307

Walker M. A., 2001, Monthly Notices of the Royal Astronomical Society, 321, 176

Walker M. A., Tuntsov A. V., Bignall H., Reynolds C., Bannister K. W., Johnston S., Stevens J., Ravi V., 2017, The Astrophysical Journal, 843, 15

Wall J. V., 1975, The Observatory, 95, 196

Wang Y., Tuntsov A., Murphy T., Lenc E., Walker M., Bannister K., Kaplan D. L., Mahony E. K., 2021, Monthly Notices of the Royal Astronomical Society, 502, 3294

Wayth R. B., et al., 2015, Publications of the Astronomical Society of Australia, 32, e025

Wayth R. B., et al., 2018, Publications of the Astronomical Society of Australia, 35, e033

Wells D. C., 1985, Nrao'S Astronomical Image Processing System (AIPS). Springer US, Boston, MA, pp 195–209, doi:10.1007/978-1-4615-9433-8˙18, https://doi.org/10.1007/978-1-4615-9433-8_18

Werner M. W., et al., 2004, The Astrophysical Journal Supplement Series, 154, 1

Wes McKinney 2010, in Stéfan van der Walt Jarrod Millman eds, Proceedings of the 9th Python in Science Conference. pp 56 – 61, doi:10.25080/Majora-92bf1922-00a

Wilkinson P. N., Booth R. S., Cornwell T. J., Clark R. R., 1984, Nature, 308, 619

Wilson W. E., et al., 2011, Monthly Notices of the Royal Astronomical Society, 416, 832

Wołowska A., Kunert-Bajraszewska M., Mooley K., Hallinan G., 2017, Frontiers in Astronomy and Space Sciences, 4, 38

Wołowska A., et al., 2021, The Astrophysical Journal, 914, 22

Worrall D. M., Birkinshaw M., Young A. J., Momtahan K., Fosbury R. A. E., Morganti R., Tadhunter C. N., Verdoes Kleijn G., 2012, Monthly Notices of the Royal Astronomical Society, 424, 1346

Wright E. L., 2006, The Publications of the Astronomical Society of the Pacific, 118, 1711

Wright E. L., et al., 2010, The Astronomical Journal, 140, 1868

Yang X.-h., Chen P.-s., Huang Y., 2015, Monthly Notices of the Royal Astronomical Society, 449, 3191

de Vries W. H., Becker R. H., White R. L., Helfand D. J., 2004, The Astronomical Journal, 127, 2565

pandas development team T., 2020, pandas-dev/pandas: Pandas, doi:10.5281/zenodo.3509134, https://doi.org/10.5281/zenodo.3509134

van Breugel W., Miley G., Heckman T., 1984, The Astronomical Journal, 89, 5

van der Laan H., 1966, Nature, 211, 1131

van der Walt S., Colbert S. C., Varoquaux G., 2011, Computing in Science Engineering, 13, 22

# Appendices

# Appendix A

## A    Detailed List of Spectral Models

As there are several spectral models, this section aims to summarise the physical and non-physical models relevant to this Thesis as well as modifications for various physical scenarios. We do not comment on the feasibility of differentiating between these models here, nor the difficulties for spectral models with a large number of parameters. For discussions on these limitations, see Section 1.1.3 and Ross et al. (2022).

### A.1    Non-Peaked Spectral Models

A synchrotron emitting component, can be modelled according to a power-law spectral model with spectral index $\alpha$. As the synchrotron emission of the component is a combination of the emission due to individual particles, we define $\beta$ as the spectral index for the electron energy distribution. The power-law, non-thermal, synchrotron emission is thus written as:

$$S_\nu = S_0 \nu^\alpha \tag{A5}$$

where $\alpha = (\beta - 1)/2$.

As discussed in Section 1.2.2.1, the ageing of a synchrotron emitting region results in a spectral break at higher frequencies. This is separate to the spectral peak due to absorption (see Section A.2). This can be modelled by including a

multiplicative factor according to:

$$S_\nu = S_0 \nu^\alpha e^{\nu/\nu_b} \tag{A6}$$

This can also be modelled according to the continuous injection model, where the injection of energy producing the overall synchrotron emission is assumed to stay constant, but the plasma has aged. Thus the spectral break, $\nu_b$, is evident as a result of the inverse Compton loses, synchrotron losses and adiabatic expansion.

$$S_\nu = S_0 \left(\frac{\nu}{\nu_b}\right)^\alpha \tag{A7}$$

where at $\nu > \nu_b$, $\alpha$ steepens by 0.5.

For a plasma where the injection has been stopped and the plasma is only ageing, there are several further spectral models. These models can determine physical parameters of the plasma based on the $\nu_b$ and steepening of the spectrum above $\nu_b$, see Turner et al. (2018); Quici et al. (2021) for more details.

## A.2 Curved Spectral Models

### A.2.1 Non-Physical Curved Spectral Models

With sufficient spectral coverage, it is possible to detect curvature within the bandwidth without sufficiently sampling both above and below the peak frequency, $\nu_p$. Duffy & Blundell (2012) introduce a multiplicative factor in which $q$ parameterised the spectral curvature. This model assumes a typical power-law spectral model according to:

$$\begin{aligned} S_\nu &= S_0 \nu^\alpha e^{q(\ln \nu)^2}, \\ \nu_p &= e^{-\alpha/2q} \end{aligned} \tag{A8}$$

where $\nu_p$ is the peak frequency. Typically, significant curvature is determined when $|q| > 0.2$ (Callingham et al., 2017), and as $q$ approaches zero, Equation A8

approaches a typical power-law spectral model as defined in Equation A5.

A curved spectral model can also be modelled according to two separate power-law models for frequencies above and below the spectral peak. This model introduces two spectral indices, $\alpha_{\text{thick}}$ and $\alpha_{\text{thin}}$, describing the optically thick and optically thin regions of the SED respectively, but is not based on any physical modelling (Snellen et al., 1998). As such, it does not assume any underlying process behind the absorption causing the spectral peak and cannot be used to differentiate between SSA and FFA. The entire spectrum can be modelled using the double power-law model according to:

$$S_\nu = \frac{S_p}{(1 - e^{-1})} \left(1 - e^{-(\nu/\nu_p)^{\alpha_{\text{thin}} - \alpha_{\text{thick}}}}\right) \left(\frac{\nu}{\nu_p}\right) \tag{A9}$$

where $S_p$ is the flux density at the peak frequency $\nu_p$.

### A.2.2 Synchrotron Self-Absorption

A single SSA model assumes a single synchrotron emitting region that is compact enough that the synchrotron emission can be scattered by the same relativistic electrons that produced the initial radiation. In this case, we define the optical depth as $\tau_\nu$, and the peak frequency is the frequency where the optical depth of the plasma is unity. This spectral model assumes the plasma is emitting synchrotron radiation according to the typical power-law spectral model described in Equation A5. The single SSA spectral model is:

$$S_\nu = S_0 \left(\frac{\nu}{\nu_p}\right)^{\frac{\beta-1}{2}} \left[\frac{1 - e^{-\tau_\nu}}{\tau_\nu}\right],$$

$$\text{where} \tag{A10}$$

$$\tau_\nu = \left(\frac{\nu}{\nu_p}\right)^{\frac{-(\beta+4)}{2}}.$$

where again, $\beta$ is the spectral index of the electron energy distribution.

This can be modified to introduce multiple synchrotron emitting regions, each

of which is also self-absorbed. Such a model includes spectral indices for each component as well as a $\nu_p$ for each region according to:

$$S_\nu = \sum_{i=1}^{n} S_{i,0} \left(\frac{\nu}{\nu_{i,p}}\right)^{\frac{\beta_i - 1}{2}} \left[\frac{1 - e^{-\tau_{i,\nu}}}{\tau_{i,\nu}}\right],$$

where (A11)

$$\tau_{i,\nu} = \left(\frac{\nu}{\nu_{i,p}}\right)^{\frac{-(\beta_i + 4)}{2}}.$$

where $n$ is the number of SSA components.

Furthermore, the SSA spectral models can also be modified to introduce the multiplicative factor to account for the ageing of the plasma, as with the power-law spectral model, such that:

$$S_\nu = \sum_{i=1}^{n} S_{i,0} \left(\frac{\nu}{\nu_{i,p}}\right)^{\frac{\beta_i - 1}{2}} \left[\frac{1 - e^{-\tau_{i,\nu}}}{\tau_{i,\nu}}\right] e^{\nu/\nu_b},$$

where (A12)

$$\tau_{i,\nu} = \left(\frac{\nu}{\nu_{i,p}}\right)^{\frac{-(\beta_i + 4)}{2}}.$$

### A.2.3   Homogeneous Free-Free Absorption

In some cases, the peaked spectral model is not well modelled by a double power-law spectral model associated with non-physical models and SSA models. One can model the spectrum assuming the emission from the plasma, following a non-thermal power-law, is surrounded by a homogeneous ionized plasma. This plasma absorbs emission from the plasma due to FFA (inverse Bremsstrahlung):

$$S_\nu = S_0 \nu^\alpha e^{-\tau_\nu},$$

where (A13)

$$\tau_\nu = \left(\frac{\nu}{\nu_p}\right)^{-2.1}$$

where $\tau$ is the optical depth due to FFA, and $\nu_p$ is the peak frequency and is the frequency at which $\tau$ is unity. In this case, the optically thick region of the spectrum is not modelled by a power-law but is exponentially attenuated.

As with the SSA spectral model, the homogeneous FFA spectral model can also be modified assuming multiple components. This multi-component FFA model assumes each region is a synchrotron emitting component each surrounded by a homogeneous ionised screen:

$$S_\nu = \sum_{i=1}^{n} S_{i,0} \nu^{\alpha_i} e^{-\tau_{i,\nu}},$$

where $\qquad\qquad\qquad\qquad\qquad\qquad$ (A14)

$$\tau_{i,\nu} = \left( \frac{\nu}{\nu_{i,p}} \right)^{-2.1}$$

where each component has a peak frequency $\nu_{i,p}$.

Furthermore, the absorbing ionised screen may be mixed with relativistic electrons. In which case, the FFA spectral model is adapted to include a factor for this relativistic electrons based on Equation A10:

$$S_\nu = \sum_{i=1}^{n} S_0 \nu^{\alpha_i} \left[ \frac{1 - e^{-\tau_{i,\nu}}}{\tau_{i,\nu}} \right],$$

where $\qquad\qquad\qquad\qquad\qquad\qquad$ (A15)

$$\tau_\nu = \left( \frac{\nu}{\nu_{i,p}} \right)^{-2.1}$$

Lastly, each of the homogeneous FFA spectral models can each be modified to include the multiplicative factor, $e^{\nu/\nu_p}$ to account for ageing of the synchrotron emitting component.

### A.2.4 Inhomogeneous Free-Free Absorption

If the ionised screen is inhomogeneous, the absorbing screen can be modelled using a range of optical depths. Bicknell et al. (1997) suggest the range of optical

depths can be modelled by a power-law relating to the electron energies and temperatures of the overall cloud. This power-law is parameterised by the factor $p$, such that the overall spectrum for a synchrotron emitting component with absorption due to an inhomogeneous screen is:

$$S_\nu = S_0(p+1)\gamma\left[p+1, \left(\frac{\nu}{\nu_p}\right)^{-2.1}\right]\left(\frac{\nu}{\nu_p}\right)^{2.1(p+1)+\alpha} \tag{A16}$$

where $\gamma$ is the lower incomplete gamma function of order $p+1$. If $p = -1$, this just becomes the FFA descried in Equation A13.

As with the SSA and homogeneous FFA spectral models, the inhomogeneous FFA model can also be modified to include multiple regions:

$$S_\nu = \sum_{i=1}^{n} S_{i,0}(p_i+1)\gamma\left[p_i+1, \left(\frac{\nu}{\nu_{i,p}}\right)^{-2.1}\right]\left(\frac{\nu}{\nu_{i,p}}\right)^{2.1(p_i+1)+\alpha_i} \tag{A17}$$

Likewise, the inhomogeneous FFA spectral models can also be modified to also include the multiplicative factor for exponential break, $e^{\nu/\nu_p}$.

# Appendix B

## B Predicting Scintillation for a Resolved Source

Predicting the scintillation for a resolved source has often assumed a single compact component embedded within an extended structure. However, as the work of this Thesis has identified a PS source that is resolved into multiple components, it became necessary to develop a method for characterising the scintillation for a multi-component source. In this section, we derive an expression for the expected scintillation in this scenario and discuss the limitations of detecting and characterising scintillation of a resolved, multi-component source.

### B.1 Single Resolved Source with Embedded Compact Feature

Considering the case of a single source with extended structure, we can assume the resolved source can be modelled as a Gaussian intensity profile where the width of the Gaussian is larger than the scintillation screen angle ($\theta_{\mathrm{screen}}$). The detected overall variability is the sum of flux variations for each region (Narayan, 1992). If the bright scintillating compact region dominates the overall flux, the summed flux variations will also be dominated by the scintillation of the compact region. However, the extended structure dampens the overall detected scintillation compared to an isolated compact region, thus producing a decreased modulation index and increased timescale. Furthermore, if the source is far more extended (i.e. $\theta_{\mathrm{src}} >> \theta_{\mathrm{screen}}$) and/or the flux of the compact region is not the dominant

source of emission, the overall modulation due to scintillation is dampened beyond a level of possible detection. Thus in the first scenario, scintillation can be detected for an extended source provided the overall flux density is dominated by the compact region.

## B.2   Multiple Compact Components

Now considering the case of multiple compact components separated by a small angle. Narayan (1992) demonstrate that for two compact components separated by an angle $\phi$, the intensity profiles of each component will be equal with a shift in the observer plane relative to the angle and distance to the scattering screen, $D$. To understand this scenario, we consider the scintillation of an individual component, $i$, as a time-varying signal, $s_i(t)$, with amplitude $A_i$ and phase $\omega_i$ for some random noise and/or measurement error, $\eta$. Therefore, the overall scintillation can also be represented as a signal, $S(t)$, produced from the superposition of the signals from individual components, such that:

$$S(t) = \sum_{i=1}^{n} s_i(t)$$

where

$$s_i(t) = A_i(t) \sin\left(\omega_i t\right) + \eta(t)$$

(B1)

for a source with a finite number of components, $n$. The expression of $s_i(t)$ in Equation B1 is a simplification of the power spectrum of flux variations presented by Gochelashvili & Shishov (1975), which incorporates the properties of the scattering screen, assuming Kolmogorov turbulence. For the purpose of this discussion, it is sufficient to simplify the flux variations as a harmonic component with some additive noise.

In the case where components have some angular separation, $\phi$, we can thus

represent the angular separation as a phase shift in the signal such that:

$$s_{i+1}(t) = A_i(t) \sin{(\omega_i t + \phi)} + \eta(t) \tag{B2}$$

for a component, $i + 1$, with angular separation $\phi$ from a distinct separate component $i$. In this case, we assume each component is compact relative to the scattering disk and that $\phi$ is sufficiently small, thus the scattering screen through each line-of-sight for each component is the roughly same, and the timescale will also be the same. Thus, the small angle separation between components is equivalent to a time-delay in the flux variations. This time delay will also depend on the velocity of the screen (and thus the distance to the screen), as the regions of focusing and de-focusing pass across each component. Likewise, it is clear from Equation B2, the phase of the flux variations for the individual components, equivalent to $\omega_i$, is the same, thus each component has the same timescale of variability.

In the case where $\theta_i >> \theta_{\text{screen}}$ for the individual components, Equation B2 no longer holds as the timescales are no longer necessarily the same. Furthermore, the amplitudes of modulation for the extended sources will be dampened, as discussed in Section B.1. In Figure B.2, we present an example similar to that presented in Figure B.1, but with a random timescale and amplitude for each component. With the added variable timescales and amplitudes for a multi-component source, the overall scintillation of the source becomes far more complex and observing sufficient scintillation to characterise the contributing components is unlikely.

## B.3 Detecting Scintillation of a Resolved Structure

In practice, the detection of the overall flux variation arising from several compact components would be limited by the out-of-phase signals where a large amount of flux variation cancel each other out and the total flux variations is below a sig-
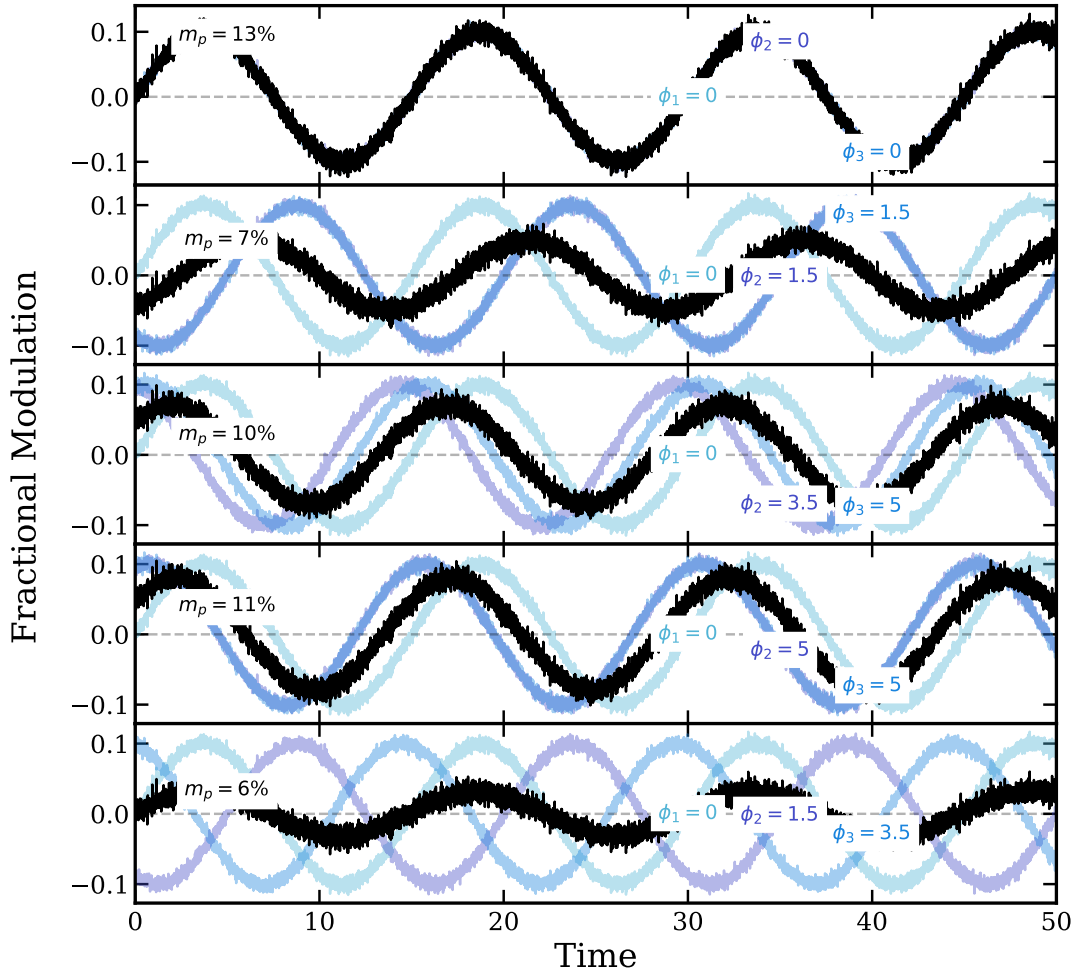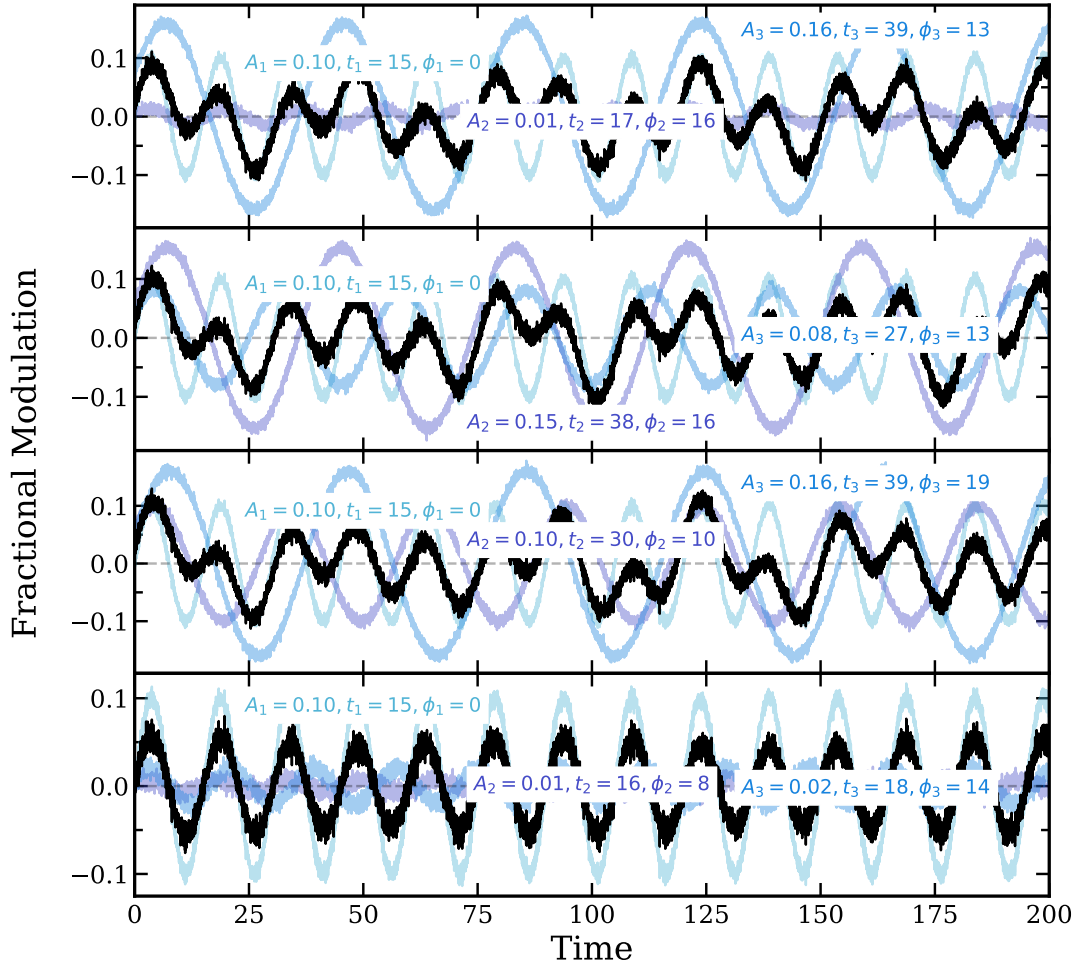
Figure B.1: Example predicted total scintillation (black) for a three component source (turquoise, purple, blue) with various phase shifts between the three components. Each component is modelled assuming a timescale of scintillation of 15 arbitrary units and 10% modulation index with an 0.5% random noise. One component is assumed to contain 50% of the overall flux density, with the other 50% split between the other two components (i.e. 25% of the overall flux density each). For varying phase shifts $\phi_2$ and $\phi_3$ relative to $\phi_1$, the overall superposition of the scintillation has varying modulation indices, $m_p$, corresponding to additive scintillation and de-constructive scintillation. When the scintillation of each component is in phase (top), the modulation of the overall source increases above the the modulation of individual components (i.e. from 10% for each component, to 13% for the total source). Conversely, when $\phi_2$ and $\phi_3$ are out of phase with $\phi_1$, the modulation decreases to just 6%.

Figure B.2: Example predicted total scintillation (black) for a three component source (turquoise, purple, blue) with various phase shifts between the three components. Each component is modelled assuming a timescale of scintillation of 15 arbitrary units and 10% modulation index with an 0.5% random noise. One component is assumed to contain 50% of the overall flux density, with the other 50% split between the other two components (i.e. 25% of the overall flux density each). For varying phase shifts $\phi_2$ and $\phi_3$ relative to $\phi_1$, the overall superposition of the scintillation has varying modulation indices, $m_p$, corresponding to additive scintillation and de-constructive scintillation. When the scintillation of each component is in phase (top), the modulation of the overall source increases above the the modulation of individual components (i.e. from 10% for each component, to 13% for the total source). Conversely, when $\phi_2$ and $\phi_3$ are out of phase with $\phi_1$, the modulation decreases to just 6%.

nificance threshold. However, for a source with a small number of components, with a separation or phase difference between components large enough (relative to the timescale of variability), that the total flux variations add constructively for a long enough period to be detected, it is theoretically possible to extract the timescale and modulation index of scintillation for the resolved source. Furthermore, if the flux density of each component is comparable, the overall combined scintillation may be hard to detect, particularly if they are partially (or fully) out of phase. In Figure B.1, we present an example of scintillation for a source with three compact components with each component scintillating with different phase shifts. Furthermore, in Figure B.2, we present an example of scintillation for a source with three components, two of which are resolved relative to the scattering disk, with a random phase shift. It is clear, when one component is not the dominant source of flux density, and the components are out of phase, the overall detected variations are minimal, compounded if the components are also resolved.

Several observational limitations make such a detection of variability above a reasonable significance threshold, and further determining the parameters producing the observed scintillation, highly unlikely. Despite this, it is possible to get the frequency of the input signals using signal processing techniques involving Fourier transforms. There are several transforms to extract the time-varying properties of such signals including short time Fourier transform (STFT), continuous wavelet transform (CWT), and Synchrosqueezing (Rioul & Vetterli, 1991). Such algorithms and analyses can be used in signal processing of time-varying signals in a range of circumstances from gravitational wave chirps to earthquake seismic signals (Tary et al., 2018). Thus, with sufficient sampling of the time-varying signal of the multi-component source, it is possible to extract the properties of the individual component signals, such as the timescale and modulation index of the scintillation. However, obtaining a light-curve with sufficient time sampling at appropriate cadences and with large enough modulation to be above a certain

detection threshold is both observationally and computationally expensive. Furthermore, accurately measuring the timescale requires sufficient time sampling to avoid under-sampling the combined signal. According to Nyquist-Shannon sampling theorem, if the discrete sampling rate under-samples the signal, it is impossible to accurately recover the signal frequency (Nyquist, 1928; Shannon, 1949). In practice, measuring the scintillation is also further limited by non-uniform sampling and the addition of noise and measurement errors. Consequently, to accurately recover the timescale of scintillation for a resolved, multi-component source, one requires sufficient time sampling of the modulation in periods of "activity" where the modulation is large enough it is above a detection threshold.

# Appendix C

## C   Accepted Papers

### Milliarcsecond Structures of Variable Peaked-Spectrum Sources

*The contents of Chapter 4 has been accepted as "Milliarcsecond Structures of Variable Peaked-Spectrum Sources" to the Publications of the Astronomical Society of Australia (PASA). The accepted version of this manuscript is available on arXiv https://arxiv.org/abs/2301.00977.*

# Statement of Contributions by Co-Authors

The published paper titled *"Spectral variability of radio sources at low frequencies"* (Ross et al., 2021) is my own work except for the following contributions:

- Discussion and interpretation of results: J. R. Callingham, N. Hurley-Walker, N. Seymour, P. Hancock;

- MWA processing and mosaic imaging of SGP region: T. M. O. Franzen and S. V. White;

- Interpretation of scintillation variability: P. Hancock and M. E. Bell ;

- Scripts for PS source classification: J. R. Callingham;

- Discussions of PS population variability: J. Morgan;

- Cross-matching for NVSS and WISE: P. Patil;

- Manual inspection of variability and error analysis: J. R. Callingham, N. Hurley-Walker and N. Seymour.

All Co-authors provided feedback and comments during preparation of the manuscript.

The published paper titled *"Wide-band spectral variability of peaked-spectrum sources"* (Ross et al., 2022) is my own work except for the following contributions:

- Discussion and interpretation of the results: N. Hurley-Walker, N. Seymour, J. R. Callingham, T. J. Galvin, M. Johnston-Hollitt

- Observations with the ATCA: N. Seymour, J. R. Callingham

- MWA reduction pipeline development: T. J. Galvin, N. Hurley-Walker;

- ATCA data reduction debugging: J. R. Callingham, N. Seymour;

- Discussion and interpretation of scintillation: H. Bignall;

- Discussions of spectral fitting and statistical analysis: N. Hurley-Walker, N. Seymour, J. R. Callingham;

- Comments on the manuscript and results: M. Johnston-Hollitt.

All Co-authors provided feedback and comments during preparation of the manuscript.

For Chapter 4, titled *"Milliarcsecond structures in variable peaked-spectrum sources"* all work is my own except for the following contributions:

- LBA scheduling, data-processing and calibration: C. Reynolds;

- Discussion and interpretation of results: N. Seymour, J. R. Callingham, N. Hurley-Walker, H. Bignall, C. Reynolds;

- Discussion of theoretical scintillation in particular: H. Bignall;

- Scripts for plotting linear size vs turnover relation: M. Keim;

- Comments and feedback on the preparation of the Chapter: J. R. Callingham, N. Seymour and N. Hurley-Walker;

All Co-authors provided feedback and comments during the preparation of the submitted manuscript.

# To whom it may concern

I, Kathryn Ross, have outlined my contributions and the contributions of Co-authors to the chapters in this Thesis that have been published as *"Spectral variability of radio sources at low frequencies"* and *"Wide-band spectral variability of peaked-spectrum sources"* and contributions to Chapter 4, *"Milliarcsecond structures of variable peaked-spectrum sources"*.
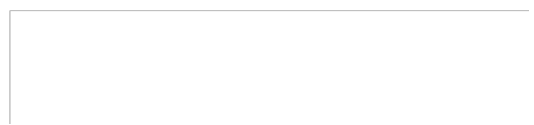
_____

(Signature of candidate)

I, as a Co-author, endorse that the level of contribution indicated by the candidate as in the "Statement of contribution by Co-authors" is appropriate.

Martin Bell

_____          _____

(Full name of Co-author)                        (Signature of Co-author)

# To whom it may concern

I, Kathryn Ross, have outlined my contributions and the contributions of Co-authors to the chapters in this Thesis that have been published as *"Spectral variability of radio sources at low frequencies"* and *"Wide-band spectral variability of peaked-spectrum sources"* and contributions to Chapter 4, *"Milliarcsecond structures of variable peaked-spectrum sources"*.

_____

(Signature of candidate)

I, as a Co-author, endorse that the level of contribution indicated by the candidate as in the "Statement of contribution by Co-authors" is appropriate.

Hayley Emma Bignall

_____        _____

(Full name of Co-author)                          (Signature of Co-author)

# To whom it may concern

I, Kathryn Ross, have outlined my contributions and the contributions of Co-authors to the chapters in this Thesis that have been published as *"Spectral variability of radio sources at low frequencies"* and *"Wide-band spectral variability of peaked-spectrum sources"* and contributions to Chapter 4, *"Milliarcsecond structures of variable peaked-spectrum sources"*.

_____

(Signature of candidate)

I, as a Co-author, endorse that the level of contribution indicated by the candidate as in the "Statement of contribution by Co-authors" is appropriate.

Joseph Callingham
_____

(Full name of Co-author)                                   (Signature of Co-author)

# To whom it may concern

I, Kathryn Ross, have outlined my contributions and the contributions of Co-authors to the chapters in this Thesis that have been published as *"Spectral variability of radio sources at low frequencies"* and *"Wide-band spectral variability of peaked-spectrum sources"* and contributions to Chapter 4, *"Milliarcsecond structures of variable peaked-spectrum sources"*.

_____

(Signature of candidate)

I, as a Co-author, endorse that the level of contribution indicated by the candidate as in the "Statement of contribution by Co-authors" is appropriate.

Thomas Franzen
_____            _____

(Full name of Co-author)                                  (Signature of Co-author)

# To whom it may concern

I, Kathryn Ross, have outlined my contributions and the contributions of Co-authors to the chapters in this Thesis that have been published as *"Spectral variability of radio sources at low frequencies"* and *"Wide-band spectral variability of peaked-spectrum sources"* and contributions to Chapter 4, *"Milliarcsecond structures of variable peaked-spectrum sources"*.

_____

(Signature of candidate)

I, as a Co-author, endorse that the level of contribution indicated by the candidate as in the "Statement of contribution by Co-authors" is appropriate.

_____

(Full name of Co-author)                                        (Signature of Co-author)

# To whom it may concern

I, Kathryn Ross, have outlined my contributions and the contributions of Co-authors to the chapters in this Thesis that have been published as *"Spectral variability of radio sources at low frequencies"* and *"Wide-band spectral variability of peaked-spectrum sources"* and contributions to Chapter 4, *"Milliarcsecond structures of variable peaked-spectrum sources"*.

_____
(Signature of candidate)

I, as a Co-author, endorse that the level of contribution indicated by the candidate as in the "Statement of contribution by Co-authors" is appropriate.

Dr Paul Hancock
_____          _____
(Full name of Co-author)                              (Signature of Co-author)

I, Kathryn Ross, have outlined my contributions and the contributions of Co-authors to the chapters in this Thesis that have been published as *"Spectral variability of radio sources at low frequencies"* and *"Wide-band spectral variability of peaked-spectrum sources"* and contributions to Chapter 4, *"Milliarcsecond structures of variable peaked-spectrum sources"*.

_____

(Signature of candidate)

I, as a Co-author, endorse that the level of contribution indicated by the candidate as in the "Statement of contribution by Co-authors" is appropriate.

Natasha Hurley-Walker

_____         \_\_                                   \_

(Full name of Co-author)                                                    (Signature of Co-author)

# To whom it may concern

I, Kathryn Ross, have outlined my contributions and the contributions of Co-authors to the chapters in this Thesis that have been published as *"Spectral variability of radio sources at low frequencies"* and *"Wide-band spectral variability of peaked-spectrum sources"* and contributions to Chapter 4, *"Milliarcsecond structures of variable peaked-spectrum sources"*.

_____

(Signature of candidate)

I, as a Co-author, endorse that the level of contribution indicated by the candidate as in the "Statement of contribution by Co-authors" is appropriate.

Professor Melanie Johnston-Hollitt

(Full name of Co-author)                                    (Signature of Co-author)

# To whom it may concern

I, Kathryn Ross, have outlined my contributions and the contributions of Co-authors to the chapters in this Thesis that have been published as *"Spectral variability of radio sources at low frequencies"* and *"Wide-band spectral variability of peaked-spectrum sources"* and contributions to Chapter 4, *"Milliarcsecond structures of variable peaked-spectrum sources"*.

_____

(Signature of candidate)

I, as a Co-author, endorse that the level of contribution indicated by the candidate as in the "Statement of contribution by Co-authors" is appropriate.

Michael Alan Keim
_____

(Full name of Co-author)

(Signature of Co-author)

# To whom it may concern

I, Kathryn Ross, have outlined my contributions and the contributions of Co-authors to the chapters in this Thesis that have been published as *"Spectral variability of radio sources at low frequencies"* and *"Wide-band spectral variability of peaked-spectrum sources"* and contributions to Chapter 4. *"Milliarcsecond structures of variable peaked-spectrum sources"*.

(Signature of candidate)

I, as a Co-author, endorse that the level of contribution indicated by the candidate as in the "Statement of contribution by Co-authors" is appropriate.

John Morgan

(Full name of Co-author)

(Signature of Co-author)

# To whom it may concern

I, Kathryn Ross, have outlined my contributions and the contributions of Co-authors to the chapters in this Thesis that have been published as *"Spectral variability of radio sources at low frequencies"* and *"Wide-band spectral variability of peaked-spectrum sources"* and contributions to Chapter 4, *"Milliarcsecond structures of variable peaked-spectrum sources"*.

_____

(Signature of candidate)

I, as a Co-author, endorse that the level of contribution indicated by the candidate as in the "Statement of contribution by Co-authors" is appropriate.

_____Pallavi Patil_____          _____

(Full name of Co-author)                         (Signature of Co-author)

# To whom it may concern

I, Kathryn Ross, have outlined my contributions and the contributions of Co-authors to the chapters in this Thesis that have been published as *"Spectral variability of radio sources at low frequencies"* and *"Wide-band spectral variability of peaked-spectrum sources"* and contributions to Chapter 4, *"Milliarcsecond structures of variable peaked-spectrum sources"*.

_____

(Signature of candidate)

I, as a Co-author, endorse that the level of contribution indicated by the candidate as in the "Statement of contribution by Co-authors" is appropriate.

Cormac Reynolds    25/7/2022
_____          _____

(Full name of Co-author)                          (Signature of Co-author)

# To whom it may concern

I, Kathryn Ross, have outlined my contributions and the contributions of Co-authors to the chapters in this Thesis that have been published as *"Spectral variability of radio sources at low frequencies"* and *"Wide-band spectral variability of peaked-spectrum sources"* and contributions to Chapter 4, *"Milliarcsecond structures of variable peaked-spectrum sources"*.

_____

(Signature of candidate)

I, as a Co-author, endorse that the level of contribution indicated by the candidate as in the "Statement of contribution by Co-authors" is appropriate.

Nick Seymour

_____          _____

(Full name of Co-author)                                   (Signature of Co-author)

# To whom it may concern

I, Kathryn Ross, have outlined my contributions and the contributions of Co-authors to the chapters in this Thesis that have been published as *"Spectral variability of radio sources at low frequencies"* and *"Wide-band spectral variability of peaked-spectrum sources"* and contributions to Chapter 4, *"Milliarcsecond structures of variable peaked-spectrum sources"*.

_____

(Signature of candidate)

I, as a Co-author, endorse that the level of contribution indicated by the candidate as in the "Statement of contribution by Co-authors" is appropriate.

Sarah V. White

_____           _____

(Full name of Co-author)                                    (Signature of Co-author)

# Funding, facility and software acknowledgements

bourg, France. The original description of the VizieR service was published in Ochsenbein et al. (2000). This research has made use of the NASA/IPAC Extragalactic Database (NED), which is operated by the Jet Propulsion Laboratory, California Institute of Technology, under contract with the National Aeronautics and Space Administration.

We also make use of the IPYTHON package (Pérez & Granger, 2007); SciPy (Virtanen et al., 2020); MATPLOTLIB, a PYTHON library for publication quality graphics (Hunter, 2007); ASTROPY, a community-developed core PYTHON package for astronomy (Astropy Collaboration et al., 2013; Price-Whelan et al., 2018); PANDAS, a data analysis and manipulation PYTHON module (pandas development team, 2020; Wes McKinney, 2010); and NUMPY (van der Walt et al., 2011). We also made extensive use of the visualisation and analysis packages DS9, ds9.si.edu, and Topcat (Taylor, 2005) and Ned Wright's Cosmology calculator (Wright, 2006).

# Acronyms

**AGN** active galactic nuclei.

**ALMA** Atacama Large Millimeter Array.

**ASKAP** Australian SKA Pathfinder.

**CMB** cosmic microwave background.

**CSO** compact symmetric object.

**CSS** compact steep spectrum.

**CWT** continuous wavelet transform.

**DESI** Dark Energy Spectroscopic Instrument.

**DISS** diffractive interstellar scintillation.

**ESEs** extreme scattering events.

**FFA** free-free absorption.

**FR** Fanaroff-Riley.

**FSRQ** flat spectrum radio quasar.

**GPS** Gigahertz-peaked spectrum.

**GRGs** giant radio galaxies.

**HFP** high frequency peak.

**IDV** intraday variability.

**inFFA** inhomogeneous free-free absorption.

**IPS** interplanetary scintillation.

**ISM** interstellar medium.

**ISS** interstellar scintillation.

**LERGs** low-excitation radio galaxies.

**LOFAR** LOw Frequency ARray.

**MASIV** MicroArcsecond Scintillation-Induced Variability.

**MeerKAT** Karoo Array Telescope.

**MIR** mid infra-red.

**MPS** Megahertz-peaked spectrum.

**MRO** Murchison Radio-astronomy Observatory.

**MWA** Murchison Widefield Array.

**OVRO** Owens Valley Radio Observatory.

**PS sources** peaked-spectrum sources.

**PSF** point spread function.

**RACS** Rapid ASKAP Continuum Survey.

**RFI** radio frequency interference.

**RISS** refractive interstellar scintillation.

**RMS** root mean squared.

**SGP** South Galactic Pole.

**SKA** Square Kilometre Array.

**SMBH** supermassive black hole.

**SSA** synchrotron-self absorption.

**STFT** short time Fourier transform.

**TDEs** tidal disruption events.

**uGMRT** upgraded Giant Metrewave Radio Telescope.

**VAST** variables and slow transients.

**VLASS** VLA Sky Survey.

**VLBI** very long baseline interferometry.

**WAVES** Wise Area VISTA Extra-Galactic Survey.

**WEAVE** WHT Enhanced Area Velocity Explorer.

**WISE** Wide-Field Infrared Survey Explorer.

**WISS** weak interstellar scintillation.